


 Cite this: *RSC Adv.*, 2020, **10**, 30529

## A review of molybdenum disulfide ( $\text{MoS}_2$ ) based photodetectors: from ultra-broadband, self-powered to flexible devices

 Hari Singh Nalwa 

Two-dimensional transition metal dichalcogenides (2D TMDs) have attracted much attention in the field of optoelectronics due to their tunable bandgaps, strong interaction with light and tremendous capability for developing diverse van der Waals heterostructures (vdWHs) with other materials. Molybdenum disulfide ( $\text{MoS}_2$ ) atomic layers which exhibit high carrier mobility and optical transparency are very suitable for developing ultra-broadband photodetectors to be used from surveillance and healthcare to optical communication. This review provides a brief introduction to TMD-based photodetectors, exclusively focused on  $\text{MoS}_2$ -based photodetectors. The current research advances show that the photoresponse of atomic layered  $\text{MoS}_2$  can be significantly improved by boosting its charge carrier mobility and incident light absorption *via* forming  $\text{MoS}_2$  based plasmonic nanostructures, halide perovskites– $\text{MoS}_2$  heterostructures, 2D–0D  $\text{MoS}_2$ /quantum dots (QDs) and 2D–2D  $\text{MoS}_2$  hybrid vdWHs, chemical doping, and surface functionalization of  $\text{MoS}_2$  atomic layers. By utilizing these different integration strategies,  $\text{MoS}_2$  hybrid heterostructure-based photodetectors exhibited remarkably high photoresponsivity ranging from  $\text{mA W}^{-1}$  up to  $10^{10} \text{ A W}^{-1}$ , detectivity from  $10^7$  to  $10^{15}$  Jones and a photoresponse time from seconds (s) to nanoseconds ( $10^{-9}$  s), varying by several orders of magnitude from deep-ultraviolet (DUV) to the long-wavelength infrared (LWIR) region. The flexible photodetectors developed from  $\text{MoS}_2$ -based hybrid heterostructures with graphene, carbon nanotubes (CNTs), TMDs, and  $\text{ZnO}$  are also discussed. In addition, strain-induced and self-powered  $\text{MoS}_2$  based photodetectors have also been summarized. The factors affecting the figure of merit of a very wide range of  $\text{MoS}_2$ -based photodetectors have been analyzed in terms of their photoresponsivity, detectivity, response speed, and quantum efficiency along with their measurement wavelengths and incident laser power densities. Conclusions and the future direction are also outlined on the development of  $\text{MoS}_2$  and other 2D TMD-based photodetectors.

 Received 9th April 2020  
 Accepted 17th July 2020

 DOI: 10.1039/d0ra03183f  
[rsc.li/rsc-advances](http://rsc.li/rsc-advances)

 Advanced Technology Research, 26650 The Old Road, Valencia, California 91381,  
 USA. E-mail: [nalwa@mindspring.com](mailto:nalwa@mindspring.com)


Dr Hari Singh Nalwa is a distinguished independent scientist and scholar working in the fields of nanotechnology and materials science. Dr Nalwa has authored more than 170 scientific articles, 26 book chapters, and 125 volumes of scientific books, as well as 18 patents in cross-disciplinary research areas of nanotechnology, materials science and polymer science. Dr Nalwa's research interests include ferroelectric polymers, conducting polymers, organic nonlinear optical materials for integrated optics, low- and high-dielectric constant materials for microelectronics packaging, 3D printing, two-dimensional (2D) nanomaterial-based bulk heterojunction and dye-sensitized solar cells, and multifunctional sensors for wearable technology. He received the "Award of Excellence" from the Association of American Publishers for the "Handbook of Nanostructured Materials and Nanotechnology," a 5-volume set (Academic Press, 2000), and "Best Reference Work Award" from the American Society for Engineering Education for "The Encyclopedia of Nanoscience and Nanotechnology," a 10-volume set (American Scientific Publishers, 2004). He is Founder, President, and Chief Executive Officer (CEO) of American Scientific Publishers (<http://www.aspbs.com>), which he established in 2000.



## 1. Introduction

Advances in the fields of electronics, optoelectronics and photonics have created a great demand for new functional materials that possess ease of synthesis, processing and fabrication and enable desired tailoring of the physical and chemical properties by chemical functionalization and/or formation of hybrid structures for potential applications in electronic and optoelectronic devices.<sup>1,2</sup> In this context, earth-abundant two-dimensional (2D) nanomaterials, including graphene<sup>3–12</sup> and transition metal dichalcogenides (TMDs),<sup>13–20</sup> have emerged as novel functional materials of choice due to their low-cost production, easy processing and easy deposition on different substrates with precise thickness control of the atomic layers *via* mechanical and chemical exfoliation, chemical vapor deposition (CVD) and atomic layer etching (ALE) methods. Flexible graphene nanosheets have been explored for developing wearable and portable devices, including field-effect transistors (FETs),<sup>21,22</sup> sensors,<sup>23–25</sup> supercapacitors,<sup>26–28</sup> lithium-ion batteries,<sup>29</sup> triboelectric nanogenerators,<sup>30</sup> solar cells<sup>31–33</sup> and photodetectors.<sup>34,35</sup> Following the research progress of graphene, a similar wide range of applications for flexible atomic layered TMDs have been anticipated and are now slowly emerging, from wearable electronics to optoelectronics.<sup>36–40</sup> Flexible photodetectors are becoming a key component of optoelectronic technology for a wide range of applications in the fields of surveillance, soft robotics, sensors for wearable and portable healthcare and sports, light-emitting diodes (LEDs), high-speed optical communication, and biomedical imaging.<sup>34,35,41</sup> Flexible photodetectors are gaining much attention for use in wearable optoelectronics, for which many different types of nanostructures, such as atomic layered nanosheets, nanowires (NWs), fibers, quantum dots and 3D networks of inorganic and organic materials and their nano-hybrids, have been studied. These nanostructures have been used as phototransistors, photoconductors and photodiodes for developing photodetectors from a wide variety of nanomaterials, including silicon (Si) and germanium (Ge),<sup>42,43</sup> selenium (Se),<sup>44</sup> GaP and InP,<sup>45,46</sup> CdS,<sup>47,48</sup> ZnSe,<sup>49</sup> ZnO and its hybrids with PbS, ZnS, CdO, gold (Au) and polymers,<sup>50–55</sup> ZnGa<sub>2</sub>O<sub>4</sub>,<sup>56</sup> Zn<sub>2</sub>GeO<sub>4</sub> and In<sub>2</sub>Ge<sub>2</sub>O<sub>7</sub>,<sup>57</sup> CuInSe<sub>2</sub>,<sup>58,59</sup> In<sub>2</sub>S<sub>3</sub>,<sup>60</sup> In<sub>2</sub>Se<sub>3</sub>,<sup>61</sup> Sb<sub>2</sub>S<sub>3</sub>,<sup>62</sup> Sb<sub>2</sub>Se<sub>3</sub>,<sup>63</sup> Bi<sub>2</sub>S<sub>3</sub>,<sup>64</sup> SnS,<sup>65</sup> SnS<sub>2</sub>,<sup>66</sup> ZrS<sub>3</sub>,<sup>67</sup> Zn<sub>3</sub>P<sub>2</sub>,<sup>68</sup> PbI<sub>2</sub>,<sup>69</sup> MoO<sub>3</sub>,<sup>70</sup> GaS,<sup>71</sup> SnO<sub>2</sub>,<sup>72</sup> ZnTe,<sup>73</sup> GaTe,<sup>74</sup> perovskites,<sup>75,76</sup> their hybrid composites with ZnO, gold, poly(diketopyrrolopyrrole-terthiophene) (PDPP3T) conjugated polymer, and graphene,<sup>77–80</sup> polythiophene,<sup>81</sup> carbon nanotubes (CNTs),<sup>82</sup> graphene nanocomposites with CNTs<sup>83</sup> and with ZnO quantum dots,<sup>84</sup> transition-metal trichalcogenides (MX<sub>3</sub>, where M represents a transition metal, Ti, Zr, Hf, Nb, or Ta, and X is a chalcogen, S, Se, or Te), *e.g.*, hafnium trisulfide (HfS<sub>3</sub>),<sup>85</sup> HfS<sub>3</sub> and HfSe<sub>3</sub> nanocomposites with graphene,<sup>86</sup> and graphene-based materials.<sup>87–89</sup> The important parameters including photoresponsivity, specific detectivity, noise equivalent power (NEP), photogain, external quantum efficiency (EQE), linear dynamic range (LDR), and response speed of photodetectors have already been well defined in the literature;<sup>1</sup> here, these parameters are discussed in reference to the nanomaterial-based photodetectors and especially for the MoS<sub>2</sub> atomic layer-based hybrid photodetectors.

Many research articles have been published on atomically thin layered MoS<sub>2</sub> based photodetectors, however, a comprehensive review summarizing the recent developments in MoS<sub>2</sub> photodetectors is completely lacking in the scientific literature. This review briefly introduces TMDs, including the applications of MoS<sub>2</sub> atomic layers in developing photodetectors. The tuning of optoelectronic properties by boosting the carrier mobility of and incident light absorption by MoS<sub>2</sub> atomic layers through the use of plasmonic and halide perovskite–MoS<sub>2</sub> hybrid heterostructures, 2D–0D and 2D–2D MoS<sub>2</sub> heterostructures, interface coupling effect (ICE), or chemical doping of MoS<sub>2</sub> films is discussed in order to evaluate the performance of MoS<sub>2</sub> photodetectors from the perspective of their based phototransistors, photoconductors and photodiode components. Particular emphasis is placed on atomic layered MoS<sub>2</sub>-based ultra-broadband photodetectors, from their fundamental development to self-powered to flexible photodetectors for wearable optoelectronics. The performance of pristine MoS<sub>2</sub> atomic layers and MoS<sub>2</sub> hybrid heterostructures with graphene, CNTs, TMDs, ZnO and surface functionalized MoS<sub>2</sub> atomic layers for developing flexible photodetectors is discussed in terms of their broadband photoresponsivity, detectivity, NEP, photogain, EQE, photoresponse speed, mechanical flexibility and environmental stability. Strain-induced and self-powered MoS<sub>2</sub> based hybrid photodetectors has also been summarized. Finally, the challenges in developing flexible photodetectors from TMDs are analyzed. This review should be a useful source for and inspire a wide range of audience, including researchers working in the fields of optoelectronics, sensors, materials science, nanotechnology, physics, electrical engineering, and communications.

## 2. Molybdenum disulfide (MoS<sub>2</sub>) for photodetectors

Fig. 1 shows the wide range of the electromagnetic spectrum covered by 2D nanomaterials, from the near-infrared (NIR) and mid-IR (MIR) to the far-IR (FIR), the related applications of these nanomaterials in electronics, optoelectronics and photonics, and the atomic and band structures of 2D materials, including hexagonal boron nitride (h-BN), molybdenum disulfide (MoS<sub>2</sub>), black phosphorus (BP) and graphene.<sup>90</sup> h-BN is an insulator with a large bandgap of 6.0 eV,<sup>91–95</sup> whereas MoS<sub>2</sub><sup>96–98</sup> and BP<sup>99–101</sup> are semiconductors with sizeable bandgaps that vary with the number of atomic layers. Graphene is a zero bandgap semimetal<sup>102,103</sup> and monolayer graphene exhibits 97.7% optical transparency independent of the optical wavelength in the 450–800 nm spectral region; the transparency decreases proportionally with an increasing number of graphene layers.<sup>104</sup> Monolayer graphene absorbs only 2.3% of incident white light; therefore, the photoresponsivity of monolayer (1L) graphene is rather limited due to the low absorbance in the visible region. The insulating layers of an h-BN dielectric have been used along with other 2D materials, such as graphene, BP and TMDs, including MoS<sub>2</sub>, MoSe<sub>2</sub>, WS<sub>2</sub>, WSe<sub>2</sub>, MoTe<sub>2</sub>, *etc.*, to develop electronic and optoelectronic devices.<sup>105–109</sup> Though graphene-based



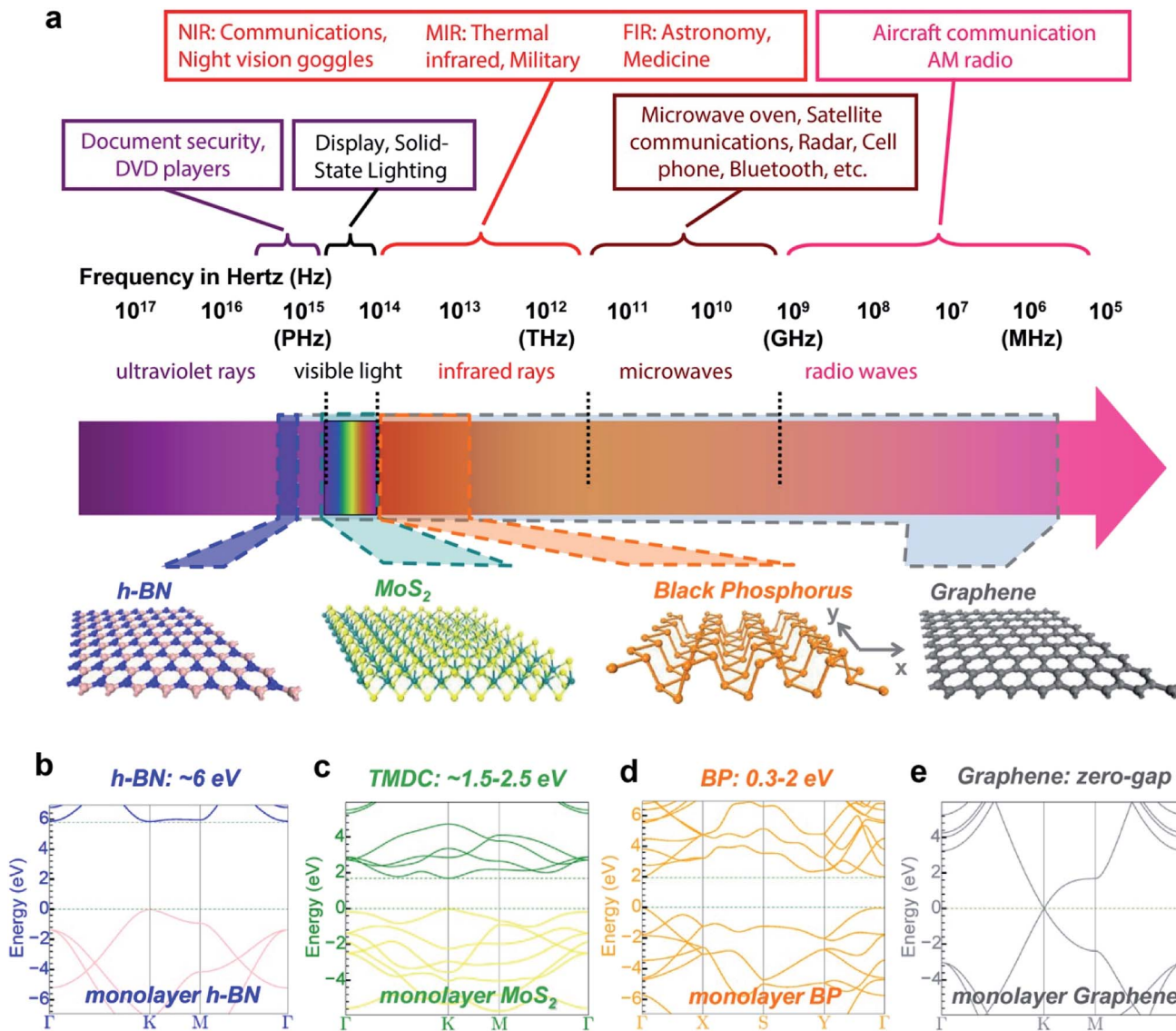


Fig. 1 (a) 2D materials covering a very wide range of the electromagnetic spectrum, from the NIR and MIR to the FIR, and their corresponding applications. The bottom section shows the atomic structures of h-BN, MoS<sub>2</sub>, black phosphorus (BP) and graphene from left to right. The electromagnetic spectral ranges covered by different 2D materials are depicted using colored polygons. (b–e) Band structures and bandgaps of monolayer h-BN (b), MoS<sub>2</sub> (c), BP (d) and gapless graphene (e). Reprinted with permission from ref. 90, copyright © 2014 Macmillan Publishers Limited.

materials have been extensively studied for use in photodetectors because of their high carrier mobility and strong interaction with light over a broad spectral range,<sup>110–113</sup> graphene-based photodetectors suffer from low photoresponsivity due to graphene's weak optical absorption.<sup>104,114</sup> Broadband photodetectors utilizing multilayer BP operating over the 532 nm to 3.39  $\mu$ m wavelength range have been fabricated by Guo *et al.*<sup>115</sup> Comparatively, TMDs have a large electronic density of states, giving rise to high optical absorption and ultrafast charge transfer, making them more suitable for photodetectors. Bernardi *et al.*<sup>116a</sup> reported 5–10% incident sunlight absorption by MoS<sub>2</sub>, MoSe<sub>2</sub>, and WS<sub>2</sub> monolayers for a thickness of  $>1$  nm, which is higher than the value of 2.3% exhibited by monolayer graphene<sup>104</sup> and one

order of magnitude higher than those of thin films of the conventional semiconductors GaAs and Si, generally used for solar energy applications. Fig. 2(a) compares the computed and measured absorbance of monolayer (1L) MoS<sub>2</sub>. The computed absorbance of 1L MoS<sub>2</sub> was obtained using density functional theory (DFT) calculations, GW method and the Bethe-Salpeter equation (BSE) while experimental absorbance was reported by Mak *et al.*<sup>96</sup> The quantitative agreement was observed between the computed and experimentally measured absorbance of 1L MoS<sub>2</sub>. Fig. 2(b) compares the optical absorbance of MoS<sub>2</sub>, MoSe<sub>2</sub>, and WS<sub>2</sub> monolayers with that of graphene, clearly showing that TMD monolayers absorb much more sunlight than graphene. The calculated flux of absorbed photons was 4.6, 3.9, 2.3, and 2.0 mA cm<sup>-2</sup> for monolayer

$\text{MoSe}_2$ ,  $\text{MoS}_2$ ,  $\text{WS}_2$  and graphene, respectively, compared with  $0.3 \text{ mA cm}^{-2}$  for GaAs and  $0.1 \text{ mA cm}^{-2}$  for Si in the form of 1 nm thin films. A monolayer TMD can absorb as much sunlight as a 50 nm thick Si film. Wang *et al.*<sup>116b</sup> summarized the band-gaps of different atomic layered 2D nanomaterials including  $\text{MoS}_2$ ,  $\text{MoSe}_2$ ,  $\text{MoTe}_2$ ,  $\text{WS}_2$ ,  $\text{WSe}_2$ ,  $\text{ReS}_2$ ,  $\text{ReSe}_2$ ,  $\text{SnS}_2$ ,  $\text{SnSe}_2$ ,  $\text{HfS}_2$ ,  $\text{HfSe}_2$ ,  $\text{ZrS}_2$ ,  $\text{ZrSe}_2$ ,  $\text{In}_2\text{Se}_3$ , black AsP, black phosphorus (BP), and h-BN with their corresponding photodetection range, varying from near ultraviolet (NUV) to long infrared (LIR) as shown in Fig. 2(c).  $\text{MoS}_2$ ,  $\text{WSe}_2$ ,  $\text{SnS}_2$ , and black phosphorus show a broadband spectral range from NUV

wavelength to mid-infrared (MIR) wavelength. The optical absorbance of  $\text{MoS}_2$  thin films can be further extended by developing diverse hybrid heterostructures.

The figure-of-merit for a photodetector is generally evaluated in terms of their photoresponsivity ( $R$ ), specific detectivity ( $D^*$ ), noise equivalent power (NEP), and the photoresponse time. The photoresponsivity is an electrical response to an incident light illumination and detectivity is associated with the lowest required optical power intensity for a photodetector to differentiate signal from the actual noise. The intensities of dark and photo currents generated as a function of applied bias voltage

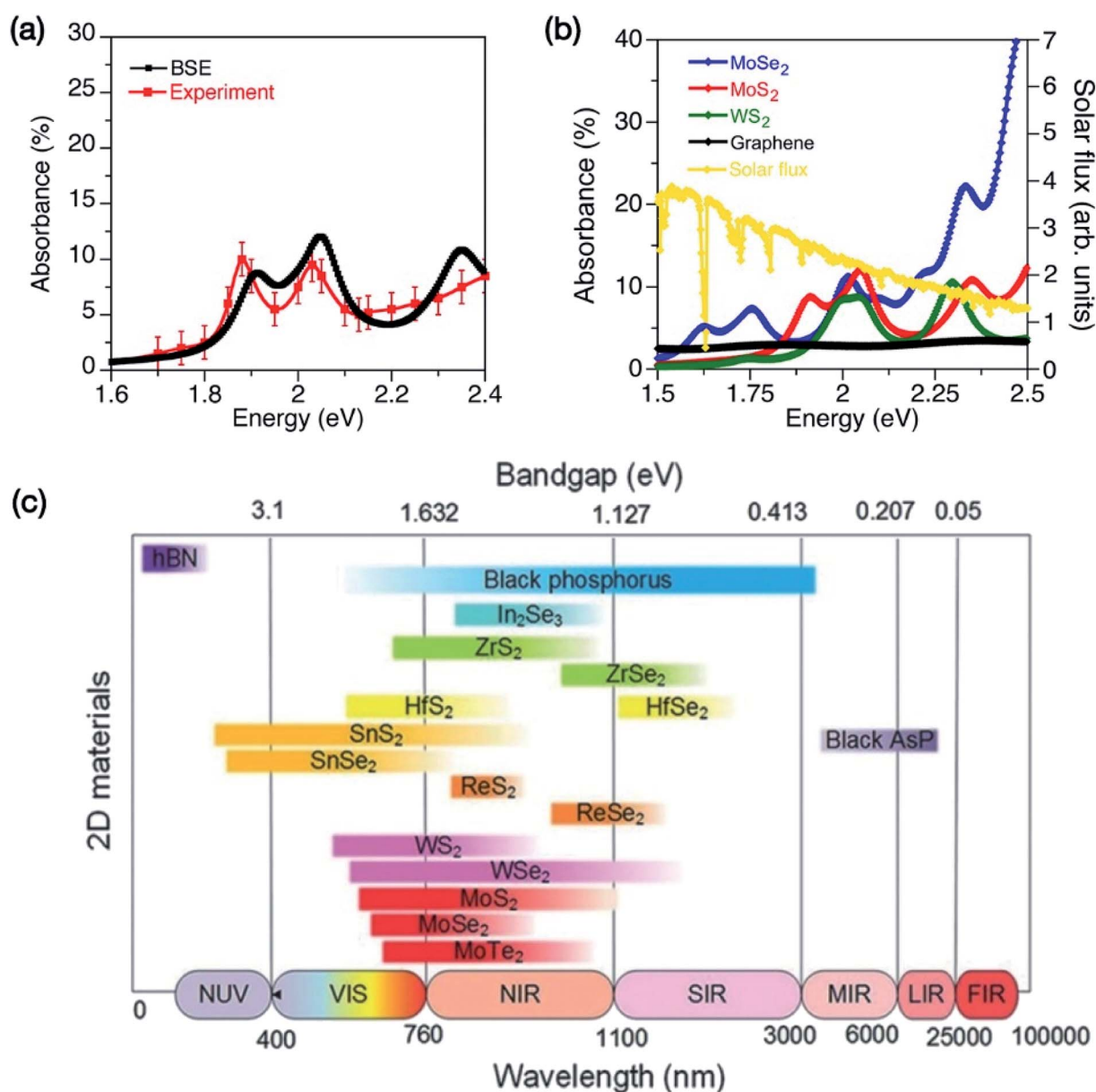


Fig. 2 (a) A comparison of the computed absorbance obtained by Bethe–Salpeter equation (BSE) with experimentally measured absorbance of a  $\text{MoS}_2$  monolayer. (b) A comparison of the optical absorbance of  $\text{MoS}_2$ ,  $\text{MoSe}_2$ , and  $\text{WS}_2$  monolayers with that of graphene along with the incident AM1.5G solar flux. Reprinted with permission from ref. 116a, copyright © American Chemical Society. (c) Band-gaps of different atomic layered 2D nanomaterials ( $\text{MoS}_2$ ,  $\text{MoSe}_2$ ,  $\text{MoTe}_2$ ,  $\text{WS}_2$ ,  $\text{WSe}_2$ ,  $\text{ReS}_2$ ,  $\text{ReSe}_2$ ,  $\text{SnS}_2$ ,  $\text{SnSe}_2$ ,  $\text{HfS}_2$ ,  $\text{HfSe}_2$ ,  $\text{ZrS}_2$ ,  $\text{ZrSe}_2$ ,  $\text{In}_2\text{Se}_3$ , black AsP, black phosphorus (BP) and h-BN) with their corresponding photodetection range varying from near ultraviolet (NUV) to long infrared (LIR). Reprinted with permission from ref. 116b, copyright © Wiley.



and the values of photoresponsivity and detectivity at different operation wavelengths and optical power intensity are compared. The photoresponse rise and decay times are also measured to find out the speed of a photodetector. TMDs, such as  $\text{MoS}_2$ ,  $\text{WS}_2$ ,  $\text{MoSe}_2$ , and  $\text{WSe}_2$ , show a tunable bandgap that change from a direct bandgap in monolayers to an indirect bandgap in multilayers. Therefore, the optoelectronic

properties of atomically thin layered TMDs can be tailored by utilizing their variable bandgaps and by improving the optical absorption by forming hybrid heterostructures. The large family of atomic layered TMDs is very attractive for their application in broadband photodetectors. For example, the internal quantum efficiency (IQE) of 85% for  $\text{MoS}_2$ ,<sup>117</sup> IQE of 70% with an ultrafast photoresponse time of 5.5 ps for  $\text{WSe}_2$ ,<sup>118</sup> IQE of 91% for  $\text{WSe}_2$ /

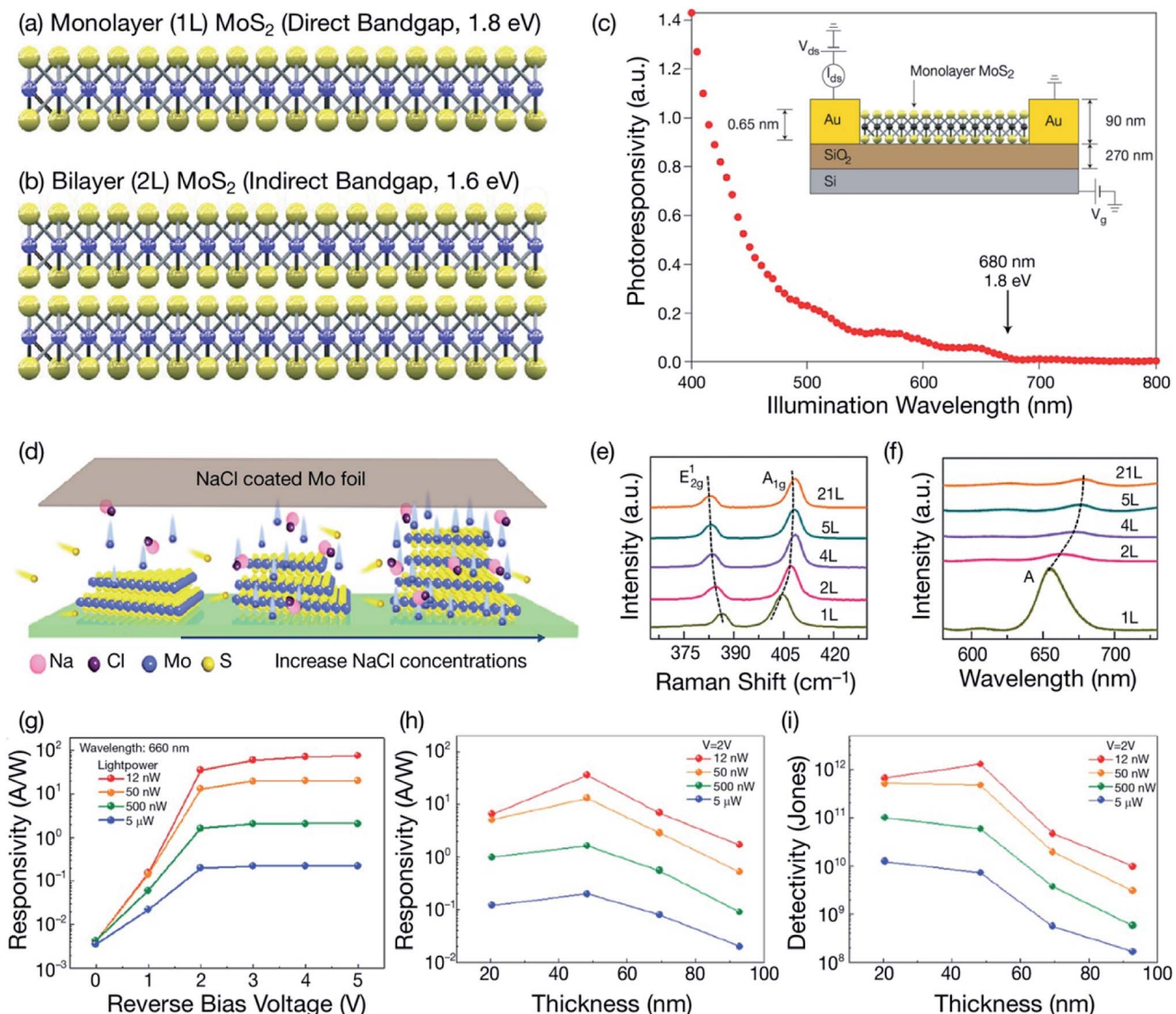


Fig. 3 (a and b) Schematic illustration of monolayer and bilayer  $\text{MoS}_2$  on an atomic scale. The blue balls represent Mo atoms, while the yellow balls represent S atoms in  $\text{MoS}_2$ . The direct bandgap of 1.8 eV observed in monolayer (1L)  $\text{MoS}_2$  transits to the indirect bandgap of 1.6 eV for bilayer (2L)  $\text{MoS}_2$  and to 1.2 eV for multilayer (ML)  $\text{MoS}_2$ .<sup>96–98</sup> In a bilayer (2L),  $\text{MoS}_2$  single layers are bound by van der Waals forces having a nanoscale distance between the adjacent layers. (c) Photoresponsivity of a monolayer  $\text{MoS}_2$  photodetector measured as a function of illumination wavelength in the 400 nm to 800 nm range. The photodetector shows an increasing photoresponsivity as the illumination wavelength is decreased from 680 nm to 400 nm. The monolayer  $\text{MoS}_2$ -based photodetectors can be used over a broad spectral range. The inset shows the structural view of a monolayer (6.5 Å thick)  $\text{MoS}_2$  photodetector deposited on a back gate substrate with Au electrodes. Reprinted with permission from ref. 171, copyright © 2013 Macmillan Publishers Limited. (d) Schematic of NaCl-assisted layer-controlled low pressure CVD growth of  $\text{MoS}_2$  flakes. (e) Layer-dependent Raman spectra of  $\text{MoS}_2$  flakes showing the variation in the modes with increasing layer thickness. (f) Layer-dependent PL spectra of  $\text{MoS}_2$  flakes. Reprinted with permission from ref. 174, copyright © American Chemical Society. (g) Photoresponsivity of the  $\text{MoS}_2$ /Si heterojunction photodetector as a function of reverse bias voltage at a 660 nm illumination wavelength under different incident laser powers. (h) Photoresponsivity of the  $\text{MoS}_2$ /Si photodetector as a function of the thickness of  $\text{MoS}_2$  flakes at a bias voltage of 2.0 V under different incident powers. (i) Detectivity of the  $\text{MoS}_2$ /Si photodetector as a function of the thickness of  $\text{MoS}_2$  flakes. Reprinted with permission from ref. 175, copyright © American Chemical Society.



MoSe<sub>2</sub> heterostructures,<sup>119</sup> photoresponsivity of 2578 A W<sup>-1</sup> for monolayer WSe<sub>2</sub>/nitrogen-doped graphene quantum dots (N-GQDs),<sup>120</sup> ultrafast charge transfer of 50 fs for MoS<sub>2</sub>/WS<sub>2</sub> heterostructures after photoexcitation,<sup>121</sup> and, interestingly, photoresponsivity as high as  $1 \times 10^{10}$  A W<sup>-1</sup> at 130 K and  $5 \times 10^8$  A W<sup>-1</sup> at room temperature for a monolayer graphene/multilayer MoS<sub>2</sub> hybrid structure illuminated at 632 nm with a power of 376 fW  $\mu\text{m}^{-2}$  with a response time of  $1 \times 10^3$  s,<sup>122</sup> demonstrate the suitability of atomic layered TMDs for developing optoelectronic devices, including photodetectors,<sup>123,124</sup> LEDs,<sup>125,126</sup> and solar cells.<sup>127-132</sup>

The bandgap in TMDs can be adjusted by changing the number of layers, which allows tuning of the optical response over a broad range of wavelengths, from the ultraviolet (UV)-visible to NIR.<sup>133-135</sup> Furthermore, the high carrier mobility and strong interaction of TMDs with light make these 2D materials interesting for optoelectronic applications. Atomically thin layered TMDs, including MoS<sub>2</sub>,<sup>136-140</sup> MoSe<sub>2</sub>,<sup>141-144</sup> MoTe<sub>2</sub>,<sup>145,146</sup> WS<sub>2</sub>,<sup>147,148</sup> WSe<sub>2</sub>/WS<sub>2</sub>,<sup>149</sup> WSe<sub>2</sub>,<sup>120,150</sup> WSe<sub>2</sub>/h-BN,<sup>151</sup> HfS<sub>2</sub>,<sup>152,153</sup> ReS<sub>2</sub>,<sup>154,155</sup> ReSe<sub>2</sub>,<sup>156,157</sup> SnS<sub>2</sub>,<sup>158,159</sup> and WSe<sub>2</sub>/SnSe<sub>2</sub>,<sup>160</sup> and the doped MoS<sub>2</sub> heterostructures<sup>161</sup> have been studied for use in broadband photodetectors. Among 2D TMDs, MoS<sub>2</sub> atomic layers have also been extensively investigated for developing MoS<sub>2</sub> hybrid heterostructure-based photodetectors in combination with other materials, including MoS<sub>2</sub>/Si,<sup>162</sup> AuNPs/MoS<sub>2</sub>,<sup>163</sup> MoS<sub>2</sub>/WS<sub>2</sub>,<sup>164</sup> MoS<sub>2</sub>/WSe<sub>2</sub>,<sup>165</sup> graphene/MoS<sub>2</sub>/WSe<sub>2</sub>/graphene,<sup>165</sup> MoTe<sub>2</sub>/MoS<sub>2</sub>,<sup>166</sup> GaTe/MoS<sub>2</sub>,<sup>167</sup> PdSe<sub>2</sub>/MoS<sub>2</sub>,<sup>168</sup> MoS<sub>2</sub>/graphene,<sup>169</sup> and MoS<sub>2</sub>/BP.<sup>170</sup> The formation of hybrid heterostructures with other materials facilitates the modification of electronic and optoelectronic properties in order to improve the photoresponse of MoS<sub>2</sub>-based photodetectors.

Several studies have demonstrated that the bandgap in MoS<sub>2</sub> can be tuned by changing the number of layers (thickness), from 1.8 eV for monolayer MoS<sub>2</sub> to 1.2 eV for multilayer MoS<sub>2</sub>.<sup>96-98</sup> This strategy could be used to adjust the optical response of MoS<sub>2</sub> over a broad spectral range. Mak *et al.*<sup>96</sup> reported the strongest direct bandgap photoluminescence (PL) in monolayer (1L) MoS<sub>2</sub>, with 1000-fold enhancement of the PL intensity compared with bilayer (2L) MoS<sub>2</sub> as well as strong emergence of photoconductivity near the direct bandgap of 1.8 eV in monolayer MoS<sub>2</sub> and approximately 1.6 eV in bilayer MoS<sub>2</sub>. These results confirm the occurrence of an indirect to direct bandgap transition using photoconductivity spectroscopy. Fig. 3(a and b) shows a schematic illustration of monolayer and bilayer MoS<sub>2</sub> on an atomic scale. In a bilayer (2L), MoS<sub>2</sub> single layers are bound by van der Waals (vdW) forces having a nanoscale distance between the adjacent layers. Atomic layer MoS<sub>2</sub> consisting of S-Mo-S atomic structures bonded through vdW forces show strong photodetection over a broad optical spectral range from the UV to IR. Lopez-Sanchez *et al.*<sup>171</sup> reported a photoresponsivity of 880 A W<sup>-1</sup> and a detectivity of  $2.5 \times 10^{10}$  Jones (Jones = cm Hz<sup>1/2</sup> W<sup>-1</sup>) for monolayer MoS<sub>2</sub> at a bias gate voltage ( $V_{BG}$ ) of -70 V and a  $V_{ds}$  of 8 V for a 561 nm wavelength under a 150 pW incident power ( $2.4 \times 10^{-1}$  mW  $\text{cm}^{-2}$ ), along with a photoresponse in the 400-680 nm wavelength range, as shown in Fig. 3(c). CVD-grown monolayer MoS<sub>2</sub> phototransistors exhibit a photoresponsivity as high as

2200 A W<sup>-1</sup>, a photogain of 5000 and a response time of 500 s at room temperature.<sup>172</sup> Pang *et al.*<sup>173</sup> developed a MoS<sub>2</sub>-based triboelectric phototransistor by combining a few-layer MoS<sub>2</sub> phototransistor with a sliding mode triboelectric nanogenerator (TENG). The photoresponsivity of the MoS<sub>2</sub> triboelectric phototransistor increased from 221.03 A W<sup>-1</sup> to 727.87 A W<sup>-1</sup> with increasing sliding distance from 0 mm to 8 mm under 10 mW  $\text{cm}^{-2}$  laser power intensity and a 1.0 V drain voltage. This result indicates that the photoresponsivity of the MoS<sub>2</sub> phototransistor can be tuned by controlling the sliding distance, enabling self-powered photodetection with a TENG.

The number of MoS<sub>2</sub> atomic layers also significantly affects the electronic and optoelectronic properties. Yang *et al.*<sup>174</sup> reported the thickness-controlled growth of MoS<sub>2</sub> using the NaCl-assisted low pressure CVD method, where the number of layers of MoS<sub>2</sub> flakes was precisely controlled by simply increasing the concentration of the NaCl promoter. The Raman and PL spectra of 1L, 2L, 4L, 5L, and 21L MoS<sub>2</sub> flakes showed an increase in the frequency difference ( $\Delta$ ) between the two characteristic Raman peaks ( $E_{2g}^1$  and  $A_{1g}$  vibration modes) from 18.3 to 25.7 cm<sup>-1</sup> and a redshift in the PL peak from 655 nm to 678 nm as the MoS<sub>2</sub> layer thicknesses increased from 1L to 21L (Fig. 3(d-f)). The intensity of the PL emission from MoS<sub>2</sub> flakes decreased dramatically with increasing number of layers because of the direct to indirect bandgap transition, and similarly, the bandgap of MoS<sub>2</sub> layers decreased with increasing layer thickness, from 1.8 eV for 1L to 1.5 eV for 2L and 1.2 eV for 25L. The optical transmittance measured at 550 nm gradually decreased with an increasing number of MoS<sub>2</sub> layers, ranging from 85.0% to 57.7%, 50.1% and 24.8% for 1L, 2L, 5L and 21L MoS<sub>2</sub>. The UV-B absorptions of 1L, 2L, 5L and 21L MoS<sub>2</sub> flakes were over 95%. The thickness-dependent optoelectronic properties of multilayer MoS<sub>2</sub> have been studied. The highest values of photoresponsivity and detectivity reached  $1 \times 10^4$  A W<sup>-1</sup> and  $8 \times 10^{12}$  Jones for monolayer-bilayer (1L-2L) heterojunctions and  $4 \times 10^3$  A W<sup>-1</sup> and  $6 \times 10^{12}$  Jones for monolayer-8-layer (1L-8L) MoS<sub>2</sub> heterojunctions at 660 nm.

In another study, Shin *et al.*<sup>175</sup> deposited mechanically exfoliated multilayer MoS<sub>2</sub> flakes onto a Si layer to develop MoS<sub>2</sub>/Si p-n heterojunction photodiodes; the optoelectronic properties were improved and optimized by controlling the number of layers of MoS<sub>2</sub> flakes. The photoresponse of the MoS<sub>2</sub>/Si photodetector was measured at 405, 520, and 660 nm wavelengths under different incident power intensities and for various thicknesses of multilayer MoS<sub>2</sub> flakes. The 2 nm thick MoS<sub>2</sub> flake-based photodiodes showed very poor performance with low photoresponsivities of  $3.36 \times 10^{-3}$  and  $6.64 \times 10^{-5}$  A W<sup>-1</sup> and detectivities of  $2.08 \times 10^6$  and  $4.11 \times 10^5$  Jones at a 660 nm wavelength under incident optical powers of 50 nW and 50  $\mu\text{W}$  at 2 V, respectively. The thickness-dependent maximum values of the photoresponsivity and detectivity were obtained for 48 nm MoS<sub>2</sub> flakes at 12 nW and 2 V. Photoresponsivities of 6.54, 35.7, 6.94, and 1.70 A W<sup>-1</sup> and detectivities of  $2.33 \times 10^9$ ,  $1.52 \times 10^{11}$ ,  $8.31 \times 10^9$ , and  $8.64 \times 10^7$  Jones were measured for the 20, 48, 69, and 92 nm thick multilayer MoS<sub>2</sub> flakes at 2 V, respectively. The thickness-dependent optoelectronic properties for atomic layered MoS<sub>2</sub> have been



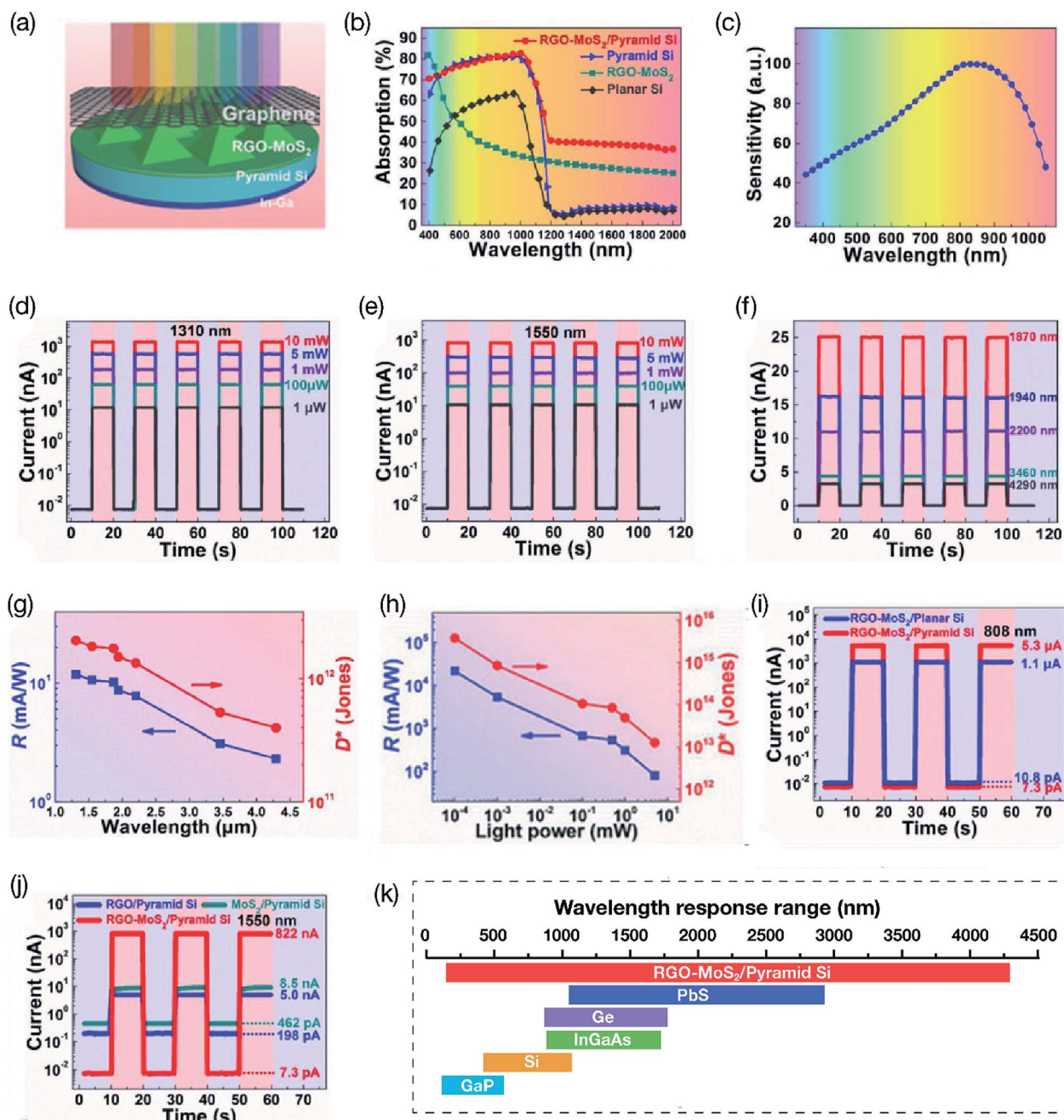


Fig. 4 (a) Schematic illustration of the 3D RGO–MoS<sub>2</sub>/pyramid Si heterojunction-based photodetector. (b) A comparison of the absorption spectra of planar and pyramid Si, RGO (also referred as rGO), and RGO–MoS<sub>2</sub>/Si heterojunction devices. (c) Photosensitivity of the RGO–MoS<sub>2</sub>/pyramid Si heterojunction-based device between 350 to 1100 nm wavelength region. (d and e) Photocurrent switching behavior of heterojunction device measured under light illuminations at 1310 and 1550 nm at zero bias voltage ( $V = 0$ ), self-powered devices. (f) Photocurrent switching behavior of heterojunction devices measured under 1870, 1940, 2200, 3460 and 4290 nm (NIR–MIR) light illuminations. (g) Photoresponsivity ( $R$ ) and specific detectivity ( $D^*$ ) curves of the heterojunction photodetector measured as a function of wavelength from 1310 nm to 4290 nm at a fixed laser power intensity of 50 mW under zero bias voltage. (h)  $R$  and  $D^*$  curves of the heterojunction photodetector measured as a function of laser power intensity at 808 nm at the 100 nW laser power under zero bias voltage. (i) A comparison of the photocurrent switching behavior of RGO–MoS<sub>2</sub>/pyramid Si and RGO–MoS<sub>2</sub>/planar Si heterojunction devices measured at 808 nm wavelength under 1  $\mu$ W laser power intensity. (j) A comparison of the photocurrent switching behavior of RGO–MoS<sub>2</sub>/pyramid Si heterojunction device with RGO/pyramid Si and MoS<sub>2</sub>/pyramid Si devices measured at 1550 nm wavelength under 10 mW laser power intensity. (k) A comparison of the wavelength coverage by the RGO–MoS<sub>2</sub>/pyramid Si heterojunction-based photodetector along with other traditional semiconductor-based photodetectors. The RGO–MoS<sub>2</sub>/pyramid Si hybrid heterojunction-based photodetectors operated from 350 nm to 4.3  $\mu$ m (UV to MIR) ultra-broadband spectral range due to the bandgap narrowing caused by the S vacancy defects in MoS<sub>2</sub> crystals. Reprinted with permission from ref. 178, copyright © Wiley.

studied. Yang *et al.*<sup>176</sup> fabricated photodetectors using MoS<sub>2</sub> films with thicknesses greater than 6 nm, which showed a fast photoresponse time of <1 ms and a current  $I_{on}/I_{off}$  ratio of  $\sim 10^4$ . The MoS<sub>2</sub> photodetector developed from a 9 nm thick MoS<sub>2</sub> film showed an 8 nA current at a 3 V bias voltage in the dark. The current increased to 1.47 and 13.5  $\mu$ A at 30 and 140  $\mu$ W, respectively. The current  $I_{on}/I_{off}$  ratio of the MoS<sub>2</sub> photodetector increased from  $\sim 10^1$  to  $\sim 10^4$  for the 2 nm to 9 nm thick MoS<sub>2</sub> film but decreased by two orders of magnitude to  $10^2$  for the 32 nm thick film. Therefore, a MoS<sub>2</sub> film with a 9 nm thickness was used as the active layer for fabricating a MoS<sub>2</sub> photodetector. The current of the MoS<sub>2</sub> photodetector measured by irradiating it with 532 nm laser light at a 3 V bias showed a rapid increase to 25  $\mu$ A and then decreased to 8 nA after turning off the laser light. Fig. 3(g-i) shows the photoresponsivity of the MoS<sub>2</sub>/Si heterojunction photodetector as a function of reverse bias voltage and thickness of MoS<sub>2</sub> flakes under different incident powers. The photodetector based on 48 nm thick MoS<sub>2</sub> flakes showed a low noise equivalent power (NEP) value of  $7.82 \times 10^{-15}$  W Hz<sup>-1/2</sup> at a 10 Hz frequency and a reverse bias voltage of 4.0 V, lower than the NEP of  $3 \times 10^{-14}$  W Hz<sup>-1/2</sup> for the Si avalanche photodiode.<sup>177</sup> Ling *et al.*<sup>139</sup> also studied thickness-dependent photoresponse of MoS<sub>2</sub> photodetectors. The photoresponsivity increased from 0.4 A W<sup>-1</sup> for bilayer MoS<sub>2</sub> photodetector to 1.8 A W<sup>-1</sup> for 5L MoS<sub>2</sub> at 850 nm wavelength under a bias voltage of 5 V because of the enhanced photoabsorption. The EQE value of a 5L MoS<sub>2</sub> photodetector was found to increase from 30% at 1 V to 263% at 5 V. The 2L MoS<sub>2</sub> photodetector showed detectivity over  $10^9$  Jones, much higher compared with 3L and 5L MoS<sub>2</sub> photodetectors due to the low dark current. As seen from the above studies, multilayer MoS<sub>2</sub> is more appealing for developing broadband photodetectors due to its smaller indirect bandgap and extended optical spectral range compared with monolayer MoS<sub>2</sub>, although further improvement of the photoresponsivity and detectivity is still needed.

### 3. Strategies for boosting the performance of MoS<sub>2</sub> photodetectors using hybrid heterostructures

The outstanding features of atomic layered MoS<sub>2</sub>, such as the high optical transparency and carrier mobility, ultrafast photoresponse, and photodetection from the UV to IR, make MoS<sub>2</sub> highly desirable for developing broadband photodetectors. However, the low optical absorption by MoS<sub>2</sub> atomic layers hinders in achieving the high performance of photodetectors; therefore, different strategies have been applied to improve the photoresponse by generating abundant photo-excited carriers. Though the absorption of light by the MoS<sub>2</sub> atomic layers is an intrinsic property, the light absorption can be further enhanced in MoS<sub>2</sub> hybrid heterostructures by utilizing the supplementary light absorption of secondary integrated components in the hybrid structures. In addition to the incident light absorption, the carrier mobility of MoS<sub>2</sub> can be dramatically increased by forming hybrid heterostructures and nanocomposites with

a diverse range of inorganic, organic and polymeric materials to develop MoS<sub>2</sub> hybrid heterostructure-based high-performance ultrabroadband photodetectors. The large bandgap and limited absorption of visible light ( $\sim 10\%$ ) displayed by monolayer MoS<sub>2</sub> hinder the attainment of a high power conversion efficiency, which eventually restricts the application of MoS<sub>2</sub> atomic layers in broadband photodetectors. The intrinsic photoresponse of atomic layered MoS<sub>2</sub> is rather constrained; therefore, different strategies have been explored to boost the carrier mobility and optical absorption of MoS<sub>2</sub> layers to improve the overall optoelectronic properties by maneuvering the electronic band structure. Different strategies such as control of atomic-layer thickness, hybrid heterostructures formation, chemical doping, surface functionalization, strain and defect engineering have been used for boosting the performance of MoS<sub>2</sub> photodetectors which are discussed throughout this article.

Diverse MoS<sub>2</sub> hybrid heterostructures with other inorganic, organic and 2D nanomaterials have been developed for extending the light absorption wavelengths and improving the charge transfer process. For example, Xiao *et al.*<sup>178</sup> reported reduced graphene oxide (RGO)-MoS<sub>2</sub>/pyramid Si heterostructure-based photodetectors where 3L graphene and indium-gallium (In-Ga) alloy were used as top and bottom electrodes, respectively. Fig. 4 shows a schematic illustration of the 3D RGO-MoS<sub>2</sub>/pyramid Si heterojunction-based photodetector, a comparison of the absorption spectra of planar and pyramid Si, RGO (also referred to as rGO), and RGO-MoS<sub>2</sub>/Si heterojunction devices, photosensitivity between 350 to 1100 nm wavelength region, photocurrent switching behavior under light illuminations, wavelength and laser-power dependent photoresponsivity ( $R$ ) and specific detectivity ( $D^*$ ) of RGO-MoS<sub>2</sub>/Si heterojunction-based photodetector under zero bias voltage and wavelength range covered by the RGO-MoS<sub>2</sub>/pyramid Si heterojunction-based photodetector. The photovoltage of RGO-MoS<sub>2</sub>/Si heterojunction photodetector increased from 180 to 276 mV as the light power intensity was increased from 100 nW to 1 mW, which evidenced the self-powered operation of this photodetector at zero bias voltage ( $V = 0$ ). Furthermore, hetero-junction photodetector showed the photoresponsivity of 21.8 A W<sup>-1</sup> and detectivity of  $3.8 \times 10^{15}$  Jones at an 880 nm wavelength and a very broad optical spectrum range from the UV (350 nm) to mid-IR (4.3  $\mu$ m). The self-driven heterojunction photodetectors exhibited photoresponsivity values of 2 to 11 mA W<sup>-1</sup> and detectivity of 0.4 to  $2 \times 10^{12}$  Jones in the NIR-MIR (1870–4290 nm) range. The origin of high photoresponse over such an ultra-broadband range lies on several factors. In this RGO-MoS<sub>2</sub>/pyramid Si heterostructure, the light absorption was increased by the pyramid Si structure while highly conductive RGO assisted in enhancing the charge separation and transfer process. The RGO-MoS<sub>2</sub>/Si heterojunction shows maximum photoresponse at 800–900 nm. The light-harvesting by nanostructured pyramid Si surface was found to be 20% higher compared to planar Si in the 400 to 1000 nm spectral range. The photocurrent of RGO-MoS<sub>2</sub>/pyramid Si device (5.3  $\mu$ A) was found to be five times higher than that of the RGO-MoS<sub>2</sub>/planar Si device (1.1  $\mu$ A) at 808 nm.



Both pyramid and planar Si substrates barely absorb light over 1100 nm due to the bandgap of 1.1 eV. The integration of pyramid Si nanostructured surface assisted in extending the light absorption of the heterojunction in the NIR range. On the other hand, the RGO–MoS<sub>2</sub> composite exhibits strong light absorption up to 2 μm and dominant photovoltaic property at 1310 and 1550 nm where the corresponding current  $I_{on}/I_{off}$  ratios of  $1.9 \times 10^6$  and  $1.2 \times 10^6$  and detectivity values of  $2.04 \times 10^{12}$  and  $1.8 \times 10^{12}$  Jones were measured, respectively. Electron–hole pairs are generated in the RGO–MoS<sub>2</sub>/Si heterojunction under light illumination and then get separated at the heterojunction interface due to the built-in-electric field. The RGO–MoS<sub>2</sub>/pyramid Si heterojunction device also displayed faster rise/decay times of 2.8 μs/46.6 μs compared with 32.6 μs/87.8 μs for the MoS<sub>2</sub>/pyramid Si device due to the increased conductivity and internal electric field. The defects in MoS<sub>2</sub> assist in absorbing the light from NIR to MIR wavelength range, as a result photoexcited carriers from MoS<sub>2</sub> are transferred to the RGO layer, giving rise to the photocurrent in the NIR–MIR region. Therefore, the RGO–MoS<sub>2</sub>/pyramid Si heterojunction-based photodetector was able to operate from 350 nm to 4.3 μm (UV to MIR) ultrabroad spectral range due to the bandgap narrowing caused by the S vacancy defects in MoS<sub>2</sub> crystals. XPS measurements and theoretical calculation also confirmed the existence of S vacancies where Mo/S atomic ratios of 1 : 2, 1 : 1.87 and 1 : 163 yielded bandgaps of 1.18, 0.30 and 0.28 eV, respectively, indicating a dramatic reduction in the bandgap of MoS<sub>2</sub>. These results demonstrated that the formation of a hybrid heterostructure and occurring S vacancy defects in MoS<sub>2</sub> crystals contributed to the high performance of the RGO–MoS<sub>2</sub>/pyramid Si heterojunction-based ultra-broadband photodetectors. In another study, Peng *et al.*<sup>179</sup> used an rGO layer as the conducting channel and a perovskite/MoS<sub>2</sub> bulk heterojunction (BHJ) as a photosensitizer for developing a hybrid photodetector that showed a photoresponsivity of  $1.08 \times 10^4$  A W<sup>-1</sup>, a detectivity of  $4.28 \times 10^{13}$  Jones, an EQE value of  $2.0 \times 10^6\%$ , and a >45 ms photoresponse time. The high photoresponse in the hybrid heterostructured system originated from the hole transfer from the perovskite to the rGO layer, facilitated by the suppression of the recombination of photocarriers from the perovskite/MoS<sub>2</sub> BHJ along with electron trapping in the MoS<sub>2</sub> layers.

Another common technique of improving the performance of MoS<sub>2</sub> photodetectors is *via* chemical doping. For example, Kang *et al.*<sup>180</sup> demonstrated that the field-effect mobility increased from  $28.75 \text{ cm}^2 \text{ V}^{-1} \text{ s}^{-1}$  to  $142.2 \text{ cm}^2 \text{ V}^{-1} \text{ s}^{-1}$  and the photoresponsivity increased from  $219 \text{ A W}^{-1}$  to  $5.75 \times 10^3 \text{ A W}^{-1}$  for APTES/MoS<sub>2</sub> hybrid phototransistors after aminopropyltriethoxysilane (APTES) doping of monolayer MoS<sub>2</sub>. The 24.5-fold increase in the photoresponsivity of the APTES/MoS<sub>2</sub> photodetector resulted from the enhanced photocurrent after APTES doping. The photoresponsivity of APTES/MoS<sub>2</sub> devices reached  $1212.8 \text{ A W}^{-1}$  at a gate bias voltage of  $V_g = 0$  and a  $V_{ds}$  of 5 V for a 520 nm wavelength under an incident power of  $5.8 \text{ mW cm}^{-2}$ . Yu *et al.*<sup>181</sup> used mechanically exfoliated monolayer MoS<sub>2</sub> nanosheets sensitized with rhodamine 6G (R6G) organic dye to develop a photodetector with an enhanced photoresponse. The

dye-sensitized MoS<sub>2</sub>/R6G-based photodetector showed a photoresponsivity of  $1.17 \text{ A W}^{-1}$ , a detectivity of  $1.5 \times 10^7$  Jones, an EQE of 280% at 520 nm under an incident power of 1 μW and a photoresponse between wavelengths of 405 and 980 nm arising from charge transfer from the rhodamine 6G dye to monolayer MoS<sub>2</sub>. In addition to photosensitive dyes, the high- $\kappa$  Al<sub>2</sub>O<sub>3</sub> dielectric has been used for enhancing the photoresponse of MoS<sub>2</sub> photodetectors. Huang *et al.*<sup>182</sup> used zinc phthalocyanine (ZnPc) organic dye on the surface of monolayer MoS<sub>2</sub> to create a charge transfer interface. Dark and photocurrent of the dye-sensitized ZnPc-treated MoS<sub>2</sub> photodetectors increased by  $10^3$  to  $10^5$  times after a 30 nm thick top Al<sub>2</sub>O<sub>3</sub> passivation layer was used. The photoresponsivity of 281 and  $1.74 \text{ A W}^{-1}$  were recorded for the bare MoS<sub>2</sub> and ZnPc-treated MoS<sub>2</sub> devices at 532 nm under light intensity of  $0.07 \text{ mW cm}^{-2}$ , respectively. The photoresponse of the Al<sub>2</sub>O<sub>3</sub>-passivated MoS<sub>2</sub>/ZnPc hybrid photodetector was significantly improved: the photoresponsivity increased from  $430 \text{ A W}^{-1}$  to  $1.4 \times 10^4 \text{ A W}^{-1}$  as the light intensity changed from  $3.64 \text{ mW cm}^{-2}$  to  $0.07 \text{ mW cm}^{-2}$  under a gate bias of 40 V, respectively. The photoresponse of the MoS<sub>2</sub>/ZnPc hybrid device was 100 times faster than that of a pristine MoS<sub>2</sub> device. Wu *et al.*<sup>183</sup> demonstrated a photoresponsivity of  $2.7 \times 10^4 \text{ A W}^{-1}$  for a MoS<sub>2</sub> photodetector using an Al<sub>2</sub>O<sub>3</sub>/ITO/SiO<sub>2</sub> substrate, which increased the light absorption of MoS<sub>2</sub> thin films. The high- $\kappa$  Al<sub>2</sub>O<sub>3</sub> dielectric also yielded a current  $I_{on}/I_{off}$  ratio of  $10^9$  under a 2 V gate bias voltage, a mobility of  $84 \text{ cm}^2 \text{ V}^{-1} \text{ s}^{-1}$  and a subthreshold swing of 104 mV dec<sup>-1</sup>.

Several different strategies including MoS<sub>2</sub> plasmonic heterostructures, chemical doping of MoS<sub>2</sub> layers, halide perovskites, 2D–0D MoS<sub>2</sub>/QDs heterostructures, and 2D–2D MoS<sub>2</sub>/vdWHs hybrid heterostructures have been employed for boosting the light absorption efficiency of MoS<sub>2</sub> thin films, hence improving the performance of MoS<sub>2</sub> photodetectors. The strategies assist in terms of increasing the carrier mobility and the absorption of incident sunlight by MoS<sub>2</sub> hybrid heterostructures.

### 3.1 MoS<sub>2</sub> plasmonic heterostructures

The plasmonic nanostructures have been used for enhancing the optical absorption of semiconductor-based photodetectors. The photoresponse of atomic layered MoS<sub>2</sub> photodetectors has been optimized by forming hybrid plasmonic heterostructures for light-harvesting. The gold nanoparticles (AuNPs)@MoS<sub>2</sub> heterostructure-based plasmonic photodetectors having AuNPs core and ML MoS<sub>2</sub> shell showed 10-fold increase in photoresponsivity ( $0.5 \text{ A W}^{-1}$ ) compared with pristine MoS<sub>2</sub> phototransistors ( $0.057 \text{ A W}^{-1}$ ).<sup>163</sup> The maximum photoresponsivity of  $30 \text{ A W}^{-1}$  was achieved for the Si-supported AuNPs@MoS<sub>2</sub> heterojunction-based gateless photodetector greater than that of Si/MoS<sub>2</sub> heterojunction ( $1.1 \text{ A W}^{-1}$ ) phototransistors. Bang *et al.*<sup>184</sup> developed a monolayer (1L) MoS<sub>2</sub> photodetector exploiting the surface plasmon of a one-dimensional (1D) silver nanowire (AgNW) network. Fig. 5(a–d) shows the schematic diagram of the 1L-MoS<sub>2</sub>/AgNW-based photodetector, dark field image of a hybrid photodetector, and photocurrent–voltage



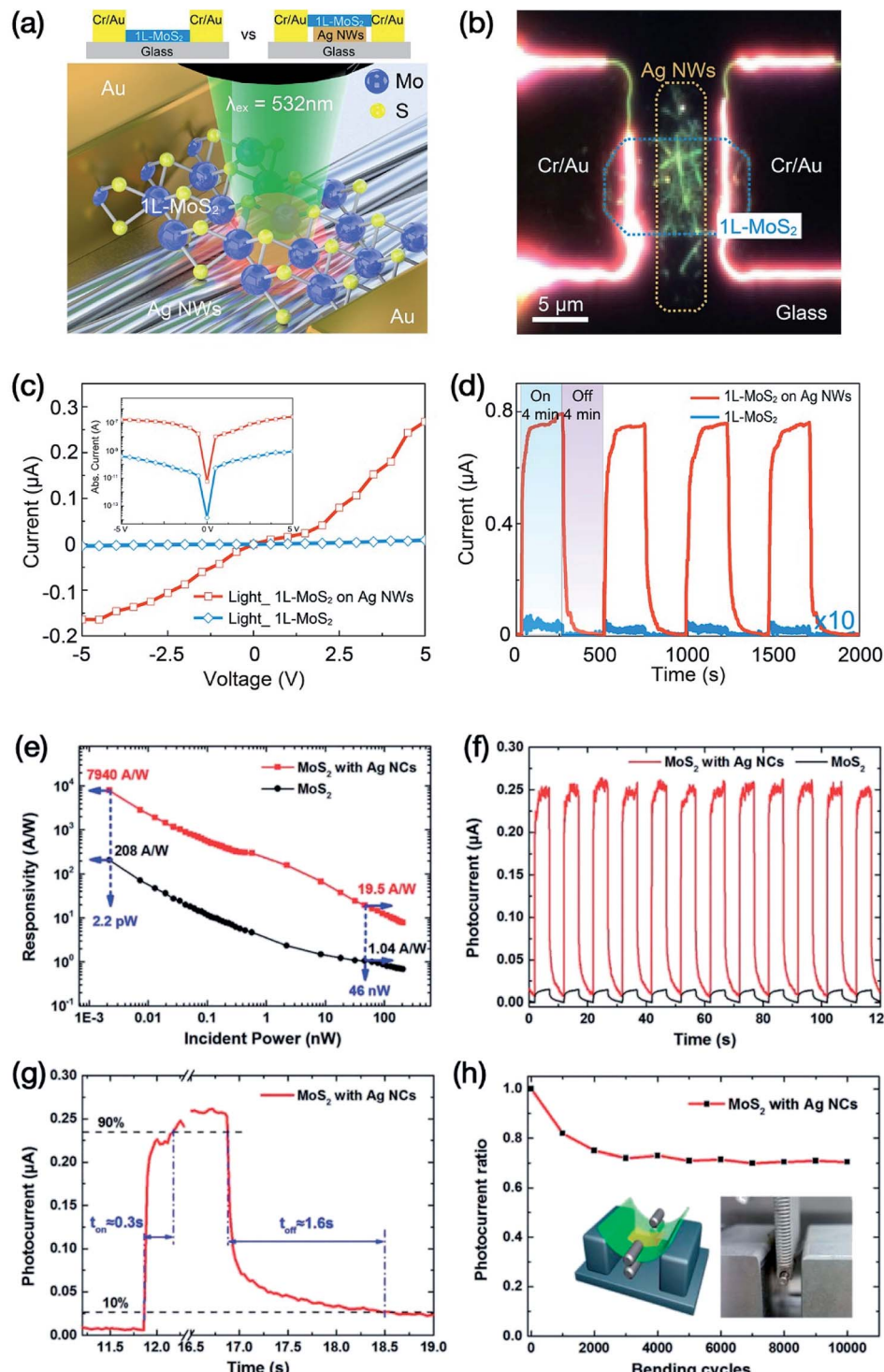


**Fig. 5** (a) Schematic diagram of the 1L-MoS<sub>2</sub> and Ag nanowires (NWs) based photodetector. Upper area shows the schematic diagrams of the pristine 1L-MoS<sub>2</sub> and the 1L-MoS<sub>2</sub>/AgNWs hybrid photodetector on a glass substrate along with Cr/Au electrodes. (b) Dark field image of the 1L-MoS<sub>2</sub>/AgNWs hybrid photodetector (60% density of AgNWs). (c) A comparison of the photocurrent–voltage curves between pristine 1L-MoS<sub>2</sub> (blue line) and the 1L-MoS<sub>2</sub>/AgNWs hybrid photodetector (red line) measured at 532 nm. The inset represents a logarithmic scale of the photocurrent–voltage characteristic. (d) Time dependent photocurrent of the pristine 1L-MoS<sub>2</sub> (blue) and 1L-MoS<sub>2</sub>/AgNWs hybrid photodetectors (red) recorded with an  $I_{on}/I_{off}$  time of 4 min. Reprinted with permission from ref. 184, copyright © American Chemical Society. (e) Photoresponsivity of MoS<sub>2</sub> and MoS<sub>2</sub>/Ag nanocubes (NCs) hybrid-based photodetectors as a function of incident laser power. (f) A comparison of the transient photocurrent of MoS<sub>2</sub> and MoS<sub>2</sub>/Ag nanocubes (NCs) photodetectors under periodical  $I_{on}/I_{off}$  illumination at 1 V. (g) Photocurrent rise ( $t_{on}$ ) and decay ( $t_{off}$ ) times of MoS<sub>2</sub>/Ag NCs hybrid-based photodetector. (h) Photocurrent of MoS<sub>2</sub>/Ag NCs hybrid-based photodetector as a function of number of bending cycles, where the insets show schematic and photograph of a bending setup. Reprinted with permission from ref. 186, copyright @ Wiley.

curves of pristine 1L-MoS<sub>2</sub> and the 1L-MoS<sub>2</sub>/AgNWs hybrid photodetectors as a function of applied voltage (from -5 V to +5 V) and the time-dependent photocurrents. The current  $I_{\text{on}}/I_{\text{off}}$  ratios of  $1.39 \times 10^4$  and 62.97 were measured for the 1L MoS<sub>2</sub>/AgNW hybrid and pristine 1L-MoS<sub>2</sub> photodetectors, respectively. The 1L MoS<sub>2</sub>/AgNW hybrid heterostructure-based device showed 560- and 250-fold increases in the PL and photocurrent, respectively, compared with the pristine 1L MoS<sub>2</sub> device. Similarly, the photoresponsivity of  $59.60 \text{ A W}^{-1}$  and detectivity of  $4.51 \times 10^{10} \text{ Jones}$  for the 1L MoS<sub>2</sub>/AgNW hybrid photodetector were 1000 times enhanced compared to those of the pristine 1L-MoS<sub>2</sub> photodetector ( $0.05 \text{ A W}^{-1}$  and  $4.11 \times 10^7 \text{ Jones}$ ). The significant improvement in the optoelectronic properties of the 1L MoS<sub>2</sub>/AgNW hybrid photodetector occurred due to the surface plasmon coupling of the AgNW network. In another study, Jing *et al.*<sup>185</sup> enhanced the localized surface plasmon resonance (LSPR) by depositing Ag nanoparticles onto monolayer MoS<sub>2</sub> for developing phototransistors. AgNPs/MoS<sub>2</sub> hybrid-based phototransistors showed a 470% increase in photoresponsivity, changing from  $5.35 \times 10^3 \text{ A W}^{-1}$  to  $2.97 \times 10^4 \text{ A W}^{-1}$  at 610 nm for 25 nm AgNPs. The interactions between MoS<sub>2</sub> layers and light are enhanced by the integrated Au or Ag nanostructures due to the LSPR, which significantly improves the photoresponse of plasmon heterostructure-based hybrid MoS<sub>2</sub> photodetectors. Sun *et al.*<sup>186</sup> used silica layer-coated silver nanocubes (AgNCs) with optimized LSP in the gap mode for developing a flexible MoS<sub>2</sub> photodetector. The PL spectrum of MoS<sub>2</sub>/Ag nanocubes hybrid was found to be significantly enhanced compared with MoS<sub>2</sub> film after modifying of Ag NCs with underneath Ag thin film due to interactions between the MoS<sub>2</sub> excitons and LSP in the gap mode. Fig. 5(e–g) compare the photoresponsivity and photocurrent of MoS<sub>2</sub> and flexible MoS<sub>2</sub>/Ag nanocubes (NCs) hybrid-based photodetectors as a function of incident laser power and time, respectively. Photocurrent rise ( $\tau_{\text{rise}}$ ) and decay ( $\tau_{\text{decay}}$ ) times and mechanical stability of flexible MoS<sub>2</sub>/AgNCs hybrid-based photodetector are also depicted. The photocurrents of the photodetectors fabricated using pristine MoS<sub>2</sub> film and MoS<sub>2</sub> film with underneath Ag film were almost the same (48–50 nA) at 3 V under 520 nm laser illumination with 46 nW incident power whereas the photocurrent of flexible photodetector having MoS<sub>2</sub> film in the gap of Ag layer and AgNCs was considerably increased to 0.91  $\mu\text{A}$  under similar experimental conditions due to the Ag nanocubes. The AgNCs decorated MoS<sub>2</sub> film shows 19-fold increment in photocurrent compared with pristine MoS<sub>2</sub> film. The photoresponsivity of MoS<sub>2</sub> with AgNCs based flexible photodetector increased 38 times to  $7940 \text{ A W}^{-1}$  at 3 V under 2.2 pW incident power compared with pristine MoS<sub>2</sub> film with decreasing incident power intensity due to the reduced scattering and recombination of the photogenerated charge carriers. Photocurrent rise time ( $\tau_{\text{rise}}$ ) of 0.3 s and decay time ( $\tau_{\text{decay}}$ ) of 1.6 s were estimated for the flexible MoS<sub>2</sub>/AgNCs hybrid-based photodetector. The flexible photodetector showed good mechanical stability after bending at a curvature of 8 mm for 10 000 times because 71% photocurrent ratio of devices was retained. The photocurrent initially decreased up to 3000 bending cycles, but no noticeable decrease in photocurrent ratio was observed thereafter. These

studies show that the integration of plasmonic nanostructures with MoS<sub>2</sub> atomic layers can significantly increase the photoresponsivity of MoS<sub>2</sub> based photodetectors.

### 3.2 Chemical doping of MoS<sub>2</sub> layers

As discussed above, performance of MoS<sub>2</sub> photodetectors can be significantly increased by doping MoS<sub>2</sub> layers with APTES,<sup>180</sup> rhodamine 6G<sup>181</sup> and ZnPc<sup>182</sup> organic dyes, which efficiently generate charge transfer interfaces between MoS<sub>2</sub> and chemical dopants. A few examples of boosting the performance of MoS<sub>2</sub> photodetectors *via* chemical doping are presented here. Heo *et al.*<sup>187</sup> used n-type doping of MoS<sub>2</sub> flakes with triphenylphosphine (PPh<sub>3</sub>) to improve the electronic and optoelectronic properties of multilayer MoS<sub>2</sub> by utilizing charge transfer from PPh<sub>3</sub> to MoS<sub>2</sub>, in which the PPh<sub>3</sub> doping concentration ranged from  $1.56 \times 10^{11}$  to  $9.75 \times 10^{12} \text{ cm}^{-2}$ . The PPh<sub>3</sub> doping considerably increased the mobility from 12.1 to  $241 \text{ cm}^2 \text{ V}^{-1} \text{ s}^{-1}$  and the  $I_{\text{on}}/I_{\text{off}}$  current ratio from  $8.72 \times 10^4$  to  $8.70 \times 10^5$  for the MoS<sub>2</sub> transistor. The photoresponsivity of the MoS<sub>2</sub> photodetector similarly increased from  $2.77 \times 10^3$  to a maximum value of  $3.92 \times 10^5 \text{ A W}^{-1}$  under an applied laser power of 5 pW. The detectivity decreased by three orders of magnitude, from  $6.82 \times 10^{13} \text{ Jones}$  to  $2.36 \times 10^{10} \text{ Jones}$ , as the device doping temperature was increased from 150 °C to 350 °C. The MoS<sub>2</sub> photodetector also showed long-term stability, where the photoresponsivity decreased by 1.58% after 14 days of exposure to air; additionally, the PPh<sub>3</sub> doping was reversible, allowing repetitive use of the photodetector device. For example, a MoS<sub>2</sub>/Si heterojunction-based photodetector showed no degradation in the photovoltage after storing in an air atmosphere over a period of a month.<sup>162</sup>

The chemical doping of monolayer MoS<sub>2</sub> film over a  $13 \text{ cm}^2$  area for developing photodetector devices was reported by Kim *et al.*<sup>161</sup> The n-type MoS<sub>2</sub> semiconductor transitions into the p-type semiconductor after doping with Nb. Raman spectroscopy, X-ray photoelectron spectroscopy (XPS), and photoluminescence (PL) spectroscopy were used to characterize the doped MoS<sub>2</sub>. The Nb-doped MoS<sub>2</sub> showed binding energy peaks at lower values compared with MoS<sub>2</sub>. The Nb- and Mn-doped monolayer MoS<sub>2</sub> FETs showed p-type and n-type doped MoS<sub>2</sub> characteristics, respectively. Fig. 6 shows doped MoS<sub>2</sub> photodetectors, transfer curves (drain current *versus* gate voltage) and photoresponsivity of Nb-doped MoS<sub>2</sub> photodetectors as a function of optical power and compares the photoresponsivity, EQE, and detectivity of Nb-doped MoS<sub>2</sub> photodetectors with undoped MoS<sub>2</sub> photodetectors at different laser wavelengths. A sublinear relationship ( $R \propto P^\alpha$ ) was observed for Nb-doped MoS<sub>2</sub> photodetector between photoresponsivity ( $R$ ) and optical power ( $P$ ), which yielded an  $\alpha$  value of -0.9 using the power function fitting method. The Nb-doped MoS<sub>2</sub> photodetector showed photoresponsivity of  $2 \times 10^5 \text{ A W}^{-1}$ , which is  $10^6$  times higher compared with the photoresponsivity of  $0.52 \text{ A W}^{-1}$  for the MoS<sub>2</sub> film measured under similar conditions at a 550 nm laser wavelength. The highest photoresponsivity of  $4.83 \times 10^5 \text{ A W}^{-1}$  was recorded at 750 nm wavelength for the Nb-doped MoS<sub>2</sub> photodetector. Likely, the EQE for Nb-doped MoS<sub>2</sub>



photodetector was found to be  $9.31 \times 10^7\%$ , which was 10 times higher compared with EQE of 107% for the MoS<sub>2</sub> device at 450 nm wavelength. The Nb-doped MoS<sub>2</sub> photodetector showed detectivity of  $5.0 \times 10^{12}$  Jones, compared with the detectivity of  $3.93 \times 10^8$  Jones for the updoped MoS<sub>2</sub> photodetector at 750 nm wavelength, which resulted in 10<sup>5</sup> times higher detectivity after Nb-doping. The photocurrent values of Nb-doped MoS<sub>2</sub> devices were also increased by 10<sup>5</sup> folds due to the charge-transfer process. The Nb-doped MoS<sub>2</sub> devices also exhibited faster rise/decay times of 4.9 ms and 5.7 ms compared with 0.63 s and 1.63 s for the updoped MoS<sub>2</sub> devices at 550 nm laser wavelength, respectively. The Nb-doped MoS<sub>2</sub> photodetector devices showed stability for 30 days under ambient conditions.

The phototransistors utilizing hybrid MoS<sub>2</sub>/PbS QDs, were fabricated by Pak *et al.*<sup>188</sup> in which the PbS QDs were surface modified with n-type tetrabutylammonium iodide (TBAI) and p-type 1,2-ethanedithiol (EDT) ligands to develop p-n junctions. The MoS<sub>2</sub>/PbS-TBAI/PbS-EDT hybrid device showed a photoresponsivity of  $5700 \pm 71.2$  A W<sup>-1</sup> for a single-junction device and  $6120 \pm 96.9$  A W<sup>-1</sup> for a double-junction device at an incident laser power of 20 pW. The photocurrent rise time of 40 ms for the single-junction device was reduced to 950  $\mu$ s for the double-junction device. The efficient charge transfer occurring in the MoS<sub>2</sub>/PbS QD hybrid photodetector yielded a maximum

photoresponsivity of  $5.4 \times 10^4$  A W<sup>-1</sup> and a detectivity of  $1 \times 10^{11}$  Jones. High photoresponsivity of 2570 A W<sup>-1</sup> and detectivity of  $2.2 \times 10^{12}$  Jones at 635 nm in a few-layer MoS<sub>2</sub> photodetector have been demonstrated under zero gate voltage with the use of a poly(vinylidene fluoride-trifluoroethylene) [P(VDF-TrFE)] ferroelectric polymer gate.<sup>137</sup> This MoS<sub>2</sub>/P(VDF-TrFE) hybrid photodetector also showed photodetection over the 0.85  $\mu$ m to 1.55  $\mu$ m spectral region and excellent stability over 90 000 repeated cycles of operation.

Organic molecules and polymers have been hybridized with MoS<sub>2</sub> to develop photodetectors. Sun *et al.*<sup>189</sup> used narrow bandgap organic semiconducting polymer, poly(diketopyrrolopyrrole-terthiophene) (PDPP3T), into large bandgap monolayer MoS<sub>2</sub> to develop UV-NIR photodetectors. The photoresponsivities of MoS<sub>2</sub>/PDPP3T based phototransistors were enhanced by one to two orders of magnitude compared with MoS<sub>2</sub>. Flexible MoS<sub>2</sub>/PDPP3T photodetectors that were fabricated on a PET substrate. The MoS<sub>2</sub>/PDPP3T hybrid showed photoresponsivities of 276, 445, and 269 mA W<sup>-1</sup> and detectivity values of  $2.59 \times 10^8$ ,  $3.14 \times 10^8$ , and  $2.53 \times 10^8$  Jones at 365, 660, and 850 nm, respectively. The flexible MoS<sub>2</sub>/PDPP3T photodetectors were developed on a PET substrate which exhibited photoresponse from 365 nm to 940 nm. The bending testing of flexible MoS<sub>2</sub>/PDPP3T

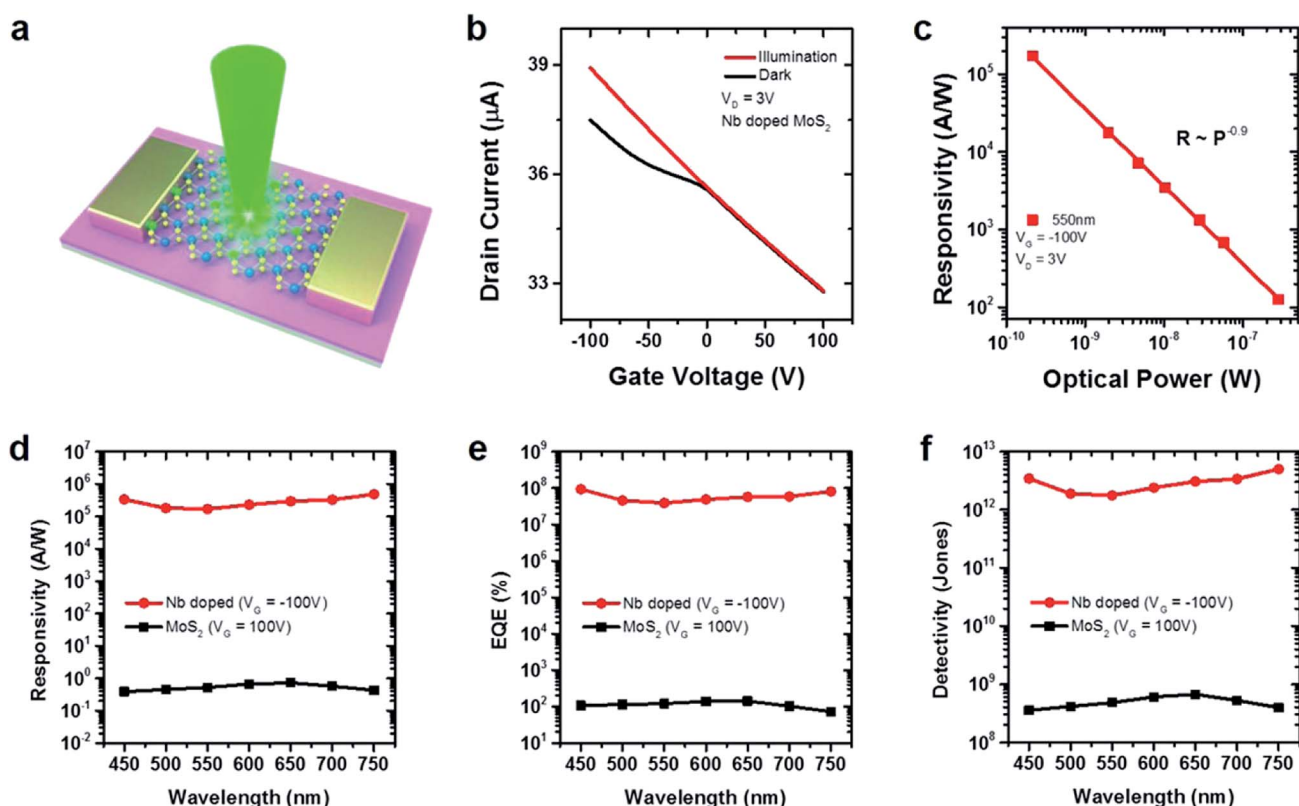


Fig. 6 (a) Schematic illustration of doped MoS<sub>2</sub> photodetectors. (b) Transfer curves of Nb-doped MoS<sub>2</sub> photodetectors at 550 nm laser wavelength under 282 nW optical power. (c) Photoresponsivity ( $R$ ) of Nb-doped MoS<sub>2</sub> photodetectors as a function of optical power ( $P$ ) at 550 nm laser wavelength and at  $V_d = 3$  V and  $V_g = -100$  V. A comparison of photoresponse characteristics of Nb-doped MoS<sub>2</sub> photodetectors with updoped MoS<sub>2</sub> photodetectors. (d) Photoresponsivity, (e) EQE, and (f) detectivity of Nb-doped MoS<sub>2</sub> photodetectors and updoped MoS<sub>2</sub> photodetectors at  $V_g = -100$  V as a function of laser wavelength. Reprinted with permission from ref. 161, copyright © American Chemical Society.



photodetector was conducted under 660 nm light illumination a 9 mm bending radius where some decrease in the photocurrent was noticed after 10 000 bending cycles. Likely, the environmental stability of the flexible MoS<sub>2</sub>/PDPP3T photodetector was also evaluated without any encapsulation in an air atmosphere for 35 days where slight changes were observed both in the dark and photo currents. MoS<sub>2</sub>/PDPP3T hybrid photodetector devices demonstrated both mechanical stability and durability in the air.

### 3.3 Halide perovskite MoS<sub>2</sub> heterostructures

Organometallic halide perovskites have emerged as an important class of light harvesting materials for developing solar cells<sup>8,9,130,131</sup> because of their tunable bandgap, extended light absorption over a broad spectral range, high photoconversion efficiencies, charge-carrier mobilities, and ease of solution processing into ultrathin layers. These unique optoelectronic properties of perovskites have been utilized in improving the performance of MoS<sub>2</sub> photodetectors. Wu *et al.*<sup>190</sup> developed hybrid phototransistors using 0D cesium lead halides perovskite (CsPbI<sub>3-x</sub>Br<sub>x</sub>) QDs and 2D monolayer MoS<sub>2</sub>. The CsPbI<sub>3-x</sub>Br<sub>x</sub> QD/1L MoS<sub>2</sub> 0D-2D mixed-dimensional vdW heterostructure-based photodetectors showed a high photoresponsivity of  $7.7 \times 10^4$  A W<sup>-1</sup>, a detectivity of  $5.6 \times 10^{11}$  Jones, and an EQE value greater than 10<sup>7</sup>% at 532 nm light illumination under optical power of 1.5  $\mu$ W due to the photogating effect. Also under similar illumination conditions, the photocurrent of CsPbI<sub>3-x</sub>Br<sub>x</sub> QDs/1L MoS<sub>2</sub> hybrid phototransistor was found to be increased by 15.3 times that of a pristine MoS<sub>2</sub> phototransistor, indicating the efficient separation of photo-generated carriers and the strong absorption of 0D CsPbI<sub>3-x</sub>Br<sub>x</sub> QDs.

MoS<sub>2</sub> layers combined with perovskite CsPbBr<sub>3</sub> nanosheets have been investigated for fabricating photodetectors, as reported by Song *et al.*<sup>191</sup> The MoS<sub>2</sub>/CsPbBr<sub>3</sub> hybrid-based photodetector showed a photoresponsivity of 4.4 A W<sup>-1</sup>, a detectivity of  $2.5 \times 10^{10}$  Jones, and a 302% EQE arising from photoexcited carrier separation at the interface of the perovskite CsPbBr<sub>3</sub> nanosheet and MoS<sub>2</sub> layer. The photoresponsivity of the MoS<sub>2</sub>/CsPbBr<sub>3</sub> hybrid-based photodetector increased by three orders of magnitude compared to the MoS<sub>2</sub> photodetector without the perovskite CsPbBr<sub>3</sub>. The response time of the hybrid photodetector decreased from 65.2 to 0.72 ms after adding MoS<sub>2</sub> layers. The high photon absorption by the CsPbBr<sub>3</sub> perovskite layer and the carrier transport by the MoS<sub>2</sub> layer contributed to the high performance of the photodetector devices. The 3 MoS<sub>2</sub>/CsPbBr<sub>3</sub> hybrid, CsPbBr<sub>3</sub> and MoS<sub>2</sub> photodetector devices showed current in the 0.1–1 nA range. Photocurrents of 5030, 1230, and 54 nA were measured for the MoS<sub>2</sub>/CsPbBr<sub>3</sub> hybrid, CsPbBr<sub>3</sub>, and MoS<sub>2</sub>, respectively. Light on/off ratios of 16 700, 14 300, and 150 were calculated for the MoS<sub>2</sub>/CsPbBr<sub>3</sub> hybrid, CsPbBr<sub>3</sub>, and MoS<sub>2</sub> photodetector devices, respectively. PL quenching, as well as a fast decay time, was observed for the MoS<sub>2</sub>/CsPbBr<sub>3</sub> hybrid due to the charge transfer from the perovskite CsPbBr<sub>3</sub> nanosheet to the MoS<sub>2</sub> atomic layers. Kang *et al.*<sup>192</sup> reported perovskite/MoS<sub>2</sub>/APTES

hybrid heterostructure-based photodetector devices. The photoresponsivity of a MoS<sub>2</sub> photodetector was enhanced from 636 to  $4.9 \times 10^3$  A W<sup>-1</sup> and detectivity from  $1.53 \times 10^9$  to  $8.76 \times 10^{10}$  Jones for a perovskite/MoS<sub>2</sub> hybrid device after applying the perovskite layer at 520 nm. The similar increment was also observed for 655 and 785 nm laser wavelengths, but for 850 nm. The photocurrent of the perovskite/MoS<sub>2</sub>/APTES hybrid photodetector was increased by 25.9 times that of the MoS<sub>2</sub> photodetector at 520 nm wavelength. The photoresponsivity and detectivity of the perovskite/MoS<sub>2</sub>/APTES hybrid photodetector device were enhanced from 816.6 to  $2.11 \times 10^4$  A W<sup>-1</sup> and from  $3.93 \times 10^9$  to  $1.38 \times 10^{10}$  Jones after APTES n-doping, respectively. The photoresponsivity of the perovskite/MoS<sub>2</sub>/APTES hybrid photodetector was increased by 94.2 times, from  $2.11 \times 10^4$  to  $1.94 \times 10^6$  A W<sup>-1</sup> at 520 nm as a function of incident laser power (1.57 nW to 4.63 pW), while the highest detectivity value was  $1.29 \times 10^{12}$  Jones due to the decreased scattering between photogenerated electrons. The perovskite/MoS<sub>2</sub>/APTES hybrid photodetectors showed significantly higher photoresponsivity values compared with the MoS<sub>2</sub>/APTES photodetector.<sup>180</sup> The performance of photodetector devices followed the sequence as: perovskite/MoS<sub>2</sub>/APTES > perovskite/MoS<sub>2</sub> > MoS<sub>2</sub>, as clearly evident from the above-mentioned results. Since perovskites are susceptible to environmental degradation,<sup>8,130</sup> therefore, the stability of perovskite/MoS<sub>2</sub>/APTES photodetectors was improved by applying encapsulating layers of octadecyltrichlorosilane (OTS) and PMMA. The stability of non-encapsulated, PMMA and OTS/PMMA encapsulated perovskite/MoS<sub>2</sub>/APTES photodetector devices in air was measured at different wavelengths: 520, 655, 785 and 850 nm. Photoresponsivity and detectivity deteriorated by 50% and 70% after 68 h for PMMA and 20.4% and 28.7% after 200 h for OTS/PMMA encapsulated devices, and 20.4–24.8% and 28.7–34.2% for perovskite/MoS<sub>2</sub>/APTES photodetectors at different wavelengths, respectively. These data showed that performance of MoS<sub>2</sub> photodetectors can be improved by applying a perovskite absorption layer and furthermore *via* a chemical doping process.

The flexible perovskite/MoS<sub>2</sub> hybrid photodetectors were developed using a polyethylene terephthalate (PET) substrate. Sun *et al.*<sup>76</sup> used CVD grown atomic layered MoS<sub>2</sub> film, deposited a 20 nm Ti/50 nm Au thick electrode and then spin-coated a triple cations  $[\text{Cs}_{0.05}(\text{MA}_{0.17}\text{FA}_{0.83})_{0.95}\text{Pb}(\text{I}_{0.83}\text{Br}_{0.17})]_3$  lead mixed-halide perovskite layer to fabricate a hybrid photodetector. Fig. 7 shows the schematics and energy-band diagram of the perovskite/MoS<sub>2</sub> hybrid photodetector under illumination, photoresponse of the pristine MoS<sub>2</sub> and perovskite/MoS<sub>2</sub> hybrid photodetector devices and mechanical stability test of the flexible hybrid photodetector device up to 20 000 bending cycles. The flexible perovskite/MoS<sub>2</sub> hybrid photodetectors showed photoresponsivity of 342 A W<sup>-1</sup> at 2 V bias potential without any gate voltage at 520 nm under 2.2 pW incident power. The hybrid photodetector devices showed high stability without any encapsulation, photoresponse and decay times of 27 ms and 21 ms, respectively. The hybrid devices were fabricated on rigid SiO<sub>2</sub>/Si, glass and flexible PET substrates. The pristine MoS<sub>2</sub> photodetector device showed the photocurrent of 32 nA at 2 V



bias potential with 20 nW incident power, which increased to 84 nA after spin-coating the perovskite layer. The perovskite/MoS<sub>2</sub> hybrid device showed photocurrent of 2 pA at 1 V and 3.8 pA at 2 bias potential. At 1 V bias potential, the photocurrent of the hybrid device increased from 2 pA in the dark to 40 nA under illumination. The hybrid photodetector device having 10  $\mu$ m channel exhibited the highest photoresponsivity value of 1.7 A W<sup>-1</sup> under 50 nW incident power. The estimated detectivity was  $1.14 \times 10^{12}$  Jones. The photocurrent of the hybrid devices increased as a function of increased incident power. The photoresponsivity of the hybrid photodetector device was dramatically increased to 342 A W<sup>-1</sup> as the incident power decreased to 2.2 pW because of the suppressed scattering between the photogenerated charge carriers, and mechanical stability test on flexible perovskite/MoS<sub>2</sub> hybrid photodetectors was performed with 5 mm curvature up to 20 000 bending cycles. The device retained 91% photocurrent value under bending compared with the corresponding *I*-*V* curves of a device without bending. There was no noticeable decline in photocurrent ratio from 2000 to 20 000 bending cycles, indicating the strong mechanical stability of the flexible perovskite/MoS<sub>2</sub> hybrid devices.

### 3.4 2D-0D MoS<sub>2</sub>-quantum dots (QDs) heterostructures

As discussed above, photodetectors fabricated with hybrid MoS<sub>2</sub>/PbS QDs yield significantly high photoresponsivity.<sup>188</sup> 0D QDs have been used for improving the performance of MoS<sub>2</sub>

photodetectors. Huo *et al.*<sup>193</sup> developed photodetectors by incorporating mercury telluride (HgTe) colloidal QD film into a TiO<sub>2</sub>-encapsulated few-layer MoS<sub>2</sub> channel. In the MoS<sub>2</sub>/TiO<sub>2</sub>/HgTe hybrid heterostructure, TiO<sub>2</sub> is a buffer layer between the MoS<sub>2</sub> channel and the HgTe QD layer that acts as an electron accepting medium to form a p-n junction with the HgTe QDs to facilitate the transfer of photogenerated charges from the HgTe QDs to the MoS<sub>2</sub> channel. MoS<sub>2</sub>/TiO<sub>2</sub>/HgTe hybrid photodetectors showed a high photoresponsivity of 10<sup>6</sup> A W<sup>-1</sup> under an incident power of 70 fW (0.35  $\mu$ W cm<sup>-2</sup>) at a gate voltage ( $V_g$ ) of -15 V and a  $V_{ds}$  of 1 V, which is seven orders of magnitude higher than that of the HgTe QD photodetector due to the low carrier mobility ( $2 \times 10^{-3}$  cm<sup>2</sup> V<sup>-1</sup> s<sup>-1</sup>) of the HgTe QDs. The detectivity of MoS<sub>2</sub>/TiO<sub>2</sub>/HgTe hybrid photodetectors was  $1 \times 10^{12}$  Jones at a 2.0  $\mu$ m wavelength, which is four orders of magnitude higher than that of pure HgTe-based photodetectors ( $10^7$  to  $10^8$  Jones). This study is an excellent example of extending the spectral wavelengths of a MoS<sub>2</sub>-based photodetector over 2.0  $\mu$ m. In another study, Zhang *et al.*<sup>194</sup> reported 2D MoS<sub>2</sub>-0D zinc cadmium selenide (ZnCdSe)/zinc sulfide (ZnS) colloidal QD-based photodetectors, where monolayer (1L) to multilayer (ML) MoS<sub>2</sub> thin film acts as a carrier transport channel and a core/shell ZnCdSe/ZnS QDs sensitizing thin layer functions as a light harvester. Fig. 8 compared the photoresponsivity and detectivity as a function of laser incident power for the pristine MoS<sub>2</sub> based photodetectors with hybrid MoS<sub>2</sub>-ZnCdSe/ZnS QD-based photodetectors having monolayer MoS<sub>2</sub> (1L), bilayer MoS<sub>2</sub> (2L), trilayer MoS<sub>2</sub> (3L), and multilayer MoS<sub>2</sub>

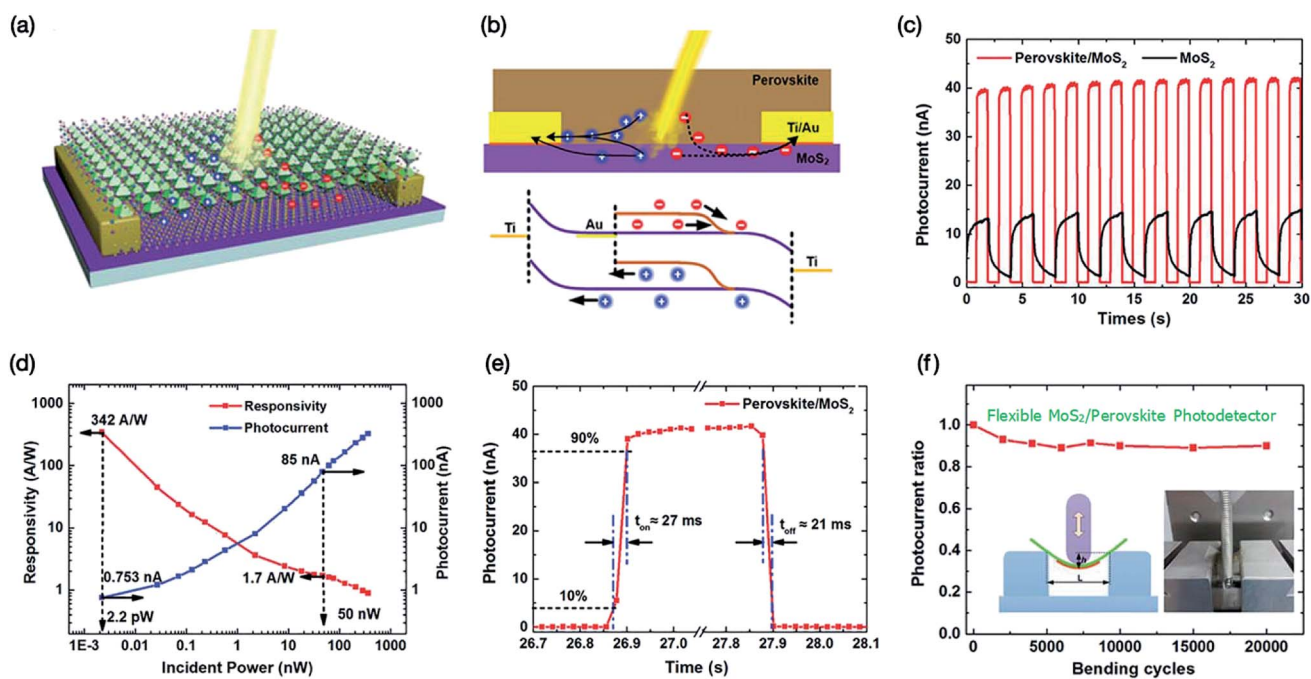


Fig. 7 (a) Schematic illustration of perovskite/MoS<sub>2</sub> hybrid based photodetector. (b) Working mechanism and energy-band diagram of flexible perovskite/MoS<sub>2</sub> hybrid photodetector under illumination. (c) A comparison of the transient photoresponse of the pristine MoS<sub>2</sub> and flexible perovskite/MoS<sub>2</sub> hybrid based photodetectors under on/off illumination. (d) Photoresponsivity and photocurrent of the flexible perovskite/MoS<sub>2</sub> hybrid photodetector devices as a function of laser incident power. (e) Photoresponse rise and decay time of the flexible perovskite/MoS<sub>2</sub> hybrid photodetector. (f) Mechanical stability test of the flexible perovskite/MoS<sub>2</sub> hybrid photodetector device up to 20 000 bending cycles. Reprinted with permission from ref. 76, copyright © Elsevier.



(ML). There is a very significant increase in photocurrent, photoresponsivity, and detectivity after adding ZnCdSe/ZnS QD sensitizing layer. The photocurrent of hybrid MoS<sub>2</sub>–ZnCdSe/ZnS QD-based photodetectors increased by 1000 folds compared with pristine MoS<sub>2</sub> photodetectors. The response time of the MoS<sub>2</sub>–ZnCdSe/ZnS QD-based photodetector was reduced to 0.3 s from 15 s for MoS<sub>2</sub> layers, making the hybrid device 50 times faster. The schematic of the MoS<sub>2</sub>–ZnCdSe/ZnS QD interface and their energy diagram depict the transfer of electrons from ZnCdSe/ZnS QDs to MoS<sub>2</sub> layers *via* a tunneling process and the transfer of excitons from ZnCdSe/ZnS QDs to the MoS<sub>2</sub> layer *via* nonradiative energy transfer (NRET) processes after a heterojunction formation. In the NERT process, the MoS<sub>2</sub> layer acts as an acceptor, whereas the ZnCdSe/ZnS QDs thin layer acts as a donor. The photoresponsivity of the hybrid MoS<sub>2</sub>–ZnCdSe/ZnS QD-based photodetectors increased by three orders of magnitude to  $3.7 \times 10^4$  A W<sup>-1</sup> compared to pristine MoS<sub>2</sub> layers of 10 A W<sup>-1</sup>. Likely, the detectivity of the MoS<sub>2</sub>–ZnCdSe/ZnS QD-based photodetector increased to  $1.0 \times 10^{12}$  Jones, and the gain increased by five orders of magnitude to  $1.08 \times 10^5$  after adding a layer of QDs due to the increased absorption and efficient transfer of energy from the photoexcited ZnCdSe/ZnS QDs layer to MoS<sub>2</sub> layers. The better performance of the 2D–0D hybrid photodetector is associated with high carrier mobility in the MoS<sub>2</sub> layer and the creation of effective photon absorption/exciton in the ZnCdSe/ZnS QDs layer. The MoS<sub>2</sub> layers efficiently quench the

fluorescence of the ZnCdSe/ZnS QDs in the 2D–0D hybrid nanostructures exhibiting ultrasensitivity and high gain.

### 3.5 2D–2D MoS<sub>2</sub>–2D van der Waals heterostructures (vdWHs)

MoS<sub>2</sub>-based photodetectors have been designed and developed using different electrode materials and van der Waals heterostructures (vdWHs) to improve their optoelectronic properties. The performance of MoS<sub>2</sub>-based photodetectors can be increased using rGO layers.<sup>178,179</sup> Fig. 9(a–c) shows a schematic of the multilayer MoS<sub>2</sub> photodetector developed with Mo bottom contacts (100 nm) on thermally oxidized SiO<sub>2</sub>/Si substrates (270 nm) and the photoresponsivity and EQE of the ML MoS<sub>2</sub> photodetector measured over the 400–1100 nm spectral region, as reported by Saenz *et al.*<sup>195</sup> The photodetector exhibited ultrahigh photoresponsivity of  $1.4 \times 10^4$  A W<sup>-1</sup> and detectivity of  $2.3 \times 10^{11}$  Jones at a 700 nm wavelength with a 14.5 pW laser power for the multilayer MoS<sub>2</sub> device fabricated using 100 nm thick Mo bottom electrodes, with a broadband photoresponse from the UV to IR regime. The photoresponsivity increased from  $8 \times 10^3$  A W<sup>-1</sup> at 400 nm to  $1.4 \times 10^4$  A W<sup>-1</sup> at 1100 nm at a bias voltage of 20 V, and the EQE varied from  $3.6 \times 10^4$  to  $1.4 \times 10^4$  within the 400 nm to 1100 nm wavelength range. Photoresponsivities of  $1 \times 10^3$  A W<sup>-1</sup> and 42 A W<sup>-1</sup> were recorded at incident powers of 70 pW and 15.85 nW, respectively, at a bias voltage of 5 V and 300 K. The decrease in the photoresponsivity resulted from the loss of photocarriers due to

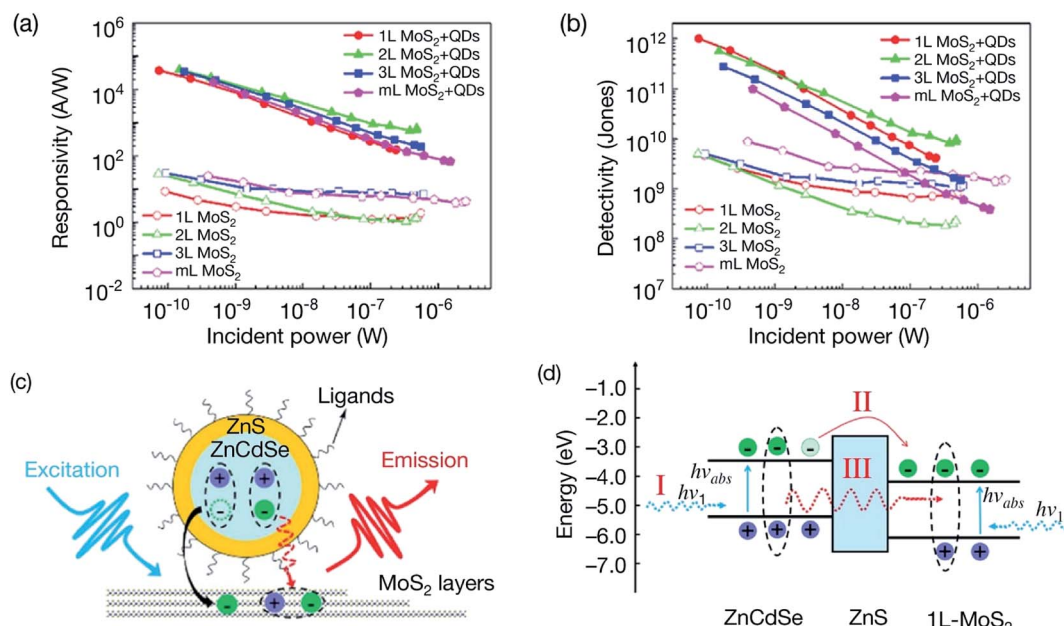


Fig. 8 (a and b) A comparison of photoresponsivity and detectivity of pristine MoS<sub>2</sub> based photodetectors having different MoS<sub>2</sub> layers; monolayer MoS<sub>2</sub> (1L), bilayer MoS<sub>2</sub> (2L), trilayer MoS<sub>2</sub> (3L), and multilayer MoS<sub>2</sub> (ML) as a function of laser incident power. Both responsivity and detectivity increased significantly after adding QD sensitizing layer. (c) Schematic of the MoS<sub>2</sub>–ZnCdSe/ZnS QD interface showing the transfer of electrons from ZnCdSe/ZnS QDs to MoS<sub>2</sub> layers *via* a tunneling process (represented by black arrow) and the transfer of excitons from ZnCdSe/ZnS QDs to MoS<sub>2</sub> layer *via* nonradiative energy transfer (NRET) processes (represented by red dashed arrow) under an illumination. (d) Energy diagram of the 1L MoS<sub>2</sub>–ZnCdSe/ZnS QD interface after a heterojunction formation where three photoelectrical processes are involved; (I) photon excitation in 1L-MoS<sub>2</sub> and ZnCdSe/ZnS QDs; (II) transfer of electrons from the ZnCdSe/ZnS QDs to 1L-MoS<sub>2</sub> *via* a tunneling process and (III) exciton transfer from the ZnCdSe/ZnS QDs to 1L-MoS<sub>2</sub> *via* NRET processes. Reprinted with permission from ref. 194, copyright © American Chemical Society.



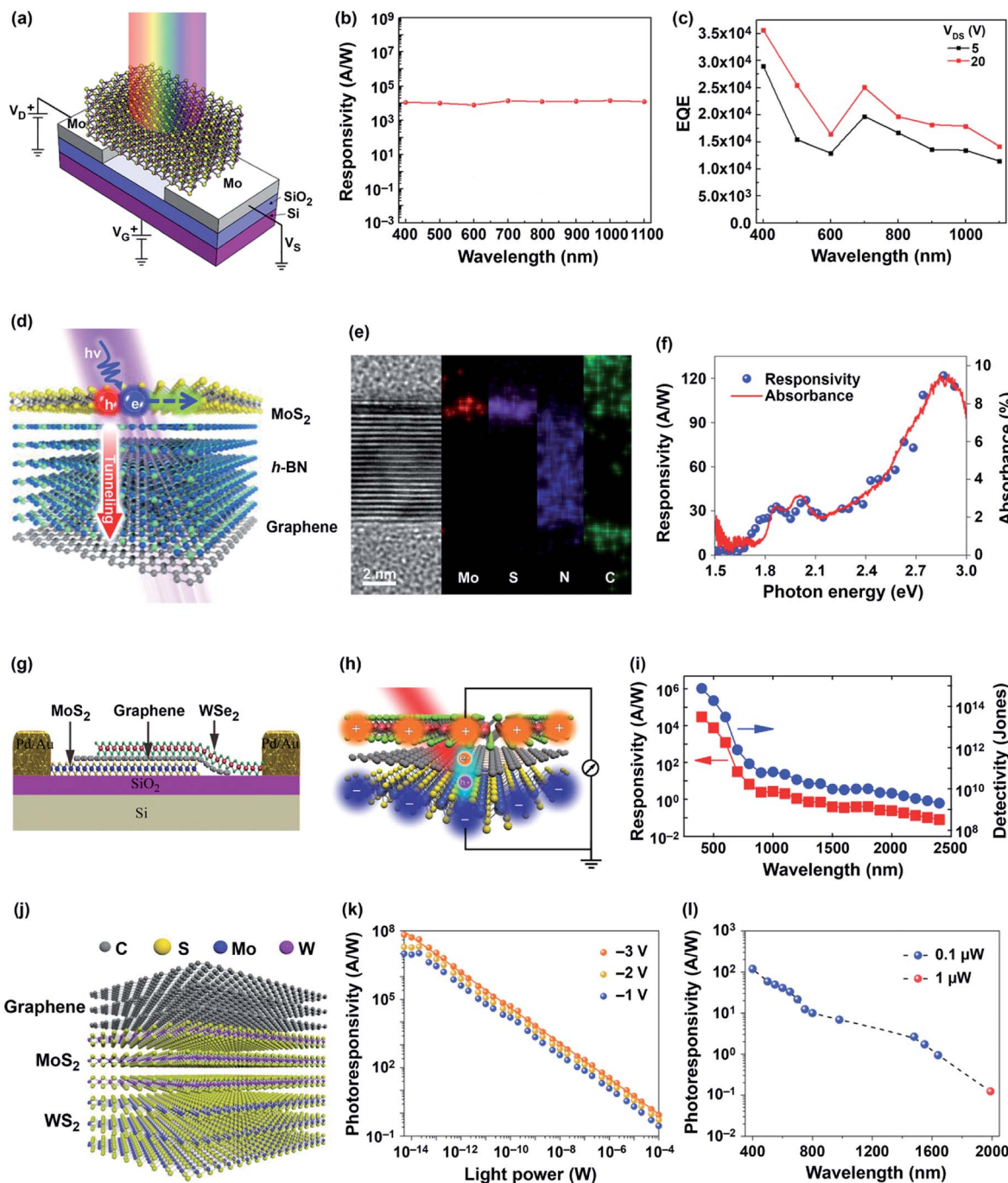


Fig. 9 (a) Schematic of the multilayer MoS<sub>2</sub> photodetector fabricated using 100 nm thick Mo bottom contacts on 270 nm thick thermally oxidized SiO<sub>2</sub>/Si substrates. (b) Photoreponsivity and (c) external quantum efficiency (EQE) of the ML MoS<sub>2</sub> photodetector as a function of wavelength over the 400–1100 nm spectral region. Reprinted with permission from ref. 195, copyright © 2018 Springer Nature Limited. (d) Schematic of the MoS<sub>2</sub>/h-BN/graphene vdWH photodetector using the MoS<sub>2</sub> layer as a photon absorber, the h-BN layer as a selective hole tunneling layer and the graphene layer as a bottom electrode. The generation of an electron–hole pair upon light illumination and occurrence of selective hole carrier tunneling through the h-BN layer. (e) Cross-sectional STEM image and energy dispersive X-ray spectroscopy (EDS) elemental mapping of the MoS<sub>2</sub>/h-BN/graphene vdWHs. (f) Photoreponsivity and absorbance of the MoS<sub>2</sub>/h-BN/graphene photodetector as a function of photon energy. Reprinted with permission from ref. 196, copyright © American Chemical Society. (g) Side view of MoS<sub>2</sub>/graphene/WSe<sub>2</sub> vdWHs. (h) Schematic drawing of atomically layered MoS<sub>2</sub>/graphene/WSe<sub>2</sub> vdWHs for broadband photodetection. (i) Photoreponsivity and detectivity ( $D^*$ ) of the MoS<sub>2</sub>/graphene/WSe<sub>2</sub>-based broadband photodetector in the 400 nm to 2400 nm wavelength range. Reprinted with permission from ref. 198, copyright © American Chemical Society. (j) Schematic of the graphene/MoS<sub>2</sub>/WS<sub>2</sub> vdWH-based optical-fiber compatible photodetector. (k) Photoreponsivity of the graphene/MoS<sub>2</sub>/WS<sub>2</sub>-based broadband optical-fiber compatible photodetector as a function of laser illumination power at different bias voltages. (l) Photoreponsivity of the graphene/MoS<sub>2</sub>/WS<sub>2</sub>-based broadband optical-fiber compatible photodetector as a function of wavelength in the 400 nm to 2000 nm spectral range. Reprinted with permission from ref. 199, copyright © Wiley.



recombination effects. Vu *et al.*<sup>196</sup> used MoS<sub>2</sub>/h-BN/graphene vdWHs to develop a photodetector. Fig. 9(d–f) depicts a schematic of the MoS<sub>2</sub>/h-BN/graphene photodetector, its cross-sectional STEM image, its energy dispersive X-ray spectroscopy (EDS) elemental mapping and its photoresponsivity and absorbance as a function of photon energy. An h-BN insulating layer was inserted between the MoS<sub>2</sub> photoabsorber and the graphene electrode. In these vdWHs, the dark carriers are suppressed at the graphene/h-BN barrier (2.7 eV), whereas the tunneling of photocarriers is facilitated at the MoS<sub>2</sub>/h-BN junction (1.2 eV). Varying the thickness of the h-BN insulating layer from 0–25 nm played an important role in the tunneling of the dark carriers and photocarriers; a 7 nm thick h-BN barrier layer was most effective in blocking the conduction of dark carriers and facilitating the tunneling of photocarriers through the low-hole MoS<sub>2</sub>/h-BN junction. The photodetector fabricated from MoS<sub>2</sub>/h-BN/graphene vdWHs with a 7 nm thick h-BN layer exhibited a photoresponsivity of 180 A W<sup>-1</sup> with a maximum photocurrent/dark current ( $I_{\text{photo}}/I_{\text{dark}}$ ) ratio of 10<sup>5</sup> and a detectivity of  $2.6 \times 10^{13}$  Jones. The detectivity of the vdWH-based photodetector was 1000 higher compared with the values of  $2.5 \times 10^{10}$  Jones for the lateral MoS<sub>2</sub> p–n junction<sup>170</sup> and  $5 \times 10^{10}$  Jones for monolayer MoS<sub>2</sub>-based photodetectors.<sup>197</sup> Furthermore, the rise/fall times of 0.23 s/0.25 s for the vdWH-based photodetector were 1000 times faster than those of the monolayer MoS<sub>2</sub>-based photodetector.<sup>171</sup>

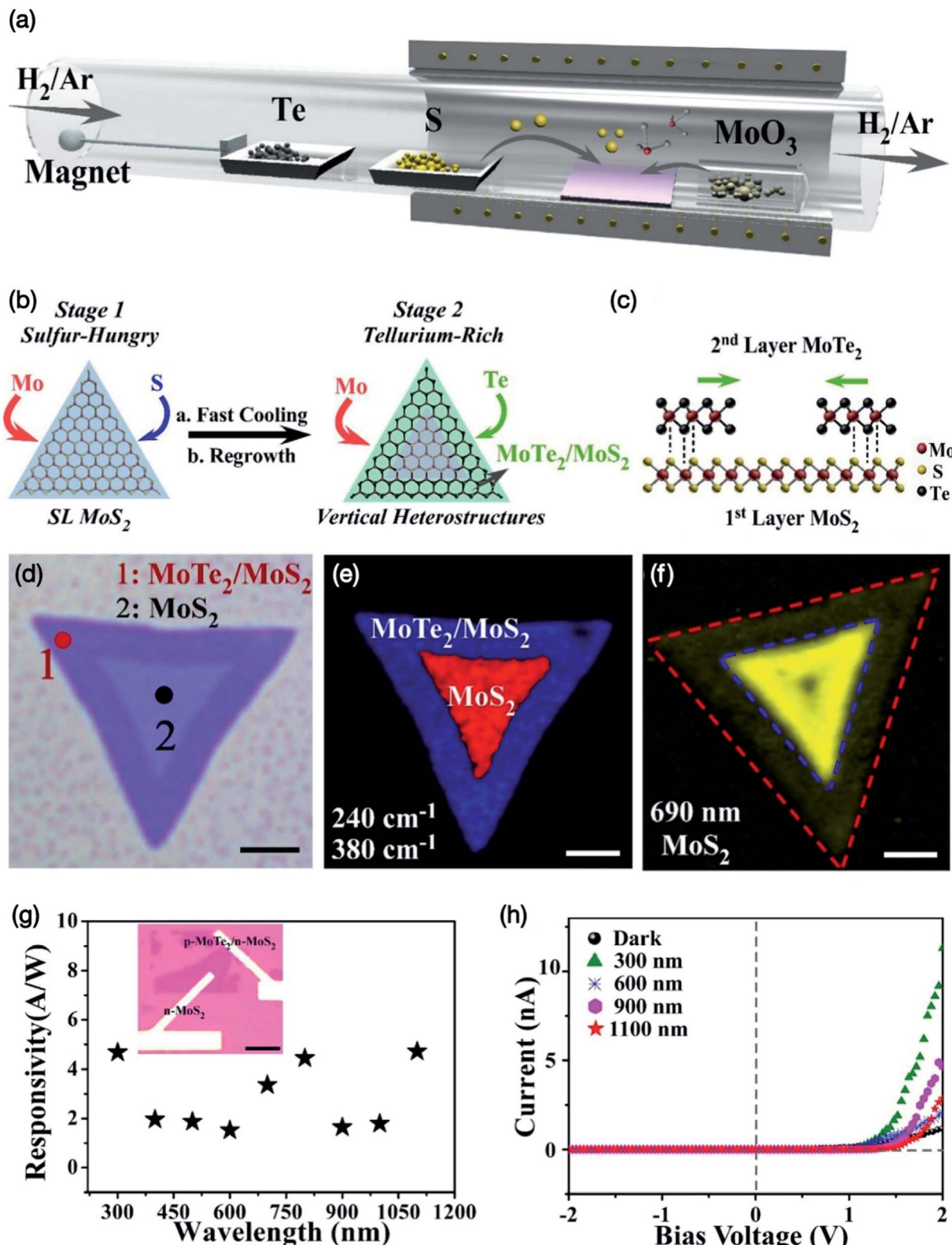
Similarly, atomically thin layered MoS<sub>2</sub>/graphene/WSe<sub>2</sub> (p–g–n) vdWHs were developed by Long *et al.*<sup>198</sup> In this vdWH, graphene was sandwiched within the p–n junction to broaden the absorption spectral range and photodetection sensitivity. Fig. 9(g–i) shows a side view of MoS<sub>2</sub>/graphene/WSe<sub>2</sub> vdWHs, a schematic for the broadband photodetection and the wavelength-dependent photoresponsivity and detectivity (D) of the MoS<sub>2</sub>/graphene/WSe<sub>2</sub>-based broadband photodetector over the 400 nm to 2400 nm wavelength range. Both the photoresponsivity and detectivity decreased with increasing excitation laser wavelength. The maximum photoresponsivity and detectivity values of the p–g–n heterostructure-based photodetector were on the order of 10<sup>4</sup> A W<sup>-1</sup> and 10<sup>15</sup> Jones in the visible range and decreased to a few mA W<sup>-1</sup> and 10<sup>9</sup> Jones at the 2400 nm wavelength, respectively. A photoresponsivity of 4250 A W<sup>-1</sup>, a detectivity of  $2.2 \times 10^{12}$  Jones and an EQE value of  $1.0 \times 10^{6}\%$  were measured at 532 nm with a 0.2 nW laser power intensity for the p–g–n heterostructure-based photodetector, while the photoresponsivity dropped to 306 mA W<sup>-1</sup> in the near-IR region, 940 nm with a 17 nW laser power. The photocurrent mapping conducted at 830 nm with a 20.5  $\mu$ W laser power indicated that the overlapping regions of the MoS<sub>2</sub>, graphene and WSe<sub>2</sub> atomic layers are responsible for the strong photoresponse instead of the electrode regions. The MoS<sub>2</sub>/graphene/WSe<sub>2</sub> heterostructure-based broadband photodetector also showed a fast photoresponse with a 53.6  $\mu$ s rise time and a 30.3  $\mu$ s fall time, and can be used from the visible to near-IR spectral range at room temperature.

Fig. 9(j–l) illustrates a schematic of the graphene/MoS<sub>2</sub>/WS<sub>2</sub> vdWH-based optical-fiber compatible photodetector fabricated by Xiong *et al.*<sup>199</sup> The photoresponsivity of this optical-fiber

tuned photodetector was recorded as a function of applied laser power at different bias voltages and in the 400 nm to 2000 nm spectral range. The photoresponsivity increased with increasing bias voltage at a fixed incident light power of 1 pW. The fiber-based photodetector was impacted by the trap state of MoS<sub>2</sub> and WS<sub>2</sub>. The optical fiber-based photodetector exhibited a photoresponsivity of 17.1 A W<sup>-1</sup> at 1550 nm, and an optimum photoresponsivity of  $6.6 \times 10^7$  A W<sup>-1</sup> was measured at 400 nm under an incident light power of 6.35 nW cm<sup>-2</sup> (5 fW) at a –3 V bias voltage. The EQE value of graphene/MoS<sub>2</sub>/WS<sub>2</sub> vdWH reached  $2.06 \times 10^8$  at a 5 fW incident power input (400 nm) and 13.71 at 1550 nm, orders of magnitude higher compared with multilayer graphene and MoS<sub>2</sub>/WS<sub>2</sub> heterostructure. The photoconductive photobolometric mechanism involved in graphene/MoS<sub>2</sub>/WS<sub>2</sub> vdWH yielded the photoresponse times of 7 ms and 160 ms at the illumination power of 200  $\mu$ W and 5 mW, respectively, quite different than those of graphene (photobolometric) and MoS<sub>2</sub>/WS<sub>2</sub> heterostructure (photoconductive) resulting from different photogeneration mechanisms. The photoresponsivity was measured as a function of the wavelength by maintaining the incident light power at 100 nW for the 400 nm to 1640 nm range and 1.0  $\mu$ W for the 2.0  $\mu$ m wavelength. The photodetection limit of graphene/MoS<sub>2</sub>/WS<sub>2</sub> vdWH was between 400 nm (5 fW) and 1550 nm (20 nW), compared with 0.1 mW at 1550 nm for graphene and 0.2 nW at 400 nm for MoS<sub>2</sub>/WS<sub>2</sub> heterostructure. The photodetector exhibited a decrease in photoresponsivity as the wavelength was increased from 400 nm to 2.0  $\mu$ m but retained a high photoresponsivity. This result demonstrates the broadband photodetection of the graphene/MoS<sub>2</sub>/WS<sub>2</sub> vdWH-based photodetector from the visible to IR ranges.

The MoS<sub>2</sub>-based vdWHs are also interesting for developing highly sensitive photodetectors. Liu *et al.*<sup>200</sup> developed photodetectors using vertically stacked p-Sb<sub>2</sub>Te<sub>3</sub>/n-MoS<sub>2</sub> vdWHs, which showed a photoresponsivity of 330 A W<sup>-1</sup>, a fast response time of <500  $\mu$ s and a power conversion efficiency of 4.5%. Yang *et al.*<sup>201</sup> fabricated few-layer SnSe/MoS<sub>2</sub> vdWHs with a current  $I_{\text{on}}/I_{\text{off}}$  ratio of  $1 \times 10^5$ . The type-II SnSe/MoS<sub>2</sub> heterostructure FET showed a fast response time of <10 ms, a photoresponsivity ( $R_{\lambda}$ ) of 100 A W<sup>-1</sup>, and an EQE of  $23.3 \times 10^3\%$  under 532 nm light illumination. The gallium telluride (GaTe)-MoS<sub>2</sub> p–n vdW heterojunction FET showed a fast response time of <10 ms, a photoresponsivity of 1.365 A W<sup>-1</sup>, and an EQE of 266% under 633 nm light illumination,<sup>167</sup> much higher compared with the photoresponsivity of 0.03 A W<sup>-1</sup> for a flexible GaTe photodetector measured at a wavelength of 473 nm under an incident laser power of 80.5 mW cm<sup>-2</sup>.<sup>202</sup> The electronic and optoelectronic properties of MoS<sub>2</sub> have been improved by fabricating vdWH-based FETs with other 2D materials.<sup>36,203</sup> The vertically stacked vdWHs of SnS<sub>2</sub>/MoS<sub>2</sub> monolayers showed improved mobility of  $27.6 \text{ cm}^2 \text{ V}^{-1} \text{ s}^{-1}$ ,  $I_{\text{on}}/I_{\text{off}}$  ratio of  $10^6$ , and photoresponsivity of  $1.36 \text{ A W}^{-1}$ .<sup>204</sup> 2D layered vdW semiconductor MoTe<sub>2</sub> has been used with MoS<sub>2</sub> to develop vdW heterojunction p–n diodes for extending the range of photodetection in the NIR region. Ding *et al.*<sup>166</sup> fabricated vertically stacked 2H-MoTe<sub>2</sub>/MoS<sub>2</sub> bilayer heterostructures using CVD technique for broadband photodetectors ranging from 200 nm (UV) to 1100 nm





**Fig. 10** (a) Schematic diagram of experimental set-up showing magnet-assisted CVD growth method for preparing  $MoTe_2/MoS_2$  heterostructure. (b) Vertically stacking approach of  $MoTe_2/MoS_2$  bilayer heterostructures. (c) Schematic side view of the  $MoTe_2/MoS_2$  bilayer heterostructure where Mo atoms are represented in red, S atoms in yellow, Te atoms in black. (d) Optical image of the  $MoTe_2/MoS_2$  flake. (e) Raman intensity mapping at  $240\ cm^{-1}$  shown in blue and  $380\ cm^{-1}$  in red. (f) PL intensity mapping at  $690\ nm$  wavelength where the red dash lines detect the  $MoTe_2/MoS_2$  heterojunction and the blue dash lines indicates the interface of regions with the inner core and outside ring. (g) Photoreponsivity of  $MoTe_2/MoS_2$  photodetectors as a function of wavelength between  $300\ nm$  to  $1100\ nm$  region. (h)  $I-V$  current characteristics of the  $MoTe_2/MoS_2$  photodetectors at different applied bias voltage. Reprinted with permission from ref. 166, copyright © Elsevier.



(NIR) regions. Fig. 10 shows the magnet-assisted CVD growth method, stacking approach of  $\text{MoTe}_2/\text{MoS}_2$  bilayer heterostructures, optical image of the  $\text{MoTe}_2/\text{MoS}_2$  flake, Raman intensity and PL mapping, photoresponsivity and  $I-V$  current of the  $\text{MoTe}_2/\text{MoS}_2$  heterostructure-based photodetectors.  $\text{MoTe}_2$  was observed to grow along the edges of  $\text{MoS}_2$  seeds. During the first stage, the sulfur-hungry environment assisted in growing the initial  $\text{MoS}_2$  seeds. In the second stage,  $\text{MoTe}_2$  was seen to grow over the first  $\text{MoS}_2$  monolayer from the edge nucleation and thereafter epitaxial growth of  $\text{MoTe}_2$  occurred from the center area on the  $\text{MoS}_2$  surface to create a vertically stacked  $\text{MoTe}_2/\text{MoS}_2$  bilayer heterostructure. Atomic force microscopy (AFM) evidenced from the height image of a triangular  $\text{MoTe}_2/\text{MoS}_2$  bilayer heterostructure that center and outside regions have a thickness of 0.8 nm and 1.6 nm, respectively. The center area is the  $\text{MoS}_2$  monolayer whereas the outside area is a vertically stacked  $\text{MoTe}_2/\text{MoS}_2$  bilayer heterostructure. The core-ring structure of vertically stacked  $\text{MoTe}_2/\text{MoS}_2$  bilayer heterostructures also was confirmed by the Raman mapping of  $\text{MoTe}_2$  at  $240\text{ cm}^{-1}$  and  $\text{MoS}_2$  mapping at  $380\text{ cm}^{-1}$  and  $375\text{ cm}^{-1}$ . PL spectra showed emission peaks at 640 nm and 690 nm for the  $\text{MoS}_2$  flake where the peak at 690 nm indicates a significant quenching for the  $\text{MoS}_2$ . A band alignment occurred when the  $\text{MoS}_2$  monolayer was vertically stacked with the  $\text{MoTe}_2$  monolayer due to the interlayer coupling interactions. The vertically stacked  $\text{MoTe}_2/\text{MoS}_2$  bilayer heterostructures also showed higher image contrast than that of the  $\text{MoS}_2$  monolayer with high-angle annular dark field (HAADF) STEM. The photoresponsivity and external quantum efficiency (EQE) of  $4.71\text{ A W}^{-1}$  and  $532\%$  at  $1100\text{ nm}$  and  $4.67\text{ A W}^{-1}$  and  $1935\%$  at  $300\text{ nm}$  under the light power density of  $4.209\text{ mW cm}^{-2}$  were measured for the  $\text{MoTe}_2/\text{MoS}_2$  bilayer heterostructure-based photodetectors, respectively, which was up to two orders of magnitude higher compared with an exfoliated  $\text{MoTe}_2$  heterostructure-based photodetector. Epitaxial growth of  $\text{MoTe}_2$  monolayer on the top and along the edges of  $\text{MoS}_2$  monolayer having a 2H-stacking mode dramatically enhanced the contact and interfacial interactions of the  $\text{MoTe}_2/\text{MoS}_2$  bilayer heterostructures, which yielded a better performance of photodetectors from UV to infrared regions. Ahn *et al.*<sup>205a</sup> fabricated self-powered visible-invisible multiband photodetectors using  $\text{MoTe}_2/\text{MoS}_2$  multilayer-based semivertical heterojunction p-n diodes, which showed an ideality factor of less than 1.5 and current  $I_{\text{on}}/I_{\text{off}}$  ratio of more than  $10^4$ . The  $\text{MoTe}_2/\text{MoS}_2$  photodiodes showed photodetection from  $405\text{ nm}$  (violet) to  $1310\text{ nm}$  (NIR) wavelength region and a linear dynamic range (LDR) of  $130\text{ dB}$  between  $10^{-5}$  to  $1\text{ W cm}^{-2}$  applied laser power intensity in the photovoltaic mode. The  $\text{MoTe}_2/\text{MoS}_2$  photodetectors showed photoresponsivity of  $0.62\text{ A W}^{-1}$  and  $0.86\text{ A W}^{-1}$  at  $532\text{ nm}$  laser illumination, and LDR of  $132\text{ dB}$  and  $84\text{ dB}$  in the photoconduction mode ( $V = -2\text{ V}$ ), respectively. The values of detectivity ranged from  $10^8$  to  $10^{10}\text{ Jones}$  within  $405\text{--}1310\text{ nm}$  wavelength range. A prototype self-powered visible-invisible multiband image sensor was also constructed with  $\text{MoTe}_2/\text{MoS}_2$  photodiodes in the photovoltaic mode operation. Wang *et al.*<sup>205b</sup> developed p- $\text{MoTe}_2$ /n- $\text{MoS}_2$  based van der Waals heterojunctions for photodetectors. The multilayer  $\text{MoTe}_2/\text{MoS}_2$

vdWH-based FETs showed a photocurrent that increased by several orders of magnitude with increasing laser power density, a photoresponsivity of  $0.15\text{ A W}^{-1}$  and an EQE value of  $39.4\%$  at a  $473\text{ nm}$  laser wavelength, a photocurrent  $I_{\text{on}}/I_{\text{off}}$  ratio of 780 and a field-effect mobility of  $1.9\text{ cm}^2\text{ V}^{-1}\text{ s}^{-1}$ , much larger compared with pure  $\text{MoTe}_2$ -based FETs. The photoelectric response of vertically stacked  $\text{MoTe}_2/\text{MoS}_2$  bilayer heterostructure-based photodetectors<sup>166</sup> was much higher compared with these  $\text{MoTe}_2/\text{MoS}_2$  FET-based photodetectors. The  $\text{PdSe}_2/\text{MoS}_2$ <sup>168</sup> vdWH-based photodetectors exhibiting a very broad spectral range from  $450\text{ nm}$  (visible) to  $10.6\text{ }\mu\text{m}$  (LWIR) have been reported. The photoresponsivity of  $\text{PdSe}_2/\text{MoS}_2$  vdWH-based devices reached  $22.86\text{ A W}^{-1}$  at  $450\text{ nm}$ ,  $11.15\text{ A W}^{-1}$  at  $637\text{ nm}$ ,  $4.24\text{ A W}^{-1}$  at  $940\text{ nm}$  and  $28.83\text{ A W}^{-1}$  at  $4.012\text{ }\mu\text{m}$  at the  $V_{\text{ds}}$  of  $1\text{ V}$ . The photoresponsivity of heterostructure photodetectors at  $4.012\text{ }\mu\text{m}$  was higher than those of  $2.7\text{ }\mu\text{m}$ ,  $3.1\text{ }\mu\text{m}$ , and  $10.6\text{ }\mu\text{m}$  wavelengths. The detectivity was more than  $6.88 \times 10^9\text{ Jones}$  over the full spectral range and reached a maximum value of  $6.09 \times 10^{10}\text{ Jones}$  at  $4.012\text{ }\mu\text{m}$ . The low NEP value of  $0.13\text{ pW Hz}^{-1/2}$  was measured for the heterostructure device in the full spectral region. The photoresponse for heterostructure devices was much faster having rise/fall times of  $65.3\text{ }\mu\text{s}/62.4\text{ }\mu\text{s}$  at  $637\text{ nm}$  illumination.

A significant improvement in mobility was also observed for  $\text{NbS}_2/\text{MoS}_2$  vdWH-based Schottky-effect FETs, which yielded a mobility of  $800\text{ cm}^2\text{ V}^{-1}\text{ s}^{-1}$  at room temperature with graphene source/drain (S/D) contacts, compared with the low mobility values of  $15\text{--}170\text{ cm}^2\text{ V}^{-1}\text{ s}^{-1}$  for pure  $\text{MoS}_2$  FETs with Au contacts, depending on the annealing conditions.<sup>206</sup> In contrast, lower photoresponsivities were recorded for  $\text{GaSe}/\text{MoS}_2$  vertical heterostructure-based FETs at wavelengths from  $300\text{ nm}$  to  $670\text{ nm}$  under  $6.412\text{ mW cm}^{-2}$  to  $2.169\text{ mW cm}^{-2}$  optical power, as were a low mobility of  $0.026\text{ cm}^2\text{ V}^{-1}\text{ s}^{-1}$  and a low  $I_{\text{on}}/I_{\text{off}}$  current ratio of  $10^3$ , compared with pure  $\text{MoS}_2$  FETs due to the increased scattering of charge transport carriers at the interface of the vdW heterojunctions.<sup>207a</sup> Atomic layer vdW heterostructure-based photodiodes were fabricated using n-type  $\text{MoS}_2$  on top of p-type  $\text{GaSe}$  crystals, which showed photoresponsivity of  $\sim 3\text{ A W}^{-1}$  at  $532\text{ nm}$  when symmetric FL graphene contacts were used.<sup>207b</sup> However, the asymmetric  $\text{GaSe}/\text{FL}$  graphene and  $\text{MoS}_2/\text{Au}$  contacts based vdW photodiodes resulted in a low NEP value of  $10^{-14}\text{ W Hz}^{-1/2}$  because of the reduced dark current and a large LDR of  $\approx 70\text{ dB}$ .

### 3.6 Interface coupling effect in dual-gated $\text{MoS}_2$ phototransistors

Different strategies have been used to improve photoresponse of photodetectors. Deng *et al.*<sup>208</sup> demonstrated that the interface coupling effect (ICE) enhanced photoresponse in fully-depleted silicon-on-insulator (FD-SOI) metal-oxide-semiconductor field-effect transistors (MOSFETs). The thinner Si film-based photodetectors exhibited higher photoresponsivity due to a stronger ICE. CMOS-compatible SOI photodetectors achieved a high photoresponsivity of  $3.3 \times 10^4\text{ A W}^{-1}$ . This ICE strategy was also employed for improving the performance of  $\text{MoS}_2$ -based phototransistors. Liao *et al.*<sup>209</sup> first reported interface coupling effect



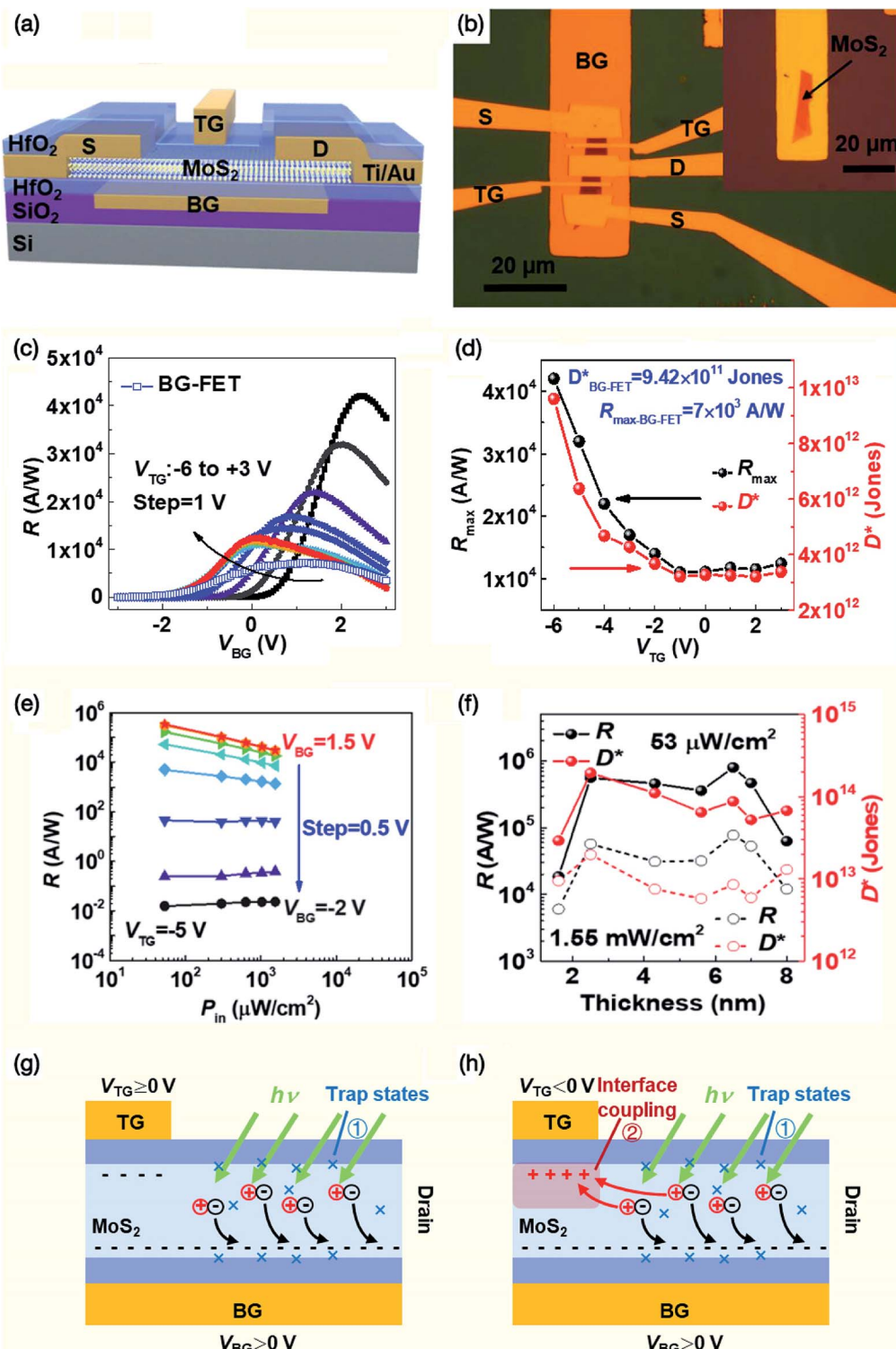


**Fig. 11** (a) 3D schematic of a dual-gated (DG) MoS<sub>2</sub> phototransistor on a Si/SiO<sub>2</sub> substrate showing location of top-gate (TG), bottom-gate (BG), source (S), drain (D) and HfO<sub>2</sub> layer as a BG dielectric. (b) Optical microscopic image of a DG MoS<sub>2</sub> phototransistor. Inset is an optical microscopic image of the ML MoS<sub>2</sub> flake. (c) Photoresponsivity ( $R$ ) of DG MoS<sub>2</sub> phototransistor as a function of back-gate voltage ( $V_{BG}$ ) under different top-gate voltage ( $V_{TG}$ ) with illumination power density ( $P_{in}$ ) of 1.55 mW cm<sup>-2</sup> at 550 nm wavelength. Blueline + square symbol represent photoresponsivity of MoS<sub>2</sub> BG-FET. (d) The maximum photoresponsivity ( $R_{max}$ ) and detectivity ( $D^*$ ) as a function of applied  $V_{TG}$ . (e)  $P_{in}$  dependence of photoresponsivity the DG MoS<sub>2</sub> phototransistor with varying  $V_{BG}$  at  $V_{TG} = -5$  V. (f) The MoS<sub>2</sub> thickness (1.6 to 8 nm) dependence of  $R$  and  $D^*$  under the illumination power density of 53 μW cm<sup>-2</sup> (solid sphere) and 1.55 mW cm<sup>-2</sup> (open circle). Schematic illustrating generated electron–hole pairs in the DG MoS<sub>2</sub> phototransistor with a positive  $V_{TG}$  bias (g) and a negative (h)  $V_{TG}$  bias in connection with interface coupling effect (ICE). Reprinted with permission from ref. 209, copyright © Wiley.

(ICE) phenomenon in dual-gated (DG) MoS<sub>2</sub> phototransistors. Both negative top-gate (TG) voltage ( $V_{TG}$ ) as well as the positive back-gate (BG) voltage ( $V_{BG}$ ) is simultaneously applied to the MoS<sub>2</sub> channel in order to facilitate the trapping of photo-generated holes in the depleted region beneath top-gate. In fabricating DG MoS<sub>2</sub> phototransistors, two metal gates were placed on the top and bottom of a MoS<sub>2</sub> layer. Fig. 11 shows a 3D schematic and optical microscopic image of a DG MoS<sub>2</sub> phototransistor, photoresponsivity ( $R$ ) of DG MoS<sub>2</sub> phototransistor as a function of  $V_{BG}$  under different  $V_{TG}$  with illumination power density ( $P_{in}$ ) of 1.55 mW cm<sup>-2</sup> at 550 nm wavelength,  $R_{max}$  and detectivity ( $D^*$ ) as a function of applied  $V_{TG}$ ,  $P_{in}$  dependent  $R$  with different  $V_{BG}$ , MoS<sub>2</sub> thickness dependent  $R$  and  $D^*$  values and schematic illustration of ICE in the DG MoS<sub>2</sub> phototransistor with positive and negative  $V_{TG}$  biases. The DG MoS<sub>2</sub> photodetector, having varied thickness between 2.5 nm to 6.5 nm, showed the highest photoresponsivity of  $7.7 \times 10^5$  A W<sup>-1</sup> and detectivity of  $1.9 \times 10^{14}$  Jones under illumination power density ( $P_{in}$ ) of 53  $\mu$ W cm<sup>-2</sup> at 550 nm under  $V_{TG} = 5.0$  V and  $V_{BG} = 2.0$  V. The response and recovery time of the DG MoS<sub>2</sub> photodetector decreased from 11.9 s to 8.3 s and 76.2 s to 46.4 s as the  $V_{TG}$  decreased from -4 V to -6 V, respectively. The maximum photoresponsivity and detectivity of BG-MoS<sub>2</sub> FETs were found to be  $7 \times 10^3$  A W<sup>-1</sup> and  $9.6 \times 10^{12}$  Jones, respectively. DG MoS<sub>2</sub> photodetectors showed photoresponsivities in  $10^4$  to  $10^5$  A W<sup>-1</sup> range independent of the MoS<sub>2</sub> thickness; however, photoresponsivity decreased as the thickness of the MoS<sub>2</sub> channel was less than 2.5 nm or more than 6.5 nm. DG MoS<sub>2</sub> photodetectors having 2.5 and 6.5 nm thickness exhibit a strong ICE under applied negative  $V_{TG}$  and positive  $V_{BG}$ . The photoresponse speed of the DG MoS<sub>2</sub> phototransistors can be adjusted with ICE. This study showed that the interface coupling effect in the DG MoS<sub>2</sub> phototransistors improves the photoelectric performance of photodetectors.

Flexible photodetectors for wearable applications have been developed from a wide variety of nanomaterials, and their performance is controlled by many conditions, including the material synthesis, atomic layer processing, hybrid heterostructures, device fabrication, measurement wavelengths and incident laser power.<sup>64,87,208-214</sup> The performance of MoS<sub>2</sub>-based photodetectors, such as the detectivity, photoconductive gain, response time and broadband responsivity depends on several factors, including the number of active layers, processing, nature of doping materials, vdW interactions, barrier and junction heterostructures, transport, photocarrier generation and spectral range.<sup>215</sup> Additionally, ferroelectric polymers, such as poly(vinylidene fluoride) (PVDF), poly(vinylidene fluoride-trifluoroethylene) [P(VDF-TrFE)] copolymer and poly(vinylidene fluoride-trifluoroethylene-chlorofluoroethylene) [P(VDF-TrFE-CFE)] terpolymer are unique organic polymers that have been used in flexible electronics because they offer high piezoelectricity, pyroelectricity and ferroelectricity, tremendous mechanical strength and flexibility to integrate into devices such as transducers, sensors, actuators, nonvolatile ferroelectric random-access memory (NV-FeRAM) and ferroelectric FETs.<sup>216</sup> Additionally, in the case of MoS<sub>2</sub> photodetectors, these ferroelectric polymers help suppress the dark

current, which ultimately improves the photoresponse of photodetectors.<sup>137</sup> MoS<sub>2</sub>-based flexible photodetectors are discussed in the next section.

#### 4. MoS<sub>2</sub> based flexible photodetectors for wearable technology

Similar to graphene, applications of flexible atomic layered TMDs have been explored for wearable technologies, from electronics to optoelectronics.<sup>36</sup> Flexible photodetectors are expected to be important elements of wearable optoelectronic technology in fields from biomedical imaging to surveillance and high-speed broadband optical communication. Flexible photodetectors have been developed using a variety of nanomaterials, from traditional semiconductors, such as Si, Ge, Se, GaP, InP, CdS and ZnSe,<sup>42-49</sup> to newly emerging perovskites,<sup>75,76</sup> as a very wide variety of hybrid heterostructures involving polymers, metal oxides, CNTs, graphene, transition metal trichalcogenides, *etc.*<sup>77-89</sup> Similarly, flexible MoS<sub>2</sub> atomic layers and MoS<sub>2</sub>-based hybrid heterostructures have been explored for fabricating photodetectors for the next generation of wearable technologies. The progress made in developing flexible MoS<sub>2</sub> photodetectors is summarized in this section.

Flexible polymeric substrates based on poly(ethylene terephthalate) (PET), Kapton/polyimide/(PI), poly(methylmethacrylate) (PMMA), poly(ethylene naphthalate) (PEN), poly(dimethylsiloxane) (PDMS) and poly(4-vinylphenol) (PVP) have been generally used for developing wearable electronic and optoelectronic devices due to their inherent mechanical strength and flexibility.<sup>23,25,36</sup> In addition, textile fibers and papers have also been considered for developing flexible devices. Zhang *et al.*<sup>217</sup> reported substrate-dependent performance of MoS<sub>2</sub> photodetectors owing a dual-photogating effect where rigid silicon carbon (SiC) and flexible Kapton (polyimide) films were used as substrates for developing MoS<sub>2</sub> photodetectors. Both SiC and Kapton have strong light absorption, therefore, the dual-photogating effect induced at the interface of the MoS<sub>2</sub>/SiC or MoS<sub>2</sub>/Kapton assists in enhancing the photoresponse of MoS<sub>2</sub>-based photodetectors. Fig. 12 shows the schematic illustrations of MoS<sub>2</sub> photodetectors fabricated on undoped SiC and Kapton substrates, their energy level diagrams and the variation of photoresponsivity ( $R$ ) and on/off ratio ( $I_{photo}/I_{dark}$ ) of rigid MoS<sub>2</sub>/SiC and MoS<sub>2</sub>/SiO<sub>2</sub>/Si photodetectors as well as flexible MoS<sub>2</sub>/Kapton and MoS<sub>2</sub>/PET photodetectors as a function of optical power intensity in the UV and visible wavelengths. The bandgap of 2.7 and 3.2 eV and the electron affinity of 4.2 and 1.8 eV for MoS<sub>2</sub> and SiC are depicted, respectively. The energy level mismatch at the MoS<sub>2</sub>/SiC interface yields to a strong built-in electric field ( $E_{in}$ ) which assists in separating the photoexcited carriers in MoS<sub>2</sub>. The enhanced photoresponse was noticed for the MoS<sub>2</sub>/SiC photodetectors more than those of MoS<sub>2</sub>/SiO<sub>2</sub>/Si photodetectors. The energy band diagram in a flexible MoS<sub>2</sub>/Kapton photodetector shows the valence band of MoS<sub>2</sub> as -6.0 eV and conduction band as -4.2 eV and the HOMO level at -5.0 eV and LUMO level at -2.1 eV, *versus* vacuum. The highest photoresponsivity of  $\sim 10^4$  A W<sup>-1</sup> for MoS<sub>2</sub>/SiC photodetector and the



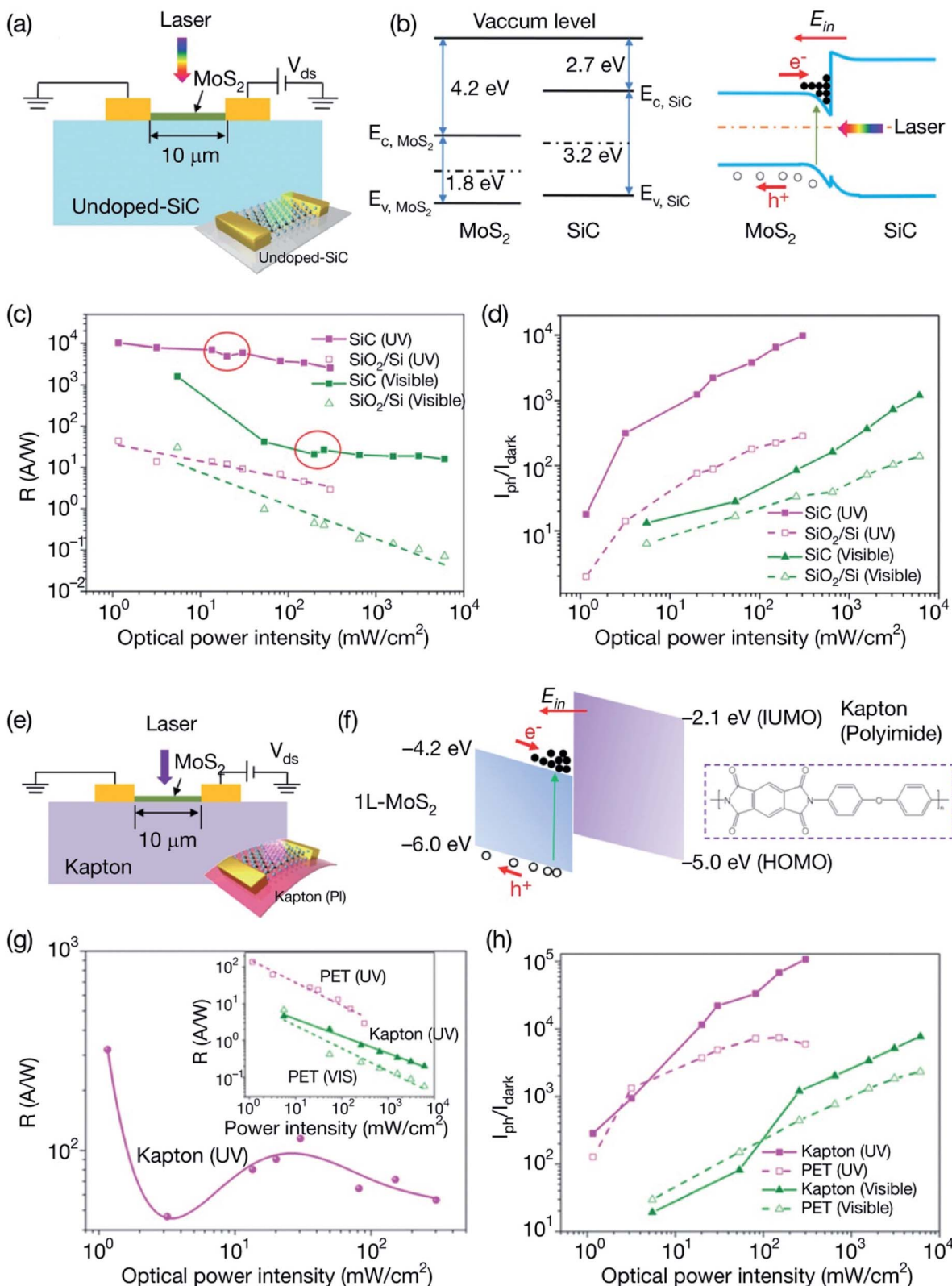


Fig. 12 (a) Schematic illustration of MoS<sub>2</sub> photodetector on a SiC substrate. (b) Energy level diagrams of the MoS<sub>2</sub> and SiC showing electron affinity and bandgap of MoS<sub>2</sub> and SiC. MoS<sub>2</sub>/SiC interface showing a band structure. (c) Variation of photoresponsivity ( $R$ ) and (d) on/off ratio ( $I_{photo}/I_{dark}$ ) of rigid MoS<sub>2</sub>/SiC and MoS<sub>2</sub>/SiO<sub>2</sub>/Si photodetectors as a function of optical power intensity in the UV and visible wavelengths. (e) Schematic illustration of MoS<sub>2</sub> photodetector on a flexible Kapton substrate. (f) Energy band diagram of a flexible MoS<sub>2</sub>/Kapton photodetector. (g) Variation of photoresponsivity ( $R$ ) and (h) on/off ratio ( $I_{photo}/I_{dark}$ ) of flexible MoS<sub>2</sub>/Kapton and MoS<sub>2</sub>/PET photodetectors as a function of optical power intensity in the UV and visible regions. Reprinted with permission from ref. 217, copyright © Royal Society of Chemistry.



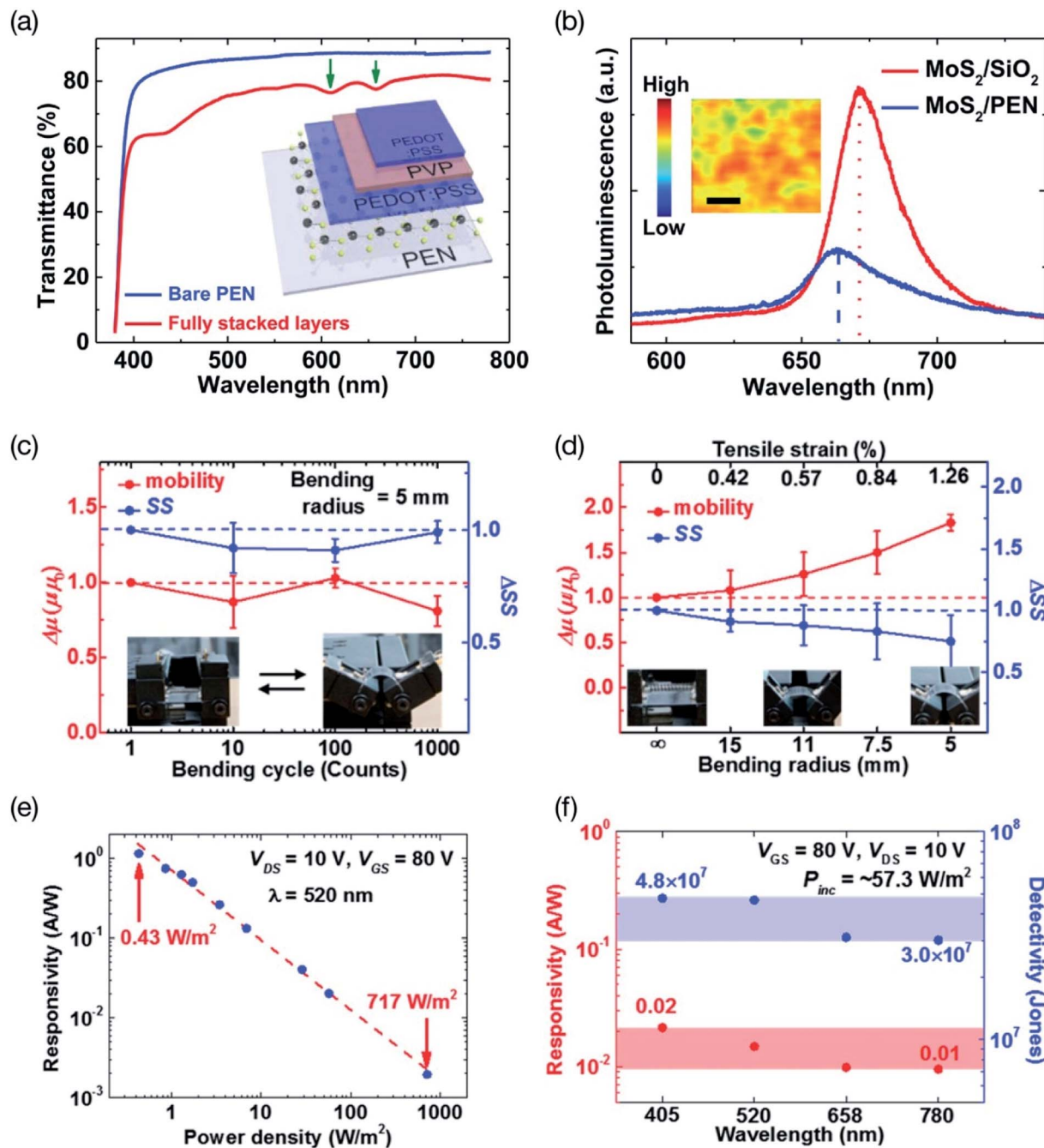


Fig. 13 (a) Transmittance spectra of the flexible bare PEN substrate, denoted by the blue line, and fully stacked PEDOT:PSS/PVP/PEDOT:PSS/MoS<sub>2</sub>/PEN layers, denoted by the red line. The inset is a schematic of the phototransistors with stacked layers. (b) PL spectra of CVD-grown monolayer MoS<sub>2</sub>/SiO<sub>2</sub>/Si and MoS<sub>2</sub>/PEN. The inset is PL intensity mapping at 670 nm (1.85 eV). (c) The variation in mobility and SS values as a function of the number of bending cycles for a 5 mm bending radius, and (d) mobility and SS values at different bending radii of 5, 7.5, 11, 15 mm, and  $\infty$ . (e) Variation of photoresponsivity MoS<sub>2</sub> phototransistors as a function of power density at 520 nm laser wavelength. (f) Photoresponsivity and photodetectivity of transparent MoS<sub>2</sub> phototransistors at different laser wavelengths. Reprinted with permission from ref. 219, copyright © American Chemical Society.

fastest current  $I_{\text{on}}/I_{\text{off}}$  ratio of  $\sim 10^5$  for MoS<sub>2</sub>/Kapton photodetector were measured at 325 nm laser illumination due to the dual-photogating effect generated at the MoS<sub>2</sub>/substrate interface. SiC and Kapton substrates improve the photoresponse of MoS<sub>2</sub> photodetectors due to the light absorption.

Transparent poly(4-vinylphenol) (PVP) as the encapsulation layer, as well as a gate dielectric was used by Ma *et al.*<sup>218</sup> for

developing flexible MoS<sub>2</sub> phototransistors on a polyarylate substrate. PVP thin film having  $\geq 80\%$  transmittance between 400 nm to 900 nm was used. The PVP encapsulation not only increased the mobility but also improved the current  $I_{\text{on}}/I_{\text{off}}$  ratio and subthreshold slope. The photoresponsivity ( $2 \text{ A W}^{-1}$ ), as well as the detectivity ( $3.1 \times 10^{12} \text{ Jones}$ ) of MoS<sub>2</sub> phototransistors, was increased by two orders of magnitude over the

visible to IR range due to the doping effect of hydroxyl groups in PVP. For a comparison, the transparent PVP polymer improved the photoresponsivity of  $\text{MoS}_2$ -based flexible phototransistor devices by ten fold over that of PMMA encapsulated devices. The photodetectors developed from monolayer and bilayer  $\text{MoS}_2$  encapsulated with a  $\text{HfO}_2$  layer showed photoresponsivity in the wide range of  $10\text{--}10^4 \text{ A W}^{-1}$  and a response time from 10 ms to 10 s.<sup>135</sup> These studies show the role of encapsulation in increasing the photoresponse of  $\text{MoS}_2$ -based photodetectors.

Transparent and flexible  $\text{MoS}_2$  phototransistor arrays using all-organic components with inkjet-printing technology were developed by Kim *et al.*<sup>219</sup> The CVD-grown monolayer  $\text{MoS}_2$  channel layers were transferred onto a flexible PEN substrate. The all-organic components, including poly(3,4-ethylenedioxythiophene)polystyrenesulfonate (PEDOT:PSS)-based source/drain electrodes, PVP as a gate dielectric layer, and PEDOT:PSS as a top-gate electrode, were consecutively inkjet printed on the monolayer  $\text{MoS}_2$ /PEN substrate. The formation of CVD-grown monolayer  $\text{MoS}_2$  was confirmed by Raman spectroscopy, XPS, scanning transmission electron microscopy (STEM) coupled with energy dispersive X-ray spectroscopy (EDS), PL spectroscopy, and optical transmittance spectroscopy as demonstrated in Fig. 13(a and b). The optical transmittance of the inkjet-printed  $\text{MoS}_2$  phototransistors was 76%, compared with 87% for the PEN substrate in the same visible wavelength range. The performance of printed  $\text{MoS}_2$  phototransistors was not degraded under 1000 repeated bending cycles, as shown by the mobility and SS values for a fixed 5 mm bending radius, which corresponds to 1.26% uniaxial tensile strain along the  $\text{MoS}_2$  channel length, demonstrating good mechanical stability as shown in Fig. 13(c and d). The mobility and SS values of  $\text{MoS}_2$  phototransistors measured at bending radii of 15, 11, 7.5, and 5 mm increased as the bending radius decreased. Fig. 13(e and f) shows the photoresponsivity and photodetectivity of transparent  $\text{MoS}_2$  phototransistors as a function of wavelength over the 405–780 nm region at a fixed laser power density of  $57.3 \text{ W m}^{-2}$ , a  $V_{\text{gs}}$  of 80 V, and a  $V_{\text{ds}}$  of 10 V. The photoresistivity, detectivity and EQE of  $\text{MoS}_2$  phototransistors showed wavelength dependence, varying between  $0.01$  and  $0.02 \text{ A W}^{-1}$ ,  $3.0$  and  $4.8 \times 10^7 \text{ Jones}$ , and  $1.5$  and  $6.6\%$ , respectively.

Flexible photodetectors obtained by depositing  $\text{MoS}_2$  layers on a PI substrate were developed by Lim *et al.*<sup>220</sup> The  $\text{MoS}_2$  layers were characterized in terms of their uniformity, stoichiometry and structural homogeneity by Raman, AFM, and XPS techniques. The frequency difference of  $23.4 \text{ cm}^{-1}$  between the  $E_{2g}^1$  and  $A_{1g}$  Raman vibration modes of the  $\text{MoS}_2$  layers indicated few-layer  $\text{MoS}_2$  thin films. TEM showed the formation of five-layer  $\text{MoS}_2$  films and an interlayer spacing of  $6 \text{ \AA}$ . The optical transmittance was 90.8% at 550 nm for the  $\text{MoS}_2$  films deposited on a glass substrate.  $\text{MoS}_2$  FETs showed a mobility of  $14 \text{ cm}^2 \text{ V}^{-1} \text{ s}^{-1}$  and an on-off current ratio of  $5 \times 10^2$ . The  $\text{MoS}_2$  photodetector arrays were also fabricated on a 4-inch  $\text{SiO}_2/\text{Si}$  wafer. Fig. 14 shows a photograph of the  $\text{MoS}_2$  layer on a flexible PI film, XPS spectra, time-dependent photocurrents before and after bending up to  $10^5$  bending cycles, and the change in the photocurrent of  $\text{MoS}_2$ -based flexible photodetectors as a function of the bending cycle at 20 V. The visible-light

photodetectors exhibited a response time of 13 s and a recovery time of 30 s.  $\text{MoS}_2$  photodetectors were formed on a flexible PI substrate, and the photocurrent decreased by 5.6% after  $10^5$  bending cycles at a bending radius of 5 mm.

Enhancement of the photocurrent and sensitivity has been observed for flexible p-CuO/n- $\text{MoS}_2$  heterojunction-based photodetectors.<sup>221</sup> The dark current of CuO/ $\text{MoS}_2$  heterojunction increased from 0.039 nA to 0.12 nA as the tensile strain was increased from 0% to 0.65%, whereas the photocurrent increased to 108 nA under 0.65% tensile strain with  $1656 \text{ mW cm}^{-2}$  light intensity, which is 2770-fold increase in the photocurrent over that of the dark current. The photocurrent of the p-CuO/n- $\text{MoS}_2$  heterojunction increased 27 times under 0.65% tensile strain compared with that of the strain-free heterojunction at 532 nm, and the sensitivity reached  $3.27 \times 10^8 \text{ Jones}$ . The photoresponse of a flexible CuO/n- $\text{MoS}_2$  heterojunction based photodetector was increased by the piezophototronic effect. Zhang *et al.*<sup>222</sup> fabricated a  $\text{MoS}_2$  phototransistor on a transparent and flexible biodegradable paper substrate using a gel electrolyte gate dielectric. The gel electrolyte thin layer was coated on top of mechanically exfoliated  $\text{MoS}_2$  flakes as the gate dielectric. The optical transmittance of the  $\text{MoS}_2$  phototransistor at 550 nm was 82%, compared with 85% for the bare nanopaper, due to the added passivation layer and gel electrolyte gate dielectric. The  $\text{MoS}_2$  phototransistor exhibited a photoresponsivity of  $1.5 \text{ kA W}^{-1}$  at an illumination power of 10 nW. The  $\text{MoS}_2$  phototransistor showed high flexibility and optical transparency with great photoresponsivity.

The solution-processed few-layer  $\text{MoS}_2$  thin films on several flexible substrates, including PI, Al, and Cu foils, cotton thread, and cellulose, carbon, and ceramic paper were developed by Sahatiya *et al.*<sup>223</sup> The growth of layers and morphologies of the  $\text{MoS}_2$  nanosheets varied depending on the substrate. The photodetectors fabricated from these  $\text{MoS}_2$  nanosheets showed that the defects introduced during growth control the photocurrent response. Sahatiya *et al.*<sup>224</sup> also fabricated a broadband flexible photodetector using 1D  $\text{V}_2\text{O}_5$  NWs and 2D  $\text{MoS}_2$  flakes covering the UV (365 nm) to NIR (780 nm) region, wherein  $\text{V}_2\text{O}_5$  NWs absorb in the UV-visible, and  $\text{MoS}_2$  absorbs in the visible-NIR regions. The  $\text{V}_2\text{O}_5/\text{MoS}_2$  hybrid device showed a responsivity of  $41.5 \text{ mA W}^{-1}$  in the UV,  $65.1 \text{ mA W}^{-1}$  in the visible, and  $29.4 \text{ mA W}^{-1}$  in the NIR. The same research team<sup>225</sup> also developed a flexible photodetector using  $\text{MoS}_2/\text{C}$  QD hybrid films. The wide UV-vis-NIR absorbance range originated from the UV absorbance of the C QDs and the visible-NIR region absorbance of  $\text{MoS}_2$ . The  $\text{MoS}_2/\text{C}$  QD sensor showed photoresponsivities of 2.62, 8.4, and  $18.12 \text{ mA W}^{-1}$  in the NIR, UV, and visible regions, respectively. The  $\text{MoS}_2/\text{C}$  QD sensor showed almost no change in photoresponse up to 500 bending cycles. These flexible  $\text{MoS}_2/\text{C}$  QD broadband photodetectors can be used for wearable electronics for surveillance purposes.

#### 4.1 $\text{MoS}_2/\text{graphene}$ hybrid heterostructures for flexible photodetectors

The indirect bandgap restricts the photodetection ability of multilayer  $\text{MoS}_2$ . Hybrids of  $\text{MoS}_2$  atomic layers with gapless



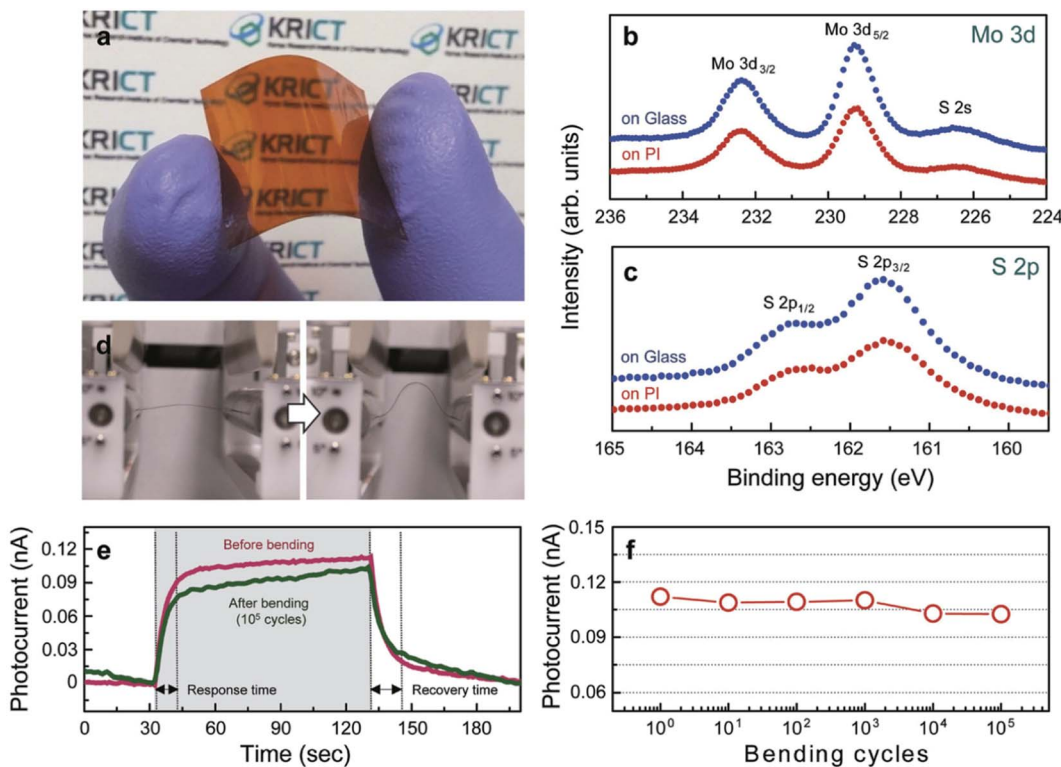


Fig. 14 (a) Photograph of the  $\text{MoS}_2$  layer on a flexible PI film. (b) XPS spectra showing the Mo 3d core level and (c) S 2p core level spectra of  $\text{MoS}_2$  layers on glass and PI substrates. (d) Bending of a flexible  $\text{MoS}_2$  layer deposited on a PI substrate at a 5 mm bending radius. (e) Time-dependent photocurrents of  $\text{MoS}_2$ -based flexible photodetectors measured at an incident power of  $12.5 \text{ mW cm}^{-2}$  and  $V = 20 \text{ V}$ , before and after bending up to  $10^5$  bending cycles. (f) The variation in the photocurrent of the  $\text{MoS}_2$  photodetector as a function of the bending cycle. Reprinted with permission from ref. 220, copyright © 2016 Wiley-VCH.

graphene have been used to improve the optoelectronic properties by utilizing the high carrier mobility, ultrafast response and broadband absorption of graphene and the generation of electron–hole pairs by  $\text{MoS}_2$ . Ross *et al.*<sup>226</sup> obtained a high carrier mobility ( $1 \times 10^4 \text{ cm}^2 \text{ V}^{-1} \text{ s}^{-1}$ ) in a graphene/ $\text{MoS}_2$  hybrid structure by placing monolayer graphene on a multilayer  $\text{MoS}_2$  nanosheet on a Si/SiO<sub>2</sub> substrate. The graphene/ $\text{MoS}_2$  hybrid-based photodetector showed high photoresponsivities of  $1 \times 10^{10} \text{ A W}^{-1}$  at 130 K under an LED power of  $1 \text{ fW } \mu\text{m}^{-2}$  and of  $5 \times 10^8 \text{ A W}^{-1}$  at room temperature under an LED power of  $6.4 \text{ fW } \mu\text{m}^{-2}$  and gate-tunable photoconductivity with a high photodetection capability. Zhang *et al.*<sup>226</sup> used CVD-grown monolayer  $\text{MoS}_2$  to develop a graphene/ $\text{MoS}_2$  hybrid structure-based phototransistor that showed a photoresponsivity of  $1.2 \times 10^7 \text{ A W}^{-1}$  at 650 nm under a light power of  $0.01 \text{ W m}^{-2}$  and a high photogain of  $10^8$ . A photoresponsivity of  $3.34 \times 10^3 \text{ A W}^{-1}$  and a detectivity of  $1.004 \times 10^{12} \text{ Jones}$  have been observed for graphene/ $\text{MoS}_2$  hybrid structure-based FETs.<sup>227</sup> The phototransistor fabricated from multilayer  $\text{MoS}_2$  using graphene source/drain electrodes showed a high photoresponsivity of  $1 \times 10^4 \text{ A W}^{-1}$  in the wavelength range of 470–600 nm.<sup>228</sup>

Chen *et al.*<sup>229</sup> developed n-n-type vdWHs using multilayer  $\text{MoS}_2$  coated with a layer of nitrogen-doped graphene QDs (N-QDs) to complement each other with their strong characteristics to improve the carrier mobility. In this hybrid structure,

$\text{MoS}_2$  was used to generate photoexcited holes, while the QDs working as a gain material contributed to the recirculation of photoexcited carriers at the heterojunction interface. Additional photocarriers were also created by the reabsorption of light emitted from the QDs by  $\text{MoS}_2$ . Fig. 15 shows a schematic of the  $\text{MoS}_2$ /QD heterostructure-based phototransistor, a comparison of the drain current ( $I_d$ ) *versus* source–drain voltage ( $V_{ds}$ ) curves of pristine  $\text{MoS}_2$  and  $\text{MoS}_2$ /QD hybrid phototransistor devices in the dark and under light illumination, and the photoresponse speed and incident light power-dependent photoresponsivity of  $\text{MoS}_2$ /QD vdWH-based phototransistors. In the case of the  $\text{MoS}_2$  phototransistor, the drain current increased to  $10.15 \mu\text{A}$  at a 405 nm wavelength under an incident laser power of  $30.1 \mu\text{W}$ , with a source–drain voltage ( $V_{ds}$ ) of  $1.68 \text{ V}$ ; this drain current was 1000 times larger compared with the  $11 \text{ nA}$  current recorded in the dark state. The  $\text{MoS}_2$  phototransistor showed a sensitivity up to  $5 \text{ nW}$  and rise/fall times longer than 50 s. The  $\text{MoS}_2$  phototransistor showed the highest photocurrent of  $16.2 \mu\text{A}$  at  $50 \text{ nW}$  and photoresponsivity of  $800 \text{ A W}^{-1}$  at  $70 \text{ V}$ . The  $\text{MoS}_2$ /QD hybrid phototransistor showed a significant change in the drain current ( $I_d$ ) *versus* source–drain voltage ( $V_{ds}$ ) curves, a higher drain current and a faster photoresponse speed compared with the pristine  $\text{MoS}_2$  phototransistor. The photocurrent of the  $\text{MoS}_2$ /QD hybrid phototransistor reached  $0.55 \text{ mA}$  at a gate bias of



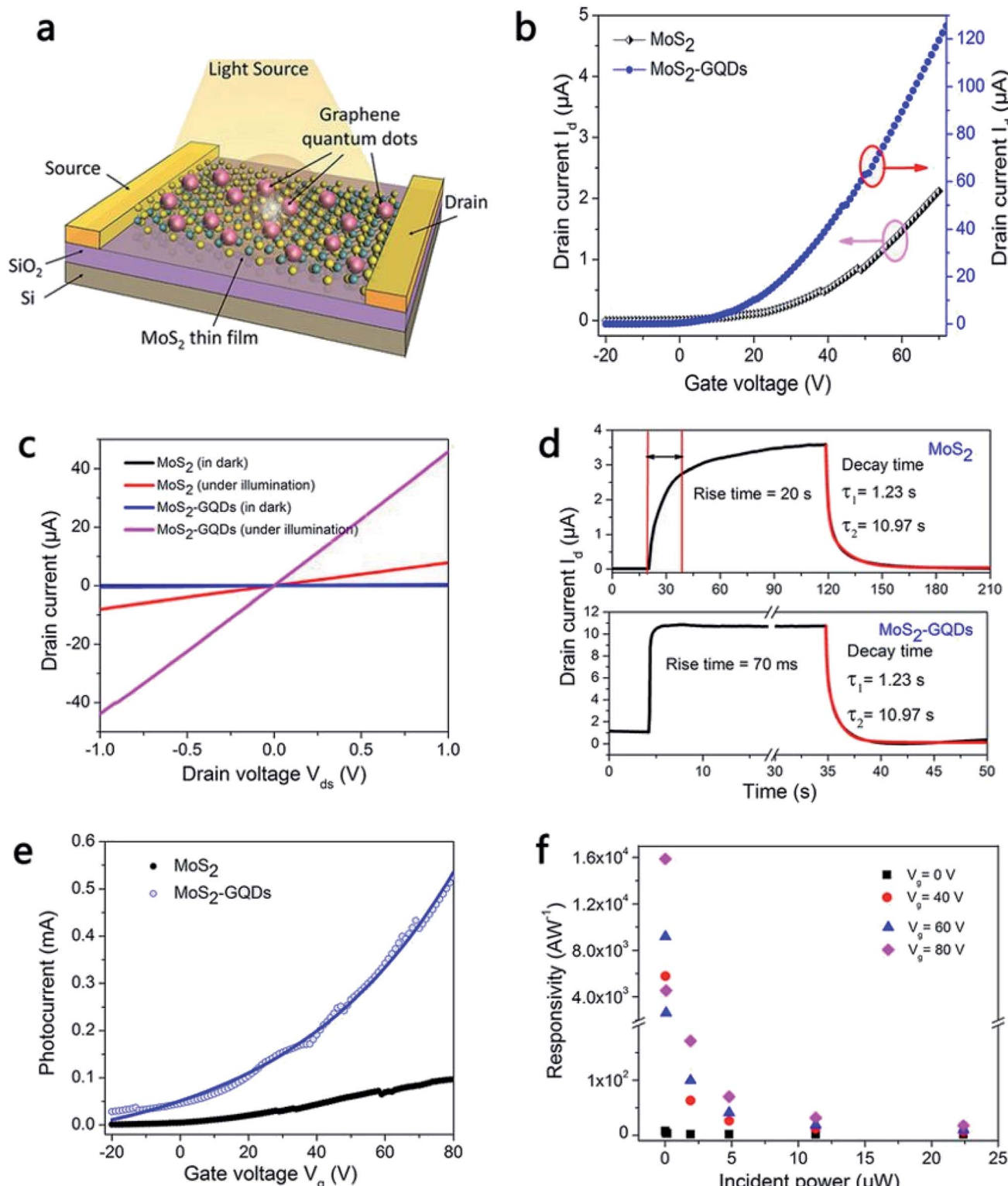


**Fig. 15** (a) Schematic of the MoS<sub>2</sub>/GQD heterostructure-based phototransistor. (b) Current vs. voltage curves of MoS<sub>2</sub> and MoS<sub>2</sub>/GQD phototransistor devices. Here,  $I_d$  is the drain current, and  $V_{ds}$  is the source-drain voltage = 1 V. (c) Drain current versus source-drain voltage curves in the dark and under light illumination for MoS<sub>2</sub> and MoS<sub>2</sub>/GQD phototransistors, measured at a 405 nm wavelength under an incident light power of 17  $\mu\text{W}$ . (d) Photoresponse times of MoS<sub>2</sub> (top) and MoS<sub>2</sub>/GQD (bottom) phototransistors. (e) Photocurrent versus back gate voltage curves for MoS<sub>2</sub> and MoS<sub>2</sub>/GQD phototransistors, measured under an incident light power of 30.1  $\mu\text{W}$ . (f) Incident light power-dependent photoresponsivity of MoS<sub>2</sub>/GQD phototransistors. Reprinted with permission from ref. 229, copyright © Springer Nature Publishing.



80 V. The  $\text{MoS}_2$ /GQD heterostructure-based photodetector showed a photoresponsivity of  $1.6 \times 10^4 \text{ A W}^{-1}$  at 80 V under an incident power of 50 nW and a photoconductive gain of  $2.4 \times 10^7$  electrons per photon. The high performance of  $\text{MoS}_2$ /GQD heterostructure-based photodetectors occurs due to their increased light absorption and the effective generation of electron-hole pairs between the GQDs and  $\text{MoS}_2$ .

Large-area  $\text{MoS}_2$  films on monolayer graphene were developed by Chen *et al.*<sup>230</sup> by adding hydrogen gas during the CVD growth process, which resulted in centimeter-long monolayer  $\text{MoS}_2$  continuous films on graphene. Hydrogen addition prevented the degradation of monolayer graphene by decreasing the oxidation. The  $\text{MoS}_2$ /graphene-based photodetector showed a photoresponsivity as high as  $2.4 \text{ A W}^{-1}$  under 532 nm illumination and a  $135 \mu\text{W}$  power density. Flexible photodetectors, consisting of an rGO fiber and  $\text{MoS}_2$  nanosheet hybrid composite, showed significant enhancement of the photocurrent.<sup>231a</sup> The Zn-doped  $\text{MoS}_2$ /rGO hybrid fiber-based flexible photodetectors showed a photoresponsivity of  $5.73 \text{ A W}^{-1}$  at laser power density of  $125.2 \text{ W m}^{-2}$  using a bias voltage of 2 V. The same research group also reported one-step synthesis for preparing Zn-doped  $\text{MoS}_2$  photodetector using Zn(II)-tetrakis(4-hydroxyphenyl)-porphyrin [Zn(II)THPP] as a dopant loaded seeding promoter.<sup>231b</sup> The Zn-doped  $\text{MoS}_2$  thin films were transferred onto a PET substrate to fabricated flexible photodetectors. The electrical resistance of the flexible photodetector increased 13% after 10 000 bending cycles at a bending radius of 3 cm while resistance increased 10% at a bending radius of 1 cm, demonstrating good mechanical stability of the flexible photodetectors. The photocurrent of Zn-doped  $\text{MoS}_2$  photodetectors was found to increase from  $0.05 \mu\text{A}$  to  $2.62 \mu\text{A}$  as the applied voltage was raised from 1 V to 40 V at a power density of  $125.2 \text{ W m}^{-2}$  and a similar trend was observed for the photoresponsivity. The photocurrent and photoresponsivity of the Zn-doped  $\text{MoS}_2$  photodetectors can be controlled by adjusting the Zn doping concentration. Asad *et al.*<sup>232</sup> used  $\text{MoS}_2$  nanoparticle ( $\text{MoS}_2$  NP)-decorated graphene nanoribbons (GNRs) to develop flexible phototransistors. In the GNR- $\text{MoS}_2$ NP hybrid, the GNRs function as carrier transport channels, whereas the  $\text{MoS}_2$  NPs offer high gain absorption. The  $\text{MoS}_2$  NPs also generate electron-hole pairs, which are separated at the GNR and  $\text{MoS}_2$  NP

interface and result in electron transfer from the  $\text{MoS}_2$  NPs to the GNRs. The flexible GNR- $\text{MoS}_2$  hybrid photodetector showed a photoresponsivity of  $66 \text{ A W}^{-1}$ , a fast rise time of 5 ms and a decay time of 30 ms under 385 nm illumination and a  $2.1 \mu\text{W}$  power density. The photoresponsivity of the GNR- $\text{MoS}_2$  hybrid photodetector was  $1.3 \times 10^5$  times larger than that of the pristine graphene photodetector and  $10^4$  times larger than that of the pristine  $\text{MoS}_2$  phototransistor. The hybrid photodetector also showed high stability for a 6 mm bending radius. De Fazio *et al.*<sup>233</sup> developed visible-light flexible photodetectors using CVD-grown single-layer graphene (SLG) and single-layer (1L)  $\text{MoS}_2$  on flexible PET substrates. Fig. 16 is a schematic of a flexible SLG/1L  $\text{MoS}_2$  photodetector on a flexible PET substrate and a photograph of the photodetector showing the optical transparency and flexibility. The polymer electrolyte-gated flexible SLG/1L  $\text{MoS}_2$  photodetector showed an external photoresponsivity of  $45.5 \text{ A W}^{-1}$  and an internal photoresponsivity of  $570 \text{ A W}^{-1}$  at 642 nm, a photoconductive gain of  $4 \times 10^5$ , and  $>82\%$  optical transparency. The flexible photodetectors showed mechanical durability upon bending at a 1.4 cm bending radius. The photoconductive gain increased by nearly one order of magnitude from 0.1 to 1.0 V, and the photoresponsivity reached  $45.5 \text{ A W}^{-1}$  at a  $V_{ds}$  of 1 V. Therefore, the photoconductive gain of the SLG/1L  $\text{MoS}_2$ -based heterostructure photodetector being four orders of magnitude larger than that of the 1L  $\text{MoS}_2$  photodetector developed without any SLG showed that the SLG/1L  $\text{MoS}_2$  heterostructure is important for high photoresponsivity.

Photodetector devices using a  $\text{MoS}_2$ /graphene hybrid pattern formed by the soft-lithographic patterning technique were reported by Kang *et al.*<sup>234</sup> The cross-stacked  $\text{MoS}_2$ /graphene patterns were transferred onto a flexible PET substrate for fabricating flexible photodetectors. Fig. 17 shows a schematic of the formation of cross-stacked  $\text{MoS}_2$ /graphene patterned nanostructures. The various fabrication steps involve the CVD growth of  $\text{MoS}_2$  nanosheets on a 5,10,15,20-tetrakis(4-hydroxyphenyl)-21H,23H-porphyrin (p-THPP) promoter layer, transfer and patterning of the  $\text{MoS}_2$  nanosheets using a PDMS mold, CVD growth of a graphene layer on Cu foil, transfer of the graphene layer onto a 300 nm thick  $\text{SiO}_2$  substrate, and transfer of the graphene layer onto the top of the  $\text{MoS}_2$  patterns by using

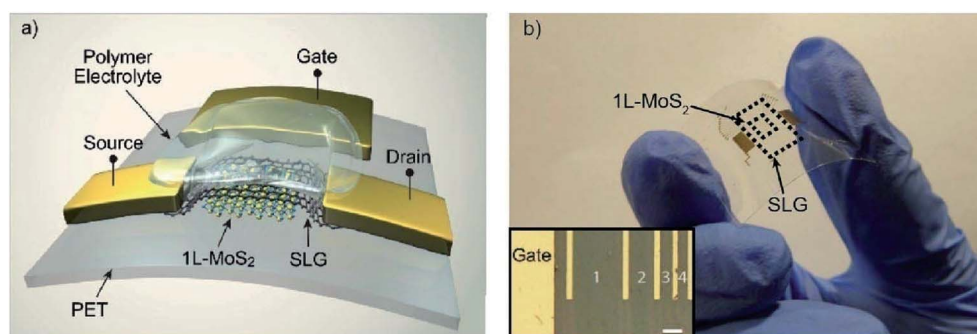


Fig. 16 (a) Schematic of the single-layer graphene (SLG)/1L  $\text{MoS}_2$  photodetector on a flexible PET substrate. (b) Photograph of the flexible photodetector showing optical transparency. The inset is an optical image of 4 photodetectors with different channel lengths. Reprinted with permission from ref. 233, copyright © 2016 American Chemical Society.



a dimethyl sulfoxide (DMSO)-coated PDMS mold—the same process that was eventually employed for the transfer and patterning of the MoS<sub>2</sub> film. The SEM images confirmed the cross-stacked MoS<sub>2</sub>/graphene line patterns with a width of 7  $\mu\text{m}$ . The Raman peak difference between the E<sub>2g</sub><sup>1</sup> and A<sub>1g</sub> vibration modes of MoS<sub>2</sub> was estimated to be 20  $\text{cm}^{-1}$ , which indicated the formation of monolayer MoS<sub>2</sub> patterns.

The photoresponsivities for cross-stacked MoS<sub>2</sub>/graphene hybrid photodetectors containing monolayer, bilayer, and trilayer MoS<sub>2</sub> films increased linearly as a function of the bias voltage from (10 to 50) V. The trilayer MoS<sub>2</sub> film-based hybrid photodetector showed the highest photoresponsivity compared with the monolayer and bilayer MoS<sub>2</sub> films, a value of 5  $\text{A W}^{-1}$  at a bias voltage of 2 V. Fig. 18 shows optical microscope images of cross-stacked patterns of MoS<sub>2</sub>/graphene based on MoS<sub>2</sub> patterns formed by the soft-lithographic patterning technique, photographs of MoS<sub>2</sub>/graphene hybrid patterns on a flexible PET substrate before and after the bending test, and the photoresponsivity of flexible MoS<sub>2</sub>/graphene hybrid photodetectors as a function of the number of bending cycles at a bending radius of 9 mm and a 1.0 V bias. The mechanical stability of cross-stacked patterns of graphene/MoS<sub>2</sub> photodetector devices fabricated on flexible PET substrates was evaluated under various bending cycles. The photocurrent of the MoS<sub>2</sub>/graphene hybrid photodetector with MoS<sub>2</sub> patterns 10  $\mu\text{m}$  in width was measured between 1 and 10 000 bending cycles. The photocurrent of the device decreased from 4.3 to 3.7  $\text{A}$  as a function of the number of bending cycles. The smallest reduction in the photoresponsivity

with increasing number of bending cycles was observed for the 10  $\mu\text{m}$  wide MoS<sub>2</sub> patterns due to the lower compressive stress. Graphene has also been used in developing flexible photodetectors with atomic layered materials. Graphene/tin monosulfide (SnS) hybrid structure-based photodetectors further substantiated that a high photoresponsivity of  $1.7 \times 10^4 \text{ A W}^{-1}$  under an optical light intensity of  $1.2 \text{ mW m}^{-2}$  can be achieved in flexible graphene/SnSe/graphene-based photodetectors and demonstrated no change in photoresponse after 25 bending cycles, indicating high mechanical strength of the devices.<sup>65</sup>

Polymer electrolytes have been used for developing flexible MoS<sub>2</sub> photodetectors. Sun *et al.*<sup>235</sup> fabricated four phototransistor arrays with 100, 200, 500, and 1000  $\mu\text{m}$  channel lengths in one flexible photodetector device based on a vertically stacked MoS<sub>2</sub>/graphene thin film deposited on a PET substrate. A polymer electrolyte consisting of PEO : LiClO<sub>4</sub> in an 8 : 1 ratio was used to fabricate a flexible side-gated photodetector. The flexible photodetector based on the MoS<sub>2</sub>/graphene film showed an external responsivity of  $3.5 \text{ A W}^{-1}$  at  $-1 \text{ V}$  ( $V_{\text{gs}}$ ) under a  $60 \mu\text{W}$  incident power. The MoS<sub>2</sub>/graphene thin film had a transmittance of 10.5% at 520 nm, and the internal photoresponsivity of the photodetector reached  $33.3 \text{ A W}^{-1}$ . The photocurrent of the MoS<sub>2</sub>/graphene film can be adjusted in the 0 to 300  $\mu\text{A}$  range.

#### 4.2 MoS<sub>2</sub>/carbon nanotube hybrid heterostructures for flexible photodetectors

CNTs show large optical absorption compared with traditional semiconductors; therefore, photodetection can be further

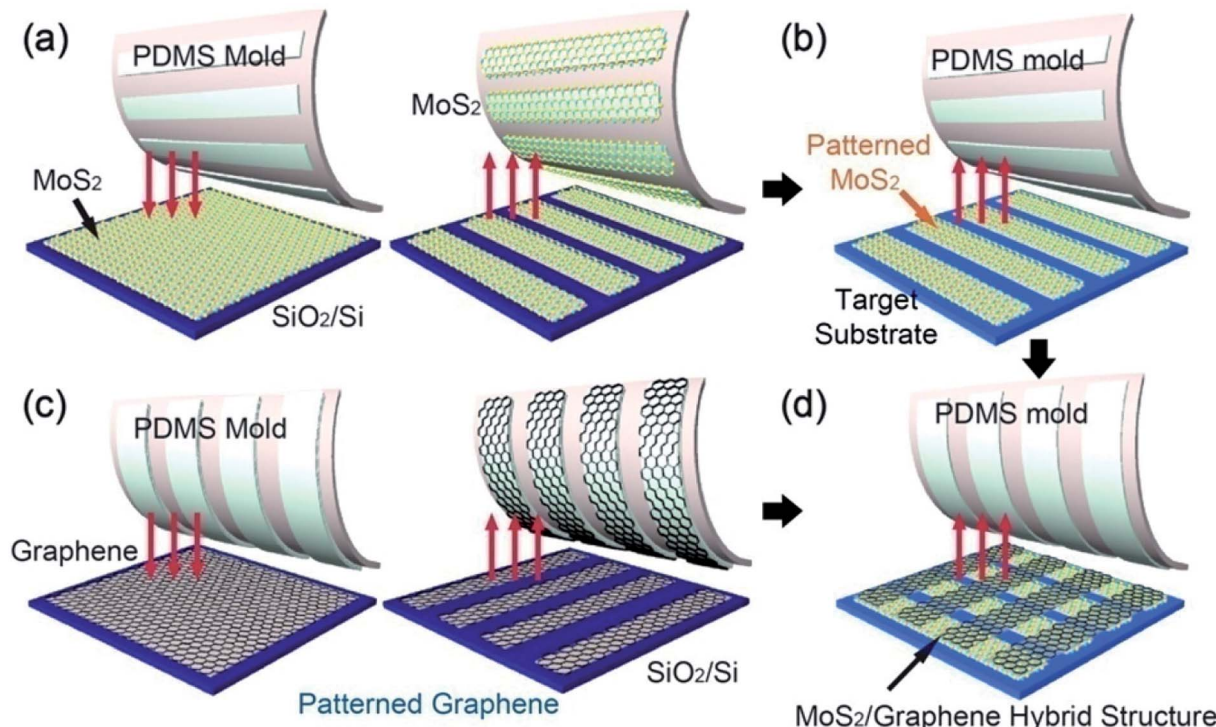


Fig. 17 Schematic of the fabrication steps for cross-stacked MoS<sub>2</sub>/graphene patterned nanostructures. (a) CVD growth of MoS<sub>2</sub> nanosheets on a SiO<sub>2</sub> substrate (left), and pattern fabrication on the MoS<sub>2</sub> layer within a target area (right). (b) Transfer of MoS<sub>2</sub> patterns on the PDMS mold onto a target substrate. (c) CVD growth of a graphene layer. (d) Transfer of graphene patterns on the PDMS mold to the top of MoS<sub>2</sub> patterns on the target substrate. Reprinted with permission from ref. 234, copyright © Elsevier.



improved by using CNTs in hybrid heterostructures.<sup>236,237</sup> CNT-based hybrid broadband photodetectors have been fabricated with a variety of functional materials, including Si, GaAs, fullerenes, graphene, ZnO, PbS, and perovskites.<sup>238–249</sup> A negative photoresponsivity on the order of  $10^8 \text{ A W}^{-1}$  has been reported in fullerene-sensitized aligned CNTs at room temperature.<sup>250</sup> Highly flexible photodetectors based on CNTs have been demonstrated for wearable technologies.<sup>251–254</sup> The outstanding electronic and optical properties have been utilized by integrating CNTs with MoS<sub>2</sub> atomic layers to develop flexible CNT/MoS<sub>2</sub> hybrid broadband photodetectors.

Photodetectors have been developed using few-layer MoS<sub>2</sub>/SWCNT hybrids,<sup>255</sup> which showed high photoresponsivities of 100 to 1000  $\text{A W}^{-1}$  at a 0.1 V bias voltage in the 500–700 nm visible range. Specifically, the MoS<sub>2</sub>/SWCNT hybrid structure exhibited a photoresponsivity of 300  $\text{A W}^{-1}$  at 532 nm under a  $V_g$  of 0 V. Large-area MoS<sub>2</sub>, WS<sub>2</sub>, and MoSe<sub>2</sub> device arrays were fabricated by Li *et al.*<sup>256</sup> MoS<sub>2</sub> channels and MoS<sub>2</sub>/CNT hybrid electrodes were simultaneously deposited on a CNT-patterned substrate by the CVD method. MoS<sub>2</sub>–MoS<sub>2</sub>/CNT devices showed ohmic contacts between MoS<sub>2</sub> channels and MoS<sub>2</sub>/CNT hybrid electrodes and exhibited better mechanical stability as well as photoresponsivity than gold-contacted devices,

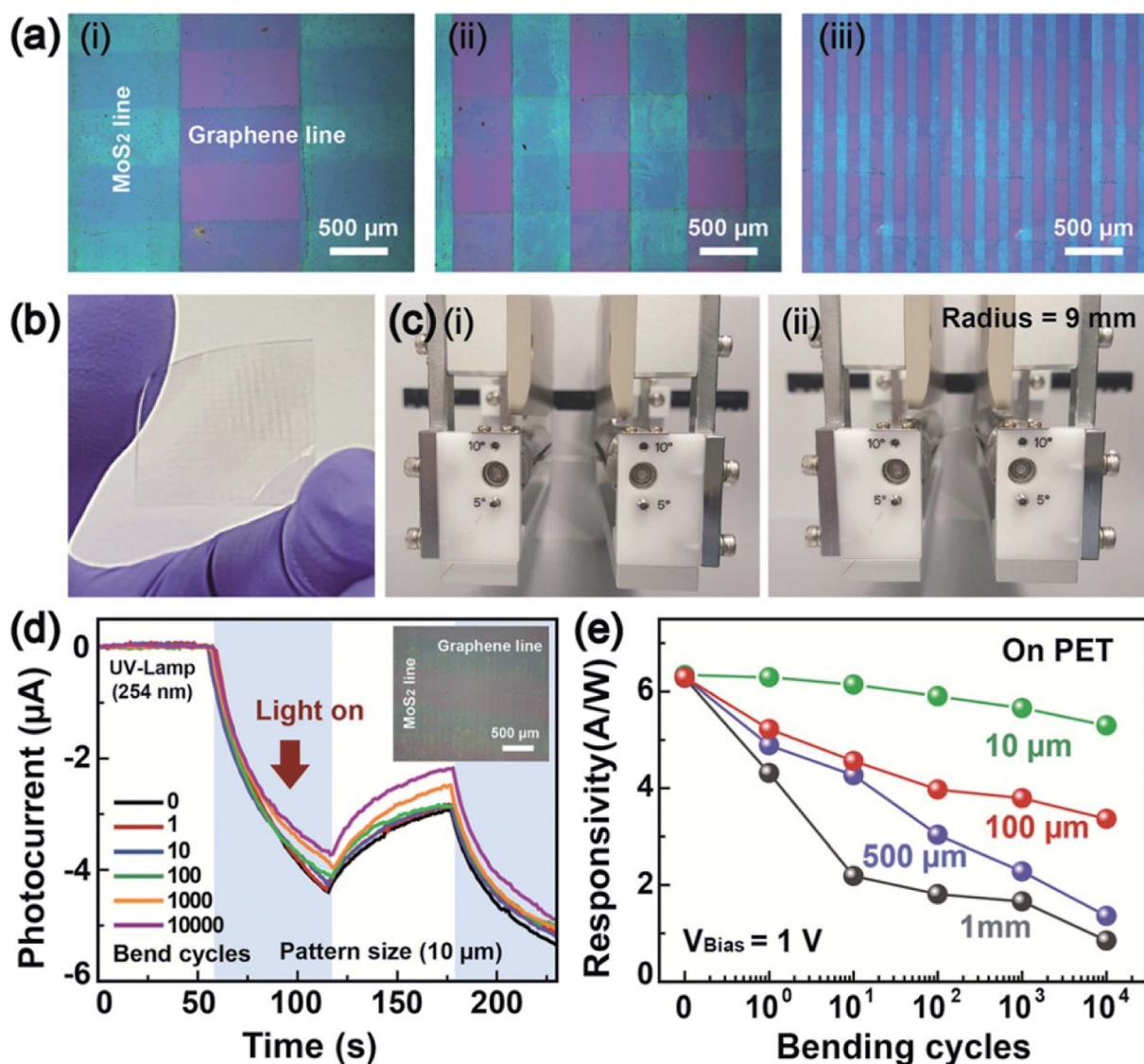


Fig. 18 (a) Optical microscope images of cross-stacked patterns of MoS<sub>2</sub>/graphene based on MoS<sub>2</sub> patterns with widths of (i) 1 mm, (ii) 500  $\mu\text{m}$ , and (iii) 100  $\mu\text{m}$ , where the graphene patterns have a fixed width of 500  $\mu\text{m}$ . (b) Photographic image of cross-linked MoS<sub>2</sub>/graphene hybrid patterns on a flexible PET substrate developed by the soft-lithographic patterning technique. (c) Photographs of MoS<sub>2</sub>/graphene hybrid patterns on a flexible PET substrate (i) before and (ii) after the photodetector device bending test. (d) Photocurrent as a function of time for a flexible MoS<sub>2</sub>/graphene hybrid photodetector under 1–10 000 bending cycles. The inset shows an optical image of cross-stacked patterned MoS<sub>2</sub> (width = 10  $\mu\text{m}$ ) and graphene (width = 500  $\mu\text{m}$ ). (e) Photoresponsivity of flexible MoS<sub>2</sub>/graphene hybrid photodetectors as a function of bending cycle (1–10 000), where the photodetectors have 1 mm, 500  $\mu\text{m}$ , 100  $\mu\text{m}$ , and 10  $\mu\text{m}$  pattern sizes for the MoS<sub>2</sub> layers. The bending test was conducted at a bending radius of 9 mm and a 1.0 V bias voltage. Reprinted with permission from ref. 234, copyright © Elsevier.



indicating the suitability of the  $\text{MoS}_2$ – $\text{MoS}_2$ /CNT hybrid for flexible electronic devices. Highly flexible pixel arrays based on  $\text{MoS}_2$ – $\text{MoS}_2$ /CNT hybrid photodetectors were developed. Fig. 19 shows the flexible  $\text{MoS}_2$ – $\text{MoS}_2$ /CNT hybrid film-based photodetector pixel array, photocurrent response at zero gate voltage, and image patterns recorded using the  $\text{MoS}_2$ – $\text{MoS}_2$ /CNT photodetector pixel array. The flexible  $\text{MoS}_2$ – $\text{MoS}_2$ /CNT photodetector arrays were deposited on a 3  $\mu\text{m}$  thick flexible SU-8 substrate. The  $\text{MoS}_2$ – $\text{MoS}_2$ /CNT device showed a current below  $10^{-11}$   $\text{A}$  at a bias voltage of 0.5 V. The  $\text{MoS}_2$ – $\text{MoS}_2$ /CNT devices showed a detectivity of  $2.4 \times 10^{10} \text{ cm Hz}^{-1/2} \text{ W}^{-1}$ . The 160 photodetector pixels formed with  $\text{MoS}_2$ – $\text{MoS}_2$ /CNT devices were arranged in 16 columns  $\times$  10 rows. Both L- and T-shaped image patterns were recorded by the pixel array.

#### 4.3 $\text{MoS}_2$ /2D TMD hybrid heterostructures for flexible photodetectors

$\text{MoS}_2$ -based vdWHs have been extensively studied for developing photodetectors, as discussed in the previous section.<sup>195–206</sup> The electronic and optoelectronic properties of  $\text{MoS}_2$ -based FETs and photodetectors have been dramatically improved by integrating atomic layered  $\text{MoS}_2$  with other vdW structures, such as 2D graphene, h-BN and TMDs. Huo *et al.*<sup>257</sup> developed a phototransistor from multilayer  $\text{MoS}_2$ /WS<sub>2</sub> vdWHs that

exhibited an on/off switching ratio  $>10^5$ , an electron mobility of  $65 \text{ cm}^2 \text{ V}^{-1} \text{ s}^{-1}$ , and a photoresponsivity of  $1.42 \text{ A W}^{-1}$ , enhanced properties compared with multilayer  $\text{MoS}_2$  or WS<sub>2</sub> transistors. Xue *et al.*<sup>164</sup> used vertical heterojunction arrays of few-layer  $\text{MoS}_2$ /WS<sub>2</sub> to develop flexible photodetectors. HRTEM and AFM images indicated three layers of  $\text{MoS}_2$  ( $\sim 2.1 \text{ nm}$ ) and five layers of WS<sub>2</sub> ( $\sim 3.9 \text{ nm}$ ) in the heterostructure layered films.  $\text{MoS}_2$ /WS<sub>2</sub> heterojunction-based FETs were fabricated on a rigid SiO<sub>2</sub>/Si substrate. Flexible  $\text{MoS}_2$ /WS<sub>2</sub> heterojunction photodetector arrays were also fabricated on a PDMS substrate. Fig. 20 shows a schematic of the  $\text{MoS}_2$ /WS<sub>2</sub> vertical heterojunction-based phototransistor, current–voltage plot, time-dependent photocurrent of the  $\text{MoS}_2$ /WS<sub>2</sub> vertical heterojunction at different incident powers during laser switching on/off, photographic image of the flexible  $\text{MoS}_2$ /WS<sub>2</sub> vertical heterojunction photodetector arrays on a PDMS substrate and time-dependent photocurrent of the flexible  $\text{MoS}_2$ /WS<sub>2</sub> vertical heterojunction photodetector device on the PDMS substrate at different incident laser powers. The  $\text{MoS}_2$ /WS<sub>2</sub>-based photodetector showed a photoresponsivity of  $2.3 \text{ A W}^{-1}$  at a 450 nm wavelength.

In another study, Lin *et al.*<sup>258</sup> fabricated flexible vdW photodiodes on flexible PET substrates using monolayer n- $\text{MoS}_2$ /few-layer p-WSe<sub>2</sub> heterojunctions. The photoresponsivity of the  $\text{MoS}_2$ /WSe<sub>2</sub> photodiode increased by 86% at  $-0.62\%$  compressive strain in the  $\text{MoS}_2$  armchair direction due to

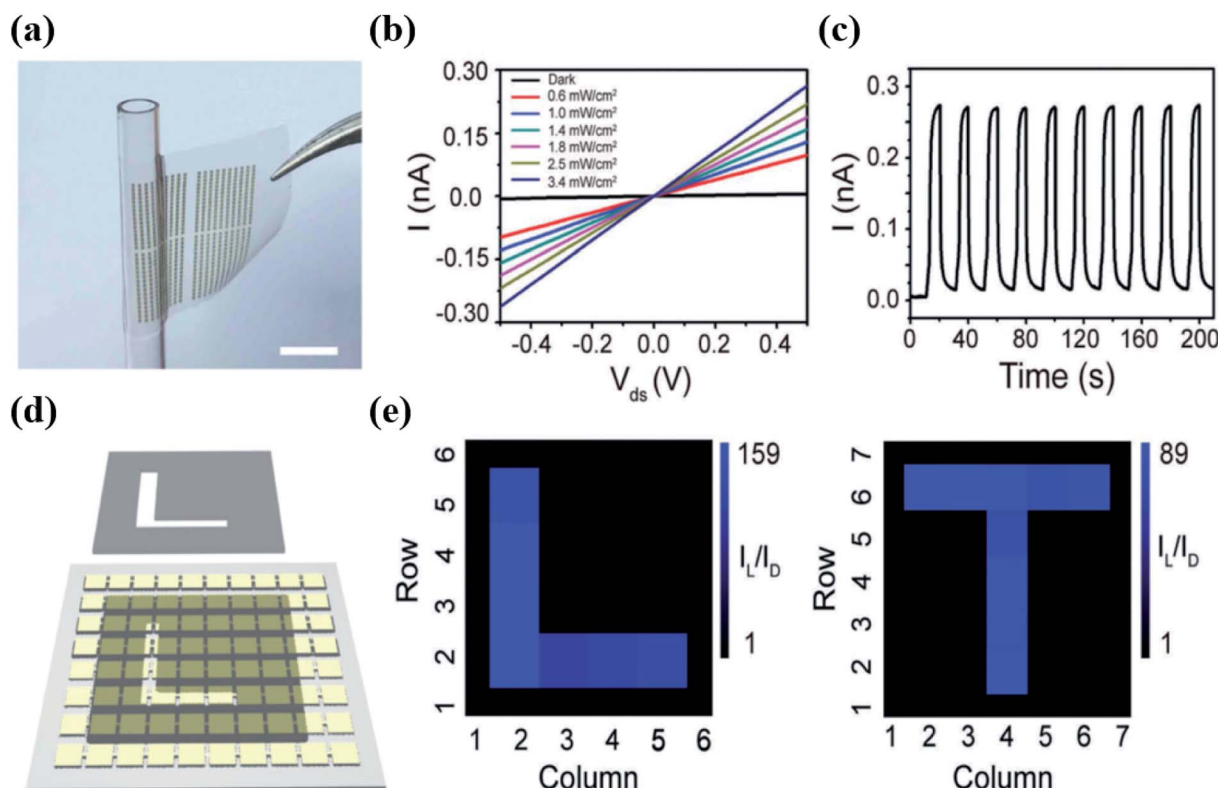


Fig. 19 Flexible  $\text{MoS}_2$ – $\text{MoS}_2$ /CNT hybrid photodetectors. (a) Flexible  $\text{MoS}_2$ – $\text{MoS}_2$ /CNT hybrid film-based electronic device array attached to the surface of a glass tube. (b)  $I$ – $V_{ds}$  curves of the  $\text{MoS}_2$ – $\text{MoS}_2$ /CNT hybrid device at 442 nm under different intensities of light illumination. (c) Photocurrent response of the  $\text{MoS}_2$ – $\text{MoS}_2$ /CNT device as a function of time. (d) Schematic representation of a photodetector pixel array of  $\text{MoS}_2$ – $\text{MoS}_2$ /CNT hybrid photodetectors. (e) L- and T-shaped image patterns (row vs. column) recorded using the  $\text{MoS}_2$ – $\text{MoS}_2$ /CNT photodetector pixel array. Reprinted with permission from ref. 256, copyright © Wiley-VCH.



realignment of the energy band at the  $\text{MoS}_2/\text{WSe}_2$  interface caused by the strain-induced piezoelectricity. The  $\text{MoS}_2/\text{WSe}_2$  photodiode showed a photoresponsivity of  $3.4 \text{ mA W}^{-1}$ . The PL peak intensity of CVD-grown monolayer  $\text{MoS}_2$  increased by three orders of magnitude after 15 min of TFSI chemical treatment. This study demonstrated that strain-tunable 2D TMD-based vdWHs could be used for developing optoelectronic devices. The photoresponse of flexible  $\text{MoS}_2/\text{WSe}_2$  vdWH-based photodiodes was enhanced by the piezophototronic effect. Alloys of TMDs have been explored for developing flexible photodetectors. In another study, Wu *et al.*<sup>264</sup> also demonstrated improved photoresponse of flexible monolayer  $\text{MoS}_2$  due to the piezophototronic effect for strain-gated photodetectors. The polarization charges induced by the applied strain can change the separation of photogenerated carriers and their transport at the interface between  $\text{MoS}_2$  and metal allowing tuning of photoresponse. The strain-induced flexible monolayer  $\text{MoS}_2$  photodetector showed high photoresponsivity of  $2.3 \times 10^4 \text{ A W}^{-1}$ , which is 26 times larger photoresponsivity compared with

monolayer  $\text{MoS}_2$  phototransistors<sup>172</sup> due to the piezophototronic effect. The current ( $I_{ds}$ ) monolayer  $\text{MoS}_2$  increased by 2.5 times, from 90 nA in dark to 220 nA under  $4.297 \text{ mW cm}^{-2}$  optical power intensity at a drain voltage of  $-2 \text{ V}$ . The photocurrent was 40 nA at  $3.4 \mu\text{W cm}^{-2}$  power intensity under strain of  $-0.38\%$ , which increased to 207 nA at  $4.29 \text{ mW cm}^{-2}$  power intensity under increased strain of  $-0.45\%$ . Zheng *et al.*<sup>259</sup> developed  $\text{Mo}_{0.5}\text{W}_{0.5}\text{Se}_2$  alloy-based photodetectors on a  $\text{SiO}_2/\text{Si}$  rigid substrate and a PI flexible substrate for photodetection over a broadband spectrum ranging from the UV to NIR region (370 nm to 808 nm). The  $\text{Mo}_{0.5}\text{W}_{0.5}\text{Se}_2$  photodetectors on the  $\text{SiO}_2/\text{Si}$  substrate exhibited a photoresponsivity of  $77.1 \text{ A W}^{-1}$  and a detectivity of  $1.1 \times 10^{12} \text{ Jones}$  with a rapid response speed of 8.3 ms, whereas the photodetector on the flexible PI substrate showed a photoresponsivity of  $63.5 \text{ A W}^{-1}$  and a detectivity of  $3.56 \times 10^{12} \text{ Jones}$ . The  $\text{Mo}_{0.5}\text{W}_{0.5}\text{Se}_2$  photodetectors showed no noticeable degradation in performance over 100 bending cycles, showing their suitability for flexible optoelectronic devices.

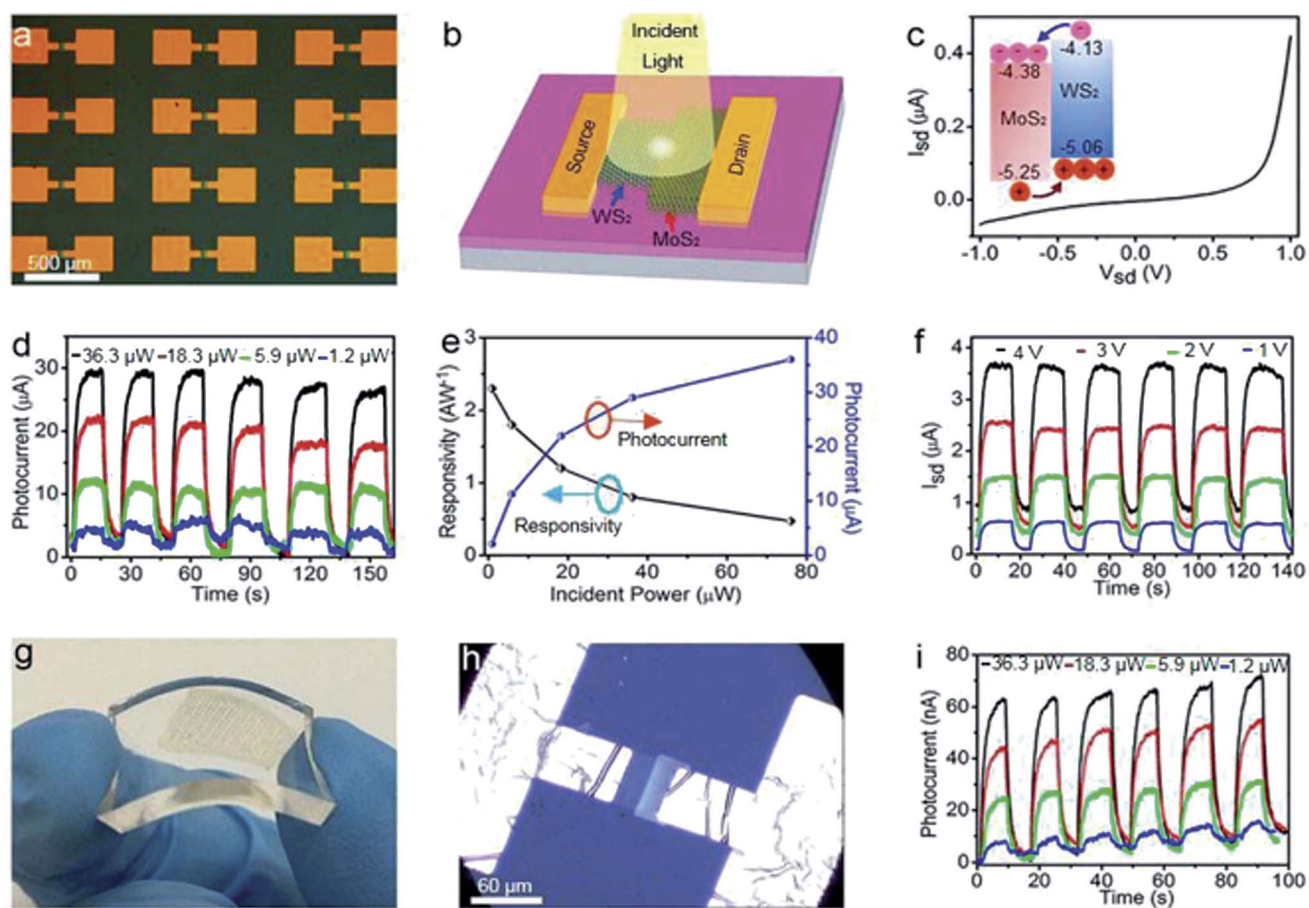


Fig. 20 (a) Vertical heterojunction arrays fabricated from few-layer  $\text{MoS}_2/\text{WS}_2$  on a  $\text{SiO}_2/\text{Si}$  substrate. (b) Schematic illustration of the  $\text{MoS}_2/\text{WS}_2$  vertical heterojunction-based phototransistor. (c) Current–voltage plot of a  $\text{MoS}_2/\text{WS}_2$  vertical heterojunction-based phototransistor without illumination. The inset indicates the band alignment for few-layer  $\text{MoS}_2$  and  $\text{WS}_2$ . (d) Time-dependent photocurrent of the  $\text{MoS}_2/\text{WS}_2$  vertical heterojunction at different incident powers. (e) Photocurrent and photoresponsivity as a function of incident light power at a 405 nm wavelength. (f) Time dependence of the photocurrent based on the  $\text{MoS}_2/\text{WS}_2$  vertical heterojunction photodetector during switching on/off of the laser with varying source–drain voltage ( $V_{sd}$ ) from 1 to 4 V. (g) Photographic image of the flexible  $\text{MoS}_2/\text{WS}_2$  vertical heterojunction photodetector array on a PDMS substrate. (h) Optical microscope image of a single flexible  $\text{MoS}_2/\text{WS}_2$  vertical heterojunction photodetector device on a PDMS substrate. (i) Time-dependent photocurrent of the flexible  $\text{MoS}_2/\text{WS}_2$  vertical heterojunction photodetector device on the PDMS substrate at different incident laser powers. Reprinted with permission from ref. 164, copyright © 2017 American Chemical Society.



#### 4.4 MoS<sub>2</sub>/ZnO hybrid heterostructures for flexible photodetectors

Ultrahigh photoresponsivity has been observed in ZnO-based hybrid heterostructures, and flexible broadband photodetectors have been fabricated using ZnO nanostructures (NWs, nanorods, QDs, nanoparticles) combined with other functional nanomaterials, including graphene, CNTs, carbon nanodots, Au, Cu, ZnS, CdO, SnO<sub>2</sub>, and Zn<sub>2</sub>SnO<sub>4</sub>, for wearable technologies.<sup>52–54,260–271</sup> Hybrid heterostructures of ZnO with MoS<sub>2</sub> have similarly been used to develop photodetectors. The electronic and optoelectronic properties of MoS<sub>2</sub> atomic layers have been improved by ZnO doping. A photoresponsivity of  $3.18 \times 10^3$  A W<sup>-1</sup> and a detectivity of  $5.94 \times 10^{12}$  Jones have been observed for the ZnO-doped MoS<sub>2</sub> photodetector at a wavelength of 520 nm due to the suppression of the recombination rate of photocarriers induced by ZnO doping.<sup>272</sup> Nazir *et al.*<sup>273</sup> used ZnO QD-decorated multilayer MoS<sub>2</sub> nanosheets to develop ZnO QD/MoS<sub>2</sub> heterostructure-based photodetectors. The field-effect mobility of ML MoS<sub>2</sub> increased from 5.75 to 25.09 cm<sup>2</sup> V<sup>-1</sup> s<sup>-1</sup> after decorating ML MoS<sub>2</sub> with ZnO QDs due to the charge transfer from the deposited ZnO QD thin layer to the surface of the pristine ML MoS<sub>2</sub> nanosheet. The ML MoS<sub>2</sub> photodetector showed a photoresponsivity of 1913 A W<sup>-1</sup> at a  $V_{BG}$  of 30 V and a  $V_{ds}$  of 1 V at 220 nm under an incident laser power of 11 mW cm<sup>-2</sup>, which increased to 2267 A W<sup>-1</sup> under similar conditions after decorating the ML with a ZnO QD thin layer. The flexible MoS<sub>2</sub>/ZnO/PEN photodetectors showed an  $I_{on}/I_{off}$  current ratio of  $10^4$ , compared with  $10^3$  for the pure ZnO/PEN photodetector.<sup>274</sup> The highest photocurrent was obtained for the device with a 5 wt% MoS<sub>2</sub> layer. The  $I_{on}/I_{off}$  current ratio increased from 8840 to 17 800 for 0 to 5 wt% MoS<sub>2</sub> in the MoS<sub>2</sub>/ZnO hybrid structure along with the highest photocurrent and photoresponsivity values for the photodetectors. Pak *et al.*<sup>275</sup> reported a photoresponsivity of 14.9 mA W<sup>-1</sup> at 1100 nm for the  $\alpha$ -IGZO photodetector capped by a MoS<sub>2</sub> layer, which was five times higher compared with the pure  $\alpha$ -IGZO photodetector with no MoS<sub>2</sub> layer. Yang *et al.*<sup>276</sup> used few-layer MoS<sub>2</sub> (bandgap of 1.7 eV) with amorphous indium–gallium–zinc oxide (InGaZnO:  $\alpha$ -IGZO) (bandgap of 3.0 eV) to develop a hybrid heterostructure-based phototransistor. The MoS<sub>2</sub>/ $\alpha$ -IGZO hybrid formation imparted enhanced visible light absorption and a high carrier mobility. The band alignment at the heterostructure junction facilitated the transfer of electrons generated by visible light within the upper few-layer MoS<sub>2</sub> to the underlying  $\alpha$ -IGZO layer. The photocurrent of the MoS<sub>2</sub>/ $\alpha$ -IGZO heterostructure-based phototransistors was four orders of magnitude higher than that of the MoS<sub>2</sub> phototransistor at an incident laser power of 1.0  $\mu$ W; the photoresponsivity was 1.7 A W<sup>-1</sup> at a wavelength of 520 nm, and the extrapolated photoresponsivity exceeded  $10^3$  A W<sup>-1</sup> under an incident laser power of 1.0 pW. The MoS<sub>2</sub>/ $\alpha$ -IGZO phototransistors showed an  $I_{on}/I_{off}$  current ratio of  $10^5$  and photoresponse times of 2.6 s and 1.7 s.

The morphology of nanomaterials also plays an important role in controlling the electrical properties. Lee *et al.*<sup>277</sup> reported different ZnO morphological nanostructures, such as NWs, nanostars (NSs), and nanoflowers (NFs), which were

hydrothermally grown on graphene monolayer and MoS<sub>2</sub> multilayer films by adjusting the pH of the solution, and used these ZnO hybrid nanostructures to fabricate photodetectors. ZnO-based NWs, NSs, and NFs were obtained at pH values of 6.53, 8.18, and 9.18, respectively, and characterized by field-emission (FE)-SEM, resonant Raman spectroscopy, and XPS methods. The photodetectors fabricated from ZnO NWs/graphene, ZnO NSs/graphene, and ZnO NFs/graphene showed high photoresponsivity values of 145, 302, and 350 A W<sup>-1</sup>, respectively. However, the photodetectors fabricated from ZnO NW/MoS<sub>2</sub>, ZnO NS/MoS<sub>2</sub>, and ZnO NF/MoS<sub>2</sub> hybrids showed very low photoresponsivities of  $7.91 \times 10^{-6}$ ,  $1.02 \times 10^{-4}$ , and  $8.99 \times 10^{-4}$  A W<sup>-1</sup>, respectively. The EQE of photodetectors developed from ZnO NWs, NSs, and NFs in combination with graphene were  $5.14 \times 10^4$ ,  $1.07 \times 10^5$ , and  $1.24 \times 10^5$ %, compared with  $2.81 \times 10^{-3}$ ,  $3.63 \times 10^{-2}$ , and  $3.19 \times 10^{-1}$ % for ZnO NWs, NSs, and NFs with MoS<sub>2</sub>, respectively. Fig. 21 shows a photograph of the ZnO NF/MoS<sub>2</sub> photodetector fabricated on a flexible PI substrate, time-dependent photocurrents of hybrid photodetectors developed from ZnO NWs, ZnO NSs, and ZnO NFs along with graphene and MoS<sub>2</sub>, and the variation in the photocurrent of the ZnO NF/graphene hybrid and ZnO NF/MoS<sub>2</sub> hybrid as a function of the bending cycle. The photocurrents of the ZnO NW, NS, and NF hybrids with graphene decrease, whereas the photocurrents of the ZnO NW, NS, and NF hybrids with MoS<sub>2</sub> increase under UV illumination at 256 nm owing to the difference in the electronic structures of graphene and MoS<sub>2</sub>. The photocurrent of the ZnO hybrid photodetectors shows an increasing trend of ZnO NWs < NSs < NFs, regardless of whether graphene or MoS<sub>2</sub> is used, because of the increased oxygen vacancies induced by adjusting the pH. The response and decay times were 10 and 67 s for the ZnO NF/graphene hybrid and 61 and 90 s for the ZnO NF/MoS<sub>2</sub> hybrid-based photodetector devices, respectively. The photocurrent decreased by 74% for the ZnO NF/graphene hybrid and by 76% for the ZnO NF/MoS<sub>2</sub> hybrid-based devices from the initial values after 10 000 bending cycles at a bending radius of 6 mm.

Flexible photodetectors have been developed using MoS<sub>2</sub> and graphitic carbon nitride (g-C<sub>3</sub>N<sub>4</sub>) hybrid thin films on a paper substrate, as reported by Velusamy *et al.*<sup>278</sup> The dark current of MoS<sub>2</sub> decreased as the amount of g-C<sub>3</sub>N<sub>4</sub> increased in the hybrid films because of the resistivity of g-C<sub>3</sub>N<sub>4</sub>, although the photocurrent was significantly improved due to the photocarriers generated under light illumination. The photocurrent of the MoS<sub>2</sub>/g-C<sub>3</sub>N<sub>4</sub> hybrid increased linearly as a function of increasing laser power density, yielding  $I_{on}/I_{off}$  current ratios of  $4 \times 10^3$  and  $1 \times 10^4$ , photoresponsivities of 700 mA W<sup>-1</sup> and 4 A W<sup>-1</sup>, and detectivities of  $8 \times 10^{10}$  Jones and  $4 \times 10^{11}$  Jones at 532 nm and 365 nm wavelengths under laser power densities of 0.225 W cm<sup>-2</sup> and 0.5 W cm<sup>-2</sup> for MoS<sub>2</sub>/g-C<sub>3</sub>N<sub>4</sub> (5 : 5) hybrid thin film, respectively. The photodetectors showed stability, retaining 90% of their initial photocurrent after a time period of 3000 s. The MoS<sub>2</sub>/g-C<sub>3</sub>N<sub>4</sub> (5 : 5) hybrid film-based photodetectors showed no significant decrease in the photocurrent after bending the thin films to radii of 10, 7, 5, 4, 3, and 2 mm; and no deformation up to 400 bending cycles at a 4 mm bending radius under the measurement conditions described above. Yu *et al.*<sup>279</sup>



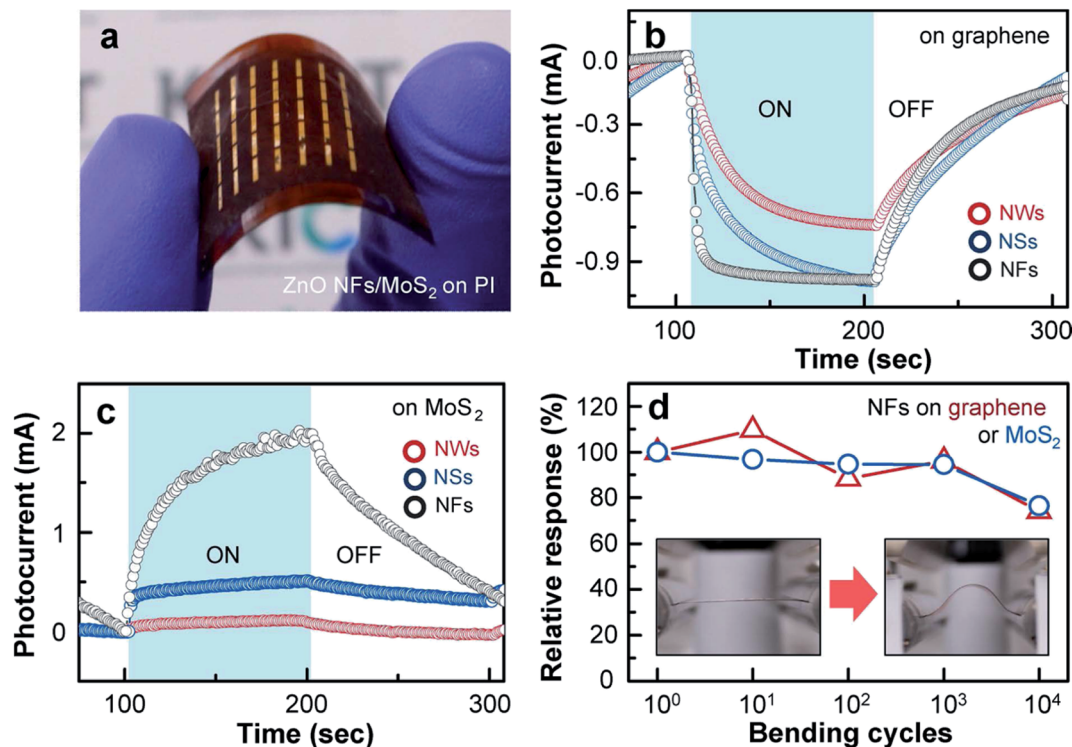


Fig. 21 (a) Photograph of the ZnO NF/MoS<sub>2</sub> photodetector fabricated on a flexible PI substrate. (b) Time-dependent photocurrents for ZnO NW/graphene, ZnO NS/graphene, and ZnO NF/graphene hybrids measured at 1 V. (c) Time-dependent photocurrents for ZnO NW/MoS<sub>2</sub>, ZnO NS/MoS<sub>2</sub>, and ZnO NF/MoS<sub>2</sub> hybrids measured at 1 V. (d) The change in the photocurrent of the ZnO NF/graphene hybrid (red) and ZnO NF/MoS<sub>2</sub> hybrid (blue) as a function of the bending cycle. Insets show the bending process of photodetectors at a bending radius of 6 mm. Reprinted with permission from ref. 277, copyright © 2017 American Chemical Society.

developed flexible photodetectors by transferring MoS<sub>2</sub> layers onto interdigital electrodes patterned on a PET substrate which showed a photoresponsivity of 20 mA W<sup>-1</sup>, with response rise/fall times of 12 s and 19 s. Seo *et al.*<sup>280</sup> developed inkjet printed flexible photodetector devices using MoS<sub>2</sub> nanosheets and graphene electrodes. MoS<sub>2</sub>/graphene photodetectors were fabricated on a rigid glass substrate applying thermal annealing and a flexible polyimide (PI) substrate using photonic annealing. Thermally annealed MoS<sub>2</sub>/graphene photodetectors showed photoresponsivity of 1 mA W<sup>-1</sup> and detectivity of  $4.37 \times 10^7$  Jones at 515.6 nm, which increased many folds for the photonically annealed photodetectors because more charge carriers were generated by the photothermal effect associated with lower thermal conductivity and larger heat capacity of polyimide thin film substrate than that of a rigid glass substrate. The photonically annealed flexible MoS<sub>2</sub>/graphene photodetectors also showed retained mechanical stability over 500 bending cycles at 8.1 mm radius of curvature.

#### 4.5 Surface functionalized MoS<sub>2</sub> layers for flexible photodetectors

The electrical, optical, mechanical, thermal, chemical, and biological properties of MoS<sub>2</sub> atomic layers can be altered by covalent surface functionalization. Different organic functional groups can be covalently attached to the MoS<sub>2</sub> atomic layers by exploiting vacancies mainly on surface atoms and consequently

their physical and chemical properties can be tuned.<sup>281-284</sup> Tang *et al.*<sup>285</sup> reported that the bandgap of 1T-phase MoS<sub>2</sub> monolayer can be tuned between zero to 1.0 eV depending upon the chemical bonding of CH<sub>3</sub>, CF<sub>3</sub>, OCH<sub>3</sub>, NH<sub>2</sub> and H functional groups. Ding *et al.*<sup>286</sup> demonstrated covalent functionalization of 2H-phase MoS<sub>2</sub> monolayers can be achieved and tuned by thiol (SH) group functionalization and controlling the vacancies of sulfur atoms on the basal planes. The covalent functionalization by thiol groups can modulate both photoluminescence and catalytic behavior of functionalized MoS<sub>2</sub> monolayers. The applications of PEGylated MoS<sub>2</sub> atomic layers and carboxyl (-COOH) functionalized MoS<sub>2</sub> nanosheets have been reported in cancer therapy<sup>287</sup> and surface plasmon resonance (SPR) immunosensors.<sup>288</sup> Various studies have shown that the covalent surface functionalization can be used for controlling the phase stability, surface characteristics, chemical reactivity, mechanical, and electrical properties of MoS<sub>2</sub>.<sup>289-292</sup>

Flexible MoS<sub>2</sub> photodetectors have been fabricated using surface-functionalized monolayer MoS<sub>2</sub>. Pak *et al.*<sup>293</sup> developed flexible photodetectors based on CVD-grown monolayer MoS<sub>2</sub> surface-functionalized with electron accepting (p-doping) octadecyltrichlorosilane (ODTS, -CH<sub>3</sub> groups) or electron donating (n-doping) (3-aminopropyl)triethoxysilane (APTES, -NH<sub>2</sub> groups) organic molecules. The PL spectrum of ODTS-MoS<sub>2</sub> layer was found to increase in the intensity and blue-shifted by 11 meV whereas the PL intensity of APTES-MoS<sub>2</sub> layer decreased and red-

shifted by 15 meV, compared with the pristine  $\text{MoS}_2$  layer due to the different process of exciton recombination. Fig. 22 shows the schematics of a flexible  $\text{MoS}_2$  based photodetector, ODTs functionalized monolayer  $\text{MoS}_2$ , and mechanical stability test and then compares the incident power dependent photoresponsivity and detectivity of the pristine  $\text{MoS}_2$  with APTES- $\text{MoS}_2$  and ODTs- $\text{MoS}_2$  photodetector devices. The lower dark and photo current values of 475 pA and 202 nA for ODTs- $\text{MoS}_2$  device and higher values 1.2  $\mu\text{A}$  and 4.6  $\mu\text{A}$  for APTES- $\text{MoS}_2$  device were associated with their charge carrier concentrations, respectively. The photoresponsivity of the ODTs- $\text{MoS}_2$  device increased from  $2.5 \text{ A W}^{-1}$  to  $37.5 \text{ A W}^{-1}$  and from  $25.2 \text{ A W}^{-1}$  to  $1500 \text{ A W}^{-1}$  for the APTES- $\text{MoS}_2$  device at the lowest incident power. The functionalized  $\text{MoS}_2$  channel assisted in transporting more excitons that yielded higher photoresponsivity for the APTES- $\text{MoS}_2$  device. The ODTs- $\text{MoS}_2$  photodetector showed highest detectivity of  $10^{11} \text{ Jones}$  under the lowest incident power, which may be associated with the dropping of the dark level due to the electrons withdrawal from the channel. The photoresponse decay time of flexible APTES- $\text{MoS}_2$  photodetector was decreased to 0.7 s compared with 1.45 s for the pristine 1L- $\text{MoS}_2$  photodetector. The mechanical stability of the flexible ODTs- $\text{MoS}_2$ /PET device was studied as a function of bending radius and bending cycles. At 2 mm bending radius, less than 10% degradation in photocurrent occurred while 20% degradation was noticed at bending radius of 4 mm up to 1000 bending cycles. This study demonstrated that a flexible  $\text{MoS}_2$  photodetector can be fabricated with surface-functionalization of a  $\text{MoS}_2$  monolayer. Kang *et al.*<sup>180</sup> also observed the similar phenomenon for the  $\text{MoS}_2$

photodetector devices n-doped by APTES organic molecules where photoresponsivity was improved from  $219 \text{ A W}^{-1}$  to  $5.75 \times 10^3 \text{ A W}^{-1}$  for the APTES- $\text{MoS}_2$  devices.

Several other studies have been reported on  $\text{MoS}_2$  hybrid based flexible photodetectors. In-plane lateral graphene/ $\text{MoS}_2$  heterostructure showed photoresponsivity of  $1.1 \times 10^5 \text{ A W}^{-1}$ , detectivity of  $1.4 \times 10^{14} \text{ Jones}$  and  $I_{\text{on}}/I_{\text{off}}$  current ratio of  $10^6$  due to the strong absorption and increased separation of the photoexcited charge carriers and the charge transportation.<sup>294</sup>  $\text{MoS}_2$  phototransistors have been prepared on flexible polyarylate substrate where poly(4-vinylphenol) (PVP) was used both as a gate dielectric and an encapsulating layer material.<sup>295</sup> The encapsulation with PVP improved the field-effect mobility ( $\mu_{\text{FE}}$ ) and the current  $I_{\text{on}}/I_{\text{off}}$  ratio, which resulted in two orders of magnitude enhancement in photoresponsivity as well as in detectivity from visible to infrared wavelength. The hydroxyl functional groups in PVP improved the performance of  $\text{MoS}_2$  phototransistors due to the n-doping effect and decreased the recombination of photoexcited carriers. Kang *et al.*<sup>296</sup> developed  $\text{MoS}_2$ -ZnO hybrid based flexible photodetectors using  $\text{MoS}_2$  nanosheets with atomic layer deposition (ALD) deposited ZnO nanopatches. The photocurrent was found to increase with an increasing number of ALD cycles where the highest photocurrent was measured for the  $\text{MoS}_2$  nanosheets having 40 cycles ZnO nanopatches. The sulfur vacancies in defected  $\text{MoS}_2$  structure disappeared with increasing ZnO cycles and the recombination of photoexcited carriers decreased. The photocurrent of pristine  $\text{MoS}_2$  and flexible

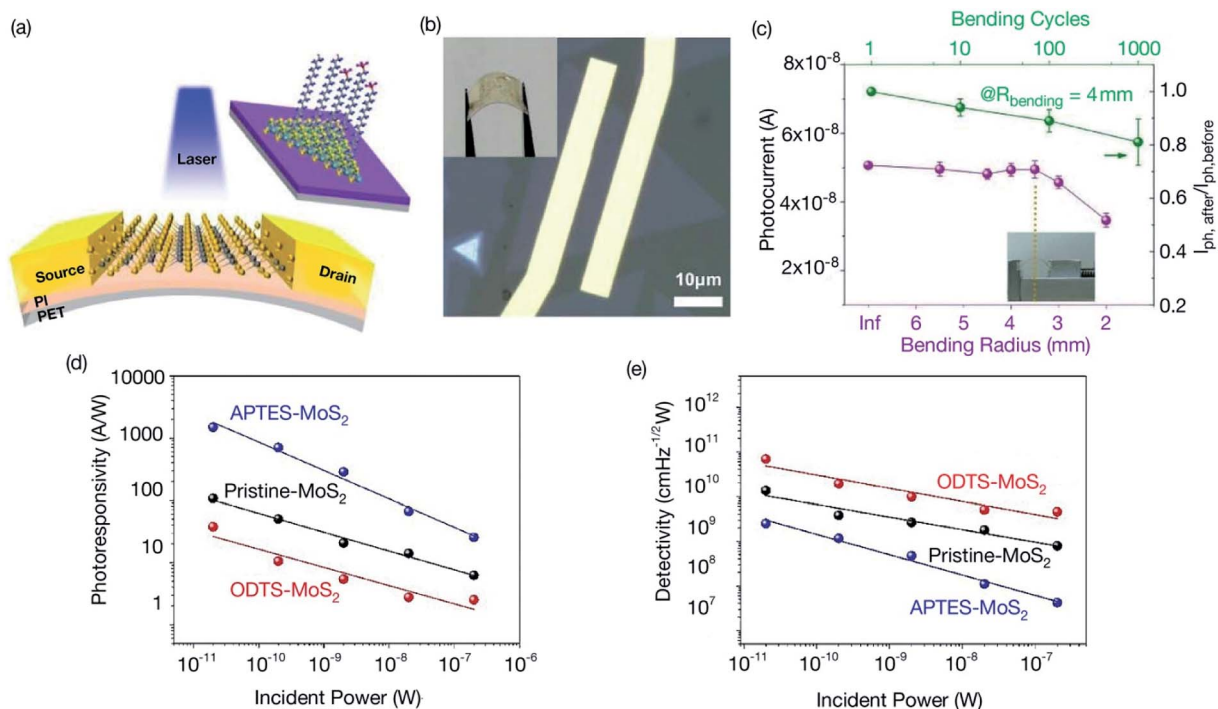


Fig. 22 (a) Schematics of a flexible  $\text{MoS}_2$  based photodetector on a PET substrate and the surface-functionalized monolayer  $\text{MoS}_2$  with ODTs ( $-\text{CH}_3$  groups). (b) Schematics and optical image of flexible  $\text{MoS}_2$  photodetector device developed using e-beam lithography. (c) Mechanical stability of flexible  $\text{MoS}_2$  devices in terms of their photocurrent at different bending radius as a function of bending cycles. A comparison of the photoresponsivity (d) and detectivity (e) of the pristine  $\text{MoS}_2$  with APTES- $\text{MoS}_2$  and ODTs- $\text{MoS}_2$  photodetector devices as a function of incident power intensity. Reprinted with permission from ref. 293, copyright © The Royal Society of Chemistry.



**Table 1** The figure of merit of different  $\text{MoS}_2$  based photodetectors. The performance of photodetectors is compared in terms of their photoresponsivity, detectivity and response/recovery time ( $\tau_{\text{rise}}/\tau_{\text{decay}}$ ) along with their measurement wavelength and incident laser power (Jones =  $\text{cm Hz}^{1/2} \text{W}^{-1}$ )<sup>a</sup>

$\text{MoS}_2$ photodetector	Conditions (wavelength, incident power)	Photoresponsivity ( $\text{A W}^{-1}$ )	Detectivity (Jones)	Response time ( $\tau_{\text{rise}}/\tau_{\text{decay}}$ )	Ref.	
<b>(i) Pristine <math>\text{MoS}_2</math> based photodetectors</b>						
1L $\text{MoS}_2$	( $\lambda = 561 \text{ nm}$ , 150 pW)	880	$2 \times 10^9$	4 s/9 s	171	
2L $\text{MoS}_2$	( $\lambda = 532 \text{ nm}$ , 35 pW)	$1.1 \times 10^5$	—	232 s	306	
	( $\lambda = 1070 \text{ nm}$ , 150 nW)	5.2	—	216.5 s	308	
3L $\text{MoS}_2$	( $\lambda = 532 \text{ nm}$ )	0.57	—	70 $\mu\text{s}$ /110 $\mu\text{s}$	307	
ML $\text{MoS}_2$	( $\lambda = 633 \text{ nm}$ , 10 nW)	0.12	$10^{10}$ to $10^{11}$	—	308	
FL $\text{MoS}_2$	( $\lambda = 520 \text{ nm}$ )	$6.3 \times 10^{-5}$	$4.2 \times 10^8$	20 ms	304	
5L $\text{MoS}_2$	( $\lambda = 850 \text{ nm}$ )	1.80	$5.0 \times 10^8$	0.3 s/0.36 s	139	
Pd/ $\text{MoS}_2$ /Cr-Au	( $\lambda = 500 \text{ nm}$ )	5.07	$3 \times 10^{10}$	100 ms/200 ms	197	
1–2L $\text{MoS}_2$ /HfO <sub>2</sub>	( $\lambda = 635 \text{ nm}$ , 3.75 pW)	$1 \times 10^4$	$7.7 \times 10^{11}$	10 ms	136	
1L $\text{MoS}_2$ /Al <sub>2</sub> O <sub>3</sub>	( $\lambda = 635 \text{ nm}$ )	406	$3.8 \times 10^{11}$	55 ms	136	
$\text{MoS}_2$ /SiC	( $\lambda = 325 \text{ nm}$ )	$1.02 \times 10^4$	$6.4 \times 10^{11}$	—	217	
	( $\lambda = 532 \text{ nm}$ )	$1.6 \times 10^3$	$1.0 \times 10^{11}$	—	217	
$\text{MoS}_2$ /SiC/Si	( $\lambda = 325 \text{ nm}$ )	44	$1.4 \times 10^{10}$	—	217	
	( $\lambda = 532 \text{ nm}$ )	30	$9.5 \times 10^9$	—	217	
2L $\text{MoS}_2$ (CVD)	( $\lambda = 532 \text{ nm}$ , 0.377 mW cm <sup>-2</sup> )	7160	$6.62 \times 10^{10}$	97 ms/291 ms	351	
MoS <sub>2</sub> layers (PLD)	( $\lambda = 365 \text{ nm}$ )	$3.0 \times 10^4$	$1.81 \times 10^{14}$	32 ms	369	
1L/6L $\text{MoS}_2$ (serial multi-heterojunction)	( $\lambda = 520 \text{ nm}$ , 1 nW)	$9.26 \times 10^4$	$2.38 \times 10^{13}$	20 ms/25 ms	348	
	( $\lambda = 520 \text{ nm}$ , 5 pW)	$2.67 \times 10^6$	—	5 ms/5 ms		
	( $\lambda = 785 \text{ nm}$ , 1 nW)	$1.86 \times 10^4$	—	15 ms/20 ms		
	( $\lambda = 850 \text{ nm}$ , 1 nW)	$1.08 \times 10^4$	—	10 ms/15 ms		
	( $\lambda = 1064 \text{ nm}$ , 1 nW)	$1.07 \times 10^3$	—	5 ms/10 ms		
	( $\lambda = 1064 \text{ nm}$ , 5 pW)	$1.65 \times 10^4$	—	1.5 ms/2.5 ms		
1L/6L $\text{MoS}_2$ (parallel multi-heterojunction)	( $\lambda = 520 \text{ nm}$ , 1 nW)	$8.74 \times 10^3$	—	465 ms/315 ms	348	
MoS <sub>2</sub> microspheres	( $\lambda = 405 \text{ nm}$ , 1.77 mW cm <sup>-2</sup> )	0.96	$2.9 \times 10^{10}$	—	384	
<b>(ii) <math>\text{MoS}_2</math> based flexible photodetectors</b>						
MoS <sub>2</sub> /Kapton (flexible)	( $\lambda = 325 \text{ nm}$ )	$3.19 \times 10^2$	$4.5 \times 10^{11}$	—	217	
	( $\lambda = 532 \text{ nm}$ )	5.0	$6.4 \times 10^9$	—	217	
MoS <sub>2</sub> /PET (flexible)	( $\lambda = 325 \text{ nm}$ )	$1.36 \times 10^2$	$2.0 \times 10^{11}$	—	217	
	( $\lambda = 532 \text{ nm}$ )	9.0	$9.7 \times 10^9$	—	217	
FL $\text{MoS}_2$ /graphene/PET (flexible)	( $\lambda = 632.8 \text{ nm}$ , 0.645 $\mu\text{W}$ )	10	—	1.5 s	309	
g-C <sub>3</sub> N <sub>4</sub> /MoS <sub>2</sub> (flexible)	( $\lambda = 365 \text{ nm}$ , 0.5 W cm <sup>-2</sup> )	4.0	$4 \times 10^{11}$	60 ms/95 ms	278	
MoS <sub>2</sub> /graphene/polyimide (flexible)	(photonic annealing at 2.8 kV for 1.36 ms)	( $\lambda = 515.6 \text{ nm}$ , 0.6 mA W <sup>-1</sup> )	50 mA W <sup>-1</sup>	$3.18 \times 10^9$	5 ms	280
MoS <sub>2</sub> /Kapton (flexible)	( $\lambda = 325 \text{ nm}$ )	319	$4.5 \times 10^{11}$	—	303	
	( $\lambda = 532 \text{ nm}$ )	5.0	$6.4 \times 10^9$	—	303	
MoS <sub>2</sub> /PET (flexible)	( $\lambda = 325 \text{ nm}$ )	136	$2.0 \times 10^{11}$	—	303	
	( $\lambda = 532 \text{ nm}$ )	9.0	$9.7 \times 10^9$	—	303	
MoS <sub>2</sub> /SiO <sub>2</sub> /Si	( $\lambda = 325 \text{ nm}$ )	44	$1.4 \times 10^{10}$	—	303	
	( $\lambda = 532 \text{ nm}$ )	30	$9.5 \times 10^9$	—	303	
MoS <sub>2</sub> /SiC	( $\lambda = 325 \text{ nm}$ )	$1.02 \times 10^4$	$6.4 \times 10^{11}$	—	303	
	( $\lambda = 532 \text{ nm}$ )	$1.6 \times 10^3$	$1.0 \times 10^{11}$	—	303	
ZnO NFs/MoS <sub>2</sub> (flexible)	( $\lambda = 350 \text{ nm}$ , 1.2 mW cm <sup>-2</sup> )	$8.99 \times 10^{-4}$	—	61 s/90 s	277	
<b>(iii) <math>\text{MoS}_2</math>/2D van der Waals heterostructure-based photodetectors</b>						
1L $\text{MoS}_2$ /1L graphene	( $\lambda = 532 \text{ nm}$ , 0.01 W m <sup>-2</sup> )	$1.2 \times 10^7$	—	2.5 s	226	
MoS <sub>2</sub> /graphene nanoribbon	( $\lambda = 385$ , 2.1 $\mu\text{W}$ )	66	—	5 ms/30 ms	232	
Graphene/ $\text{MoS}_2$ /graphene	( $\lambda = 633 \text{ nm}$ , 1 $\mu\text{W cm}^{-2}$ )	$1.14 \times 10^5$	$9. \times 10^{15}$	25.7 s/41.4 s	300	
Au/ $\text{MoS}_2$ /Au	( $\lambda = 633 \text{ nm}$ , 1 $\mu\text{W cm}^{-2}$ )	$4.8 \times 10^3$	$2.7 \times 10^{14}$	7.1 s/31.8 s	300	
Graphene/ $\text{MoS}_2$ /graphene	( $\lambda = 432 \text{ nm}$ )	$2.2 \times 10^5$	$3.5 \times 10^{13}$	1.7 ms/2.8 ms	301a	
FL $\text{MoS}_2$ /rGO NPs	( $\lambda = 460 \text{ nm}$ , 8 mW cm <sup>-2</sup> )	2.10	$5 \times 10^{11}$	18 ms	310	
ML graphene– $\text{MoS}_2$ –WS <sub>2</sub> /fiber	( $\lambda = 400 \text{ nm}$ , 6.35 nW cm <sup>-2</sup> )	$6.6 \times 10^7$	—	7 ms/21.86 ms	199	
MoS <sub>2</sub> /h-BN/graphene	( $\lambda = 532 \text{ nm}$ )	180	$2.6 \times 10^{13}$	0.23 s/0.25 s	196	
5L 2H-SnSe <sub>2</sub> /1L 2H-MoS <sub>2</sub>	( $\lambda = 500 \text{ nm}$ )	$9.1 \times 10^3$	$9.3 \times 10^{10}$	0.2 s/0.6 s	329	
1L ML $\text{MoS}_2$	( $\lambda = 500 \text{ nm}$ )	37.3	$1.4 \times 10^9$	—	329	
MoS <sub>2</sub> /SnS <sub>2</sub>	( $\lambda = 450 \text{ nm}$ )	2.3	—	—	164	



Table 1 (Contd.)

MoS <sub>2</sub> photodetector	Conditions (wavelength, incident power)	Photoresponsivity (A W <sup>-1</sup> )	Detectivity (Jones)	Response time ( $\tau_{\text{rise}}/\tau_{\text{decay}}$ )	Ref.
ML PdSe <sub>2</sub> /MoS <sub>2</sub>	( $\lambda = 10.6 \mu\text{m}$ , 435.9 nW)	42.1	$8.21 \times 10^9$	74.5 ms/93.1 ms	168
	( $\lambda = 4.012 \mu\text{m}$ )	28.83	$6.09 \times 10^{10}$	—	168
FL MoS <sub>2</sub> /FL SnSe	( $\lambda = 532$ , 0.65 nW)	100	—	4 ms/6 ms	201
MoS <sub>2</sub> /WS <sub>2</sub>	( $\lambda = 638 \text{ nm}$ )	1.36	—	—	204
ML MoS <sub>2</sub> /MoTe <sub>2</sub>	( $\lambda = 532 \text{ nm}$ , $100 \text{ mW cm}^{-2}$ )	0.62	$10^{10}$	0.01 ms	205a
ML MoS <sub>2</sub> /MoTe <sub>2</sub>	( $\lambda = 473 \text{ nm}$ , $46.8 \text{ mW cm}^{-2}$ )	0.15	—	68 ms/68 ms	205b
MoS <sub>2</sub> /MoTe <sub>2</sub>	( $\lambda = 1200 \text{ nm}$ )	0.046	—	60 $\mu\text{s}$ /25 $\mu\text{s}$	205c
ML MoS <sub>2</sub> /MoTe <sub>2</sub>	( $\lambda = 473 \text{ nm}$ )	0.064	$1.6 \times 10^{10}$	385 ms/453 ms	205d
1L MoS <sub>2</sub> /GaSe	( $\lambda = 300 \text{ nm}$ , $6.41 \text{ mW cm}^{-2}$ )	0.063	—	80 ms/20 ms	167 and 202
FL MoS <sub>2</sub> /FL black phosphorus	( $\lambda = 532 \text{ nm}$ , 1 nW)	22.3	$3.1 \times 10^{11}$	—	170
	( $\lambda = 1550 \text{ nm}$ , 1 nW)	0.1534	$2.13 \times 10^9$	15 $\mu\text{s}$ /70 $\mu\text{s}$	
MoS <sub>2</sub> /FL black phosphorus	( $\lambda = 520 \text{ nm}$ )	5000	$1.6 \times 10^{10}$	0.02 s	332
FL WSe <sub>2</sub> /FL BP/FL MoS <sub>2</sub>	( $\lambda = 532 \text{ nm}$ , 13.5 nW)	6.32	$1.25 \times 10^{11}$	—	333
	( $\lambda = 1550 \text{ nm}$ , 13.5 nW)	1.12	$2.21 \times 10^{10}$	—	333
MAPbI <sub>3</sub> /FL BP/FL MoS <sub>2</sub>	( $\lambda = 457 \text{ nm}$ , $0.02 \text{ mW cm}^{-2}$ )	11	$1.3 \times 10^{12}$	0.15 ms/0.24 ms	341
MoS <sub>2</sub> /graphene/WSe <sub>2</sub>	( $\lambda = 532 \text{ nm}$ , 0.2 nW)	4250	$2.2 \times 10^{12}$	53.6 $\mu\text{s}$ /30.3 $\mu\text{s}$	198
GaTe/MoS <sub>2</sub>	( $\lambda = 633 \text{ nm}$ , $100 \text{ mW cm}^{-2}$ )	1.365	—	10 ms	167
GaSe/MoS <sub>2</sub>	( $\lambda = 300 \text{ nm}$ )	0.06	—	80 ms/20 ms	207a
FL graphene/GaSe/MoS <sub>2</sub>	( $\lambda = 532 \text{ nm}$ )	3.0	$10^{10}$	50 ms	207b
FL GaTe/FL MoS <sub>2</sub>	( $\lambda = 473 \text{ nm}$ , 0.04 mW)	21.83	$8.4 \times 10^{13}$	7 ms	334
1L MoS <sub>2</sub> /ML MoSe <sub>2</sub>	( $\lambda = 610 \text{ nm}$ , $0.29 \text{ mW cm}^{-2}$ )	1.3	$2.6 \times 10^{11}$	0.6 s/0.5 s	335
BL MoS <sub>2</sub> /BLWS <sub>2</sub> (CVD)	( $\lambda = 457 \text{ nm}$ , $3.57 \mu\text{W cm}^{-2}$ )	$6.7 \times 10^3$	$3.09 \times 10^{13}$	—	344
	( $\lambda = 532 \text{ nm}$ , $3.57 \mu\text{W cm}^{-2}$ )	$3.0 \times 10^3$	$1.24 \times 10^{13}$	—	344
FL $\beta$ -In <sub>2</sub> Se <sub>3</sub> /1L MoS <sub>2</sub>	( $\lambda = 532 \text{ nm}$ , 4 mW cm <sup>-2</sup> )	23.7	$5 \times 10^{11}$	4 ms/7 ms	354
WS <sub>2</sub> /MoS <sub>2</sub> vdWHS	(405 nm, $3.25 \text{ mW mm}^{-2}$ )	$7 \times 10^{-5}$	—	1.1 s/2.7 s	382
WS <sub>2</sub> /MoS <sub>2</sub> vdWHS nanoscroll	(405 nm)	0.647	—	0.7 s/2.4 s	382
<b>(iv) MoS<sub>2</sub>/perovskite heterostructure-based photodetectors</b>					
Perovskite/MoS <sub>2</sub> -rGO	( $\lambda = 660 \text{ nm}$ )	$1.08 \times 10^4$	$4.28 \times 10^{13}$	45 ms	179
ML 1T-MoS <sub>2</sub> /CH <sub>3</sub> NH <sub>3</sub> PbI <sub>3</sub>	( $\lambda = 500 \text{ nm}$ , 0.14 mW)	$3.3 \times 10^5$	$7 \times 10^{11}$	0.45 s/0.75 s	325c
ML 2H-MoS <sub>2</sub> /CH <sub>3</sub> NH <sub>3</sub> PbI <sub>3</sub>	( $\lambda = 500 \text{ nm}$ , 0.14 mW)	142	$2.6 \times 10^{11}$	25 ms/50 ms	325c
2H-MoS <sub>2</sub> /1T@2H-MoS <sub>2</sub>	( $\lambda = 532 \text{ nm}$ , $2.35 \text{ mW cm}^{-2}$ )	1917	$7.55 \times 10^{11}$	—	325d
1L 2H-MoS <sub>2</sub>	( $\lambda = 532 \text{ nm}$ , $2.35 \text{ mW cm}^{-2}$ )	56	$1.3 \times 10^{11}$	—	325d
1L MoS <sub>2</sub> /CsPbI <sub>3-x</sub> Br <sub>x</sub> QDs	( $\lambda = 532 \text{ nm}$ , 1.5 $\mu\text{W}$ )	$7.7 \times 10^4$	$5.6 \times 10^{11}$	0.59 s/0.32 s	190
1L MoS <sub>2</sub> /CsPbBr <sub>3</sub>	( $\lambda = 442 \text{ nm}$ , 20 $\mu\text{W cm}^{-2}$ )	4.4	$2.5 \times 10^{10}$	0.72 ms/1.01 ms	191a
MoS <sub>2</sub> /CsPbBr <sub>3</sub> QDs	( $\lambda = 405 \text{ nm}$ , $12.8 \mu\text{W cm}^{-2}$ )	$4.68 \times 10^4$	—	7.5 ms/8 ms	191b
1L MoS <sub>2</sub> /CsPbBr <sub>3</sub> NCs	( $\lambda = 405 \text{ nm}$ , 0.6 mW cm <sup>-2</sup> )	24.34	$3.93 \times 10^{12}$	5.5 $\mu\text{s}$ /24 $\mu\text{s}$	191c
1L MoS <sub>2</sub> /CsPbBr <sub>3</sub> NCs	( $\lambda = 532 \text{ nm}$ )	$6.4 \times 10^2$	$3.38 \times 10^{11}$	—	191d
ML MoS <sub>2</sub> /CH <sub>3</sub> NH <sub>3</sub> PbI <sub>3</sub> /APTES	( $\lambda = 520 \text{ nm}$ , 4.63 pW)	$2.12 \times 10^4$	$1.38 \times 10^{10}$	6.17 s/4.5 s	192
ML MoS <sub>2</sub> /APTES	( $\lambda = 520 \text{ nm}$ )	$2.38 \times 10^3$	$4.23 \times 10^9$	—	192
ML MoS <sub>2</sub>	( $\lambda = 520 \text{ nm}$ )	$8.16 \times 10^2$	$3.93 \times 10^9$	10.7 s/6.2 s	192
FL MoS <sub>2</sub> /MA <sub>3</sub> Bi <sub>2</sub> Br <sub>9</sub>	( $\lambda = 530 \text{ nm}$ , $18 \mu\text{W cm}^{-2}$ )	112	$3.8 \times 10^{12}$	0.3 ms/0.3 ms	326
MoS <sub>2</sub> /CH <sub>3</sub> NH <sub>3</sub> PbI <sub>3</sub> (vertical)	—	68.11	—	205 ms/206 ms	327
MoS <sub>2</sub> /CH <sub>3</sub> NH <sub>3</sub> PbI <sub>3</sub> (planar)	—	28	—	356 ms/204 ms	327
(PEA) <sub>2</sub> SnI <sub>4</sub> /FL MoS <sub>2</sub> /graphene	( $\lambda = 451 \text{ nm}$ , 36 pW)	1100	$8.09 \times 10^9$	34 ms/38 ms	328
(PEA) <sub>2</sub> PI <sub>4</sub> /ML MoS <sub>2</sub>	( $\lambda = 637 \text{ nm}$ , 0.1 nW)	16.8	$1.06 \times 10^{13}$	6 ms/4 ms	322b
<b>(v) MoS<sub>2</sub>/inorganic semiconductor heterostructure-based photodetectors</b>					
ML MoS <sub>2</sub> /Si	( $\lambda = 808 \text{ nm}$ , $1 \text{ mW cm}^{-2}$ )	300	$10^{13}$	$4 \mu\text{s}/42 \mu\text{s}$	162
ML MoS <sub>2</sub> /Si	( $\lambda = 780 \text{ nm}$ , $45 \mu\text{W cm}^{-2}$ )	23.1	$1.63 \times 10^{12}$	$21.6 \mu\text{s}/65.5 \mu\text{s}$	311
ML MoS <sub>2</sub> /Si	( $\lambda = 580 \text{ nm}$ , $5 \text{ mW cm}^{-2}$ )	8.75	$1.4 \times 10^{12}$	$10 \mu\text{s}/19 \mu\text{s}$	312a
MoS <sub>2</sub> /Si (porous)	( $\lambda = 550 \text{ nm}$ )	9	$8 \times 10^{12}$	$9 \mu\text{s}/7 \mu\text{s}$	312b
V-ML MoS <sub>2</sub> /Si	( $\lambda = 650 \text{ nm}$ , $90 \text{ mW cm}^{-2}$ )	11.9	$2.1 \times 10^{10}$	$30.5 \mu\text{s}/71.6 \mu\text{s}$	313
V-FL MoS <sub>2</sub> /Si	( $\lambda = 808 \text{ nm}$ , $1.6 \text{ mW cm}^{-2}$ )	908.2	$1.88 \times 10^{13}$	$56 \text{ ns}/825 \text{ ns}$	305
V-ML MoS <sub>2</sub> /Si	( $\lambda = 660 \text{ nm}$ , $12 \text{ nW}$ )	76.1	$1.6 \times 10^{12}$	48.9 s	175
V-FL MoS <sub>2</sub> /Si	( $\lambda = 808 \text{ nm}$ , $5 \text{ mW cm}^{-2}$ )	0.746	$6.03 \times 10^{11}$	$178 \mu\text{s}/198 \mu\text{s}$	356
FL MoS <sub>2</sub> /Si FET	( $\lambda = 850 \text{ nm}$ , $50 \mu\text{W cm}^{-2}$ )	$1.78 \times 10^4$	$3.0 \times 10^{13}$	$1.44 \text{ ms}/1.45 \text{ ms}$	315
MoS <sub>2</sub> /SiNWA	( $\lambda = 650 \text{ nm}$ , $6.3 \mu\text{W cm}^{-2}$ )	53.5	$2.8 \times 10^{13}$	$2.9 \mu\text{s}/7.3 \mu\text{s}$	366



Table 1 (Contd.)

MoS <sub>2</sub> photodetector	Conditions (wavelength, incident power)	Photoresponsivity (A W <sup>-1</sup> )	Detectivity (Jones)	Response time ( $\tau_{\text{rise}}/\tau_{\text{decay}}$ )	Ref.
Si/MoS <sub>2</sub>	( $\lambda = 660$ nm)	1.1	—	0.38 s/0.1 s	138
Si-(Au@MoS <sub>2</sub> )	( $\lambda = 800$ nm)	30	—	0.02 s	138
Au@MoS <sub>2</sub> core-shell	( $\lambda = 660$ nm, 50 $\mu\text{W}$ )	0.5	—	3.2 s/0.28 s	138
ML MoS <sub>2</sub> /GaN	( $\lambda = 405$ nm, 2 mW)	17.2	$1.8 \times 10^{12}$	0.1 s/9 s	317a
ML MoS <sub>2</sub> /GaN	( $\lambda = 365$ nm, 4.351 $\mu\text{W}$ )	11.3	$1.34 \times 10^{10}$	21.1 s/19.7 s	317b
Al <sub>2</sub> O <sub>3</sub> /MoS <sub>2</sub> /GaN	( $\lambda = 365$ nm, 3.141 $\mu\text{W}$ )	24.62	$7.2 \times 10^9$	12.8 s/26.4 s	317b
MoS <sub>2</sub> /GaAs (CVD)	( $\lambda = 635$ nm)	0.321	$3.5 \times 10^{13}$	17 $\mu\text{s}$ /31 $\mu\text{s}$	318
SiQDs/MoS <sub>2</sub> /h-BN/GaAs	( $\lambda = 635$ nm)	0.419	$1.9 \times 10^{14}$	—	318
FL MoS <sub>2</sub> /CdSe	( $\lambda = 405$ nm, 8.52 $\mu\text{W cm}^{-2}$ )	$2.5 \times 10^5$	$1.24 \times 10^{14}$	60 ms/60 ms	323
MoS <sub>2</sub> /ZnCdSe/ZnS QDs	( $\lambda = 450$ nm, 400 nW)	$3.7 \times 10^4$	$1 \times 10^{12}$	0.3 s/1.2 s	194
FL MoS <sub>2</sub> /TiO <sub>2</sub> /HgTe QDs	( $\lambda = 635$ nm, 0.35 $\mu\text{W cm}^{-2}$ )	$5 \times 10^5$	$6.4 \times 10^{12}$	—	193
	( $\lambda = 1310$ nm, 53 mW $\text{cm}^{-2}$ )	$2 \times 10^4$	$3 \times 10^{11}$	4 ms	
ML MoS <sub>2</sub> /TiO <sub>2</sub> /PbS QDs	( $\lambda = 635$ nm, 10 nW $\text{cm}^{-2}$ )	$10^5$	$5 \times 10^{12}$	12 ms	319
MoS <sub>2</sub> /PbS	( $\lambda = 800$ nm, 0.15 mW $\text{cm}^{-2}$ )	$4.5 \times 10^4$	$3 \times 10^{13}$	7.8 ms	321
FL MoS <sub>2</sub> /PbS QDs	( $\lambda = 635$ nm, 1 mW)	$6.0 \times 10^5$	$7 \times 10^{14}$	0.35 s	322
1L MoS <sub>2</sub> /PbS QDs	( $\lambda = 850$ nm)	$5.4 \times 10^4$	$1 \times 10^{11}$	950 $\mu\text{s}$ /1 ms	188
MoS <sub>2</sub> -ZnO/PET	(254 nm, 2.65 W $\text{m}^{-2}$ )	2.7	—	13.96 s/55.33 s	296
p-MoS <sub>2</sub> /n-ZnO	(365 nm, 5.7 mW $\text{cm}^{-2}$ )	24.36	—	0.9 s/1.04 s	360
n-MoS <sub>2</sub> /n-ZnO	(532 nm)	0.35	—	1.3 s/2.2 s	360
1L MoS <sub>2</sub> /TiO <sub>2</sub> nanoflowers	( $\lambda = 370$ nm)	35.9	$1.98 \times 10^{13}$	33.7 ms/28.3 ms	320
	( $\lambda = 570$ nm)	18.5	$1.09 \times 10^{13}$	—	320
1L MoS <sub>2</sub> /Ti	( $\lambda = 570$ nm)	8.6	$5.7 \times 10^{12}$	741 ms/128 ms	320
1L MoS <sub>2</sub> /SiO <sub>2</sub>	( $\lambda = 570$ nm)	6.2	$3.49 \times 10^{12}$	642 ms/214 ms	320
V-MoS <sub>2</sub> /TiO <sub>2</sub>	( $\lambda = 532$ nm, 856 nW)	133	$3.325 \times 10^{11}$	27.8 ms/48 ms	346b
MoS <sub>2</sub> /CuO nanowires (strain)	( $\lambda = 600$ nm, 55 $\mu\text{W}$ )	157.6	$3.3 \times 10^8$	34.6 ms/51.9 ms	331
V-ITO/MoS <sub>2</sub> /Cu <sub>2</sub> O/Au	( $\lambda = 500$ nm, 0.26 W $\text{m}^{-2}$ )	$5.77 \times 10^4$	$3.2 \times 10^{14}$	70 ms	302
<b>(vi) Chemically doped MoS<sub>2</sub> photodetectors</b>					
1L MoS <sub>2</sub> /methylene blue doping	( $\lambda = 610$ nm)	9.09	$2.2 \times 10^{11}$	27.1 s/39.2 s	140
1L MoS <sub>2</sub> /R6G doping	( $\lambda = 520$ nm, 1 $\mu\text{W}$ )	1.17	$1.5 \times 10^7$	5.1 $\mu\text{s}$ /2.3 s	181
ML MoS <sub>2</sub> /PPh <sub>3</sub> doping	( $\lambda = 520$ nm, 5 pW)	$3.92 \times 10^5$	$2.36 \times 10^{10}$	13.2 ms/17.2 ms	187
1L MoS <sub>2</sub> /HAuCl <sub>4</sub> doping	( $\lambda = 532$ nm, 0.15 mW $\text{cm}^{-2}$ )	99.9	$9.4 \times 10^{12}$	16.6 s/5.2 s	337
1L MoS <sub>2</sub> /pentacene	( $\lambda = 655$ nm, 28.18 mW $\text{cm}^{-2}$ )	0.31	$1.55 \times 10^{13}$	—	330
1L MoS <sub>2</sub> /ZnPc/Al <sub>2</sub> O <sub>3</sub>	( $\lambda = 532$ nm, 0.07 mW $\text{cm}^{-2}$ )	$1.4 \times 10^4$	$3 \times 10^{11}$	—	182
	( $\lambda = 532$ nm, 3.64 mW $\text{cm}^{-2}$ )	$4.3 \times 10^2$	—	—	
1L MoS <sub>2</sub> /ZnPc	( $\lambda = 532$ nm, 3.64 mW $\text{cm}^{-2}$ )	7.84	—	100 ms/10 ms	182
3L MoS <sub>2</sub> /P(VDF-TrFE)	( $\lambda = 635$ nm, 1 nW)	$2.579 \times 10^3$	$2.2 \times 10^{12}$	1.8 ms/2 ms	137
MoS <sub>2</sub> /P(VDF-TrFE-CFE)	( $\lambda = 450$ nm, 20 nW)	346.24	—	—	324
MoS <sub>2</sub> /P(VDF-TrFE)	( $\lambda = 637$ nm, 1 nW)	$3.26 \times 10^3$	$9.0 \times 10^{14}$	480 $\mu\text{s}$ /320 $\mu\text{s}$	340
MoS <sub>2</sub> /polyaniline (PANI)	( $\lambda = 785$ nm, 1.4 mW $\text{mm}^{-2}$ )	25	—	—	338
MoS <sub>2</sub> -MoO <sub>x</sub>	( $\lambda = 405$ nm, 1 mW $\text{cm}^{-2}$ )	1.09	$2.08 \times 10^{11}$	9.8 s/12.6 s	339
MoS <sub>2</sub> /UCNPs	( $\lambda = 325$ nm, 50 W $\text{m}^{-2}$ )	192	$1.61 \times 10^{14}$	—	364
	( $\lambda = 532$ nm, 50 W $\text{m}^{-2}$ )	81	$6.80 \times 10^{13}$	16 s/18 s	364
	( $\lambda = 980$ nm, 50 W $\text{m}^{-2}$ )	1254	$1.05 \times 10^{15}$	11 s/17 s	364
	( $\lambda = 1064$ nm, 50 W $\text{m}^{-2}$ )	127.5	$1.05 \times 10^{14}$	—	364
MoS <sub>2</sub> /Mo <sub>2</sub> C (multiple grating)	( $\lambda = 665$ nm)	$3.7 \times 10^3$	—	0.13 s/0.95 s	387
Sb <sub>2</sub> O <sub>3</sub> /MoS <sub>2</sub>	( $\lambda = 532$ nm, 0.057 W $\text{cm}^{-2}$ )	$4.5 \times 10^4$	$1.0 \times 10^{15}$	63 ms/71 ms	372
BaTiO <sub>3</sub> /MoS <sub>2</sub>	(365 nm, 1.0 mW $\text{cm}^{-2}$ )	120	$1.1 \times 10^{11}$	0.7 s/2 s	375
MoS <sub>2</sub>	(660 nm, 1.75 mW $\text{mm}^{-2}$ )	$1.75 \times 10^{-3}$	—	4.7 ms	385
MoS <sub>1.15</sub> Se <sub>0.85</sub>	(532 nm)	2.06	—	18 ms/35 ms	386
MoS <sub>2(1-x)</sub> Se <sub>2x</sub>	(650 nm)	191.5	$10^{12}$	51 ms	435

<sup>a</sup> 1L: single-layer, BL: bi-layer, FL: few-layer, ML: multilayer, V: vertically oriented, PET: poly(ethylene terephthalate), PPh<sub>3</sub>: triphenylphosphine, QDs: quantum dots, SiNWA: Si nanowire array, P(VDF-TrFE): poly(vinylidene fluoride-trifluoroethylene) [P(VDF-TrFE)] ferroelectric polymer, P(VDF-TrFE-CFE): poly(vinylidene fluoride-trifluoroethylene-chlorofluoroethylene), APTES: (3-aminopropyl)triethoxysilane, ZnPc: zinc phthalocyanine, Jones =  $\text{cm Hz}^{1/2} \text{W}^{-1}$ , polymer stabilizer ethyl cellulose (EC), 2D Ruddlesden-Popper perovskites: (C<sub>6</sub>H<sub>5</sub>C<sub>2</sub>H<sub>4</sub>NH<sub>3</sub> = PEA)<sub>2</sub>SnI<sub>4</sub>, PANI: polyaniline, Mo<sub>2</sub>C: molybdenum carbide.



$\text{MoS}_2$ –ZnO/PET hybrid photodetectors showed no significant degradation after bending at 3 mm radius; up to 10 000 cycles were examined.

0D PbS QDs were deposited onto few layered 2H- $\text{MoS}_2$  to develop flexible photodetectors on a PET substrate.<sup>297</sup> The 0D/2D PbS/ $\text{MoS}_2$  hybrid photodetectors showed the photoresponsivity of 0.398 to 0.543  $\text{A W}^{-1}$  and the detectivity of  $2 \times 10^{12}$  to  $2.68 \times 10^{12}$  Jones between 480 to 1200 nm at a 2 V bias. The 2H- $\text{MoS}_2$  based stretchable photodetectors were fabricated on polydimethylsiloxane (PDMS) substrates.<sup>298</sup> The photoresponsivity of  $2.52 \mu\text{A W}^{-1}$  and response times of 122 ms/120 ms were recorded at 515.6 nm. The stretchable photodetectors retained the photoconductivity up to 5.72% tensile strain and over 1000 stretching cycles.  $\text{MoS}_2$  was deposited on a flexible cellulose ester paper and the inkjet-printed PEDOT:PSS electrodes were used to develop  $\text{MoS}_2$  paper based photodetectors, which showed internal quantum efficiency of 0.063%, photoresponsivity of  $0.134 \text{ mA W}^{-1}$  and photoresponse response/recovery times of 17.5 s/15.3 s at 405 nm.<sup>299</sup>

## 5. Analysis and factors affecting the figure of merit of $\text{MoS}_2$ photodetectors

All these studies show that  $\text{MoS}_2$  atomic layers can be used to develop high-performance photodetectors. The analysis and factors affecting the parameters such as photoresponsivity, specific detectivity, NEP, photogain, EQE, LDR, and response time of the  $\text{MoS}_2$  photodetectors have been further discussed in this section. Table 1 summarizes the research data collected on the figure-of-merit of a wide variety of  $\text{MoS}_2$  based photodetectors in terms of their key parameters such as photoresponsivity, detectivity and response/recovery time ( $\tau_{\text{rise}}/\tau_{\text{decay}}$ ) of photodetectors and their performance measured at various laser wavelengths under different incident laser powers/intensities.<sup>138,171,175,179,190–199,217,226,300–435</sup> The  $\text{MoS}_2$  based photodetectors have been analyzed taking into account the factors affecting their performance.  $\text{MoS}_2$  based photodetectors have also been discussed and categorized as (i) pristine  $\text{MoS}_2$  based photodetectors, (ii) flexible  $\text{MoS}_2$  photodetectors, (iii)  $\text{MoS}_2$ /2D van der Waals heterostructure-based photodetectors, (iv)  $\text{MoS}_2$ /perovskite heterostructure-based photodetectors, (v)  $\text{MoS}_2$ /inorganic semiconductor heterostructure-based photodetectors, (vi) chemically doped  $\text{MoS}_2$  photodetectors, and (vii) self-powered  $\text{MoS}_2$  photodetectors.

The influence of different types of substrate materials on the performance of  $\text{MoS}_2$  photodetectors has been extensively studied.<sup>164,178,184,217–220,222,223,234,256,259,278,298,311–313</sup>  $\text{MoS}_2$ @ $\text{TiO}_2$  core-shell heterojunction-based photodetectors were prepared by Paul *et al.*<sup>320</sup> where 1L  $\text{MoS}_2$  was used as the shell and  $\text{TiO}_2$  nanoflowers as the core. The 83 and 30 times increase in PL intensity was observed from the 1L  $\text{MoS}_2$  shell/ $\text{TiO}_2$  nanoflowers p-n heterojunction more than that of 1L  $\text{MoS}_2$ /Ti and 1L  $\text{MoS}_2$ /sapphire substrates, respectively. The 1L  $\text{MoS}_2$ @ $\text{TiO}_2$  heterojunction-based photodetectors showed photoresponsivity of  $35.9 \text{ A W}^{-1}$  and detectivity of  $1.98 \times 10^{13}$  Jones in the UV region and  $18.5 \text{ A W}^{-1}$  and  $1.09 \times 10^{13}$  Jones in

the visible region. 1L  $\text{MoS}_2$ @ $\text{TiO}_2$  heterojunction also exhibited an order of magnitude faster photoresponse compared to the 1L  $\text{MoS}_2$ @Ti and 1L  $\text{MoS}_2$ @ $\text{SiO}_2$  devices due to the fast photoexcited carrier transport at the p-n heterojunction associated with the substantial built-in electric field. In another study,  $\text{MoS}_2$  nanosheets were placed on top of a CuO nanowire by wet transfer printing method.<sup>331</sup>  $\text{MoS}_2$ /CuO heterojunction-based photodetectors showed the photoresponsivity  $157.6 \text{ A W}^{-1}$ , rectification ratio of 6000, and low dark current of 38 fA at  $-2 \text{ V}$ .

### 5.1 0D/2D quantum dots/ $\text{MoS}_2$ hybrid heterostructures

The performance of  $\text{MoS}_2$  photodetectors can be significantly enhanced by developing hybrid heterostructures as discussed in the earlier sections. Kufer *et al.*<sup>322a</sup> showed significantly increased light absorption and carrier mobility in the 2D–0D  $\text{MoS}_2$ /PbS QDs hybrid phototransistors. The photoresponsivity of pristine bilayer  $\text{MoS}_2$  with  $\text{MoS}_2$ /PbS hybrid were compared as a function of wavelength between 600 nm to 1200 nm. The bilayer  $\text{MoS}_2$  absorbs up to 700 nm whereas the  $\text{MoS}_2$ /PbS hybrid extends the absorption up to 1200 nm with an excitation peak at 980 nm. Bilayer  $\text{MoS}_2$  phototransistors showed field-effect mobility of  $10\text{--}20 \text{ cm}^2 \text{ V}^{-1} \text{ s}^{-1}$  and current  $I_{\text{on}}/I_{\text{off}}$  ratios of  $10^5$  to  $10^6$  which is further increased after PbS QDs doping. The photoresponsivity of pristine bilayer  $\text{MoS}_2$  is  $5 \text{ A W}^{-1}$  at 1.8 eV, which is dramatically enhanced to  $10^5$  to  $10^6 \text{ A W}^{-1}$  for the  $\text{MoS}_2$ /PbS hybrid phototransistor due to the PbS DQs. The multilayer  $\text{MoS}_2$ /PbS hybrid photodetector showed photoresponsivity up to  $10^6 \text{ A W}^{-1}$  at the lowest laser power intensity. The photoresponsivity of the hybrid photodetector varies by six orders of magnitude as a function of applied laser power intensity, which decreased as the laser intensity increases. The photoresponse of hybrid photodetector to light can be tailored by adjusting the size of PbS QDs. The photoresponsivity of the hybrid photodetector ( $6 \times 10^5 \text{ A W}^{-1}$ ) was found to be three orders of magnitude higher than that of PbS QDs ( $4.3 \times 10^2 \text{ A W}^{-1}$ ). The NEP were found to be  $2 \times 10^{-15} \text{ W Hz}^{-1/2}$  for the bilayer  $\text{MoS}_2$  and  $7 \times 10^{-16} \text{ W Hz}^{-1/2}$  for few-layer  $\text{MoS}_2$ /PbS hybrids at 1 Hz frequency, yielding corresponding detectivity of  $2 \times 10^{11}$  Jones and  $5 \times 10^{11}$  Jones, respectively. The  $\text{MoS}_2$ /PbS hybrid photodetector reached detectivity as high as  $7 \times 10^{14}$  Jones at applied negative back-gate bias  $V_g$  of  $-100 \text{ V}$ . The study showed that  $\text{MoS}_2$ /PbS hybrid photodetector can achieve several orders of magnitude higher photoresponsivity than those of individual bilayer  $\text{MoS}_2$  and PbS QD-based photodetectors. In another study, Pak *et al.*<sup>322b</sup> fabricated hybrid photodetectors by decorating n-type  $\text{MoS}_2$  with p-type manganese oxide QDs ( $\text{MnO}$  QDs), which showed suppressed dark current (5 nA) and an enhancement of photocurrent (52 nA) compared to a pristine  $\text{MoS}_2$  photodetector (10 nA and 32 nA) at under  $100 \text{ mW cm}^{-2}$  incident light intensity.  $\text{MoS}_2$ /MnO QDs hybrid photodetectors showed the photoresponsivity of  $20 \text{ A W}^{-1}$  and detectivity of  $5 \times 10^{11}$  Jones at 260 nm light illumination where increased detection was noticed in DUV range below 300 nm. The absorption of  $\text{MnO}$  QDs on  $\text{MoS}_2$  surface suppressed dark current and increased photogeneration of charge carriers.



Ferroelectric polymers have been used with  $\text{MoS}_2$  to improve the performance of photodetectors. Wang *et al.*<sup>340</sup> developed an ultrabroad band photodetector integrating unique pyroelectric properties of organic ferroelectric copolymer P(VDF-TrFE) with  $\text{MoS}_2$ , which operated from 375 nm (ultraviolet) to 10  $\mu\text{m}$  (LWIR) spectral range. The photocurrent of  $\text{MoS}_2$  was improved in the 2.76  $\mu\text{m}$  to 10  $\mu\text{m}$  spectral range due to the pyroelectricity of P(VDF-TrFE). The photoresponsivity of  $140 \text{ mA W}^{-1}$ ,  $I_{\text{on}}/I_{\text{off}}$  current ratio of  $10^3$  and a response time of 5.5 ms was achieved for the  $\text{MoS}_2/\text{P}(\text{VDF-TrFE})$  hybrid photodetector. Though the highest photoresponsivity of  $3.26 \times 10^3$  and detectivity of  $9.0 \times 10^{14}$  Jones were observed at 637 nm illumination at the drain bias of 5 V, the ferroelectric polarization field of P(VDF-TrFE) significantly improved the photoconductivity of  $\text{MoS}_2$  and curtailed the dark current as well as the noise. The single-pixel imaging was also recorded by the photodetector. In a recent study, Li *et al.*<sup>337</sup> showed that the photoresponsivity and detectivity of n-doped monolayer  $\text{MoS}_2$  photodetector increased by 14.6 and 4.8 times compared with pristine  $\text{MoS}_2$  photodetector, after *in situ* chemical doping with gold chloride hydrate ( $\text{HAuCl}_4 \cdot x\text{H}_2\text{O}$ ). The *in situ* n-doped  $\text{MoS}_2$  based photodetector exhibited the photoresponsivity of  $99.9 \text{ A W}^{-1}$  and detectivity of  $9.4 \times 10^{12}$  Jones under  $V_{\text{ds}} = 0.1 \text{ V}$  and  $V_g = 0 \text{ V}$ , much higher compared with pristine  $\text{MoS}_2$  photodetectors. The enhanced photoresponse originated from n-type chlorine doping of CVD-grown  $\text{MoS}_2$  film which decreased the trapping of photoexcited electrons. Both photoresponsivity and detectivity of doped and pristine  $\text{MoS}_2$  photodetectors were found to decrease with increasing incident laser power intensity. The chlorine n-type doping of  $\text{MoS}_2$  photodetector increased the photoresponse due to improved photogating effect. The n-doped  $\text{MoS}_2$  photodetector exhibited EQE over 100% which was found to increase as a function of decreasing wavelength, confirming photoconversion efficiency under shorter light illuminating wavelengths because of the higher excitation energy. Furthermore, these n-doped  $\text{MoS}_2$  photodetectors also showed long-term stability as demonstrated by retaining 94% of the initial photocurrent after up to nine months.

Perovskites, van der Waals and plasmonic materials have been used with  $\text{MoS}_2$  to improve the performance of photodetectors. Wang *et al.*<sup>341a</sup> reported perovskite/black phosphorus/ $\text{MoS}_2$  photogate photodiode, which utilizes black phosphorus/ $\text{MoS}_2$  photodiodes with perovskite in order to induce high photoresponsivity and a fast photoresponse. This device architecture is constructed based on the fast photovoltaic operation together with the high-gain photogating effect. Under reverse bias condition, the 2D photogate photodiode showed photoresponsivity of  $11 \text{ A W}^{-1}$ , detectivity of  $1.3 \times 10^{12}$  Jones, fast response times of 150/240  $\mu\text{s}$ , and a low dark current of  $3 \times 10^{-11} \text{ A}$  in reverse bias. The photogate photodiode device yielded detectivity of  $3 \times 10^{11}$  Jones, external quantum efficiency (EQE) of 80% and  $I_{\text{on}}/I_{\text{off}}$  current ratio of  $3 \times 10^7$  in a zero bias (self-powered mode) indicating their potential in fabricating photodetectors and photovoltaic devices. The black arsenic phosphorus (b-AsP) which is a p-type semiconductor was used with  $\text{MoS}_2$  n-type semiconductor to develop vdW p-n heterojunction-based MIR photodetectors.<sup>341b</sup> The

photoresponsivity of AsP/ $\text{MoS}_2$  photodetectors varied from  $216.1 \text{ mA W}^{-1}$  to  $115.4 \text{ mA W}^{-1}$  as the laser wavelength was increased from 2.36  $\mu\text{m}$  to 4.29  $\mu\text{m}$  and the value of EQE decreased from 11.36% to 3.33%, respectively. The NEP of vdW p-n junction was less than  $0.24 \text{ pW Hz}^{-1/2}$ , while that of FET device below  $4.35 \text{ pW Hz}^{-1/2}$  for 8.05  $\mu\text{m}$  MIR wavelength at room temperature. The detectivity of the AsP/ $\text{MoS}_2$  vdW p-n junction remained higher than  $4.9 \times 10^9$  Jones over the 3  $\mu\text{m}$  to 5  $\mu\text{m}$  spectral range and larger than the detectivity of  $1.06 \times 10^8$  Jones for AsP FET device at 8.05  $\mu\text{m}$  wavelength. These studies demonstrated fabrication of  $\text{MoS}_2$  based MIR photodetectors. Wu *et al.*<sup>342</sup> used a Au-supported gap-mode surface plasmon increasing configuration to improve the optoelectronic properties, with which a monolayer  $\text{MoS}_2$  photodetector exhibited a photoresponsivity of  $287.5 \text{ A W}^{-1}$  and a 880% increment in the photocurrent.

The self-powered photovoltaic photodetector developed from individual monolayer  $\text{MoS}_2$ - $\text{WS}_2$  heterostructures showed photoresponsivity of  $4.36 \text{ mA W}^{-1}$ , EQE of 1.02%, and detectivity of  $4.36 \times 10^{13}$  Jones at 532 nm under laser power intensity of  $28.64 \text{ mW cm}^{-2}$  under 0 V bias.<sup>343</sup> Photoresponsivity of  $4.34 \text{ mA W}^{-1}$  and  $10.44 \text{ mA W}^{-1}$  were measured for positive bias (3 V) and reversed bias (-3 V), respectively. Ye *et al.*<sup>344</sup> used individual bilayers of  $\text{MoS}_2$ - $\text{WS}_2$  heterostructures to develop photodetectors which showed photoresponsivity of  $6.72 \times 10^3 \text{ A W}^{-1}$  and detectivity of  $3.09 \times 10^{13}$  Jones at 457 nm laser illumination. The performance of bilayered  $\text{MoS}_2$ - $\text{WS}_2$  heterostructure photodetectors were several orders of magnitude higher compared with  $\text{MoS}_2$  and  $\text{WS}_2$  monocrystals. All-2D photodetectors were developed using the type-II band alignment of vertically stacked  $\text{WS}_2/\text{MoS}_2$  heterobilayers and graphene electrodes.<sup>359</sup>  $\text{WS}_2/\text{MoS}_2$  heterobilayer-based photodetectors showed over an order of magnitude increase in the photoresponsivity than that of homobilayer photodetector and two orders of magnitude increase compared to  $\text{WS}_2$  and  $\text{MoS}_2$  monolayer-based photodetectors. The photoresponsivity of  $10^3 \text{ A W}^{-1}$  was measured under a power density of  $1.7 \times 10^2 \text{ mW cm}^{-2}$ . The significant increase in photoresponsivity resulted from the strong Coulomb interactions occurring between  $\text{WS}_2$  and  $\text{MoS}_2$  layers.

Color-selective and flexible  $\text{MoS}_2$  phototransistors on poly-arylate substrates using integrated Fabry-Perot cavity filters were developed by Yoo *et al.*<sup>345</sup> The multilayer  $\text{MoS}_2$  phototransistors showed a mobility of  $>64.4 \text{ cm}^2 \text{ V}^{-1} \text{ s}^{-1}$  and an  $I_{\text{on}}/I_{\text{off}}$  current ratio  $>10^6$ . The Fabry-Perot filters facilitated the coverage of the visible spectral range from 495 to 590 nm. The  $\text{MoS}_2$  phototransistors showed no significant degradation after integrating the Fabry-Perot cavity and the SU-8 interlayer. Huo and Konstantatos<sup>346a</sup> developed all-2D  $\text{MoS}_2$  phototransistors using an out-of-plane vertical  $\text{MoS}_2$  p-n junction. The vertical built-in field in the  $\text{MoS}_2$  p-n junction reduced the recombination of the photoexcited carriers and yielded a photoresponsivity of  $7 \times 10^4 \text{ A W}^{-1}$ , detectivity of  $3.5 \times 10^{14}$  Jones, a photoconductive gain of  $>10^5$  and a fast photoresponse. Liu *et al.*<sup>346b</sup> prepared a vertically oriented  $\text{MoS}_2$  nanosheets array using  $\text{TiO}_2$  buffer thin film on a  $\text{SiO}_2$  substrate which also yielded a high photoresponse. The floating monolayer  $\text{MoS}_2$



quantum well structure was also used to develop graphene/WS<sub>2</sub>/MoS<sub>2</sub> heterostructure based photodetectors, which resulted in higher photoresponsivity of  $4.4 \times 10^6$  A W<sup>-1</sup> at 851 nm laser illumination under 30 fW laser power due to the strong photogating effect.<sup>347</sup>

## 5.2 Graphene electrodes

High photoresponsivities ranging from  $10^3$  A W<sup>-1</sup> to  $10^{10}$  A W<sup>-1</sup> have been observed for the graphene/MoS<sub>2</sub> hybrid structure-based photodetectors.<sup>126,226–228</sup> Han *et al.*<sup>300</sup> developed photodetectors using CVD-grown MoS<sub>2</sub> monolayers with both Au and graphene electrodes. MoS<sub>2</sub> photodetectors with graphene electrodes showed the current  $I_{on}/I_{off}$  ratio of  $1 \times 10^5$  and mobility of  $0.48 \text{ cm}^2 \text{ V}^{-1} \text{ s}^{-1}$  compared to  $2 \times 10^3$  and  $0.1 \text{ cm}^2 \text{ V}^{-1} \text{ s}^{-1}$  with gold electrodes. The shot-noise-limited detectivity of MoS<sub>2</sub> photodetectors was  $8.7 \times 10^{14}$  Jones for the graphene electrode and  $2.7 \times 10^{14}$  Jones for the Au electrode for 1 Hz bandwidth at the gate voltage ( $V_g$ ) =  $-30$  V. The detectivity of CVD-grown MoS<sub>2</sub> photodetectors were a few orders of magnitude higher compared to photodetectors made using exfoliated MoS<sub>2</sub>. Graphene/MoS<sub>2</sub>/graphene photodetectors were also fabricated where the MoS<sub>2</sub> layer was encapsulated with a PMMA layer which showed mobility of  $0.59 \text{ cm}^2 \text{ V}^{-1} \text{ s}^{-1}$ , better than non-encapsulated devices. Photoresponsivity of the PMMA encapsulated graphene/MoS<sub>2</sub>/graphene photodetectors were measured as  $1.4 \times 10^5$  A W<sup>-1</sup> and  $1.1 \times 10^5$  A W<sup>-1</sup> at 633 nm under applied gate voltage of 10 V and  $-30$  V, respectively. The graphene electrodes were found to be instrumental in improving the photoresponse of the MoS<sub>2</sub> photodetectors. Chee *et al.*<sup>301a</sup> used graphene/Ag contacts for MoS<sub>2</sub> photodetectors where CVD-grown graphene film was inserted as an interfacial layer between the MoS<sub>2</sub> film and Ag electrode. The MoS<sub>2</sub> FETs having graphene/Ag contacts exhibited the higher mobility of  $35 \text{ cm}^2 \text{ V}^{-1} \text{ s}^{-1}$ , photoresponsivity of  $2160 \text{ A W}^{-1}$ , and current  $I_{on}/I_{off}$  ratio of  $4 \times 10^8$ , compared to those of MoS<sub>2</sub> photodetectors with Ti/Au contacts due to the low work function of Ag and the Fermi level tunability in graphene. The n-doping by Ag electrode reduced the Fermi level of graphene, which consequently decreased the Schottky barrier height as well as contact resistance between the MoS<sub>2</sub> layer and electrodes. This study demonstrated that low-resistance contacts with MoS<sub>2</sub> and graphene played a significant role in enhancing the photoresponse of MoS<sub>2</sub> photodetectors. Bipolar phototransistors were developed by Li *et al.*<sup>301b</sup> using vertical Au/graphene/MoS<sub>2</sub> vdWHs heterojunction where Au functions as the emitter and electrodes, MoS<sub>2</sub> as the collector, and graphene as the base of the bipolar phototransistor. Au/graphene/MoS<sub>2</sub> vdWHs heterojunction-based photodetectors showed the photoresponsivity of  $16\,458 \text{ A W}^{-1}$  and detectivity of  $1.75 \times 10^{14}$  Jones at 405 nm laser illumination and incident power intensity of  $0.45 \text{ mW cm}^{-2}$ . Lee *et al.*<sup>301c</sup> showed that the performance of MoS<sub>2</sub> photodetectors can be improved using graphene/MoS<sub>2</sub>/graphene heterojunction-based phototransistors having short MoS<sub>2</sub> channel length greater than that of carrier diffusion length (220 nm) of MoS<sub>2</sub> and controllable Schottky barrier height (SBH). Fig. 23 shows the schematic illustration of MoS<sub>2</sub>

phototransistor with a graphene gate electrode, change of photoresponsivity with MoS<sub>2</sub> channel length, the incident laser power dependent photoresponsivity and detectivity of graphene/MoS<sub>2</sub>/graphene heterojunction-based phototransistors at different gate bias voltage and time-dependent normalized photocurrent. The distance between the graphene source and the drain electrode was measured as 30 nm by atomic force microscopy (AFM) technique. The short channel effects were not observed in MoS<sub>2</sub> transistors in the dark state in spite of their sub-30 nm channel length. The carrier recombination as well as the carrier transit time were found to be reduced by using sub-30 nm channel length which is much shorter compared to MoS<sub>2</sub> diffusion length. Longer MoS<sub>2</sub> channel length restricts the efficient flow of carriers from the source to the drain electrode. The Schottky barrier of phototransistors was manipulated by light and gate bias which supported decreased dark current and increased photocurrent. The SBH of the graphene/MoS<sub>2</sub> heterojunction was found to be decreased as the gate bias voltage was increased which supported the formation of ohmic contact. The SBH of the graphene/MoS<sub>2</sub> heterojunction was analyzed under different laser power intensity which was found to be 0.14 eV at  $V_{gs} = -3$  V under the dark state. When 432 nm laser light was illuminated on the heterojunction, the SBH decreased with increasing laser power and, finally, disappeared at 0.14  $\mu\text{W}$  laser power due to the photoinduced doping of graphene that eventually improved the performance of the graphene/MoS<sub>2</sub> heterojunction phototransistors. Both photoresponsivity and detectivity significantly changed as a function of incident laser powers. The graphene/MoS<sub>2</sub>/graphene heterojunction-based phototransistor showed photoresponsivity of  $1996 \text{ A W}^{-1}$  and detectivity of  $3.57 \times 10^{10}$  Jones under laser power intensity of 0.34 nW at 432 nm laser wavelength and the maximum photocurrent of 2.15  $\mu\text{A}$  with  $I_{photo}/I_{dark}$  current ratio of  $4 \times 10^4$  at laser power of 0.14  $\mu\text{W}$ . These heterojunction-based phototransistors showed the maximum photoresponsivity, detectivity and response time of  $2.2 \times 10^5 \text{ A W}^{-1}$ ,  $3.5 \times 10^{13}$  Jones and 2.8 ms at 432 nm, respectively, originating from the reduced MoS<sub>2</sub> channel length and controlled Schottky barrier in the graphene/MoS<sub>2</sub> heterojunction. These studies demonstrate that graphene electrodes played an important role in enhancing the performance of MoS<sub>2</sub> photodetectors.

## 5.3 Semiconducting (2H) and metallic (1T) phases of MoS<sub>2</sub>

2D MoS<sub>2</sub> crystals exhibit several types of polymorphs, which have different electronic properties associated with semiconducting to metallic structural phase transformation.<sup>325a,b</sup> The stable polymorphs of MoS<sub>2</sub> have been used in developing ultra-broadband photodetectors. Wang *et al.*<sup>325c</sup> fabricated hybrid photodetectors using semiconducting trigonal prismatic 2H-phase and metallic octahedral 1T-phase MoS<sub>2</sub> nanosheets with organolead trihalide perovskites (MAPbX<sub>3</sub> where MA = methylammonium CH<sub>3</sub>NH<sub>3</sub> and X = I). 1T-MoS<sub>2</sub>/CH<sub>3</sub>NH<sub>3</sub>PbI<sub>3</sub> hybrid thin films showed 90% PL quenching due to the efficient charge transfer from CH<sub>3</sub>NH<sub>3</sub>PbI<sub>3</sub> to the 1T-MoS<sub>2</sub> while 2H-MoS<sub>2</sub>/CH<sub>3</sub>NH<sub>3</sub>PbI<sub>3</sub> films showed 60% PL quenching due to the



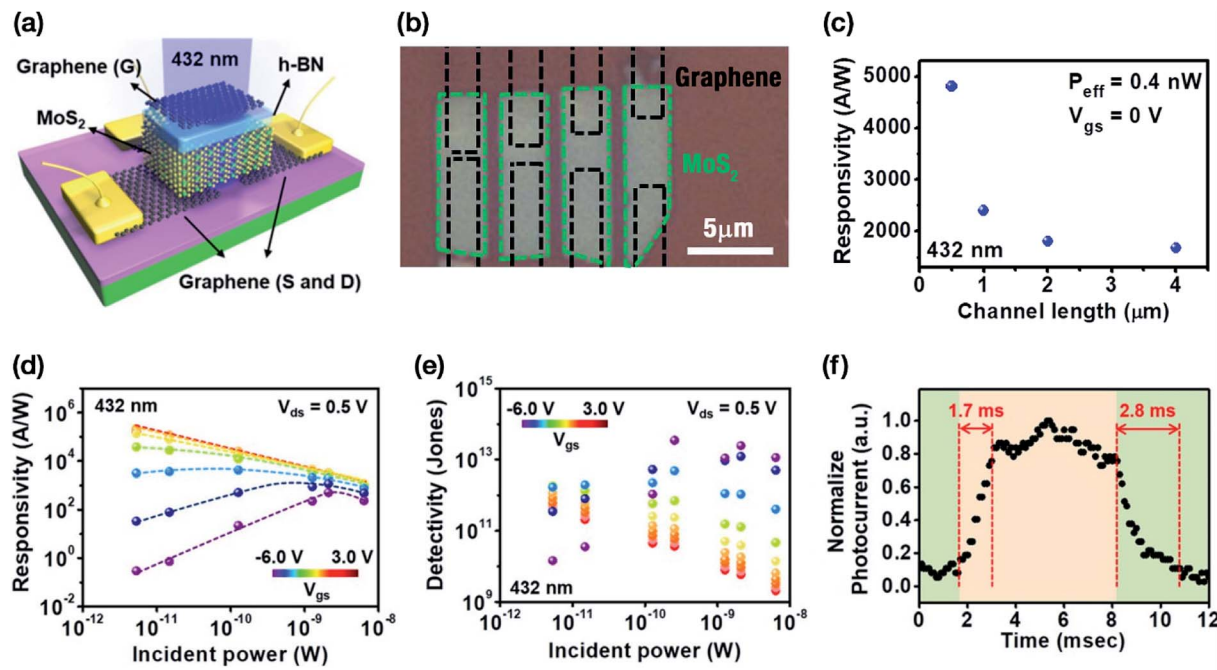


Fig. 23 (a) Schematic illustration of MoS<sub>2</sub> phototransistor with a graphene gate electrode. (b) Optical image showing different MoS<sub>2</sub> channel length. (c) Change of photoresponsivity as a function of MoS<sub>2</sub> channel length at 432 nm laser wavelength, (d) photoresponsivity (e) detectivity of graphene/MoS<sub>2</sub>/graphene heterojunction-based phototransistors as a function of incident laser power intensity at different applied gate bias voltage. (f) Normalized photocurrent as a function of time measured under low intensity light at 80 Hz frequency. Reprinted with permission from ref. 301c, copyright © American Chemical Society.

injection of electrons and holes from CH<sub>3</sub>NH<sub>3</sub>PbI<sub>3</sub> to 2H-MoS<sub>2</sub> as proposed by Kang *et al.*<sup>192</sup> 1T-MoS<sub>2</sub>/CH<sub>3</sub>NH<sub>3</sub>PbI<sub>3</sub> hybrid-based photodetector showed photoresponsivity of 3096 A W<sup>-1</sup> and EQE value of 7.7 × 10<sup>3</sup>% at 500 nm under laser power density of 37.9 μW cm<sup>-2</sup> whereas 2H-MoS<sub>2</sub>/CH<sub>3</sub>NH<sub>3</sub>PbI<sub>3</sub> hybrid-based photodetector exhibited comparatively lower photoresponsivity of 142 A W<sup>-1</sup> and EQE of 3.5 × 10<sup>4</sup>% at 500 nm under laser power density of 31.3 μW cm<sup>-2</sup>. Multilayered 1T-MoS<sub>2</sub>/CH<sub>3</sub>NH<sub>3</sub>PbI<sub>3</sub> hybrid photodetectors exhibited even higher photoresponsivity and EQE, due to the increased conductivity from the thicker multilayers of MoS<sub>2</sub>. Multilayered 1T-MoS<sub>2</sub> and 2H-MoS<sub>2</sub> based photodetectors exhibited detectivity of 7 × 10<sup>11</sup> Jones and 2.6 × 10<sup>11</sup> Jones at 0.14 μW cm<sup>-2</sup> power density, respectively. This study showed that high photoresponsivity and EQE values can be obtained by blending CH<sub>3</sub>NH<sub>3</sub>PbI<sub>3</sub> perovskite with metallic 1T-phase MoS<sub>2</sub> nanosheets greater than that of semiconducting 2H-phase MoS<sub>2</sub> nanosheets. In another interesting study, Wang *et al.*<sup>325d</sup> pointed out that photodetectors based on semiconducting 2H-phase MoS<sub>2</sub> show weak photoresponse inspite of their high optical absorption, whereas the metallic 1T-phase MoS<sub>2</sub> exhibit fast carrier transport but suffers from the low photoresponse to visible light. By integrating the positive traits of 2H and 1T phases of MoS<sub>2</sub>, hybrid phototransistors were developed using a channel consisting of monolayer 2H-phase MoS<sub>2</sub> on top of 1T@2H-MoS<sub>2</sub> layer. The 1T@2H-MoS<sub>2</sub> has metal-like properties due to the lattice matching. The photodetectors developed from vertically stacked 2H-MoS<sub>2</sub>/1T@2H-MoS<sub>2</sub> hybrid structure showed

photoresponsivity of 1917 A W<sup>-1</sup>, detectivity of 7.55 × 10<sup>11</sup> Jones, and EQE of value of 448 384% at 532 nm wavelength under an illuminating power of 2.35 mW cm<sup>-2</sup> with applied bias of 20 V due to the existing metallic 1T-phase MoS<sub>2</sub> contents in the metal-like mixture of 1T@2H-MoS<sub>2</sub>. The very high value of EQE in the 2H-MoS<sub>2</sub>/1T@2H-MoS<sub>2</sub> photodetectors indicated the Schottky barrier modulated operation mechanism. The photoresponsivity, detectivity and EQE values depended on the illuminating power intensity and were found to be varied by few orders of magnitude with different photodetector device structures. The photodetector solely based on monolayer 2H-MoS<sub>2</sub> (without 1T@2H-MoS<sub>2</sub> layer) showed comparatively low photoresponse with a photoresponsivity of 56 A W<sup>-1</sup> and detectivity of ~1.3 × 10<sup>11</sup> under the same experimental conditions with source-drain bias voltage of 10 V. Furthermore, the 1T@2H-MoS<sub>2</sub> photodetectors showed extremely low photoresponsivity of 10<sup>-4</sup> A W<sup>-1</sup>, even much lower than that of 2H-MoS<sub>2</sub> photodetectors (56 A W<sup>-1</sup>) under similar experimental conditions. The performance of photodetectors followed the sequence: 2H-MoS<sub>2</sub>/1T@2H-MoS<sub>2</sub> > 2H-MoS<sub>2</sub> > 1T@2H-MoS<sub>2</sub>. The dramatically high performance of 2H-MoS<sub>2</sub>/1T@2H-MoS<sub>2</sub> photodetectors originated from the higher carrier mobility of the 1T@2H-MoS<sub>2</sub> layer and the synergistic interfacing between 2H-phase MoS<sub>2</sub> and mixed 1T@2H-MoS<sub>2</sub> layer.

#### 5.4 Configuration of MoS<sub>2</sub> heterojunctions

The role of configuration of device heterojunctions has been emphasized for developing high performance MoS<sub>2</sub>



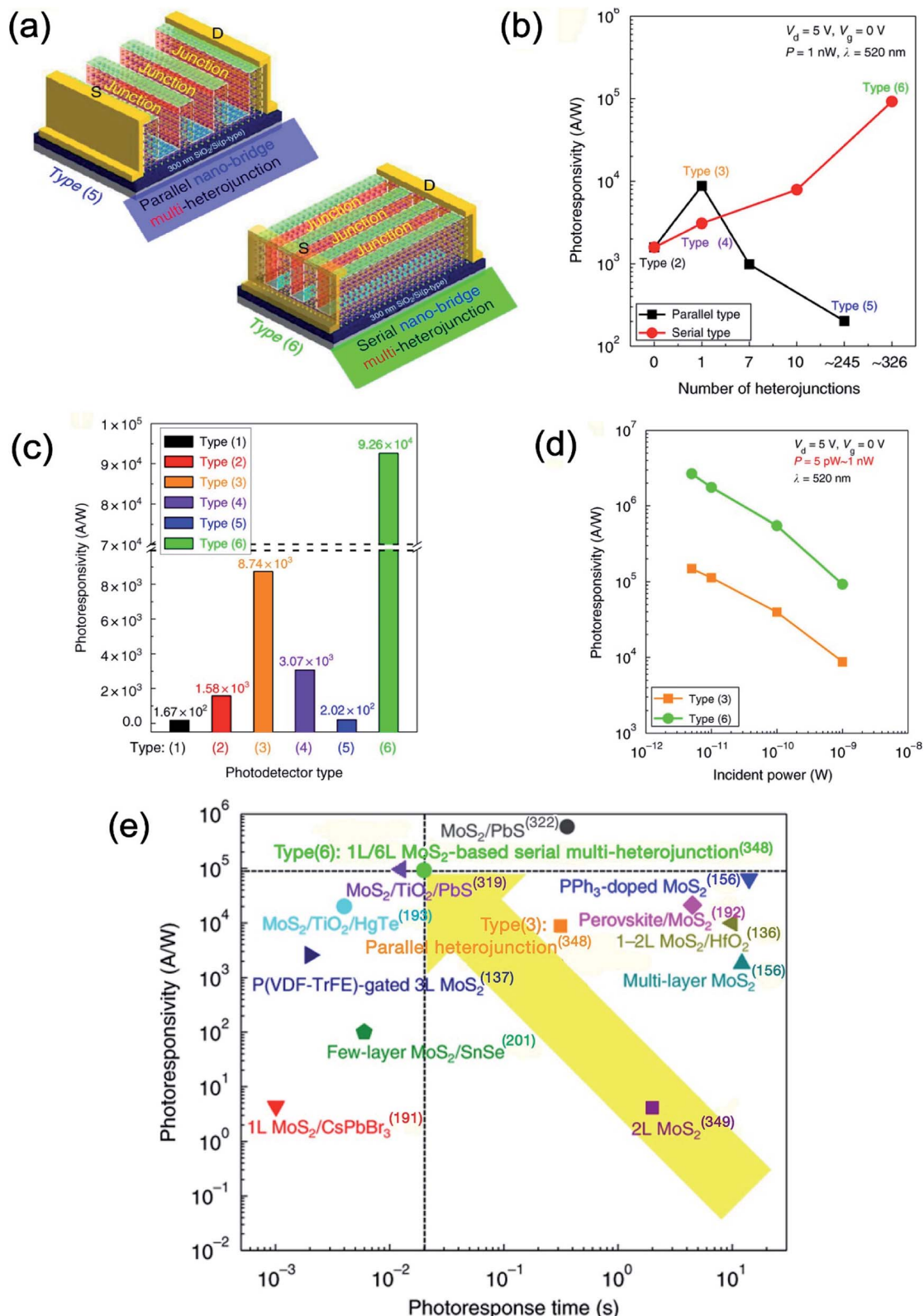


**Fig. 24** (a) The schematic diagram of MoS<sub>2</sub> FETs for parallel nano-bridge multi-heterojunction type (5) and serial nano-bridge multi-heterojunction type (6) photodetectors. (b) Photoresponsivity as a function of the number and direction (parallel and serial) of heterojunctions in the MoS<sub>2</sub> channel. (c) The photoresponsivity of type (1) to (6) MoS<sub>2</sub> multi-heterojunctions. (d) Photoresponsivity of type (3) and (6) MoS<sub>2</sub> photodetectors as a function of the incident laser power at 500 nm. (e) A comparison of photoresponsivity and photoresponse time of parallel multi-heterojunction type (3) and serial multi-heterojunction type (6) based MoS<sub>2</sub> photodetectors with previously reported data on MoS<sub>2</sub> photodetectors (see ref. 136, 137, 156, 191–193, 201, 319, 322 and 349). Reprinted with permission from ref. 348, copyright © Springer Nature.



photodetectors. Kim *et al.*<sup>348</sup> reported MoS<sub>2</sub> photodetectors using serial nano-bridge multi-heterojunctions. The MoS<sub>2</sub> photodetectors based on laser irradiation were assigned as type (1) monolayer, type (2) multilayer, type (3) parallel heterojunction, type (4) serial heterojunction, type (5) parallel nano-bridge multi-heterojunction, and type (6) serial nano-bridge multi-heterojunction. Fig. 24 shows a schematic diagram of MoS<sub>2</sub> FETs for parallel nano-bridge multi-heterojunction type (5) and serial nano-bridge multi-heterojunction type (6) photodetectors, photoresponsivity as a function of the number of heterojunctions in the MoS<sub>2</sub> channel and the incident laser power as well as their comparison with previously reported data on MoS<sub>2</sub> photodetectors.<sup>136,137,156,191–193,201,319,322,349</sup> Photoresponsivity of type (2) MoS<sub>2</sub> photodetectors ( $1.58 \times 10^3$  A W<sup>-1</sup>) was found to be  $\sim 9.46$  folds higher compared with type (1) photodetectors ( $1.67 \times 10^2$  A W<sup>-1</sup>) because more photocarriers were generated by a greater number of layers and lower exciton binding energy associated with 6L-MoS<sub>2</sub> (0.2 eV). The photoresponsivities of type (3) and type (4) MoS<sub>2</sub> photodetectors were  $8.74 \times 10^3$  A W<sup>-1</sup> and  $3.07 \times 10^3$  A W<sup>-1</sup> which were  $\sim 5.53$  and  $\sim 1.94$  times higher compared with type (2) photodetectors ( $1.58 \times 10^3$  A W<sup>-1</sup>), respectively, arising from the easier electron–hole pair generation. The highest photoresponsivity of  $2.67 \times 10^6$  A W<sup>-1</sup> at  $\lambda = 520$  nm and then  $1.65 \times 10^4$  A W<sup>-1</sup> at  $\lambda = 1064$  nm were observed for the MoS<sub>2</sub> serial-type heterojunctions with  $\sim 326$ , and monolayer/multilayer (6L) heterojunctions.

The mechanisms of photoconductivity in atomically thin layered MoS<sub>2</sub> has been described by Furchi *et al.*<sup>349</sup> Sun *et al.*<sup>350</sup> developed photodetector using multilayer/monolayer MoS<sub>2</sub> heterojunction where the source electrodes were connected to the 0.65 nm thick MoS<sub>2</sub> monolayer and the drain electrodes were connected with the 6.9 nm thick MoS<sub>2</sub> multilayer and the back gate was heavily p-doped Si. The multilayer/monolayer MoS<sub>2</sub> heterojunction showed photoresponsivity of  $10^3$  A W<sup>-1</sup>, detectivity of  $7 \times 10^{10}$  Jones and photosensitivity of  $1.7 \times 10^5$  at 470 nm. Abnormal photoresponse was noticed under positive gate voltage due to the heterojunction formation. Yan *et al.*<sup>351</sup> fabricated photodetectors using CVD-grown MoS<sub>2</sub> bilayer flakes which showed photoresponsivity of  $7160$  A W<sup>-1</sup>, detectivity of  $6.62 \times 10^{10}$  Jones and response/recovery times of 97 ms/291 ms, compared to photoresponsivity of  $2900$  A W<sup>-1</sup> and detectivity of  $2.44 \times 10^{11}$  Jones for the monolayer MoS<sub>2</sub> flakes.

## 5.5 MoS<sub>2</sub>/inorganic semiconductor heterostructures

Gallium nitride (GaN), a wide-bandgap semiconductor, has been used with MoS<sub>2</sub> for developing hybrid photodetectors. The self-powered few-layer MoS<sub>2</sub>/GaN heterojunction-based deep-ultraviolet (DUV) photodetector was developed by Zhuo *et al.*<sup>316</sup> In order to develop a MoS<sub>2</sub>/GaN p–n heterojunction photodetector, the MoS<sub>2</sub> thin films were transferred onto a GaN substrate where e-beam evaporation method was used to deposit Au electrode on the MoS<sub>2</sub> film and Ni/Au electrode on the GaN layer. The MoS<sub>2</sub>/GaN photodetector exhibited the current  $I_{on}/I_{off}$  ratio of  $10^5$  at  $2.4$  mW cm<sup>-2</sup> and over  $10^3$  at a laser light intensity of  $2$   $\mu$ W cm<sup>-2</sup>, indicating the detection of a weak UV light signal under 265 nm laser illumination at zero bias

voltage (0 V) without any external power (self-powered mode). The linear dynamic range (LDR) of 97.3 dB was calculated at zero bias voltage, much better than those of other photodetectors. The rise/fall times were found to be 0.302 ms and 3.605 ms at 100 Hz which further improved at 5 kHz. The MoS<sub>2</sub>/GaN photodetectors exhibited photoresponsivity of  $187$  mA W<sup>-1</sup>, detectivity of  $2.34 \times 10^{13}$  Jones, fast response speeds of  $46.4$   $\mu$ s/114.1  $\mu$ s at 5 kHz under a DUV light illumination of 265 nm at 0 V bias. Liu *et al.*<sup>317a</sup> fabricated ML MoS<sub>2</sub>-based phototransistor on a transparent GaN wafer using CVD technique. High quality MoS<sub>2</sub>/GaN hybrid films were obtained because of the small thermal expansion coefficient (TEC) mismatch and near lattice match between MoS<sub>2</sub> and GaN. The photocurrent MoS<sub>2</sub>/GaN-based FETs was found to be 3–4 times higher at 405 nm compared with 638 nm arising from high absorption and photocurrent gain process. The value of EQE also increased significantly, from 115% at 638 nm to 5289% at 405 nm. The photoresponsivity of 0.59, 2.78, and  $17.2$  A W<sup>-1</sup> was measured at 638, 532, and 405 nm wavelengths under 2 mW laser power, respectively. The response time ( $t_{rise}$ ) decreased from 4.2 s at 638 nm to 0.1 s at 405 nm. MoS<sub>2</sub>/GaN hybrid-based photodetector showed the maximum photoresponsivity of  $17.2$  A W<sup>-1</sup>, EQE of 5289%, and photocurrent gain of 53.6 at 405 nm under incident laser-power of 2 mW using an applied voltage of 9 V. The specific detectivity and the low noise equivalent power (NEP) varied from  $6.3 \times 10^{10}$  to  $1.8 \times 10^{12}$  Jones and  $2.8 \times 10^{-12}$  to  $9.6 \times 10^{-14}$  W Hz<sup>-1/2</sup> in 405 nm to 638 nm wavelength range, respectively. Li *et al.*<sup>317b</sup> demonstrated the improvement of photoresponse of ML MoS<sub>2</sub>/GaN photodetector by depositing 3 nm thick Al<sub>2</sub>O<sub>3</sub> layer on the surface with ALD method. The photocurrent of Al<sub>2</sub>O<sub>3</sub>/MoS<sub>2</sub>/GaN heterostructure-based photodetector increased more than twice compared to MoS<sub>2</sub>/GaN device at 365 nm wavelength under applied voltage of 20 V due to the tensile strain enhancement. The Al<sub>2</sub>O<sub>3</sub>/MoS<sub>2</sub>/GaN photodetector showed over two-fold increase in the photoresponsivity, EQE, and photogain than that of MoS<sub>2</sub>/GaN photodetector where EQE and photogain values increased from 3848% to 8381% and 239 to 520, respectively.

Indium selenide (InSe) is a well-known photodetector.<sup>352a–d</sup> The MoS<sub>2</sub> QDs decorated indium selenide (InSe) nanosheets were applied to develop hybrid phototransistors which yielded the photoresponsivity of  $9.304 \times 10^3$  A W<sup>-1</sup>, three orders ( $10^3$ ) of magnitude higher than that of InSe photodetector ( $12.3$  A W<sup>-1</sup>).<sup>336</sup> The higher photoresponsivity of hybrid photodetector originated from the MoS<sub>2</sub> QDs injected photoexcited carriers to the InSe phototransistor. Ulaganathan *et al.*<sup>353</sup> decorated MoS<sub>2</sub> quantum dots (QDs) with InSe nanosheets to develop hybrid phototransistors. The MoS<sub>2</sub>/InSe-FET showed photoresponsivity of  $9304$  A W<sup>-1</sup> under illumination at 488 nm at source–drain voltage ( $V_{ds}$ ) = 1 V and gate voltage ( $V_g$ ) = 0 V, which was  $10^5$  times higher compared to InSe based photodetector ( $0.101$  A W<sup>-1</sup> at 532 nm) and nearly 10 times higher compared to 2D-graphene/2D-InSe hybrid photodetector ( $940$  A W<sup>-1</sup> at 532 nm).<sup>352d</sup> Here again, the higher photoresponsivity of MoS<sub>2</sub>/InSe hybrid photodetectors originated due to the transfer of photogenerated charge carriers from MoS<sub>2</sub> QDs to the InSe nanosheets.  $\beta$ -In<sub>2</sub>Se<sub>3</sub> is a group IIIA–VIA atomic layered



semiconducting material having a small bandgap, which has been used for developing  $\text{MoS}_2$  hybrid photodetectors. The few layer  $\beta\text{-In}_2\text{Se}_3$  thin films were epitaxially grown on the top of CVD- $\text{MoS}_2$  monolayers by Mahapatra *et al.*<sup>354</sup> The  $\beta\text{-In}_2\text{Se}_3/\text{MoS}_2$  vdW heterostructure-based photodetectors showed significantly higher photoresponse than that of pure  $\beta\text{-In}_2\text{Se}_3$  photodetectors. The photocurrent of  $\text{In}_2\text{Se}_3/\text{MoS}_2$  hybrid-based devices was found to be  $1.3 \times 10^3$  times higher compared with the dark current at 532 nm under laser power of 8.47  $\mu\text{W}$  and the EQE value reached  $5.49 \times 10^3\%$  under laser power of 4  $\text{mW cm}^{-2}$  with applied bias.

Silicon<sup>355</sup> has been widely used for developing broadband hybrid photodetectors for communication technology. Guo *et al.*<sup>356</sup> used  $\text{MoS}_2/\text{Si}$  heterostructure to fabricate a photodetector showing photoresponsivity of  $746 \text{ mA W}^{-1}$  and detectivity of  $6.03 \times 10^{11}$  Jones and response/recovery time of  $178 \mu\text{s}/198 \mu\text{s}$  in the 405 to 980 nm range. In another study, multilayer  $\text{MoS}_2$  films were deposited on Si quantum dots (Si QDs) to develop heterojunction photodetectors which showed much faster response/recovery time of 60 ns/756 ns and detectivity of  $6.1 \times 10^{13}$  Jones.<sup>357</sup> Au nanostructure-based plasmonic-enhanced multilayer  $\text{MoS}_2$  photodetector deposited on p-type Si substrate exhibited photoresponsivity of  $\sim 37 \text{ A W}^{-1}$  and detectivity of  $\sim 10^{12}$  Jones in 405–780 nm wavelength range.<sup>358</sup> The photoresponsivity of the Au plasmonic-enhanced  $\text{MoS}_2/\text{Si}$  photodetector was enhanced by 8.0, 5.3 and 11 times at 405 nm, 650 nm and 780 nm under 5 V bias, respectively, compared to the pristine p-Si photodetector. The Au plasmonic-enhanced  $\text{MoS}_2/\text{Si}$  photodetector also displayed a fast response time of 1  $\mu\text{s}$  and a recovery time of 18  $\mu\text{s}$ .

The 2D  $\text{MoS}_2/1\text{D ZnO}$  heterostructure-based photodetectors have been developed to increase the light absorption range and photoresponsivity.<sup>360</sup> The dark current of p- $\text{MoS}_2/\text{n-ZnO}$  heterostructure was measured as 0.88 nA which increased significantly to 103.1 nA and 2.52 nA at 365 nm (light intensity of 112  $\text{mW cm}^{-2}$ ) and 532 nm (64  $\text{mW cm}^{-2}$ ) under +5 V of applied voltage, respectively, demonstrating high sensitivity to UV and visible illuminations. The current  $I_{\text{on}}/I_{\text{off}}$  ratio was found to be 109 at 365 nm and 3.3 at 532 nm. The n- $\text{MoS}_2/\text{n-ZnO}$  photodetectors showed the photocurrents of 33.6 nA to 88.2 nA and 0.3 nA to 1.86 nA at 365 nm (5.7 to 47.2  $\text{mW cm}^{-2}$ ) and at 532 nm (0.525 to 56.7  $\text{mW cm}^{-2}$ ), respectively. The p- $\text{MoS}_2/\text{n-ZnO}$  photodetectors showed photoresponsivity of  $24.36 \text{ A W}^{-1}$  and EQE of  $8.28 \times 10^3\%$  under 365 nm light illumination.

Semimetal cadmium arsenide ( $\text{Cd}_3\text{As}_2$ ) has been used for fabricating broadband photodetectors due to its higher mobility as well as high absorption of light in a broad spectral region.<sup>361</sup>  $\text{Cd}_3\text{As}_2$  nanoplates have been integrated with multilayer  $\text{MoS}_2$  to develop a heterojunction photodetector which yielded high photoresponsivity of  $2.7 \times 10^3 \text{ A W}^{-1}$  at room temperature.<sup>362</sup> Likely, CdSe nanoplates were vertically assembled on  $\text{MoS}_2$  monolayer to develop vertical  $\text{CdSe}/\text{MoS}_2$  heterostructures.<sup>363</sup> CdSe/ $\text{MoS}_2$  heterostructure-based photodetector exhibited photoresponsivity of  $1.63 \text{ A W}^{-1}$  and fast response speed of 370  $\mu\text{s}$ . In another study, 2D  $\text{MoS}_2$  nanosheet and 0D CdSe nanocrystal-based hybrid phototransistor were developed which showed substantially enhanced photoresponsivity of 2.5

$\times 10^5 \text{ A W}^{-1}$  and the rise/fall times of 60 ms.<sup>323</sup> The photocurrent of  $\text{MoS}_2/\text{CdSe}$  hybrid photodetector increased with increasing laser power intensities at 405 nm. Ghosh *et al.*<sup>364</sup> developed photodetectors using a nanocomposite of single flake  $\text{MoS}_2$  and lanthanide doped upconversion nanoparticles (UCNPs). The  $\text{MoS}_2/\text{UCNPs}$  based photodetector showed highest photoresponsivity of  $1254 \text{ A W}^{-1}$ , detectivity of  $1.05 \times 10^{15}$  Jones and a gain of  $7.12 \times 10^{-4} \text{ cm}^2 \text{ V}^{-1}$  at 980 nm for 1.0 V bias. The highest detectivity of  $9.0 \times 10^{13}$  Jones at 405 nm and the lowest detectivity of  $3.4 \times 10^{13}$  Jones at 808 nm was observed for  $\text{MoS}_2/\text{UCNPs}$  devices. Likely,  $\text{MoS}_2/\text{UCNPs}$  photodetectors showed the highest normalized gain ( $\Gamma_n$ ) of  $1.48 \times 10^{-4} \text{ cm}^2 \text{ V}^{-1}$  at 405 nm and the lowest  $\Gamma_n$  of  $2.8 \times 10^{-5} \text{ cm}^2 \text{ V}^{-1}$  at 808 nm laser wavelength, which is an order of magnitude higher compared with those reported for  $\text{MoS}_2$  monolayer ( $\Gamma_n = 4.8 \times 10^{-6} \text{ cm}^2 \text{ V}^{-1}$ ).<sup>171</sup> Multilayer  $\text{MoS}_2$  films on monocrystalline SiC substrate using CVD were deposited by Xiao *et al.*<sup>365</sup>  $\text{MoS}_2/\text{SiC}$  hybrid photodetector showed photoresponsivity of  $5.7 \text{ A W}^{-1}$  at 365 nm under 4.35  $\mu\text{W}$  incident light power. Instead of Si, Wu *et al.*<sup>366</sup> used Si nanowire arrays (SiNWA) with few-layer  $\text{MoS}_2$  films to enhanced light absorption region of photodetectors. The dark current of the  $\text{MoS}_2/\text{SiNWA}$  photodetector was found to be much lower compared with  $\text{MoS}_2/\text{bulk Si}$  photodetector; contrary to this, the photocurrent of the  $\text{MoS}_2/\text{SiNWA}$  photodetectors was much increased than that of the  $\text{MoS}_2/\text{bulk Si}$  photodetector due to the increased light absorption and contact area between  $\text{MoS}_2$  and Si. The  $I_{\text{on}}/I_{\text{off}}$  current ratio of  $\text{MoS}_2/\text{SiNWA}$  photodetectors varied from  $3.2 \times 10^2$  to  $1.1 \times 10^5$  as the light intensity changed from  $0.031 \text{ mW cm}^{-2}$  to  $32 \text{ mW cm}^{-2}$  under zero bias at 650 nm. The  $\text{MoS}_2/\text{SiNWA}$  heterojunction-based photodetector showed photoresponsivity of  $53.5 \text{ A W}^{-1}$ , and detectivity of  $2.8 \times 10^{13}$  Jones under laser power intensity of  $6.3 \mu\text{W cm}^{-2}$ , much higher than that of  $\text{MoS}_2/\text{bulk Si}$  photodetector.<sup>311–313</sup> The rise/fall times of photodetectors was found to decrease with increasing light intensity where the rise times varied from 54.2, 27.7, 23.5 to 22.8  $\mu\text{s}$ , and fall times from 69.9, 68.6, 67.4 to 61.5  $\mu\text{s}$  under laser power intensity of 2.5, 16.8, 24.5 and  $38.6 \text{ mW cm}^{-2}$ , respectively.

Organic/inorganic hybrid halide perovskite ( $\text{C}_6\text{H}_5\text{C}_2\text{H}_4\text{-NH}_3)_2\text{PbI}_4$  =  $(\text{PEA})_2\text{PbI}_4$  with ML  $\text{MoS}_2$  has been used to develop hybrid photodetectors by Wang *et al.*<sup>367</sup>  $(\text{PEA})_2\text{PbI}_4$  functions as an electron reservoir to decrease free charge carriers as well as a to passivate defects. The dark current was reduced by six orders of magnitude by depositing  $(\text{PEA})_2\text{PbI}_4$  thin film over  $\text{MoS}_2$  photodetector due to the charge transfer from ML  $\text{MoS}_2$  to  $(\text{PEA})_2\text{PbI}_4$  thin film. The use of  $(\text{PEA})_2\text{PbI}_4$  over ML  $\text{MoS}_2$  reduced the charge carrier density which yielded a broadband photodetector (200 to 900 nm) exhibiting photoresponsivity of  $16.8 \text{ A W}^{-1}$ , detectivity of  $1.06 \times 10^{13}$  Jones, EQE of  $3.3 \times 10^3$  and on/off ratio of  $10^5$ . The photoresponse speed of a hybrid photodetector was enhanced over 100-times that of a pristine  $\text{MoS}_2$  photodetector due to  $(\text{PEA})_2\text{PbI}_4$  passivation.  $(\text{PEA})_2\text{PbI}_4/\text{MoS}_2$  hybrid photodetectors also work at 0 V bias, which is a self-powered mode where photocurrent showed an increase with increasing laser power intensity from 2.8 nW to 109.8 nW and the rise/decay times of 38 ms/24 ms under 637 nm laser



wavelength. Shen *et al.*<sup>368</sup> synthesized a series of helicene 5,14-diaryldiindeno[2,1-f;1',2'-j]picene (DDP) derivatives namely 5,14-dimesityldiindeno[2,1-f;1',2'-j]picene (1ab), 5,14-bis(2,4,6-trimethoxyphenyl)diindeno[2,1-f;1',2'-j]picene (1ac), and 9,10-dimethyl-5,14-dimesityldiindeno[2,1-f;1',2'-j]picene (1bb) and integrated with monolayer MoS<sub>2</sub> to develop hybrid photodetectors. Time-resolved measurements showed the interfacial charge-transfer from the DDP derivative to the monolayer MoS<sub>2</sub> confirmed by the stability of exciton property of the (1ac)/MoS<sub>2</sub> organics/inorganic hybrid heterostructure. The 1ac/MoS<sub>2</sub> hybrid based photodetector showed high photoresponsivity of  $4.99 \times 10^7$  A W<sup>-1</sup> and response time of 45 ms at 633 nm using laser light intensity of 5.75 nW under  $V_d = 5$  V and  $V_g = 0$  V because of the efficient separation of photoexcited carriers and the alignment of type-II energy band. The photoresponsivity of the organic/inorganic hybrid photodetectors followed the sequence of (1ac)/MoS<sub>2</sub> > (1ab)/MoS<sub>2</sub> > (1bb)/MoS<sub>2</sub> as a function of light intensity and after storing for one month. Furthermore, 1ac/MoS<sub>2</sub> hybrid photodetector did not exhibit any degradation after one-month storage. MoS<sub>2</sub> hybrid heterostructure-based photodetectors have been mainly studied having a type II band alignment.

The MoS<sub>2</sub> atomic layers were also prepared by different methods. Kumar *et al.*<sup>369</sup> developed large-area MoS<sub>2</sub> layers using pulsed laser deposition (PLD) method which showed photoresponsivity of  $3 \times 10^4$  A W<sup>-1</sup> and detectivity of  $1.81 \times 10^{14}$  Jones at 365 nm under 24  $\mu$ W cm<sup>-2</sup> incident light power at applied bias of 2.0 V. The photoresponsivity of the PLD-grown few-layer MoS<sub>2</sub> photodetectors was found to be  $3 \times 10^4$ ,  $1.08 \times 10^4$ ,  $7.0 \times 10^3$ , and  $6.3 \times 10^3$  A W<sup>-1</sup> at 365, 436, 546, and 655 nm wavelengths under applied bias of 2 V, respectively. FL-MoS<sub>2</sub> photodetectors also showed low dark current of  $10^{-10}$  A and photoresponse of  $1.37 \times 10^5$ . Schneider *et al.*<sup>370</sup> used metalorganic vapor-phase epitaxy (MOVPE) method to develop FL MoS<sub>2</sub> based flexible photodetectors. The photoresponsivity and specific detectivity of MoS<sub>2</sub> photodetectors can be changed between  $150$  A W<sup>-1</sup> to  $920$  A W<sup>-1</sup> and  $10^{12}$  Jones to  $10^{10}$  Jones by using electrostatic gating, respectively.

Singh *et al.*<sup>371</sup> reported Pd/Al<sub>2</sub>O<sub>3</sub>/MoS<sub>2</sub>/ITO photodetector showing photoresponsivity of  $488$  A W<sup>-1</sup>, detectivity of  $8.22 \times 10^{12}$  Jones and EQE of  $1.9 \times 10^{5}\%$  at 308 nm wavelength under laser light intensity of  $13.6$   $\mu$ W/cm<sup>2</sup> with 1 V applied bias voltage. Ye *et al.*<sup>372</sup> demonstrated vertical growth of Sb<sub>2</sub>O<sub>3</sub> flakes on monolayer MoS<sub>2</sub> crystals by using CVD technique. The Sb<sub>2</sub>O<sub>3</sub> flakes of different thickness and size covered monolayer MoS<sub>2</sub> crystals in 10, 21, 44, 54 and 100% ratio and their based back-gated FETs fabricated on SiO<sub>2</sub>/Si wafer affected the carrier mobility and subthreshold swing (SS) of the Sb<sub>2</sub>O<sub>3</sub>/MoS<sub>2</sub> hybrid photodetectors. The photocurrent, photoresponsivity, detectivity, sensitivity and EQE of hybrid FETs were measured as a function of laser power intensity under 360, 457, 532, 671, 914, and 1064 nm light illuminations. The hybrid FET-21% exhibited photocurrents of 263 and  $2.5$   $\mu$ A at laser power intensities of 177 and  $11$  mW cm<sup>-2</sup> under 360 and 1064 nm laser illuminations, respectively. The photoresponsivity of  $5.3 \times 10^4$  A W<sup>-1</sup> and detectivity of  $2.0 \times 10^{15}$  Jones were measured at 457 nm wavelength whereas in the NIR region, Sb<sub>2</sub>O<sub>3</sub>/MoS<sub>2</sub> hybrid

photodetectors showed photoresponsivity of  $7.8$  A W<sup>-1</sup>, detectivity of  $3.4 \times 10^{11}$  Jones, and response speed of  $<60$  ms with 1064 nm laser wavelength at room temperature. Sb<sub>2</sub>O<sub>3</sub>/MoS<sub>2</sub> hybrid photodetectors (FET-21%) showed photoresponsivity of  $1.1 \times 10^4$  A W<sup>-1</sup> and detectivity of  $4.5 \times 10^{14}$  Jones under 360 nm laser wavelength. The hybrid FET-21% also showed sensitivity values of  $6 \times 10^2$ ,  $2.5 \times 10^3$ ,  $3 \times 10^3$ ,  $2.4 \times 10^3$ ,  $0.2$ , and  $0.5$  cm<sup>2</sup> W<sup>-1</sup> and EQE values of  $4.0 \times 10^6$ ,  $1.4 \times 10^4$ ,  $1.0 \times 10^4$ , and  $5.5 \times 10^3$ ,  $0.4$ , and  $0.9\%$  under laser illuminations of 360, 457, 532, 671, 914, and 1064 nm, respectively. Higher photoresponse has been observed in 2D metal NiTe<sub>2</sub> and semiconductor MoS<sub>2</sub> heterostructure-based back-gated FETs and photodetectors compared to a pristine MoS<sub>2</sub> monolayer.<sup>373</sup> As discussed earlier, that the MoS<sub>2</sub> vdWH-based photodetectors show great promise for practical applications, therefore, new vdW heterostructures have been targeted. The NiTe<sub>2</sub>/MoS<sub>2</sub> vdW heterostructure-based photodetectors showed several times faster rise/decay times than that of a MoS<sub>2</sub> photodetector due to the epitaxial grown metallic vdWHs. Photodetectors were also developed from the WSe<sub>2</sub> and MoS<sub>2</sub> vdWHs where MoS<sub>2</sub> was used as a channel in the phototransistor.<sup>374</sup> The MoS<sub>2</sub> vdWH-based phototransistor showed high photoresponsivity of  $2700$  A W<sup>-1</sup>, detectivity of  $5 \times 10^{11}$  Jones, and response speed of 17 ms. In these phototransistors, the vertical built-in electric field in the WSe<sub>2</sub>-MoS<sub>2</sub> p-n junction separated the photoexcited charge carriers, which yielded a photoconductive gain of  $10^6$ . Ying *et al.*<sup>375</sup> fabricated BaTiO<sub>3</sub>/MoS<sub>2</sub> heterostructure-based photodetectors with type I band alignment which showed photoresponsivity of  $120$  A W<sup>-1</sup> and EQE of  $4.78 \times 10^{4}\%$  compared with  $1.7$  A W<sup>-1</sup> and  $4.5 \times 10^{2}\%$  for the bare MoS<sub>2</sub> at 365 nm under low laser power intensity of  $0.095$  mW cm<sup>-2</sup>. Both micro-Raman spectroscopy and photoluminescence indicated the occurrence of carrier extraction and carrier injection processes in the MoS<sub>2</sub> layer, leading to the boosting of the number of carriers in the MoS<sub>2</sub> channel. The high performance of type-I hybrid heterostructure-based photodetectors originated from the carrier extraction process between BaTiO<sub>3</sub> NPs and MoS<sub>2</sub> layer.

## 5.6 MoS<sub>2</sub> nanoscrolls

MoS<sub>2</sub> nanoscrolls have been prepared by argon plasma treatment of monolayer MoS<sub>2</sub> nanosheet where the MoS<sub>2</sub> nanoscroll formation also results in a partial removal of sulfur atoms from the top sulfur layer in MoS<sub>2</sub>.<sup>376</sup> The luminescent MoS<sub>2</sub> nanoscrolls have also been prepared by the supercritical fluid processing method. The exfoliated MoS<sub>2</sub> nanoscrolls showed photoluminescence from 420 to 600 nm due to the size reduction and polydispersity.<sup>377</sup> The 1D MoS<sub>2</sub> nanoscrolls have been prepared from CVD-grown triangular MoS<sub>2</sub> nanosheets where the formation of a MoS<sub>2</sub> nanoscroll takes place from the edge of a triangular nanosheet along the armchair orientation of MoS<sub>2</sub>.<sup>378</sup> The carrier mobility as well as physical contact properties of 1D MoS<sub>2</sub> nanoscroll-based FETs were found to be quite different than that of 2D MoS<sub>2</sub> nanosheets. The 2D semiconductor MoS<sub>2</sub> nanosheets can be transformed into 1D metallic MoS<sub>2</sub> nanoscrolls. This demonstrated that 1D TMD-



based nanoscrolls with unique chemical, physical and electrical properties can be fabricated.

The photodetectors fabricated using  $\text{MoS}_2$  or  $\text{WS}_2$  nanoscroll were compared with monolayer  $\text{MoS}_2$  or  $\text{WS}_2$  photodetectors.<sup>379</sup>  $\text{MoS}_2$  or  $\text{WS}_2$  nanoscroll-based devices showed photosensitivity enhancement by two orders of magnitude, demonstrating the potential of 2D TMD-based 1D nanoscrolls in optoelectronic applications. 1D  $\text{MoS}_2$  and  $\text{WS}_2$  nanoscroll-based photodetectors exhibited very high photocurrent-to-dark-current ratio compared with 2D nanosheet-based photodetectors. Deng *et al.*<sup>380</sup> prepared  $\text{MoS}_2$  nanoscroll-based photodetectors using the avalanche multiplication effect where a low triggering electrical field is required than that of  $\text{MoS}_2$  atomic layers. Fig. 25(a–c) shows schematic illustration of  $\text{MoS}_2$  nanoscroll-based avalanche photodetectors having  $\text{MoS}_2$  nanoscroll channel (area of  $1.8 \mu\text{m}^2$ ) connected with source and drain metal electrodes, photoresponsivity and detectivity as a function of applied bias voltage ( $V_{\text{ds}}$ ) under 532 nm laser illumination. Self-assembled  $\text{MoS}_2$  nanoscrolls were prepared using ethanol droplet and by rolling the monolayer  $\text{MoS}_2$  flake. The doped silicon film was used as the substrate as well as a gate electrode. A  $\text{MoS}_2$  nanoscroll is formed under strain compared with a monolayer  $\text{MoS}_2$  flake, therefore, an analysis of the  $\text{MoS}_2$  bandgap was carried out under applied tensile strain. As the uniaxial tensile strain was increased from 0% to 3% for the

monolayer  $\text{MoS}_2$  flake, the bandgap of  $\text{MoS}_2$  decreased from 1.77 to 1.5 eV, associated to a decrease in avalanche critical electric field ( $E_{\text{ava}}$ ) in  $\text{MoS}_2$  nanoscrolls. The avalanche multiplication effect was noticed in  $\text{MoS}_2$  nanoscrolls which also showed high multiplication factor and impact ionization coefficient. The excess noise factor was measured as a function of the multiplication factor. The multiplication factor of 40 was recorded at  $V_{\text{ds}}$  of 45 V which depended on the applied electric field. The avalanche gain of 24 was also measured at  $V_{\text{ds}} = 45$  V for the  $\text{MoS}_2$  nanoscroll-based devices. The electrical field ( $E_{\text{ava}}$ ) to trigger avalanche multiplication in  $\text{MoS}_2$  nanoscrolls was found to be dramatically decreased compared with monolayer  $\text{MoS}_2$  flakes. The decrease of  $E_{\text{ava}}$  in  $\text{MoS}_2$  nanoscrolls was associated with several factors including reduced bandgap, substrate contacts and phonons suppressed scattering of the free carriers. The decrease in bandgap of  $\text{MoS}_2$  nanoscroll was also evidenced by a red-shift compared with the monolayer  $\text{MoS}_2$  flake.  $\text{MoS}_2$  nanoscroll-based photodetectors exhibiting photoresponsivity over  $10^4 \text{ A W}^{-1}$ , detectivity of  $2 \times 10^{12}$  Jones and 30 times higher avalanche gain compared with monolayer  $\text{MoS}_2$  flake. This study showed low-power consumption  $\text{MoS}_2$  nanoscroll-based photodetections where avalanche multiplication effect enhanced the photoresponsivity in  $\text{MoS}_2$  nanoscrolls compared with atomically thin monolayer  $\text{MoS}_2$ . Deng *et al.*<sup>381</sup> reported photodiodes having p-type  $\text{WSe}_2$  and single  $\text{MoS}_2$

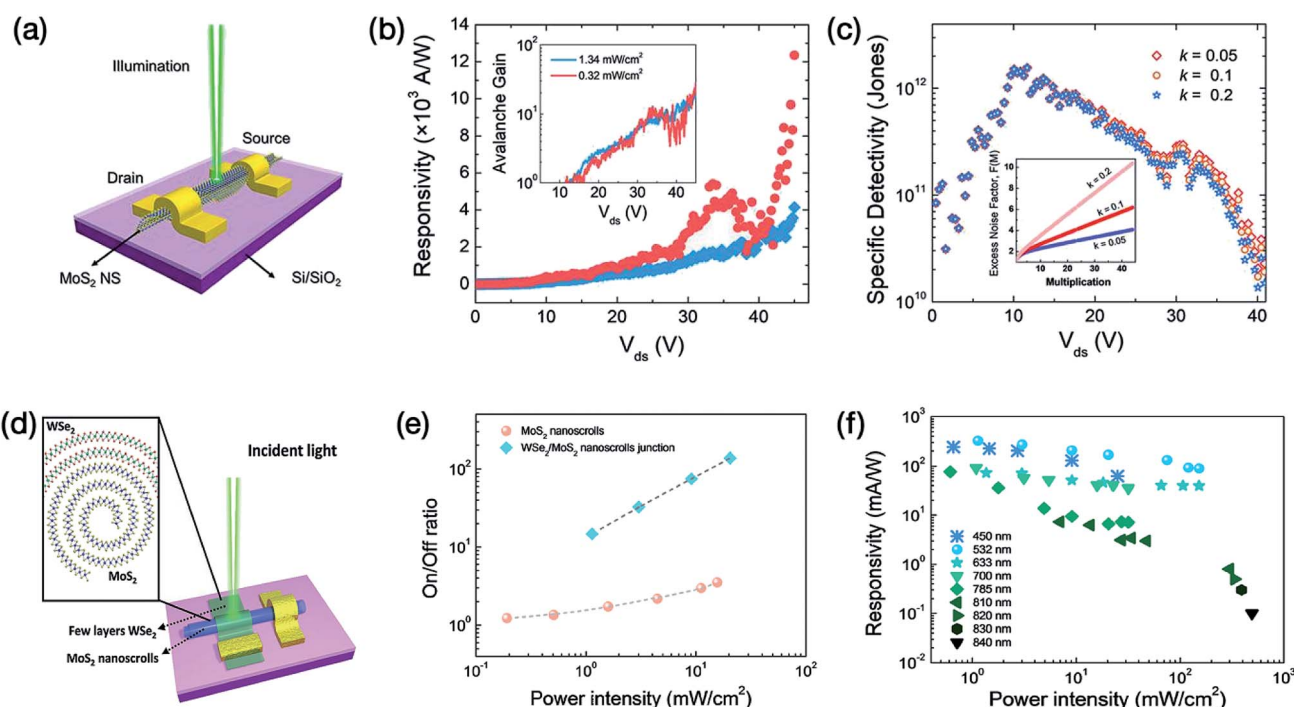


Fig. 25 (a) Schematic illustration of  $\text{MoS}_2$  nanoscroll-based avalanche photodetector under illumination. (b) Photoresponsivity of the avalanche photodetector as a function of applied bias voltage ( $V_{\text{ds}}$ ) under 532 nm laser illumination at different incident light power intensities. Inset shows the  $V_{\text{ds}}$  dependent avalanche gain. (c) Specific detectivity of the avalanche photodetector as a function of  $V_{\text{ds}}$ . The inset is a plot of excess noise factor as a function of the multiplication factor. Reprinted with permission from ref. 380, copyright © American Chemical Society. (d) Schematic illustration of the  $\text{WSe}_2/\text{MoS}_2$  nanoscroll-based photodiode along with the cross-section of the heterojunction containing  $\text{MoS}_2$  nanoscrolls and few layers  $\text{WSe}_2$  where electrodes are source and drain, respectively. (e) The current  $I_{\text{on}}/I_{\text{off}}$  ratio of single  $\text{MoS}_2$  nanoscroll and  $\text{WSe}_2/\text{MoS}_2$  nanoscroll-based heterojunction as a function of incident power intensity at 532 nm wavelength. (f) Photoresponsivity of the  $\text{WSe}_2/\text{MoS}_2$  nanoscroll-based hybrid photodetectors as a function of incident laser power intensity at different wavelengths, showing broadband photodetection by the hybrid heterostructure photodiode. Reprinted with permission from ref. 381, copyright © Wiley.



nanoscrolls which showed suppressed dark current and two orders of magnitude increase in the ratio of photocurrent to dark current compared with a single  $\text{MoS}_2$  nanoscroll-based photodiode. Fig. 25(d-f) shows schematic illustration of the  $\text{WSe}_2/\text{MoS}_2$  nanoscroll-based photodiode, incident power intensity dependent current  $I_{\text{on}}/I_{\text{off}}$  ratio of single  $\text{MoS}_2$  nanoscroll and  $\text{WSe}_2/\text{MoS}_2$  nanoscroll-based heterojunction and photoresponsivity of the  $\text{WSe}_2/\text{MoS}_2$  nanoscroll-based hybrid photodetector as a function of incident power intensity. The response speed of  $\text{WSe}_2/\text{MoS}_2$  nanoscroll-based device increased by three orders of magnitude than that of a single  $\text{MoS}_2$  nanoscroll device. The  $\text{WSe}_2/\text{MoS}_2$  nanoscroll-based photodetectors exhibited the photoresponsivity of  $0.3 \text{ A W}^{-1}$ , EQE values of 25% at zero bias voltage and 75% at a reverse bias of 1 V at 532 nm under laser power intensity of  $1.14 \text{ mW cm}^{-2}$  and response speed of 5 ms with laser power intensity of  $60 \text{ mW cm}^{-2}$ . The atomic layered  $\text{WSe}_2/\text{MoS}_2$  nanoscrolls were found to be superior to those of  $\text{MoS}_2$  nanoscrolls. Wang *et al.*<sup>382</sup> developed  $\text{WS}_2/\text{MoS}_2$  vdWH-based nanoscrolls by dropping aqueous alkaline droplets on CVD-grown BL  $\text{WS}_2/\text{MoS}_2$  vdW hybrid heterostructure, which were prepared by growing 1L  $\text{WS}_2$  islands on top of 1LMoS<sub>2</sub> nanosheets. The optical microscopy, AFM, ultralow frequency (ULF) Raman spectroscopy and TEM techniques were used to characterize the  $\text{WS}_2/\text{MoS}_2$  vdWH-based nanoscrolls and ULF breathing and shear mode peaks were observed which originated from the strong interlayer interaction. The photosensitivity of  $\text{WS}_2/\text{MoS}_2$  nanoscroll-based photodetectors were found to be ten times higher compared with  $\text{WS}_2/\text{MoS}_2$  vdWH-based photodetectors under blue, green and red laser illuminating lights; the ultrafast charge transfer process occurring in nanoscrollled structure at alternative  $\text{WS}_2/\text{MoS}_2$  and  $\text{MoS}_2/\text{WS}_2$  multi-interfaces could be associated with such a high performance.

The research data collected on the figure-of-merit of  $\text{MoS}_2$  based photodetectors have been extensively documented. Tremendous interest is growing in the field of  $\text{MoS}_2$  based photodetectors as new research ideas are emerging on a rapid pace.<sup>383-387</sup> Ahmed *et al.*<sup>388</sup> fabricated graphene/h-BN/MoS<sub>2</sub> tri-layer vdW heterostructure-based phototransistors to examine

the photogating mechanism where h-BN layer was used as an interfacial barrier to monitor the charge transfer process. Mechanically exfoliated monolayer graphene,  $\text{MoS}_2$  and multi-layer h-BN were used to fabricate the graphene/h-BN/MoS<sub>2</sub> vdW heterostructures on the  $\text{SiO}_2/(\text{p}^{++})\text{Si}$  substrate. All optoelectronic measurements were conducted at 180 K temperature under the high vacuum conditions. The incident power density dependent photoresponsivity, NEP and detectivity of vdW heterostructure-based photodetectors were measured from 640 nm to 1720 nm wavelength region. Fig. 26 shows the figure of merit of the graphene/h-BN/MoS<sub>2</sub> vdW heterostructure-based photodetectors. The photoresponsivity values of  $5 \times 10^9 \text{ A W}^{-1}$  in the visible region,  $2 \times 10^9 \text{ A W}^{-1}$  at 940 nm,  $10^8 \text{ A W}^{-1}$  at 1550 nm and  $2 \times 10^7 \text{ A W}^{-1}$  at 1720 nm were observed using source drain bias of 20 mV at low power density. The low NEP value of  $2 \times 10^{-20} \text{ W Hz}^{-1/2}$  at 940 nm was found to be further increased to  $2 \times 10^{-18} \text{ W Hz}^{-1/2}$  for 1720 nm. Being correlated to NEP, the high detectivity values of  $10^{16} \text{ Jones}$  at 640 nm,  $5 \times 10^{15} \text{ Jones}$  at 940 nm and  $5 \times 10^{13} \text{ Jones}$  at 1720 nm were deduced for the vdW hybrid photodetectors, which are two orders of magnitude higher compared to graphene-based IR photodetectors. The values of photoresponsivity, NEP and detectivity for vdWHs differ by several orders of magnitude as a function of laser power density at different measurement wavelengths. This study demonstrated that the defect states can strongly affect to the photoresponse of the graphene/h-BN/MoS<sub>2</sub> hybrid photodetectors. The strong photoresponse has been observed in  $\text{MoS}_2$  atomic layers when integrated with other vdW nanomaterials. As summarized in Table 1 and documented throughout this article,  $\text{MoS}_2$ -based photodetectors show photoresponsivity ranging from  $\text{mA W}^{-1}$  to  $10^{10} \text{ A W}^{-1}$ , detectivity from  $10^7$  to  $10^{15} \text{ Jones}$  and ultra-fast response speed up to nanoseconds ( $10^{-9} \text{ s}$ ), which varies by several orders of magnitude over an ultra-broadband spectral range from 265 nm to 10  $\mu\text{m}$  under different incident power densities. The performance of  $\text{MoS}_2$  photodetectors is derived from the design of  $\text{MoS}_2$  based phototransistors, photoconductors and photodiodes. Several different mechanisms including photoconductive, photovoltaic, photobolometric and surface plasma-wave

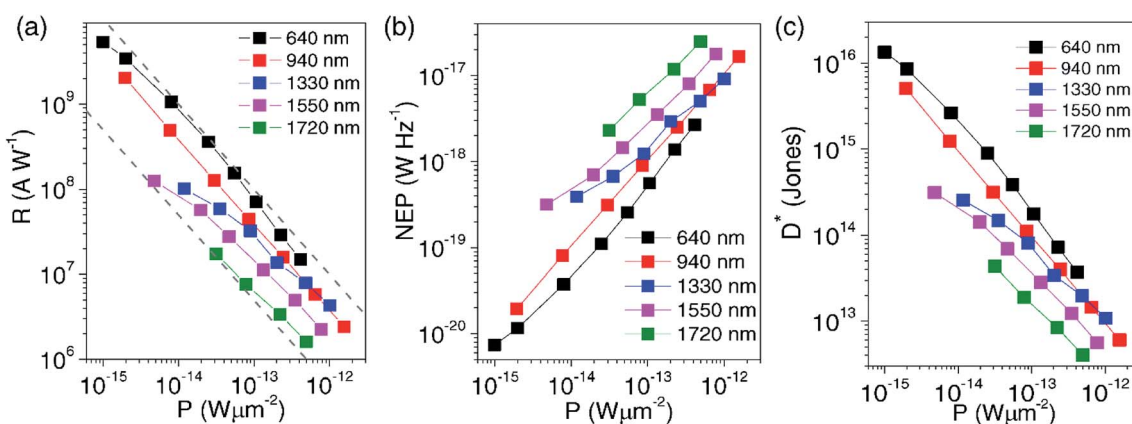


Fig. 26 Figure of merit of the graphene/h-BN/MoS<sub>2</sub> vdW heterostructure-based photodetectors. Plots of (a) photoresponsivity ( $R$ ), (b) noise equivalent power (NEP) and (c) specific detectivity ( $D^*$ ) as a function of incident power density ( $P$ ) in the 640 nm to 1720 nm wavelength region. Reprinted with permission from ref. 388, copyright © Institute of Physics Publishing.



enhanced effects contribute to the performance of  $\text{MoS}_2$  photodetectors. Abraham and Majumdar<sup>389</sup> analyzed the benchmarking and characterization protocol for photodetectors developed using various types of nanomaterials and pointed out that NEP is one of the most important sensitivity parameters for the figure of merit compared to the photoresponsivity and detectivity. The measurements of NEP as a function of modulation frequency of a photodetector could be used for a better comparison of the figure of merit of heterogeneous photodetectors. The photoresponsivity ( $R$ ) data were plotted as a function of modulation frequency ( $f$ ) and NEP for a wide variety of nanomaterial-based photodetectors. Photodetectors with vertical current transport were found to perform much better than photodetectors having lateral current transport as a function of modulation frequency with an exception of graphene-based photodetectors, which is associated with high carrier mobility. However, the measurements of photoresponsivity of these nanomaterials significantly vary depending upon the applied bias voltage and different intensity of laser power; therefore, an accurate comparison is rather convoluted. In the photoresponsivity *versus* NEP plot, the  $\text{MoS}_2$ -based photodetectors such as monolayer  $\text{MoS}_2$  phototransistors,<sup>171</sup> vertical  $\text{MoS}_2$  p-n junction,<sup>346</sup>  $\text{MoS}_2/\text{PbS}$ ,<sup>322</sup> graphene/WS<sub>2</sub>/ $\text{MoS}_2$ ,<sup>347</sup> etc., are in par with PbS-based photodetectors.<sup>390</sup> The plot of photoresponsivity *versus* NEP does not show an important correlation between these two parameters and the higher values of photoresponsivity does not inevitably lead to high sensitivity of photodetectors. High sensitivity of a photodetector can be achieved with a relatively low photoresponsivity by controlling the noise of photodetectors.

## 6. Strain-induced and self-powered $\text{MoS}_2$ photodetectors

Energy harvesting from piezoelectric materials such as ceramics, single crystals, organic polymers and their based hybrid composites has been investigated over many decades. The commonly known piezoelectric materials include lead zirconate titanate (PZT), barium titanate ( $\text{BaTiO}_3$ ), lithium niobate ( $\text{LiNbO}_3$ ), zinc oxide ( $\text{ZnO}$ ), quartz, polyvinylidene difluoride (PVDF), poly(vinylidene fluoride-trifluoroethylene) (VPF-TrFE), nylons, liquid crystal polymers, biomaterials, etc.<sup>391–398</sup> The piezoelectric, pyroelectric and ferroelectric materials offer capabilities of generating usable energy under applied mechanical strain, temperature, electric field, water, light, etc. therefore, have been integrated in energy harvesting devices for their applications in self-powering footwears, speakers and headphones, motors, batteries, sensors, actuators, catalysis, photovoltaics, optical memory devices, spintronics, robotics, triboluminescence, etc.<sup>399–402</sup> In addition to silicon, Ge, SiC,  $\text{ZnO}$ ,  $\text{TiO}_2$ , cement, polymers, diamond, and carbon nanotubes, the piezoresistive effects have been studied in 2D nanomaterials<sup>403–410</sup> for applications in piezoresistive strain/stress sensors. Black phosphorus (BP) has been used with  $\text{MoS}_2$  to develop BP/ $\text{MoS}_2$  vdW heterostructure-based photodetectors with a type-II band alignment.<sup>404</sup> The strain induced

piezoelectric effect was observed in BP and  $\text{MoS}_2$  vdW heterostructures.

Piezoelectric and pyroelectric generators have been developed using different types of inorganic and organic materials for their applications in optoelectronic and photonic devices. Kim *et al.*<sup>411</sup> reported piezoelectric effect in CVD-grown monolayer  $\text{MoS}_2$  films and fabricated direction-dependent flexible piezoelectric nanogenerators where the atomic orientation in monolayer  $\text{MoS}_2$  dictated the magnitude of the piezoelectric effect. The output power of nanogenerators (NG) was found to be two times higher for the armchair direction of  $\text{MoS}_2$  compared with zigzag direction of  $\text{MoS}_2$  under the same applied strain and the strain velocity. The armchair  $\text{MoS}_2$  showed piezoelectric coefficient  $d_{11}$  of  $3.78 \text{ pm V}^{-1}$  whereas the zigzag  $\text{MoS}_2$  exhibited much lower  $d_{11}$  value of  $1.38 \text{ pm V}^{-1}$ . The armchair  $\text{MoS}_2$  nanogenerator exhibited higher output voltage of 20 mV as well as the higher output current of 30 pA than that of 10 mV and 20 pA for the zigzag  $\text{MoS}_2$  nanogenerator, confirming the role of atomic orientation in enhancing piezoelectric effect in 1L  $\text{MoS}_2$  nanogenerators. Tsai *et al.*<sup>412</sup> reported piezoresistive effect in flexible  $\text{MoS}_2$  FETs which was associated with the strain-induced bandgap change as confirmed using optical reflection spectroscopy. The bandgap of the 3L  $\text{MoS}_2$  was found to decrease by 0.06 eV (from 1.58 eV to 1.52 eV) under 0.2% applied strain. The effects of both piezoelectricity and piezoresistivity on photoresponse of atomic layered  $\text{MoS}_2$  have been studied.

Strain-induced photodetection has been observed in  $\text{MoS}_2$  atomic layers and  $\text{MoS}_2$  based hybrid heterostructures. The monolayer  $\text{MoS}_2$  based photodetector showed photoresponsivity of  $2.3 \times 10^4 \text{ A W}^{-1}$  under a compressive strain of  $-0.38\%$  at low laser power intensity of  $3.4 \mu\text{W cm}^{-2}$  with 442 nm wavelength.<sup>264</sup> Gas sensitivity has been reported in 1L  $\text{MoS}_2$  *via* photogating and piezo-phototronic effects.<sup>413</sup> Monolayer  $\text{MoS}_2$  based flexible homogenous photodiode showed 619% and 319% enhancement in photoresponsivity and detectivity after applying 0.51% tensile strain, where the photoresponsivity and detectivity reached maximum values of  $1162 \text{ A W}^{-1}$  and  $1.72 \times 10^{12} \text{ Jones}$ , respectively, compared with a strain-free photodiode.<sup>414</sup> The in-plane anisotropic photoresponse has been reported in monolayer  $\text{MoS}_2$ .<sup>415</sup> The crystal symmetry of monolayer  $\text{MoS}_2$  was found to be reduced from  $D_{3h}$  to  $C_{2v}$  under applied uniaxial tensile strain. The absorption along the armchair direction of monolayer  $\text{MoS}_2$  was found to be two times higher compared to zigzag direction under 4.5% strain, which also increased with increasing strain, whereas the absorption along zigzag direction of monolayer  $\text{MoS}_2$  showed a slight change. The photoresponse of monolayer  $\text{MoS}_2$  changed from isotropic to anisotropic at 520 nm light illumination. The photoresponse was not observed in monolayer  $\text{MoS}_2$  devices until uniaxial tensile strain reached to a value of 3.5% and the anisotropic ratio higher than 2 was recorded under 4.5% uniaxial tensile strain at 520 nm and 830 nm wavelengths.

In another study, the photoresponsivity of flexible  $\text{MoS}_2/\text{WSe}_2$  heterojunction-based photodiodes increased by 86% under a static strain of  $-0.62\%$  when applied along the



armchair direction of  $\text{MoS}_2$  due to the piezoelectric effect.<sup>416</sup> Similar strain-induced photoresponse has been measured in  $\text{MoS}_2$  and  $\text{ZnO}$  p-n heterojunction photodiodes where photocurrent increased over four times under an applied pressure of 23 MPa.<sup>417</sup> The photoresponsivity of ML  $\text{MoS}_2/\text{GaN}$  heterojunction photodiodes was also enhanced by 3.5 times under 258 MPa applied pressure originating from strain-induced piezoelectric phenomenon.<sup>418</sup>

The effect of piezoresistivity on performance of  $\text{MoS}_2$  photodetectors has also been studied. Li *et al.*<sup>419</sup> reported piezoelectric and piezoresistive effects in a flexible CVD-grown monolayer  $\text{MoS}_2/\text{polyethylene naphthalate (PEN)}$  substrate-based photodetector. An enhancement of photoresponse such as light-dark current ratio from 29 to 1200.3 (41 times) at 1 V bias voltage and self-powered current from 25.2 to 213.6 pA (8.3 times) was observed in armchair direction monolayer  $\text{MoS}_2$  after applying 0.8% strain due to the piezoelectric effect. However, the photoresponsivity decreased from 163.9 to 95.7 A W<sup>-1</sup> under 0.8% applied strain at 5 V bias voltage. The photocurrent increased from 0.37 to 2.35  $\mu\text{A}$  and photoresponsivity from 114.3 to W to 590 A W<sup>-1</sup> in zigzag direction monolayer  $\text{MoS}_2$  under 1.4% applied strain at 5 V due to the piezoresistive effect. The zigzag direction monolayer  $\text{MoS}_2$  showed no piezoelectric effect. Kelvin probe force microscopy was used to analyze both piezoelectric and piezoresistive effects in monolayer  $\text{MoS}_2$ . Gant *et al.*<sup>420</sup> reported strain-induced increase in both photocurrent and photoresponsivity of flexible monolayer  $\text{MoS}_2$  photodetectors. The monolayer  $\text{MoS}_2$  based photodetector showed significant increase in photocurrent at 740 nm light illumination under incident power density of 5 mW cm<sup>-2</sup> with 5 V applied bias voltage when tensile biaxial strain was increased from 0.16% to 0.48%. In biaxially strained polycarbonate substrate-based flexible  $\text{MoS}_2$  photodetectors, the photoresponsivity increased 100 and 1000 times by increasing applied strains from -0.8% to 0.48% and from -1.44% to 0.48%, respectively.

2D material-based self-powered heterojunction photodetectors are also gaining much attention because no external power is required for the photodetection.<sup>421</sup> The self-powered p-MoTe<sub>2</sub>/n-MoS<sub>2</sub> vdWH-based photodetector having ITO electrodes showed photoresponsivity of 146 mA W<sup>-1</sup> and fast photoresponse of  $\sim$ 172  $\mu\text{s}$  from 450 nm to 980 nm.<sup>422</sup> The photodetector also exhibited bidirectional photocurrent response associated with type-II band aligned heterostructure and ITO electrodes. Yang *et al.*<sup>423</sup> used narrow bandgap layered semiconductor germanium selenide (GeSe) for developing hybrid photodetectors where photoconductive GeSe/graphene photodetectors were compared with photovoltaic GeSe/MoS<sub>2</sub> photodetectors. The photodetector based GeSe/graphene vdWHs showed higher photoresponsivity up to 10<sup>4</sup> A W<sup>-1</sup> under laser light intensity of 0.17 mW cm<sup>-2</sup> at 532 nm whereas the GeSe/MoS<sub>2</sub> heterostructure based photodetector exhibited low photoresponsivity of 0.1 A W<sup>-1</sup> but a faster recovery time of 5 ms compared with 2 s for GeSe/graphene heterostructure. GeSe/MoS<sub>2</sub> photodetector retained constant photoresponse under applied reverse bias because of the reduced carrier conduction within depletion region. Xin *et al.*<sup>424</sup> fabricated

polarization-sensitive self-powered photodetectors using type-II band aligned GeSe/MoS<sub>2</sub> vdWHs to increase photoresponse spectrum and support efficient separation as well as transportation of the photoexcited charge carriers. GeSe/MoS<sub>2</sub> p-n heterojunctions were developed using mechanically exfoliated GeSe and MoS<sub>2</sub> nanoflakes on p-doped Si substrate having a SiO<sub>2</sub> film of 300 nm thickness. Fig. 27(a-c) shows a type-II band aligned GeSe/MoS<sub>2</sub> p-n heterojunction photodetector with Ti/Au electrodes, and time-dependent photoresponse at different illumination wavelengths (UV-NIR region), and photoresponsivity and detectivity of the self-powered GeSe/MoS<sub>2</sub> heterojunction photodetectors as a function of wavelength from 380 to 1064 nm at  $V_{\text{ds}}$  of 0 V (zero bias). The self-powered GeSe/MoS<sub>2</sub> photodetector achieved  $I_{\text{on}}/I_{\text{off}}$  current ratio of 10<sup>4</sup> at zero bias, photoresponsivity of 105 mA W<sup>-1</sup> and EQE of 24.2%. GeSe/MoS<sub>2</sub> vdWH-based photodetectors showed photoresponse from 380 to 1064 nm and showed maximum photoresponsivity of 590 mA W<sup>-1</sup> at 532 nm wavelength. The photoresponsivity of the self-powered GeSe/MoS<sub>2</sub> p-n heterojunction photodetector varied from 6.1 mA W<sup>-1</sup> to 150 mA W<sup>-1</sup> while the detectivity remained at 10<sup>11</sup> Jones in the 380 nm to 1064 nm (UV-NIR) range. Photoresponse was also measured as a function of polarization angle from 0° to 360° where the current on/off ratios were found to be  $7.23 \times 10^3$ ,  $3.65 \times 10^4$ , and  $2.99 \times 10^3$  at 30°, 90° and 120° polarization angles under 532 nm light illumination with  $V_{\text{ds}}$  of 0 V, respectively. The highest photocurrent of  $-3.08 \times 10^{-10}$  A was recorded at 90° and 270° polarization angles corresponding to the armchair direction of GeSe which was also a parallel direction of the polarization, whereas the lowest photocurrent of  $-1.04 \times 10^{-10}$  A was measured at 0° and 180° polarization angles which corresponded to the zigzag direction of GeSe. The polarization-sensitive photodetection in the self-powered GeSe/MoS<sub>2</sub> photodetector was observed due to the absorption and anisotropic electronic transport associated with GeSe nanoflakes.

The perovskites have been used with  $\text{MoS}_2$  to develop organic/inorganic hybrid-based photodiode-solar cell bifunctional devices. Shin *et al.*<sup>425</sup> used MoS<sub>2</sub> as a hole transport layer (HTL) and graphene (GR) co-doped with AuNPs and (trifluoromethanesulfonyl)-amide (co-GR) as transparent conductive electrodes (TCE) to develop flexible p-i-n-type perovskite-based photodiode/solar cell bifunctional devices (PPSBs). Self-powered p-i-n-type PPSB devices were fabricated on both rigid glass and flexible PET substrates. Fig. 27(d-f) shows a diagram of p-i-n-type PPSB device consisting of Al/BCP/PCBM/MAPbI<sub>3</sub>/MoS<sub>2</sub>/co-GR; energy levels diagram, wavelength-dependent photoresponsivity and detectivity at 0 V bias (self-powered mode), current  $I_{\text{on}}/I_{\text{off}}$  switching curve at 500 nm and as a function of bending cycles. In the solar cell (photovoltaic) mode under 1 sun illumination (100 mW cm<sup>-2</sup>), the PPSB device on a glass substrate showed open-circuit voltage ( $V_{\text{oc}}$ ) of 0.88 V, the short circuit current density ( $J_{\text{sc}}$ ) of 19.97 mA cm<sup>-2</sup>, a fill factor (FF) of 74.46%, and power conversion efficiency (PCE) of 13.09%. PPSB device also operated without any external power (0 V bias), which is a self-powered mode. The current of the PPSB photodiode was found to increase 10<sup>6</sup> times under illumination in the self-powered mode



and the photocurrent rise/fall times ranged 0.7–0.9 s and 0.4–0.6 s, respectively. The PPSB photodiode (0 V bias) on a glass substrate showed current  $I_{on}/I_{off}$  ratio of 1310, 9580, 136 110, and 8; and photoresponsivities of 50, 309, 410, and 12 mA W $^{-1}$  at 300, 500, 700, and 800 nm, respectively. The noise equivalent power (NEP), detectivity, and linear dynamic range (LDR) were calculated as  $3.95 \times 10^{-12}$  W Hz $^{-1/2}$ ,  $7.99 \times 10^{10}$  Jones, and 117 dB, respectively. The flexible PPSB-based solar cell showed PCE of 11.91%. The flexible PPSBs also exhibited the similar photoresponse at 500 nm as glass substrate ones. The photoresponsivity and detectivity of the flexible PPSB device were measured between 350 nm to 750 nm where optimum values

reached at 0.39 A W $^{-1}$  and  $3.41 \times 10^{10}$  Jones, respectively. The same research group<sup>426</sup> also developed organic/inorganic perovskites/MoS<sub>2</sub> hybrid-based photodiode–solar cell nano-systems (PPSNs) using BL MoS<sub>2</sub> as the electron-transport layer (ETL) and triethylenetetramine-doped graphene (TETA-GR) as the transparent conductive electrode (TCE). The TETA-GR/MoS<sub>2</sub>/MAPbI<sub>3</sub>/PTAA/Au glass substrate-based rigid and PET substrate-based flexible PPSNs showed photoresponsivity of 0.42 and 0.40 A W $^{-1}$ , NEP of 37.2 and  $80.1$  pW Hz $^{-1/2}$ , detectivity of  $1.1 \times 10^{10}$  and  $5.0 \times 10^9$  Jones in the photodiode mode under zero bias (self-powered), respectively. The PPSNs exhibited the PCE value of 14.27% for rigid device and 12.12% for flexible

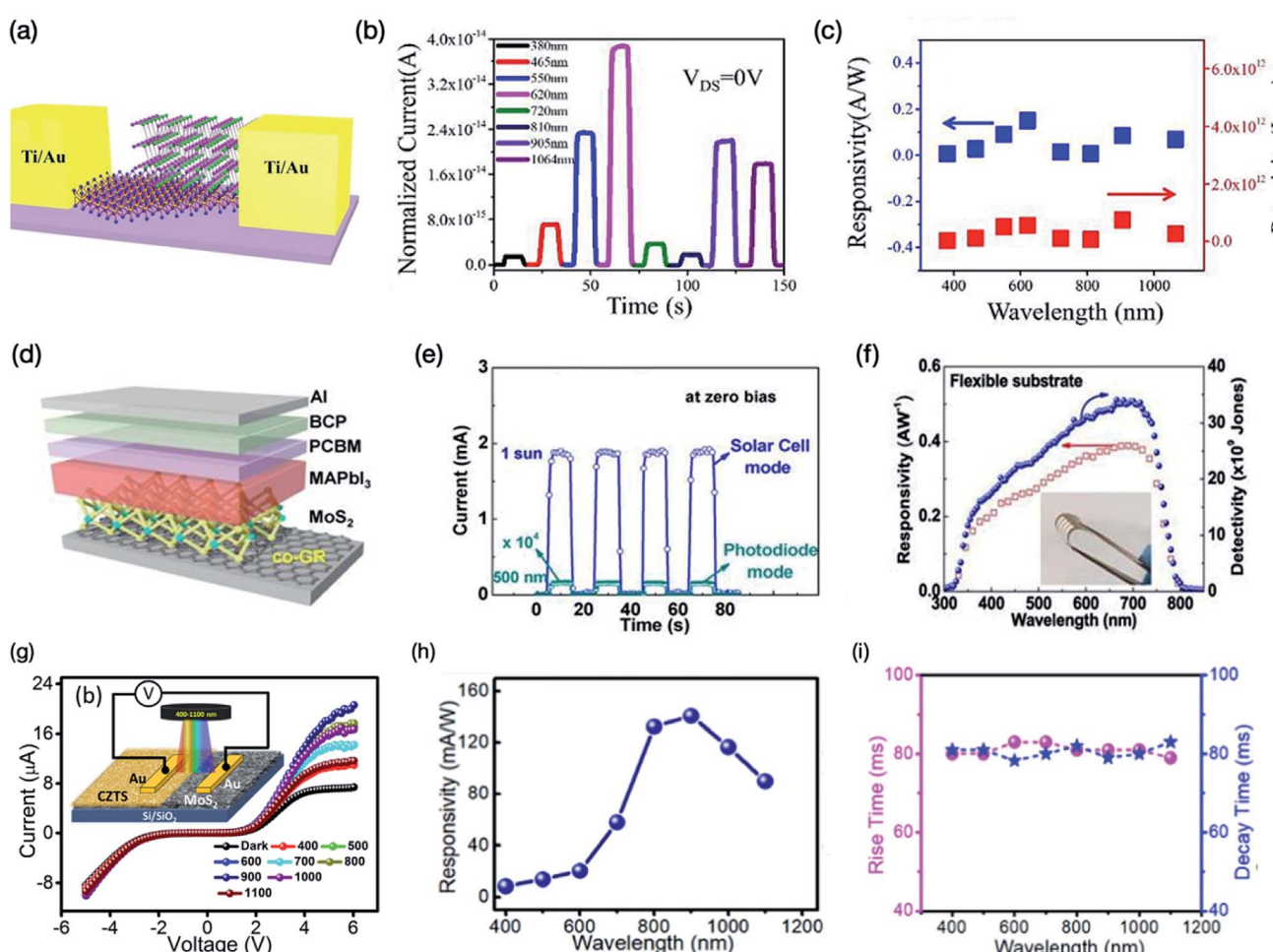


Fig. 27 (a) Schematic illustration of a type-II band aligned GeSe/MoS<sub>2</sub> p–n heterojunction photodetector having Ti/Au electrodes, separation of the photoexcited electrons–holes carriers and energy band diagram under 532 nm light illumination at  $V_{ds}$  of 0 V (zero bias). (b) Time-dependent photoresponse of the heterojunction photodetector under different illumination wavelengths at  $V_{ds}$  = 0 V. (c) Photoresponsivity and detectivity of the GeSe/MoS<sub>2</sub> heterojunction photodetectors as a function of wavelength. Reprinted with permission from ref. 424, copyright © American Chemical Society. (d) Schematic illustration of a self-powered MoS<sub>2</sub> photodetector based on p–i–n-type perovskite photodiode/solar cell bifunctional (PPSB) device consisting of Al/BCP/PCBM/MAPbI<sub>3</sub>/MoS<sub>2</sub>/co-GR; where BCP = bathocuproine, PCBM = phenyl-C<sub>61</sub>-butyric acid methyl ester, MAPbI<sub>3</sub> = methylammonium lead tri-iodide perovskite, co-GR = graphene electrode co-doped with AuNPs and (tri-fluoromethanesulfonyl)-amide. MoS<sub>2</sub> based flexible PPSB photodetector was fabricated using a PET substrate. (e) Current  $I_{on}/I_{off}$  switching behavior of flexible PPSB photodetectors at 500 nm at 0 V bias. (f) Wavelength-dependent photoresponsivity and detectivity of flexible photodetector recorded at 0 V bias, therefore in a self-powered mode. Inset is an optical image of a flexible self-powered PPSB photodetector. Reprinted with permission from ref. 425, copyright © Elsevier; (g) schematic illustration of CZTS/MoS<sub>2</sub> p–n heterojunction-based photodetector and current–voltage ( $I-V$ ) curves in the dark and at different laser wavelengths (400 nm to 1100 nm) under illumination. (h) Curve of photoresponsivity as a function of wavelength and (i) calculated rise/decay times of the self-powered CZTS/MoS<sub>2</sub> photodetector from 400 nm to 1100 nm wavelengths. Reprinted with permission from ref. 428, copyright © Elsevier.



PPSN device in the photovoltaic mode. PTAA refers to poly[bis(4-phenyl)(2,4,6-trimethylphenyl)amine] which is used as a hole transport material (HTM) in solar cells.

He *et al.*<sup>427</sup> developed broadband self-powered photodetectors using vertically-stacked multilayer GaSe/MoS<sub>2</sub> heterostructures where the thickness of GaSe and MoS<sub>2</sub> films was 6.3 nm ( $\approx 7$  L) and 6 nm ( $\approx 8$  L), respectively. Wavelength-dependent photoresponsivity, EQE, and detectivity of self-powered GaSe/MoS<sub>2</sub> hybrid heterostructure-based photodetectors were measured as a function of wavelength without bias voltage ( $V = 0$ ). The performance of photodetectors having ohmic-contact ITO electrodes were compared with Schottky-contact Ni/Au electrodes. The GaSe/MoS<sub>2</sub> heterostructure-based self-powered photodetectors covered visible to NIR spectral range. Self-powered photodetectors with ITO/GaSe/MoS<sub>2</sub>/ITO configuration showed a high rectification ratio of  $1.5 \times 10^4$  at  $V_{ds} = \pm 1$  V, EQE value of 160%, photoresponsivity of  $0.67 \text{ A W}^{-1}$ , and detectivity of  $2.3 \times 10^{11}$  Jones at 520 nm and four times faster response time than that of (Ni/Au)/GaSe/MoS<sub>2</sub>/(Ni/Au) photodetectors indicating the role of electrode-contact in influencing the performance of GaSe/MoS<sub>2</sub> hybrid photodetectors. The photoresponsivity of ITO/GaSe/MoS<sub>2</sub>/ITO photodetector was found to be very weak at 808 nm wavelength compared with visible light wavelengths.

Copper zinc tin sulfide (Cu<sub>2</sub>ZnSnS<sub>4</sub>) thin films have been used as absorbing layers in photovoltaic devices. Agrawal *et al.*<sup>428</sup> reported type-II band-alignment by forming a hybrid heterostructure between p-type 3D Cu<sub>2</sub>ZnSnS<sub>4</sub> (CZTS) and n-type 2D MoS<sub>2</sub> which showed significant PL quenching at the heterojunction interface. Fig. 27(g-i) shows a schematic illustration of CZTS/MoS<sub>2</sub> p–n heterojunction photodetector and the current–voltage ( $I$ – $V$ ) curves in the dark and at different laser wavelengths (400 nm to 1100 nm) under illumination, photoresponsivity and calculated rise/decay times of the self-powered CZTS/MoS<sub>2</sub> photodetector from 400 nm to 1100 nm wavelengths. The CZTS/MoS<sub>2</sub> p–n heterojunction-based photodetectors exhibited photovoltaic properties, with a photoresponsivity of  $141 \text{ mA W}^{-1}$ , the current  $I_{on}/I_{off}$  ratio of 112, and fast rise/decay times of 81/79 ms at 900 nm. The CZTS/MoS<sub>2</sub> p–n heterojunction photodetector also showed an increase in photoresponsivity to  $79 \text{ A W}^{-1}$  under an applied bias voltage of 6 V and high stability up to 1500 h (62.5 days) of operation. Agrawal *et al.*<sup>429</sup> also developed self-powered photodetector using p-type Cu<sub>2</sub>ZnSnS<sub>4</sub> (CZTS) active electrodes with n-type vertical MoS<sub>2</sub> flakes. The CZTS/MoS<sub>2</sub> p–n heterojunction photodetector showed photoresponsivity of  $49.31 \text{ A W}^{-1}$  and EQE value of  $7.6 \times 10^{3\%}$  with enhanced photoresponse in visible and NIR region compared with metal electrodes. The heterojunction photodetector showed detectivity of  $3.4 \times 10^{13}$  Jones in NIR and  $2.4 \times 10^{13}$  Jones in visible wavelength region. The photoresponsivity of photodetector with CZTS electrodes was increased by 11 times compared with gold electrodes at 1100 nm (NIR region). Furthermore, the photodetector with CZTS electrodes also exhibited long term stability up to 4000 h (166 days).

Self-powered photodetectors were developed using MoS<sub>2</sub> thin film and bulk GaAs.<sup>430</sup> The MoS<sub>2</sub>/GaAs heterojunction-based photodetector operated from DUV to NIR spectral region and exhibited photoresponsivity of  $35.2 \text{ mA W}^{-1}$ ,

detectivity of  $1.96 \times 10^{13}$  Jones and rise and fall times of  $3.4 \mu\text{s}/15.6 \mu\text{s}$  at zero bias. These MoS<sub>2</sub>/GaAs heterojunction photodetectors also demonstrated polarization sensitivity to an optical signal with 4.8 ratio between the peak-to-valley. The 0D/3D MoS<sub>2</sub> QDs/GaAs heterojunction photodetectors were fabricated using n-type GaAs substrates with varied doping concentrations which resulted in n–n heterojunctions between n-type MoS<sub>2</sub> QDs and bulk n-type GaAs.<sup>431</sup> The MoS<sub>2</sub>/GaAs heterojunction photodetectors operated between 400–950 nm and showed highest photoresponsivity of  $400 \text{ mA W}^{-1}$  and detectivity of  $4 \times 10^{12}$  Jones at 500 nm at zero bias voltage, which is a self-powered photodetection. Shi *et al.*<sup>432</sup> integrated 0D InP@ZnS core–shell QDs with 2D bilayer MoS<sub>2</sub> to develop self-powered hybrid phototransistors by using interdigitated Pt electrodes which acted as light collectors as well as plasmonic resonators. 0D/2D InP@ZnS/MoS<sub>2</sub> hybrid photodetectors showed photoresponsivity of  $1374 \text{ A W}^{-1}$  and self-powered properties with a fast photospeed of  $21.5 \mu\text{s}$ . The photoresponsivity of MoS<sub>2</sub> was measured as  $222.5 \text{ A W}^{-1}$  at 532 nm under illuminating power intensity of  $34 \text{ mW cm}^{-2}$  at gate voltage of 40 V, which decreased to  $81 \text{ A W}^{-1}$  as the laser power intensity was increased to  $170 \text{ mW cm}^{-2}$  due to the temperature induced increment in recombination and scattering of carries. The photocurrent of InP@ZnS/MoS<sub>2</sub> hybrid phototransistors was enhanced compared to MoS<sub>2</sub> phototransistors as a function wavelength at 447, 532 and 671 nm. The stability of hybrid photodetectors was also examined at 8%, 17%, 25%, 31%, and 42% of humidity at 532 nm illuminating laser light applying 200 Hz frequency without any applied bias voltage. InP@ZnS/MoS<sub>2</sub> hybrid phototransistor devices exhibited reproducibility over 4000 repeated cycles under 2000 Hz frequency and improved environmental stability over MoS<sub>2</sub> phototransistors over a period of three months, indicating the protecting role of InP@ZnS QDs for the MoS<sub>2</sub> layer in order to prevent the degradation of photodetectors under ambient environmental conditions.

The self-powered photodetectors were developed using MoS<sub>2</sub>/AlN/Si hybrid heterostructure where MoS<sub>2</sub> thin films were deposited on AlN/Si(111).<sup>433</sup> The hybrid photodetector exhibited photoresponse from 300 nm to 1100 nm at 0 V, having the photoresponsivity of  $9.93 \text{ A W}^{-1}$  at 900 nm and rise/decay times of  $12.5 \mu\text{s}/14.9 \mu\text{s}$ . At zero bias, the photoresponsivity of MoS<sub>2</sub>/AlN/Si hybrid ( $9.93 \text{ A W}^{-1}$ ) was found to be over five times higher than that of MoS<sub>2</sub>/Si photodetector ( $1.88 \text{ A W}^{-1}$ ). The oxygen defects in AlN supported the transportation of photo-generated charge carriers in the hybrid photodetector. Self-powered photodetectors using a vertical MoO<sub>3</sub>/MoS<sub>2</sub> heterojunction<sup>434</sup> have been fabricated which showed photoresponsivity of  $670 \text{ mA W}^{-1}$  and detectivity of  $4.77 \times 10^{10}$  Jones under 0 V bias and current  $I_{on}/I_{off}$  current ratio of  $10^3$ . MoS<sub>2(1-x)Se<sub>2x</sub></sub> nanostructured alloys have been used for developing photodetectors by atomic-level tailoring. Hou *et al.*<sup>385</sup> used hydrothermal method to prepare MoS<sub>2(1-x)Se<sub>2x</sub></sub> ( $x = 0, 0.5, 1$ ) nanostructures. The MoS<sub>2</sub> alloy-based photodetectors exhibited photocurrent of  $12.6 \mu\text{A}$ , photoresponsivity of  $1.753 \text{ mA W}^{-1}$  and rise/fall times of 4.7 s at 660 nm under laser illumination of  $1.75 \text{ mW mm}^{-2}$ . The photocurrents of MoS<sub>2</sub> alloy



based photodetectors were considerably increased compared with pure  $\text{MoS}_2$  and  $\text{MoSe}_2$  based photodetectors. The photo-responsivity of CVD-grown Au/ $\text{MoS}_{1.15}\text{Se}_{0.85}$ /Au based photodetectors was found to be much higher,  $2.06 \times 10^3 \text{ mA W}^{-1}$  at 532 nm with rise/fall times of 18 s/35 s.<sup>386</sup> In another study by Xu *et al.*,<sup>435</sup> the bandgap of  $\text{MoS}_{2(1-x)}\text{Se}_{2x}$  was tailored between 1.83 eV to 1.73 eV by adjusting the Se composition and thickness within a single domain. The spatially bandgap-graded  $\text{MoS}_{2(1-x)}\text{Se}_{2x}$  based phototransistors showed photo-responsivity of  $191.5 \text{ A W}^{-1}$ , detectivity of  $10^{12} \text{ Jones}$ , photo-conductive gain of  $10^6$  to  $10^7$  and response speed of 51 ms under  $-0.5 \text{ V}$  bias voltage. The phototransistor showed photo-responsivity values of 23.2, 191.5, and  $26.2 \text{ A W}^{-1}$  at 405, 650, and 808 nm laser illuminations under  $-0.5 \text{ V}$  bias voltage, respectively. The homojunction phototransistors yielded photo-responsivity of  $311 \text{ mA W}^{-1}$ , detectivity of  $10^{11} \text{ Jones}$ , and the current  $I_{\text{on}}/I_{\text{off}}$  ratio of  $10^4$  at 405 nm wavelength under laser power intensity of  $1.73 \text{ mW mm}^{-2}$  for the at zero bias (self-powered operation)  $\text{MoS}_{2(1-x)}\text{Se}_{2x}$  phototransistors. Han *et al.*<sup>436</sup> developed a self-driven photodetection device using an  $\text{MoS}_2$  nanosheet-based photodetector, a vertical contact-separate mode triboelectric nanogenerator (CS-TENG) as the power source, and LEDs as the alarm system. The mechanism is

based on the impedance matching effect between TENG specific output and the performance of  $\text{MoS}_2$  photodetector which is sensitive to visible light. The voltage of TENG is regulated with a Zener diode, the enabling self-powered  $\text{MoS}_2$  photodetector to function properly. The  $\text{MoS}_2$  photodetector exhibited high current  $I_{\text{on}}/I_{\text{off}}$  ratio of  $1.02 \times 10^4$  and the rise/fall times of 0.32/0.36 s at 405 nm wavelength. Zhao *et al.*<sup>437</sup> developed a surface ionic gate (SIG) transistor using  $\text{MoS}_2$  monolayer where gas ions are adsorbed by  $\text{MoS}_2$ , which functions as a gate to control the carrier concentration and transport process. The modulation can be adjusted by the TENG operation cycles and the current  $I_{\text{on}}/I_{\text{off}}$  ratio of  $10^4$  was obtained. In this SIG-based  $\text{MoS}_2$  photodetector, the photocurrent recovery time is 74 ms, much faster than devices without SIG modulation. The photocurrent of the SIG-based  $\text{MoS}_2$  photodetector was found to increase linearly as a function of time for a period of 120 s, useful for developing a photodetector with luminous flux.

Table 2 summarizes the data collected on the photo-responsivity, detectivity and response/recovery time ( $\tau_{\text{rise}}/\tau_{\text{decay}}$ ) of self-powered  $\text{MoS}_2$  based photodetectors along with their measurement wavelengths and incident laser powers. The strain-induced 2D nanomaterial-based self-powered photodetectors have been reported where piezoelectric effect also plays

**Table 2** The performance of self-powered  $\text{MoS}_2$  photodetectors in terms of their photo-responsivity, detectivity and response/recovery time ( $\tau_{\text{rise}}/\tau_{\text{decay}}$ ) along with their measurement wavelength and incident laser power (Jones =  $\text{cm Hz}^{1/2} \text{ W}^{-1}$ )<sup>a</sup>

$\text{MoS}_2$ Photodetector	Conditions (wavelength, incident power)	Photo-responsivity ( $\text{A W}^{-1}$ )	Detectivity (Jones)	Response time ( $\tau_{\text{rise}}/\tau_{\text{decay}}$ )	Ref.
RGO- $\text{MoS}_2$ /pyramid Si	( $\lambda = 808 \text{ nm}$ , 100 nW)	21.8	$3.8 \times 10^{15}$	$2.8 \mu\text{s}/46.6 \mu\text{s}$	178
p-WSe <sub>2</sub> /n- $\text{MoS}_2$	( $\lambda = 514 \text{ nm}$ , 5 $\mu\text{W}$ )	0.04	—	$100 \mu\text{s}$	123
p-WSe <sub>2</sub> /n- $\text{MoS}_2$	( $\lambda = 532 \text{ nm}$ , 7 $\mu\text{W}$ )	0.01	—	$1 \mu\text{s}$	165
p-GaTe/n- $\text{MoS}_2$	( $\lambda = 633 \text{ nm}$ , $100 \text{ mW cm}^{-2}$ )	1.365	—	$10 \text{ ms}$	167
1L $\text{MoS}_2$ /P-Si	( $\lambda = 532 \text{ nm}$ , 0.95 mW)	117	$1 \times 10^9$	$74 \text{ ms}/115 \text{ ms}$	314
$\text{MoS}_2$ /Si (PVD)	( $\lambda = 808 \text{ nm}$ )	0.21	$10^{13}$	$3 \mu\text{s}/40 \mu\text{s}$	162
ITO/GaSe/ $\text{MoS}_2$ /ITO	( $\lambda = 520 \text{ nm}$ )	0.67	$2.3 \times 10^{11}$	$155 \mu\text{s}/215 \mu\text{s}$	427
(Ni/Au)/GaSe/ $\text{MoS}_2$ /(Ni/Au)	( $\lambda = 520 \text{ nm}$ )	0.037	$1.9 \times 10^{10}$	$620 \mu\text{s}/740 \mu\text{s}$	427
p-MoTe <sub>2</sub> /n- $\text{MoS}_2$	( $\lambda = 800 \text{ nm}$ )	0.038	—	—	205e
p- $\text{MoS}_2$ /n-WS <sub>2</sub>	( $\lambda = 532 \text{ nm}$ , $28.64 \text{ mW cm}^{-2}$ )	0.043	$4.36 \times 10^{13}$	4 ms	343
p-GaN nanowires/n- $\text{MoS}_2$ (strain)	( $\lambda = 550 \text{ nm}$ )	734.5	—	5 ms	258c
p- $\text{MoS}_2$ /n-GaN	( $\lambda = 265 \text{ nm}$ )	0.187	$2.34 \times 10^{13}$	$46.4 \mu\text{s}/114.1 \mu\text{s}$	316
p-GeSe/n- $\text{MoS}_2$	( $\lambda = 532 \text{ nm}$ )	0.105	$1.03 \times 10^{10}$	$110 \text{ ms}/750 \text{ ms}$	424
$\text{MoS}_2/\text{CH}_3\text{NH}_3\text{PbI}_3$		0.06	—	$2149 \text{ ms}/899 \text{ ms}$	327
p-Cu <sub>2</sub> ZnSnS <sub>4</sub> /n- $\text{MoS}_2$	( $\lambda = 900 \text{ nm}$ )	0.141	—	$81 \text{ ms}/79 \text{ ms}$	
$\text{MoS}_2/\text{GaAs}$	( $\lambda = 780 \text{ nm}$ , $73 \text{ nW cm}^{-2}$ )	0.352	$1.96 \times 10^{13}$	$3.4 \mu\text{s}/15.6 \mu\text{s}$	430
n- $\text{MoS}_2$ /n-GaAs	( $\lambda = 650 \text{ nm}$ , $20 \text{ mW cm}^{-2}$ )	$0.43 \times 10^{-3}$	$2.28 \times 10^{11}$	$1.87 \mu\text{s}/3.53 \mu\text{s}$	438
$\text{MoS}_2/\beta\text{-Ga}_2\text{O}_3$	( $\lambda = 245 \text{ nm}$ , $20.1 \mu\text{W cm}^{-2}$ )	$2.05 \times 10^{-3}$	$1.21 \times 10^{11}$	—	439
Pd- $\text{MoS}_2$ /Si	( $\lambda = 950 \text{ nm}$ , $1.0 \text{ mW cm}^{-2}$ )	0.654	$1.0 \times 10^{14}$	$2.1 \mu\text{s}/173.8 \mu\text{s}$	440
Pd/Al <sub>2</sub> O <sub>3</sub> / $\text{MoS}_2$	( $\lambda = 532 \text{ nm}$ , 0.95 mW)	0.308	—	$972 \text{ ms}/878 \text{ ms}$	441
Pd/HfO <sub>2</sub> / $\text{MoS}_2$	( $\lambda = 532 \text{ nm}$ , 0.95 mW)	0.538	—	$969 \text{ ms}/875 \text{ ms}$	441
Graphene/InSe/ $\text{MoS}_2$	( $\lambda = 532 \text{ nm}$ , $1.26 \text{ mW cm}^{-2}$ )	0.11	$1.08 \times 10^{10}$	1 ms	442
InSe/Se	( $\lambda = 460 \text{ nm}$ , $1 \text{ mW cm}^{-2}$ )	0.032	$1.7 \times 10^{11}$	$30 \text{ ms}/37 \text{ ms}$	352c
p-Cu <sub>9</sub> S <sub>5</sub> /n- $\text{MoS}_2$	( $\lambda = 532 \text{ nm}$ , $9.36 \text{ mW cm}^{-2}$ )	76	$1.6 \times 10^{12}$	$8 \text{ ms}/2 \text{ ms}$	443
p-Cu <sub>2</sub> ZnSnS <sub>4</sub> /n- $\text{MoS}_2$	( $\lambda = 900 \text{ nm}$ , $1.02 \mu\text{W cm}^{-2}$ )	0.141	—	$81 \text{ ms}/79 \text{ ms}$	428
Au/p-Cu <sub>2</sub> ZnSnS <sub>4</sub> /n- $\text{MoS}_2$ /Au	( $\lambda = 800 \text{ nm}$ , $0.43 \mu\text{W cm}^{-2}$ )	49.31	$2.4 \times 10^{13}$	$0.5 \text{ s}/0.8 \text{ s}$	429
TETA-GR/ $\text{MoS}_2$ /MAPbI <sub>3</sub> /PTAA	( $\lambda = 500 \text{ nm}$ )	0.42	$1.1 \times 10^{10}$	$1.63 \mu\text{s}/0.98 \mu\text{s}$	426
InP@ZnS/ $\text{MoS}_2$	( $\lambda = 532 \text{ nm}$ , $34 \text{ mW cm}^{-2}$ )	$1.3 \times 10^3$	—	$21.5 \mu\text{s}/133.3 \mu\text{s}$	432
$\text{MoS}_{2(1-x)}\text{Se}_{2x}$	(405 nm, $1.73 \text{ mW mm}^{-2}$ )	0.311	$10^{11}$	—	435

<sup>a</sup> (TETA-GR): triethylenetetramine-doped graphene, PTAA: poly[bis(4-phenyl)(2,4,6-trimethylphenyl)amine].



an important role. In addition to various  $\text{MoS}_2$  hybrid heterostructures,  $\text{MoS}_2$  vdWHs with other 2D atomic layered nanomaterials have also been studied for developing self-powered photodetectors. For example,  $\text{MoS}_2$ ,<sup>173</sup>  $\text{MoS}_2$ –PDPP3T,<sup>189</sup>  $\text{MoS}_2$ /MoTe<sub>2</sub>,<sup>205</sup>  $\text{MoS}_2$ /P-Si,<sup>314</sup>  $\text{MoS}_2$ /GaN,<sup>316</sup>  $\text{MoS}_2$ /perovskite,<sup>327</sup> and  $\text{MoS}_2$ /WS<sub>2</sub>,<sup>343</sup> based self-powered photodetectors show high photoresponsivity, detectivity, fast photoresponse time and high current  $I_{\text{on}}/I_{\text{off}}$  ratio. The performance of self-powered  $\text{MoS}_2$  photodetectors can be enhanced due to the piezoelectric effect.<sup>221,258,272</sup>  $\text{MoS}_2$  based self-powered broadband photodetectors have been reported for n- $\text{MoS}_2$ /n-GaAs,<sup>438</sup>  $\text{MoS}_2$ / $\beta$ -Ga<sub>2</sub>O<sub>3</sub>,<sup>439</sup> Pd- $\text{MoS}_2$ /Si,<sup>440</sup> Pd/Al<sub>2</sub>O<sub>3</sub>/MoS<sub>2</sub>,<sup>441</sup> Pd/HfO<sub>2</sub>/MoS<sub>2</sub>,<sup>441</sup> graphene/InSe/MoS<sub>2</sub>,<sup>442</sup> p-Cu<sub>9</sub>S<sub>5</sub>/n- $\text{MoS}_2$ ,<sup>443</sup> and  $\text{MoS}_{2(1-x)}\text{Se}_{2x}$ .<sup>385,386,435</sup>  $\text{MoS}_2$  based self-powered photodetectors exhibit photoresponsivity from  $\text{mA W}^{-1}$  to  $\text{A W}^{-1}$ , detectivity from  $10^9$  to  $10^{15}$  Jones and response time from microseconds ( $\mu\text{s}$ ) to seconds (s), depending on the measurement wavelengths and incident power densities which could be used for healthcare applications.

## 7. Stability of $\text{MoS}_2$ photodetectors

Photodetectors are generally used under harsh working environmental conditions for surveillance including imaging and optical communications; therefore, long-term stability of photodetectors are of immense importance for commercial applications. The environmental stability for extended period of time has been observed in some  $\text{MoS}_2$  hybrid heterostructure-based photodetectors.<sup>162,187,192</sup> A few examples are discussed here. The detectivity of  $10^{13}$  Jones and a fast response speed of 3  $\mu\text{s}$  have been reported for the self-driven visible–NIR  $\text{MoS}_2$ /Si heterojunction-based photodetector.<sup>162</sup> These  $\text{MoS}_2$ /Si heterojunction photodetectors also showed negligible degradation of photovoltage in air for a period of one month under light illumination at 808 nm. The RGO– $\text{MoS}_2$ /pyramid Si heterojunction-based photodetectors<sup>178</sup> showed environmental stability over three months of storing in the air under 808 nm and 1550 nm light illuminations due to the synergistic effect of RGO,  $\text{MoS}_2$  and the graphene electrodes. Kang *et al.*<sup>180</sup> measured the stability of APTES-doped  $\text{MoS}_2$  photodetectors, which were (i) as-doped, (ii) exposed to the air for 36 h and (iii) for 120 h. The on-current of APTES-doped  $\text{MoS}_2$  photodetectors was found to decrease by 15% from  $273 \mu\text{A } \mu\text{m}^{-2}$  to  $231 \mu\text{A } \mu\text{m}^{-2}$  after air exposing for 36 h and 37% decrease from  $273 \mu\text{A } \mu\text{m}^{-2}$  to  $171 \mu\text{A } \mu\text{m}^{-2}$  after air-exposing for 120 h. The environmental stability of various  $\text{MoS}_2$  based photodetectors are shown in Fig. 28(a–e).  $\text{MoS}_2$ /PDPP3T heterojunction-based self-powered phototransistor showed photodetection from UV (365 nm) to NIR (859 nm) region with photoresponsivity of 276, 445, and  $269 \text{ mA W}^{-1}$  and detectivity of  $2.59 \times 10^8$ ,  $3.14 \times 10^8$ , and  $2.53 \times 10^8$  Jones at 365, 660, and 850 nm wavelengths, respectively.<sup>189</sup> Flexible  $\text{MoS}_2$ /PDPP3T photodetectors fabricated on the PET substrate were found to be mechanically stable up to 10 000 bending cycles with a little decrease in photocurrent under repeated bending test conducted at a bending radius of 9 mm with 660 nm. Furthermore,  $\text{MoS}_2$ /PDPP3T heterojunction photodetectors also exhibited stability in air atmosphere up to 35 days in

dark and light illumination without any encapsulation of devices. Gold chloride hydrate *in situ* doped  $\text{MoS}_2$  based photodetectors retained 94% of the initial photocurrent value after a period of nine months, evidencing good environmental stability.<sup>337</sup> The stability in air for one month has been measured for the self-driven an  $\text{MoS}_2$ /GaAs heterojunction photodetectors when encapsulated with poly(methyl methacrylate) to avoid oxidation.<sup>318</sup> High photoresponsivity and detectivity have been measured in  $\text{MoS}_2$ /P(VDF-TrFE) hybrid photodetector where [P(VDF-TrFE)] ferroelectric copolymer was used as a gate.<sup>137</sup> This  $\text{MoS}_2$ /P(VDF-TrFE) hybrid photodetector also displayed mechanical stability over 90 000 repeated cycles at incident light power of 100 nW at 635 nm light illumination. The mechanical stability of various flexible  $\text{MoS}_2$ -based hybrid photodetectors including  $\text{MoS}_2$ /Kapton and  $\text{MoS}_2$ /PET,<sup>217</sup>  $\text{MoS}_2$ /PI,<sup>220</sup>  $\text{MoS}_2$ /graphene,<sup>233,234</sup>  $\text{MoS}_2$ – $\text{MoS}_2$ /CNT,<sup>256</sup>  $\text{MoS}_2$ /WS<sub>2</sub>,<sup>164</sup>  $\text{MoS}_2$ /ZnO,<sup>277</sup> stacked PEDOT:PSS/PVP/PEDOT:PSS/ $\text{MoS}_2$ /PEN,<sup>219</sup>  $\text{MoS}_2$ /perovskite,<sup>76</sup>  $\text{MoS}_2$ /Ag nanocubes,<sup>186</sup> and surface-functionalized monolayer  $\text{MoS}_2$ <sup>293</sup> have been discussed in details earlier.  $\text{MoS}_2$ -based photodetectors display both environmental and mechanical stability for a long period of time against oxidative atmosphere to mechanical testing.  $\text{Cu}_2\text{ZnSnS}_4$ / $\text{MoS}_2$  p–n heterojunction-based self-powered photodetectors showed stability up to 62.5 days of operation.<sup>428</sup> When  $\text{Cu}_2\text{ZnSnS}_4$  was used on an active electrode, the self-powered  $\text{Cu}_2\text{ZnSnS}_4$ / $\text{MoS}_2$  photodetector exhibited even longer stability up to 166 days.<sup>429</sup> The photoresponse of a rigid p-i-n-type perovskite-based photodiode/solar cell bifunctional device (PPSB) device decreased by 38% after storing for 30 days under 30% humidity at 25 °C compared to 60% degradation of PEDOT:PSS HTL device after 10 days. The flexible PPSB devices showed 43% degradation of their initial photocurrent values after 3000 bending cycles at 4 mm a curvature radius. This demonstrated that use of  $\text{MoS}_2$  thin film as a HTL in perovskites-based self-powered PPBS devices and for improving their stability<sup>425</sup> The organic/inorganic perovskites/ $\text{MoS}_2$  hybrid-based photodiode–solar cell nanosystem (PPSN) rigid device retained over 78% of the initial photoresponsivity after 30 days of storing period in ambient conditions and flexible device retained 80% of the initial photoresponsivity at 600 nm wavelength up to 1000 bending cycles demonstrating strong mechanical stability due to the synergistic effect between TETA-GR electrodes and BL- $\text{MoS}_2$  ETL.<sup>426</sup>

## 8. Applications of $\text{MoS}_2$ photodetectors

The photoresponse of  $\text{MoS}_2$  photodetectors was also found to increase remarkably by the piezophototronic effect.<sup>226,263,265</sup> The photoresponse of  $\text{MoS}_2$  photodetectors significantly increases after different types of doping.<sup>183,188,194,325</sup> The photoresponsivity, detectivity and photoresponse of atomic layered  $\text{MoS}_2$ -based hybrid heterostructured photoconductors range over several orders of magnitude, from  $\text{mA W}^{-1}$  to  $10^{10} \text{ A W}^{-1}$ ,<sup>122,138,187,199,280</sup> from  $10^7$  to  $10^{15}$  Jones<sup>178,301–303</sup> and from nano/microseconds to seconds,<sup>163,170,171,304,305</sup> over an ultra-broadband spectral range



varing from DUV wavelength<sup>316</sup> to LWIR,<sup>169,340</sup> respectively. As evident from these summarized data that MoS<sub>2</sub>-based photoconductors show outstanding performance with highest photoresponsivity of  $10^{10}$  A W<sup>-1</sup>, the capability of detecting a weak signal up to 10<sup>15</sup> Jones and a very fast photoresponse speed of nanosecond over a broad spectral bandwidth. Marin *et al.*<sup>444</sup> reported the integration of an MoS<sub>2</sub> photodetector with a silicon nitride (Si<sub>3</sub>N<sub>4</sub>) photonic circuit where near-unity lateral absorption was measured that gave rise to a higher photoresponsivity. The speed of the MoS<sub>2</sub> photodetector was found to increase when MoS<sub>2</sub> channel was combined with h-BN substrate. Furthermore, low power operation in MoS<sub>2</sub>

photodetector was also achieved by using graphene gates. Kim *et al.*<sup>445</sup> proposed the application of the Ge-gated MoS<sub>2</sub> photodetector for developing a multilevel optic-neural synaptic device. Fig. 29 shows various applications of MoS<sub>2</sub> based ultra-broadband photodetectors. The MoS<sub>2</sub> based photodetectors can be used in a wide range of industrial products operating from DUV to LWIR spectral range that include optical communications, environmental monitoring, chemical and medical sensors, biomedical imaging, remote sensing, lasers, satellites, military, security systems, night vision, smartphones, laptops, computers, Internet-of-Things (IoT), LEDs, data storage, optical microscopy and other next-generation optoelectronic-based

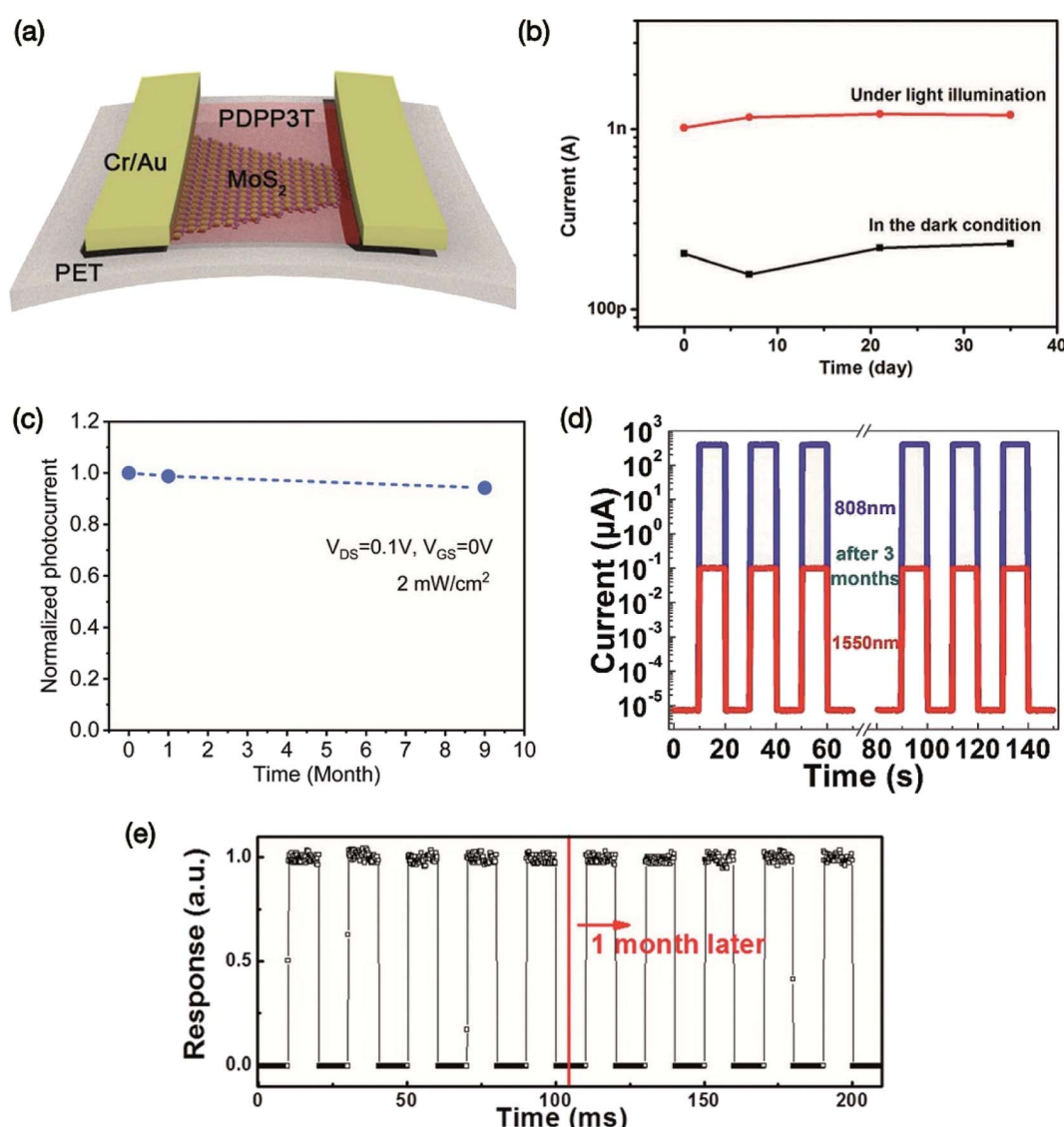


Fig. 28 (a) The schematic of the flexible MoS<sub>2</sub>/PDPP3T photodetector on the PET substrate. (b) Current versus time curves in the dark and under 660 nm light illumination when photodetectors were stored in air up to 35 days. Reprinted with permission from ref. 189, copyright © Wiley. (c) The stability of photocurrent of the gold chloride hydrate *in situ* doped MoS<sub>2</sub> photodetector measured over several months where 94% of the initial photocurrent value was retained after nine months. Reprinted with permission from ref. 337, copyright © American Chemical Society. (d) Photoresponse of RGO–MoS<sub>2</sub>/pyramid Si heterojunction photodetector measured at 808 and 1550 nm light illumination before and after storing devices in the air for three months. Reprinted with permission from ref. 178, copyright © Wiley. (e) Normalized response of the MoS<sub>2</sub>/GaAs heterojunction-based self-driven photodetector measured after storage in air atmosphere for one month. Reprinted with permission from ref. 318, copyright © Elsevier.



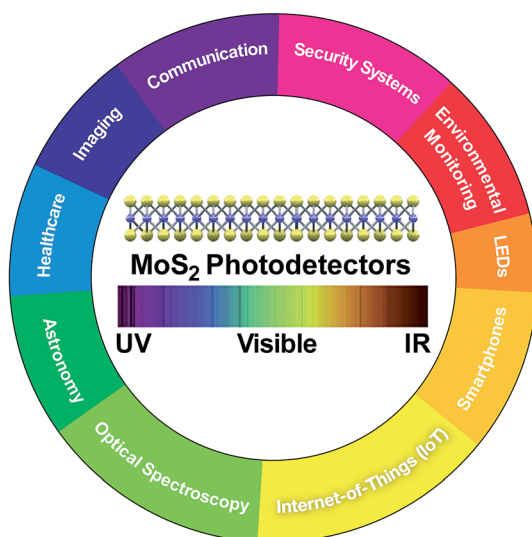


Fig. 29 Applications of atomic layered MoS<sub>2</sub> based ultra-broadband photodetectors.

devices. Self-powered flexible MoS<sub>2</sub> photodetectors have a great potential in the field of healthcare for their applications in point-of-care wearable biosensors for monitoring vital signs and metabolic parameters, bioimaging, diagnostics, and cardiac pacemakers.

## 9. Conclusions and perspective

The role of 2D TMDs, especially atomic layered MoS<sub>2</sub> and its diverse vdWHs, in developing photodetectors for optoelectronic applications has been discussed, where the photoresponse can be tailored over a broad spectral range from UV to IR regions. The review has particularly summarized the progress made in the design and fabrication of broadband photodetectors using atomic layered MoS<sub>2</sub> and MoS<sub>2</sub>-based hybrid heterostructures for wearable optoelectronics. The performance of MoS<sub>2</sub> photodetectors can be dramatically improved and optimized by forming MoS<sub>2</sub> hybrid heterostructures with 0D QDs,<sup>193,194</sup> 2D materials,<sup>169,196,226,281,309,329,334–336</sup> ferroelectric polymers,<sup>137,324</sup> halide perovskites,<sup>179,191,192,327</sup> piezo-phototronic effect,<sup>221,258,272</sup> and *via* chemical doping,<sup>187,326</sup> as has been studied for the phototransistor, photodiode and photoconductor components. The photoresponsivity, detectivity and photoresponse of MoS<sub>2</sub> hybrid heterostructure-based photodetectors vary by several orders of magnitude depending on the nature of the vdWHs, doping agents, optical wavelengths and intensity of applied incident power.<sup>122,171,178,179,199,226,321,325,326,326</sup> Temperature-dependent ultrahigh photoresponsivities of  $5 \times 10^8$  A W<sup>-1</sup> to  $1 \times 10^{10}$  A W<sup>-1</sup> have been observed for the monolayer graphene/ML MoS<sub>2</sub> hybrid vdWH-based photodetectors.<sup>122</sup> Similarly, an ultrahigh detectivity of  $3.8 \times 10^{15}$  Jones was recorded for the rGO–MoS<sub>2</sub>/pyramid Si hybrid heterostructure-based photodetector, which also operated in the ultra-broadband spectral range of 350 nm to 4.3  $\mu$ m (UV to MIR)

due to the bandgap narrowing instigated by the sulfur (S) vacancy defects in MoS<sub>2</sub> crystals.<sup>178</sup> The MoS<sub>2</sub> hybrid heterostructure-based photodetectors also exhibit improved environmental stability for extended periods of time.<sup>162,187,192</sup> The flexible photodetectors developed from MoS<sub>2</sub> layers and MoS<sub>2</sub> hybrids with TMDs, graphene, CNTs, and ZnO and their applications in wearable optoelectronics have been discussed. The figures-of-merit of a very wide range of MoS<sub>2</sub>-based photodetectors have been compared in terms of their important parameters including photoresponsivity, detectivity, and response speed measured at different wavelengths and incident laser power densities.

The integration of MoS<sub>2</sub> photodetectors with other flexible electronic, photonic and optoelectronic functional devices remains challenging. Research activities on MoS<sub>2</sub> based photodetectors is emerging on a fast pace.<sup>446–451</sup> The large family of 2D materials can be explored for developing photodetection devices. For example, 2D TMDs such as MoSe<sub>2</sub>, MoTe<sub>2</sub>, WS<sub>2</sub>, WSe<sub>2</sub>, PtS<sub>2</sub>, PtSe<sub>2</sub>, PtTe<sub>2</sub>, PdS<sub>2</sub>, PdSe<sub>2</sub>, PdTe<sub>2</sub>, GeS<sub>2</sub>, GeSe<sub>2</sub>, HfS<sub>2</sub>, TiS<sub>2</sub>, FeS<sub>2</sub>, CoS<sub>2</sub>, NiS<sub>2</sub>, SnS<sub>2</sub>, MoSe<sub>2</sub>, NbSe<sub>2</sub>, TaSe<sub>2</sub>, NiSe<sub>2</sub>, FeSe<sub>2</sub>, and CoSe<sub>2</sub> can be explored for developing new vdWHs for high-performance photodetectors. Tremendous opportunities exist for TMD-based vdWHs with other nanomaterials, including BP, graphene, h-BN, Janus TMDs, mono-chalcogenide layered materials (GaS, GaSe, GaTe, InS, InSe, InTe, SnS, SnSe, SnTe, PbS, PbTe, *etc.*), 2D transition-metal carbides, nitrides and carbonitrides (MXenes), transition-metal trichalcogenides (MX<sub>3</sub>; M = Ti, Zr, Hf, Nb, Ta, and X = S, Se, Te), perovskites, surface-functionalized 2D TMDs and transition metal oxides (TMOs), inorganic semiconductors and organic materials, which represent the future direction of TMD-based photodetectors for their application in fields from biomedical imaging to optical communication. TMDs are also advancing as multifunctional materials for future wearable electronic and optoelectronic devices as an inexpensive alternative to the costly manufactured semiconducting materials currently employed in the electronics industry. 2D atomic layered material-based hybrid vdWHs hold great potential for self-powered flexible photodetectors in the healthcare industry especially for biomedical imaging, point-of-care wearable biosensors for monitoring vital signs and metabolic parameters, cardiac pacemakers, and for patients. There are many significant challenges to producing low-cost, large-scale high-performance photodetector devices for commercial applications, therefore factors such as optimization of the photoresponse, reproducibility, long-term environmental stability of photodetector devices, mechanical flexibility, packaging, and the toxicity of nanomaterials<sup>452–460</sup> used in photodetectors need much more attention. TMDs are very promising nanomaterials for developing high-performance flexible photodetectors and for integration of such devices into the next generation of wearable technologies.

## Disclaimer

The author cannot accept liability for any kind of scientific and technical data contained in this review article whatsoever for



any omissions or any errors or the accuracy of contents or a claim of completeness.

## Conflicts of interest

There are no conflicts to declare.

## Acknowledgements

The author wishes to thank Eric Singh at Stanford University, Ravina Singh at the Wharton School of Business, University of Pennsylvania, Dr Surya Singh at the University of Oxford, and David Tebera for their valuable support. This work was sponsored by American Scientific Publishers, Los Angeles, California.

## References

- 1 RP Photonics Encyclopedia (formerly Encyclopedia of Laser Physics and Technology), RP Photonics Consulting GmbH, Bad Dürheim, Germany, 2013, <https://www.rp-photonics.com>.
- 2 (a) *Handbook of Advanced Electronic and Photonic Materials and Devices*, ed. H. S. Nalwa, Academic Press, San Diego, 2001, 10-volume set; (b) *Handbook of Organic Electronics and Photonics*, ed. H. S. Nalwa, American Scientific Publishers, Los Angeles, 2008, 3-volume set; (c) *Handbook of Luminescence, Display Materials and Devices*, ed. H. S. Nalwa and L. S. Rohwer, American Scientific Publishers, Los Angeles, 2003, 3-volume set; (d) *Encyclopedia of Nanoscience and Nanotechnology*, ed. H. S. Nalwa, American Scientific Publishers, Los Angeles, 2004, 10-volume set.
- 3 T. Ma, Z. Liu, J. Wen, Y. Gao, X. Ren, H. Chen, C. Jin, X.-L. Ma, N. Xu, H.-M. Cheng and W. Ren, Tailoring the Thermal and Electrical Transport Properties of Graphene Films by Grain Size Engineering, *Nat. Commun.*, 2017, **8**, 14486.
- 4 Z. Zhang, H. Huang, X. Yang and L. Zang, Tailoring Electronic Properties of Graphene by  $\pi$ - $\pi$  Stacking with Aromatic Molecules, *J. Phys. Chem. Lett.*, 2011, **2**, 2897–2905.
- 5 D. Wang, L. Wang, X. Dong, Z. Shi and J. Jin, Chemically Tailoring Graphene Oxides into Fluorescent Nanosheets for  $\text{Fe}^{3+}$  ion Detection, *Carbon*, 2012, **50**, 2147–2154.
- 6 D. Qu, M. Zheng, J. Li, Z. Xie and Z. Sun, Tailoring Color Emissions from N-Doped Graphene Quantum Dots for Bioimaging Applications, *Light: Sci. Appl.*, 2015, **4**, e364.
- 7 M. Yi and Z. Shen, A Review on Mechanical Exfoliation for the Scalable Production of Graphene, *J. Mater. Chem. A*, 2015, **3**, 11700–11715.
- 8 (a) E. Singh and H. S. Nalwa, Graphene-Based Bulk-Heterojunction Solar Cells: A Review, *J. Nanosci. Nanotechnol.*, 2015, **15**, 6237–6278; (b) E. Singh and H. S. Nalwa, Stability of graphene-based heterojunction solar cells, *RSC Adv.*, 2015, **5**, 73575–73600.
- 9 E. Singh and H. S. Nalwa, Graphene-Based Dye-Sensitized Solar Cells: A Review, *Sci. Adv. Mater.*, 2015, **7**, 1863–1912.
- 10 R. Muñoz and C. Gómez-Aleixandre, Review of CVD Synthesis of Graphene, *Chem. Vap. Deposition*, 2013, **19**, 297–322.
- 11 S. Bae, H. Kim, Y. Lee, X. Xu, J.-S. Park, Y. Zheng, J. Balakrishnan, T. Lei, H. Ri Kim, Y. I. Song, Y.-J. Kim, K. S. Kim, B. Özyilmaz, J.-H. Ahn, B. H. Hong and S. Iijima, Roll-to-Roll Production of 30-Inch Graphene Films for Transparent Electrodes, *Nat. Nanotechnol.*, 2010, **5**, 574–578.
- 12 K. S. Kim, Y. J. Ji, Y. Nam, K. H. Kim, E. Singh, J. Y. Lee and G. Y. Yeom, Atomic Layer Etching of Graphene Through Controlled Ion Beam for Graphene-Based Electronics, *Sci. Rep.*, 2017, **7**, 2462.
- 13 H. Wang, H. Yuan, S. S. Hong, Y. Li and Y. Cui, Physical and Chemical Tuning of Two-Dimensional Transition Metal Dichalcogenides, *Chem. Soc. Rev.*, 2015, **44**, 2664–2680.
- 14 C. R. Ryder, J. D. Wood, S. A. Wells and M. C. Hersam, Chemically Tailoring Semiconducting Two-Dimensional Transition Metal Dichalcogenides and Black Phosphorus, *ACS Nano*, 2016, **10**, 3900–3917.
- 15 S. Najmaei, X. Zou, D. Er, J. Li, Z. Jin, W. Gao, Q. Zhang, S. Park, L. Ge, S. Lei, J. Kono, V. B. Shenoy, B. I. Yakobson, A. George, P. M. Ajayan and J. Lou, Tailoring the Physical Properties of Molybdenum Disulfide Monolayers by Control of Interfacial Chemistry, *Nano Lett.*, 2014, **14**, 1354–1361.
- 16 M. Chhowalla, H. S. Shin, G. Eda, L.-J. Li, K. P. Loh and H. Zhang, The Chemistry of Two-Dimensional Layered Transition Metal Dichalcogenide Nanosheets, *Nat. Chem.*, 2013, **5**, 263–275.
- 17 R. Lv, J. A. Robinson, R. E. Schaak, D. Sun, Y. Sun, T. E. Mallouk and M. Terrones, Transition Metal Dichalcogenides and Beyond: Synthesis, Properties, and Applications of Single- and Few-Layer Nanosheets, *Acc. Chem. Res.*, 2014, **48**, 56–64.
- 18 M. Chhowalla, Z. Liu and H. Zhang, Two-Dimensional Transition Metal Dichalcogenide (TMD) Nanosheets, *Chem. Soc. Rev.*, 2015, **44**, 2584–2586.
- 19 Y. Shi, H. Li and L.-J. Li, Recent Advances in Controlled Synthesis of Two-Dimensional Transition Metal Dichalcogenides Via Vapour Deposition Techniques, *Chem. Soc. Rev.*, 2015, **44**, 2744–2756.
- 20 K. S. Kim, K. H. Kim, Y. Nam, J. Jeon, S. Yim, E. Singh, J. Y. Lee, S. J. Lee, Y. S. Jung, G. Y. Yeom and D. W. Kim, Atomic Layer Etching Mechanism of  $\text{MoS}_2$  for Nanodevices, *ACS Appl. Mater. Interfaces*, 2017, **9**, 11967–11976.
- 21 B. J. Kim, H. Jang, S.-K. Lee, B. H. Hong, J.-H. Ahn and J. H. Cho, High-Performance Flexible Graphene Field Effect Transistors with Ion Gel Gate Dielectrics, *Nano Lett.*, 2010, **10**, 3464–3466.
- 22 S. J. Park, O. S. Kwon, S. H. Lee, H. S. Song, T. H. Park and J. Jang, Ultrasensitive Flexible Graphene Based Field-Effect Transistor (FET)-Type Bioelectronic Nose, *Nano Lett.*, 2012, **12**, 5082–5090.



23 *Nanomaterial-Based Flexible and Multifunctional Sensors*, ed. E. Singh and H. S. Nalwa, American Scientific Publishers, Los Angeles, California, 2019.

24 R. Singh, E. Singh and H. S. Nalwa, Inkjet Printed Nanomaterial Based Flexible Radio Frequency Identification (RFID) Tag Sensors for the Internet of Nano Things, *RSC Adv.*, 2017, **7**, 48597–48630.

25 (a) E. Singh, M. Meyyappan and H. S. Nalwa, Flexible Graphene-Based Wearable Gas and Chemical Sensors, *ACS Appl. Mater. Interfaces*, 2017, **9**, 34544–34586; (b) E. Singh, M. Meyyappan and H. S. Nalwa, Graphene-Based Flexible and Stretchable Strain Sensors for Wearable Electronics, Chapter 1, in *Nanomaterial-Based Flexible and Multifunctional Sensors*, ed. E. Singh and H. S. Nalwa, American Scientific Publishers, Los Angeles, California, 2019, pp.1–50.

26 S. K. Krishnan, E. Singh, P. Singh, M. Meyyappan and H. S. Nalwa, A Review on Graphene-Based Nanocomposites for Electrochemical and Fluorescent Biosensors, *RSC Adv.*, 2019, **9**, 87778–8881.

27 W. K. Chee, H. N. Lim, Z. Zainal, N. M. Huang, I. Harrison and Y. Andou, Flexible Graphene-Based Supercapacitors: A Review, *J. Phys. Chem. C*, 2016, **120**, 4153–4172.

28 S. H. Aboutalebi, R. Jalili, D. Esrafilzadeh, M. Salari, Z. Gholamvand, S. A. Yamini, K. Konstantinov, R. L. Shepherd, J. Chen, S. E. Moulton, P. C. Innis, A. I. Minett, J. M. Razal and G. G. Wallace, High-Performance Multifunctional Graphene Yarns: Toward Wearable All-Carbon Energy Storage Textiles, *ACS Nano*, 2014, **8**, 2456–2466.

29 N. Li, Z. Chen, W. Ren, F. Li and H. M. Cheng, Flexible Graphene-Based Lithium Ion Batteries with Ultrafast Charge and Discharge Rates, *Proc. Natl. Acad. Sci. U. S. A.*, 2012, **109**, 17360–17365.

30 S. Kim, M. K. Gupta, K. Y. Lee, A. Sohn, T. Y. Kim, K.-S. Shin, D. Kim, S. K. Kim, K. H. Lee, H.-J. Shin, D.-W. Kim and S.-W. Kim, Transparent Flexible Graphene Triboelectric Nanogenerators, *Adv. Mater.*, 2014, **26**, 3918–3925.

31 K. Ruan, K. Ding, Y. Wang, S. Diao, Z. Shao, X. Zhang and J. Jie, Flexible Graphene/Silicon Heterojunction Solar Cells, *J. Mater. Chem. A*, 2015, **3**, 14370–14377.

32 I. A. Sahito, K. C. Sun, A. A. Arbab, M. B. Qadir, Y. S. Choi and S. H. Jeong, Flexible and Conductive Cotton Fabric Counter Electrode Coated with Graphene Nanosheets for High Efficiency Dye Sensitized Solar Cell, *J. Power Sources*, 2016, **319**, 90–98.

33 T. Jiao, D. Wei, J. Liu, W. Sun, S. Jia, W. Zhang, Y. Feng, H. Shi and C. Du, Flexible Solar Cells Based on Graphene-Ultrathin Silicon Schottky Junction, *RSC Adv.*, 2015, **5**, 73202–73206.

34 N. Liu, H. Tian, G. Schwartz, J. B. H. Tok, T.-L. Ren and Z. Bao, Large-Area, Transparent, and Flexible Infrared Photodetector Fabricated Using P-N Junctions Formed by N-Doping Chemical Vapor Deposition Grown Graphene, *Nano Lett.*, 2014, **14**, 3702–3708.

35 H. Tetsuka, A. Nagoya and S.-I. Tamura, Graphene/Nitrogen-Functionalized Graphene Quantum Dot Hybrid Broadband Photodetectors with a Buffer Layer of Boron Nitride Nanosheets, *Nanoscale*, 2016, **8**, 19677–19683.

36 E. Singh, P. Singh, K. S. Kim, G. Y. Yeom and H. S. Nalwa, Flexible Molybdenum Disulfide (MoS<sub>2</sub>) Atomic Layers for Wearable Electronics and Optoelectronics, *ACS Appl. Mater. Interfaces*, 2019, **11**, 11061–11105.

37 H.-Y. Chang, S. Yang, J. Lee, L. Tao, W.-S. Hwang, D. Jena, N. Lu and D. Akinwande, High-Performance, Highly Bendable MoS<sub>2</sub> Transistors with High- $\kappa$  Dielectrics for Flexible Low-Power Systems, *ACS Nano*, 2013, **7**, 5446–5452.

38 C. Kuru, D. Choi, A. Kargar, C. H. Liu, S. Yavuz, C. Choi, S. Jin and P. R. Bandaru, High-Performance Flexible Hydrogen Sensor Made of WS<sub>2</sub> Nanosheet-Pd Nanoparticle Composite Film, *Nanotechnology*, 2016, **27**, 195501.

39 J. Y. Oh, J. H. Lee, S. W. Han, S. S. Chae, E. J. Bae, Y. H. Kang, W. J. Choi, S. Y. Cho, J.-O. Lee, H. K. Baik and T. I. Lee, Chemically Exfoliated Transition Metal Dichalcogenide Nanosheet-Based Wearable Thermoelectric Generators, *Energy Environ. Sci.*, 2016, **9**, 1696–1705.

40 Y. Xiao, L. Huang, Q. Zhang, S. Xu, Q. Chen and W. Shi, Gravure Printing of Hybrid MoS<sub>2</sub>@S-rGO Interdigitated Electrodes for Flexible Microsupercapacitors, *Appl. Phys. Lett.*, 2015, **107**, 013906.

41 (a) *Photodetectors and Fiber Optics*, ed. H. S. Nalwa, Academic Press, San Diego, 2001; (b) *Polymer Optical Fibers*, ed. H. S. Nalwa, American Scientific Publishers, Los Angeles, 2004; (c) *Silicon-Based Materials and Devices*, ed. H. S. Nalwa, Academic Press, San Diego, 2001, 2-volume set; (d) *Handbook of Thin Films*, ed. H. S. Nalwa, Academic Press, San Diego, 2001, 5-volume set; (e) *Handbook of Surfaces and Interfaces of Materials*, ed. H. S. Nalwa, Academic Press, San Diego, 2001, 5-volume set; (f) *Handbook of Organic Conductive Molecules and Polymers*, ed. H. S. Nalwa, Wiley, Chichester, 1997, 4-volume set; (g) *Supramolecular Photosensitive and Electroactive Materials*, ed. H. S. Nalwa, Academic Press, San Diego, 2001; (h) *Handbook of Nanostructured Materials and Nanotechnology*, ed. H. S. Nalwa, Academic Press, San Diego, 1999, 5-volume set.

42 M. Dang, H.-C. Yuan, Z. Ma, J. Ma and G. Qin, The Fabrication and Characterization of Flexible Single-Crystalline Silicon and Germanium p-Intrinsic-n Photodetectors on Plastic Substrates, *Appl. Phys. Lett.*, 2017, **110**, 253104.

43 H.-C. Yuan, J. Shin, G. Qin, L. Sun, P. Bhattacharya, M. G. Lagally, G. K. Celler and Z. Ma, Flexible Photodetectors on Plastic Substrates by Use of Printing Transferred Single-Crystal Germanium Membranes, *Appl. Phys. Lett.*, 2009, **94**, 013102.

44 L.-B. Luo, X.-B. Yang, F.-X. Liang, J.-S. Jie, Q. Li, Z.-F. Zhu, C.-Y. Wu, Y.-Q. Yu and L. Wang, Transparent and Flexible Selenium Nanobelt-Based Visible Light Photodetector, *CrystEngComm*, 2012, **14**, 1942–1947.

45 G. Chen, X. Xie and G. Shen, Flexible Organic-Inorganic Hybrid Photodetectors with n-Type Phenyl-C61-Butyric



Acid Methyl Ester (PCBM) and p-Type Pearl-Like GaP Nanowires, *Nano Res.*, 2014, **7**, 1777–1787.

46 G. Chen, B. Liang, Z. Liu, G. Yu, X. Xie, T. Luo, Z. Xie, D. Chen, M.-Q. Zhu and G. Shen, High Performance Rigid and Flexible Visible-Light Photodetectors Based on Aligned X(In, Ga)P Nanowire Arrays, *J. Mater. Chem. C*, 2014, **2**, 1270–1277.

47 K. Heo, H. Lee, Y. Park, J. Park, H.-J. Lim, D. Yoon, C. Lee, M. Kim, H. Cheong, J. Park, J. Jian and S. Hong, Aligned Networks of Cadmium Sulfide nanowires for Highly Flexible Photodetectors with Improved Photoconductive Responses, *J. Mater. Chem.*, 2012, **22**, 2173–2179.

48 L. Li, Z. Lou and G. Shen, Hierarchical CdS Nanowires Based Rigid and Flexible Photodetectors with Ultrahigh Sensitivity, *ACS Appl. Mater. Interfaces*, 2015, **7**, 23507–23514.

49 Z. Wang, J. Jie, F. Li, L. Wang, T. Yan, L. Luo, B. Nie, C. Xie, P. Jiang, X. Zhang, Y. Yu and C. Wu, Chlorine-Doped ZnSe Nanoribbons with Tunable n-Type Conductivity as High-Gain and Flexible Blue/UV Photodetectors, *ChemPlusChem*, 2012, **77**, 470–475.

50 J. M. Wu, Y.-R. Chen and Y.-H. Lin, Rapidly Synthesized ZnO Nanowires by Ultraviolet Decomposition Process in Ambient Air for Flexible Photodetector, *Nanoscale*, 2011, **3**, 1053–1058.

51 Z. Zheng, L. Gan, J. Zhang, F. Zhuge and T. Zhai, An Enhanced UV-Vis-NIR and Flexible Photodetector Based on Electrospun ZnO Nanowire Array/PbS Quantum Dots Film Heterostructure, *Adv. Sci.*, 2017, **4**, 1600316.

52 W. Tian, C. Zhang, T. Zhai, S.-L. Li, X. Wang, J. Liu, X. Jie, D. Liu, M. Liao, Y. Koide, D. Golberg and Y. Bando, Flexible Ultraviolet Photodetectors with Broad Photoresponse Based on Branched ZnS-ZnO Heterostructure Nanofilms, *Adv. Mater.*, 2014, **26**, 3088–3093.

53 Z. Zheng, L. Gan, H. Li, Y. Ma, Y. Bando, D. Golberg and T. Zhai, A Fully Transparent and Flexible Ultraviolet-Visible Photodetector Based on Controlled Electrospun ZnO-CdO Heterojunction Nanofiber Arrays, *Adv. Funct. Mater.*, 2015, **25**, 5885–5894.

54 Z. Jin, L. Gao, Q. Zhou and J. Wang, High-Performance Flexible Ultraviolet Photoconductors Based on Solution-Processed Ultrathin ZnO/Au Nanoparticle Composite Films, *Sci. Rep.*, 2014, **4**, 4268.

55 F.-X. Wang, J.-M. Yang, S.-H. Nie, W.-M. Su and G.-B. Pan, All Solution-Processed Large-Area Patterned Flexible Photodetectors Based on ZnOEP/PVK Hybrid Film, *J. Mater. Chem. C*, 2016, **4**, 7841–7845.

56 Z. Lou, L. Li and G. Shen, High-Performance Rigid and Flexible Ultraviolet Photodetectors with Single-Crystalline ZnGa<sub>2</sub>O<sub>4</sub> Nanowires, *Nano Res.*, 2015, **8**, 2162–2169.

57 Z. Liu, H. Huang, B. Liang, X. Wang, Z. Wang, D. Chen and G. Shen, Zn<sub>2</sub>GeO<sub>4</sub> and In<sub>2</sub>Ge<sub>2</sub>O<sub>7</sub> Nanowire Mats Based Ultraviolet Photodetectors on Rigid and Flexible Substrates, *Opt. Express*, 2012, **20**, 2982–2991.

58 W. Bi, M. Zhou, Z. Ma, H. Zhang, J. Yu and Y. Xie, CuInSe<sub>2</sub> Ultrathin Nanoplatelets: Novel Self-Sacrificial Template-Directed Synthesis and Application for Flexible Photodetectors, *Chem. Commun.*, 2012, **48**, 9162–9164.

59 Y. Min, G. D. Moon, J. Park, M. Park and U. Jeong, Surfactant-Free CuInSe<sub>2</sub> Nanocrystals Transformed from In<sub>2</sub>Se<sub>3</sub> Nanoparticles and Their Application for a Flexible UV Photodetector, *Nanotechnology*, 2011, **22**, 465604.

60 X. Xie and G. Shen, Single-Crystalline In<sub>2</sub>S<sub>3</sub> Nanowire-Based Flexible Visible-Light Photodetectors with an Ultra-High Photoresponse, *Nanoscale*, 2015, **7**, 5046–5052.

61 Z. Q. Zheng, J. D. Yao and G. W. Yang, Growth of Centimeter-Scale High-Quality In<sub>2</sub>Se<sub>3</sub> Films for Transparent, Flexible and High Performance Photodetectors, *J. Mater. Chem. C*, 2016, **4**, 8094–8103.

62 J. Chao, B. Liang, X. Hou, Z. Liu, Z. Xie, B. Liu, W. Song, G. Chen, D. Chen and G. Shen, Selective Synthesis of Sb<sub>2</sub>S<sub>3</sub> Nanoneedles and Nanoflowers for High Performance Rigid and Flexible Photodetectors, *Opt. Express*, 2013, **21**, 13639–13647.

63 Y. Liang, Y. Wang, J. Wang, S. Wu, D. Jiang and J. Lian, High-Performance Flexible Photodetectors Based on Single-Crystalline Sb<sub>2</sub>Se<sub>3</sub> Nanowires, *RSC Adv.*, 2016, **6**, 11501–11506.

64 G. Chen, Y. Yu, K. Zheng, T. Ding, W. Wang, Y. Jiang and Q. Yang, Fabrication of Ultrathin Bi<sub>2</sub>S<sub>3</sub> Nanosheets for High-Performance, Flexible, Visible-NIR Photodetectors, *Small*, 2015, **11**, 2848–2855.

65 G. M. Kumar, X. Fu, P. Ilanchezhiyan, S. U. Yuldashev, D. J. Lee, H. D. Cho and T. W. Kang, Highly Sensitive Flexible Photodetectors Based on Self-Assembled Tin Monosulfide Nanoflakes with Graphene Electrodes, *ACS Appl. Mater. Interfaces*, 2017, **9**, 32142–32150.

66 Y. Tao, X. Wu, W. Wang and J. Wang, Flexible Photodetector from Ultraviolet to Near Infrared Based on a SnS<sub>2</sub> Nanosheet Microsphere Film, *J. Mater. Chem. C*, 2015, **3**, 1347–1353.

67 Y.-R. Tao, X.-C. Wu and W.-W. Xiong, Flexible Visible-Light Photodetectors with Broad Photoresponse Based on ZrS<sub>3</sub> Nanobelts Films, *Small*, 2014, **10**, 4905–4911.

68 G. Yu, B. Liang, H. Huang, G. Chen, Z. Liu, D. Chen and G. Shen, Contact Printing of Horizontally-Aligned p-type Zn<sub>3</sub>P<sub>2</sub> Nanowire Arrays for Rigid and Flexible Photodetectors, *Nanotechnology*, 2013, **24**, 095703.

69 M. Zhong, L. Huang, H.-X. Deng, X. Wang, B. Li, Z. Wei and J. Li, Flexible Photodetectors Based on Phase Dependent PbI<sub>2</sub> Single Crystals, *J. Mater. Chem. C*, 2016, **4**, 6492–6499.

70 Q. Zheng, J. Huang, S. Cao and H. Gao, A Flexible Ultraviolet Photodetector Based on Single Crystalline MoO<sub>3</sub> Nanosheets, *J. Mater. Chem. C*, 2015, **3**, 7469–7475.

71 P. Hu, L. Wang, M. Yoon, J. Zhang, W. Feng, X. Wang, Z. Wen, J. C. Idrobo, Y. Miyamoto, D. B. Geohegan and K. Xiao, Highly Responsive Ultrathin GaS Nanosheet Photodetectors on Rigid And Flexible Substrates, *Nano Lett.*, 2013, **13**, 1649–1654.

72 X. Hou, B. Liu, X. Wang, Z. Wang, Q. Wang, D. Chen and G. Shen, SnO<sub>2</sub>-Microtube-Assembled Cloth for Fully Flexible Self-Powered Photodetector Nanosystems, *Nanoscale*, 2013, **5**, 7831–7837.



73 Z. Liu, G. Chen, B. Liang, G. Yu, H. Huang, D. Chen and G. Shen, Fabrication of High-Quality ZnTe Nanowires Toward High-Performance Rigid/Flexible Visible-Light Photodetectors, *Opt. Express*, 2013, **21**, 7799–7810.

74 F. Liu, H. Shimatani, H. Shang, T. Kanagasekaran, V. Zólyomi, N. Drummond, V. I. Fal'ko and K. Tanigaki, High-Sensitivity Photodetectors Based on Multilayer GaTe Flakes, *ACS Nano*, 2014, **8**, 752–760.

75 G. Tong, H. Li, D. Li, Z. Zhu, E. Xu, G. Li, L. Yu, J. Xu and Y. Jiang, Dual-Phase  $\text{CsPbBr}_3\text{-CsPb}_2\text{Br}_5$  Perovskite Thin Films via Vapor Deposition for High-Performance Rigid and Flexible Photodetectors, *Small*, 2018, **14**, 1702523.

76 B. Sun, S. Xi, Z. Liu, X. Liu, Z. Wang, X. Tan, T. Shi, J. Zhou and G. Liao, Sensitive, fast, and stable photodetector based on perovskite/MoS<sub>2</sub> hybrid film, *Appl. Surf. Sci.*, 2019, **493**, 389–395.

77 T. Gao, Q. Zhang, J. Chen, X. Xiong and T. Zhai, Performance-Enhancing Broadband and Flexible Photodetectors Based on Perovskite/ZnO-Nanowire Hybrid Structures, *Adv. Opt. Mater.*, 2017, **5**, 1700206.

78 C. Bao, W. Zhu, J. Yang, F. Li, S. Gu, Y. Wang, T. Yu, J. Zhu, Y. Zhou and Z. Zou, Highly Flexible Self-Powered Organolead Trihalide Perovskite Photodetectors with Gold Nanowire Networks as Transparent Electrodes, *ACS Appl. Mater. Interfaces*, 2016, **8**, 23868–23875.

79 S. Chen, C. Teng, M. Zhang, Y. Li, D. Xie and G. Shi, A Flexible UV-Vis-NIR Photodetector Based on a Perovskite/Conjugated-Polymer Composite, *Adv. Mater.*, 2016, **28**, 5969–5974.

80 V. Q. Dang, G.-S. Han, T. Q. Trung, L. T. Duy, Y.-U. Jin, B.-U. Hwang, H.-S. Jung and N.-E. Lee, Methylammonium Lead Iodide Perovskite-Graphene Hybrid Channels in Flexible Broadband Phototransistors, *Carbon*, 2016, **105**, 353–361.

81 L. Tong, C. Li, F. E. Chen, H. Bai, L. Zhao and G. Shi, Flexible Sandwich Photodetectors Based on Thick Polythiophene Films, *J. Phys. Chem. C*, 2009, **113**, 7411–7415.

82 A. Falco, L. Cinà, G. Scarpa, P. Lugli and A. Abdellah, Fully-Sprayed and Flexible Organic Photodiodes with Transparent Carbon Nanotube Electrodes, *ACS Appl. Mater. Interfaces*, 2014, **6**, 10593–10601.

83 Y. Liu, Y. Liu, S. Qin, Y. Xu, R. Zhang and F. Wang, Graphene-Carbon Nanotube Hybrid Films for High-Performance Flexible Photodetectors, *Nano Res.*, 2017, **10**, 1880–1887.

84 D. I. Son, H. Y. Yang, T. W. Kim and W. I. Park, Transparent and Flexible Ultraviolet Photodetectors Based on Colloidal ZnO Quantum Dot/Graphene Nanocomposites Formed on Poly(Ethylene Terephthalate) Substrates, *Composites, Part B*, 2015, **69**, 154–158.

85 Y.-R. Tao, J.-Q. Chen, J.-J. Wu, Y. Wu and X.-C. Wu, Flexible Ultraviolet-Visible Photodetector Based on HfS<sub>3</sub> Nanobelts Film, *J. Alloys Compd.*, 2016, **658**, 6–11.

86 L. Fan, Y. Tao, X. Wu, Z. Wu and J. Wu, HfX<sub>3</sub> (X = Se and S)/Graphene Composites for Flexible Photodetectors from Visible to Near-Infrared, *Mater. Res. Bull.*, 2017, **93**, 21–27.

87 Y.-L. Liu, C.-C. Yu, K.-T. Lin, T.-C. Yang, E.-Y. Wang, H.-L. Chen, L.-C. Chen and K.-H. Chen, Transparent, Broadband, Flexible, and Bifacial-Operable Photodetectors Containing a Large-Area Graphene-Gold Oxide Heterojunction, *ACS Nano*, 2015, **9**, 5093–5103.

88 Z. Gao, W. Jin, Y. Zhou, Y. Dai, B. Yu, C. Liu, W. Xu, Y. Li, H. Peng, Z. Liu and L. Dai, Self-Powered Flexible and Transparent Photovoltaic Detectors Based on CdSe Nanobelts/Graphene Schottky Junctions, *Nanoscale*, 2013, **5**, 5576–5581.

89 F. H. L. Koppens, T. Mueller, P. Avouris, A. C. Ferrari, M. S. Vitiello and M. Polini, Photodetectors Based on Graphene, Other Two-Dimensional Materials and Hybrid Systems, *Nat. Nanotechnol.*, 2014, **9**, 780–793.

90 F. Xia, H. Wang, D. Xiao, M. Dubey and A. Ramasubramaniam, Two-Dimensional Material Nanophotonics, *Nat. Photonics*, 2014, **8**, 899–907.

91 K. Watanabe, T. Taniguchi and H. Kanda, Direct-Bandgap Properties and Evidence for Ultraviolet Lasing of Hexagonal Boron Nitride Single Crystal, *Nat. Mater.*, 2004, **3**, 404–409.

92 N. Alem, R. Erni, C. Kisielowski, M. D. Rossell, W. Gannett and A. Zettl, Atomically Thin Hexagonal Boron Nitride Probed by Ultrahigh-Resolution Transmission Electron Microscopy, *Phys. Rev. B: Condens. Matter Mater. Phys.*, 2009, **80**, 155425.

93 L. Song, L. Ci, H. Lu, P. B. Sorokin, C. Jin, J. Ni, A. G. Kvashnin, D. G. Kvashnin, J. Lou, B. I. Yakobson and P. M. Ajayan, Large Scale Growth and Characterization of Atomic Hexagonal Boron Nitride Layers, *Nano Lett.*, 2010, **10**, 3209–3215.

94 C. R. Dean, A. F. Young, I. Meric, C. Lee, L. Wang, S. Sorgenfrei, K. Watanabe, T. Taniguchi, P. Kim, K. L. Shepard and J. Hone, Boron Nitride Substrates for High-Quality Graphene Electronics, *Nat. Nanotechnol.*, 2010, **5**, 722–726.

95 Q. Weng, X. Wang, X. Wang, Y. Bando and D. Golberg, Functionalized Hexagonal Boron Nitride Nanomaterials: Emerging Properties and Applications, *Chem. Soc. Rev.*, 2016, **45**, 3989–4012.

96 K. F. Mak, C. Lee, J. Hone, J. Shan and T. F. Heinz, Atomically thin MoS<sub>2</sub>: A New Direct-Gap Semiconductor, *Phys. Rev. Lett.*, 2010, **105**, 136805.

97 A. Splendiani, L. Sun, Y. Zhang, T. Li, J. Kim, C.-Y. Chim, G. Galli and F. Wang, Emerging Photoluminescence in Monolayer MoS<sub>2</sub>, *Nano Lett.*, 2010, **10**, 1271–1275.

98 Y. P. V. Subbaiah, K. J. Saji and A. Tiwari, Atomically Thin MoS<sub>2</sub>: A Versatile Nongraphene 2D Material, *Adv. Funct. Mater.*, 2016, **26**, 2046–2069.

99 H. Liu, A. T. Neal, Z. Zhu, Z. Luo, X. Xu, D. Tománek and P. D. Ye, Phosphorene: An Unexplored 2D Semiconductor with a High Hole Mobility, *ACS Nano*, 2014, **8**, 4033–4041.

100 L. Kou, C. Chen and S. C. Smith, Phosphorene: Fabrication, Properties, and Applications, *J. Phys. Chem. Lett.*, 2015, **6**, 2794–2805.

101 H. Liu, Y. Du, Y. Deng and P. D. Ye, Semiconducting Black Phosphorus: Synthesis, Transport Properties and



Electronic Applications, *Chem. Soc. Rev.*, 2015, **44**, 2732–2743.

102 K. S. Novoselov, A. K. Geim, S. V. Morozov, D. Jiang, M. I. Katsnelson, I. V. Grigorieva, S. V. Dubonos and A. A. Firsov, Two-Dimensional Gas of Massless Dirac Fermions in Graphene, *Nature*, 2005, **438**, 197–200.

103 A. K. Geim, Graphene: Status and Prospects, *Science*, 2009, **324**, 1530–1534.

104 R. R. Nair, P. Blake, A. N. Grigorenko, K. S. Novoselov, T. J. Booth, T. Stauber, N. M. R. Peres and A. K. Geim, Fine Structure Constant Defines Visual Transparency of Graphene, *Science*, 2008, **320**, 1308.

105 K. K. Kim, A. Hsu, X. Jia, S. M. Kim, Y. Shi, M. Dresselhaus, T. Palacios and J. Kong, Synthesis and Characterization of Hexagonal Boron Nitride Film as a Dielectric Layer for Graphene Devices, *ACS Nano*, 2012, **6**, 8583–8590.

106 Y. Cai, G. Zhang and Y.-W. Zhang, Electronic Properties of Phosphorene/Graphene and Phosphorene/Hexagonal Boron Nitride Heterostructures, *J. Phys. Chem. C*, 2015, **119**, 13929–13936.

107 G.-H. Lee, X. Cui, Y. D. Kim, G. Arefe, X. Zhang, C.-H. Lee, F. Ye, K. Watanabe, T. Taniguchi, P. Kim and J. Hone, Highly Stable, Dual-Gated MoS<sub>2</sub> Transistors Encapsulated by Hexagonal Boron Nitride With Gate-Controllable Contact, Resistance, and Threshold Voltage, *ACS Nano*, 2015, **9**, 7019–7026.

108 M. Okada, T. Sawazaki, K. Watanabe, T. Taniguchi, H. Hibino, H. Shinohara and R. Kitaura, Direct Chemical Vapor Deposition Growth of WS<sub>2</sub> Atomic Layers on Hexagonal Boron Nitride, *ACS Nano*, 2014, **8**, 8273–8277.

109 M. W. Iqbal, M. Z. Iqbal, M. F. Khan, M. A. Shehzad, Y. Seo, J. H. Park, C. Hwang and J. Eom, High-Mobility and Air-Stable Single-Layer WS<sub>2</sub> Field-Effect Transistors Sandwiched Between Chemical Vapor Deposition-Grown Hexagonal BN Films, *Sci. Rep.*, 2015, **5**, 10699.

110 F. Xia, T. Mueller, Y.-M. Lin, A. Valdes-Garcia and P. Avouris, Ultrafast Graphene Photodetector, *Nat. Nanotechnol.*, 2009, **4**, 839–843.

111 T. Mueller, F. Xia and P. Avouris, Graphene Photodetectors for High-Speed Optical Communications, *Nat. Photonics*, 2010, **4**, 297–301.

112 X. Gan, R.-J. Shieh, Y. Gao, I. Meric, T. F. Heinz, K. Shepard, J. Hone, S. Assefa and D. Englund, Chip-Integrated Ultrafast Graphene Photodetector with High Responsivity, *Nat. Photonics*, 2013, **7**, 883–887.

113 C.-H. Liu, Y.-C. Chang, T. B. Norris and Z. Zhong, Graphene Photodetectors with Ultra-Broadband and High Responsivity at Room Temperature, *Nat. Nanotechnol.*, 2014, **9**, 273–278.

114 F. Bonaccorso, Z. Sun, T. Hasan and A. C. Ferrari, Graphene Photonics and Optoelectronics, *Nat. Photonics*, 2010, **4**, 611–622.

115 Q. Guo, A. Pospischil, M. Bhuiyan, H. Jiang, H. Tian, D. Farmer, B. Deng, C. Li, S.-J. Han, H. Wang, Q. Xia, T.-P. Ma, T. Mueller and F. Xia, Black Phosphorus Mid-Infrared Photodetectors with High Gain, *Nano Lett.*, 2016, **16**, 4648–4655.

116 (a) M. Bernardi, M. Palummo and J. C. Grossman, Extraordinary Sunlight Absorption and One Nanometer Thick Photovoltaics Using Two-Dimensional Monolayer Materials, *Nano Lett.*, 2013, **13**, 3664–3670; (b) J. Wang, H. Fang, X. Wang, X. Chen, W. Lu and W. Hu, Recent progress on localized field enhanced two-dimensional material photodetectors from ultraviolet–visible to infrared, *Small*, 2017, **13**, 1700894.

117 W. J. Yu, Y. Liu, H. Zhou, A. Yin, Z. Li, Y. Huang and X. Duan, Highly Efficient Gate-Tunable Photocurrent Generation in Vertical Heterostructures of Layered Materials, *Nat. Nanotechnol.*, 2013, **8**, 952–958.

118 M. Massicotte, P. Schmidt, F. Vialla, K. G. Schädler, A. Reserbat-Plantey, K. Watanabe, T. Taniguchi, K. J. Tielrooij and F. H. L. Koppens, Picosecond Photoresponse in van der Waals Heterostructures, *Nat. Nanotechnol.*, 2016, **11**, 42–46.

119 Y. Gong, S. Lei, G. Ye, B. Li, Y. He, K. Keyshar, X. Zhang, Q. Wang, J. Lou, Z. Liu, R. Vajtai, W. Zhou and P. M. Ajayan, Two-Step Growth of Two-Dimensional WSe<sub>2</sub>/MoSe<sub>2</sub> Heterostructures, *Nano Lett.*, 2015, **15**, 6135–6141.

120 D. A. Nguyen, H. M. Oh, N. T. Duong, S. Bang, S. J. Yoon and M. S. Jeong, Highly Enhanced Photoresponsivity of a Monolayer WSe<sub>2</sub> Photodetector with Nitrogen-Doped Graphene Quantum Dots, *ACS Appl. Mater. Interfaces*, 2018, **10**, 10322–10329.

121 X. Hong, J. Kim, S.-F. Shi, Y. Zhang, C. Jin, Y. Sun, S. Tongay, J. Wu, Y. Zhang and F. Wang, Ultrafast Charge Transfer in Atomically Thin MoS<sub>2</sub>/WS<sub>2</sub> Heterostructures, *Nat. Nanotechnol.*, 2014, **9**, 682–686.

122 K. Roy, M. Padmanabhan, S. Goswami, T. P. Sai, G. Ramalingam, S. Raghavan and A. Ghosh, Graphene-MoS<sub>2</sub> Hybrid Structures for Multifunctional Photoresponsive Memory Devices, *Nat. Nanotechnol.*, 2013, **8**, 826–830.

123 R. Cheng, D. Li, H. Zhou, C. Wang, A. Yin, S. Jiang, Y. Liu, Y. Chen, Y. Huang and X. Duan, Electroluminescence and Photocurrent Generation from Atomically Sharp WSe<sub>2</sub>/MoS<sub>2</sub> Heterojunction p–n Diodes, *Nano Lett.*, 2014, **14**, 5590–5597.

124 Y. Zhu, Z. Li, L. Zhang, B. Wang, Z. Luo, J. Long, J. Yang, L. Fu and Y. Lu, High-Efficiency Monolayer Molybdenum Ditelluride Light-Emitting Diode and Photodetector, *ACS Appl. Mater. Interfaces*, 2018, **10**, 43291–43298.

125 O. Salehzadeh, N. H. Tran, X. Liu, I. Shih and Z. Mi, Exciton Kinetics, Quantum Efficiency, and Efficiency Droop of Monolayer MoS<sub>2</sub> Light-Emitting Devices, *Nano Lett.*, 2014, **14**, 4125–4130.

126 J. S. Ross, P. Klement, A. M. Jones, N. J. Ghimire, J. Yan, D. G. Mandrus, T. Taniguchi, K. Watanabe, K. Kitamura, W. Yao, D. H. Cobden and X. Xu, Electrically Tunable Excitonic Light-Emitting Diodes Based on Monolayer WSe<sub>2</sub> p–n Junctions, *Nat. Nanotechnol.*, 2014, **9**, 268–272.

127 T. A. Shastry, I. Balla, H. Bergeron, S. H. Amsterdam, T. J. Marks and M. C. Hersam, Mutual Photoluminescence Quenching and Photovoltaic Effect in



Large-Area Single-Layer MoS<sub>2</sub>-Polymer Heterojunctions, *ACS Nano*, 2016, **10**, 10573–10579.

128 X. Yu and K. Sivula, Photogenerated Charge Harvesting and Recombination in Photocathodes of Solvent-Exfoliated WSe<sub>2</sub>, *Chem. Mater.*, 2017, **29**, 6863–6875.

129 G. Kakavelakis, A. E. Del Rio Castillo, V. Pellegrini, A. Ansaldi, P. Tzourmpakis, R. Brescia, M. Prato, E. Stratakis, E. Kymakis and F. Bonaccorso, Size-Tuning of WSe<sub>2</sub> Flakes for High Efficiency Inverted Organic Solar Cells, *ACS Nano*, 2017, **11**, 3517–3531.

130 E. Singh, K. S. Kim, G. Y. Yeom and H. S. Nalwa, Atomically Thin-Layered Molybdenum Disulfide (MoS<sub>2</sub>) for Bulk-Heterojunction Solar Cells, *ACS Appl. Mater. Interfaces*, 2017, **9**, 3223–3245.

131 E. Singh, K. S. Kim, G. Y. Yeom and H. S. Nalwa, Two-Dimensional Transition Metal Dichalcogenide-Based Counter Electrodes for Dye-Sensitized Solar Cells, *RSC Adv.*, 2017, **7**, 28234–28290.

132 G. Cao, A. Shang, C. Zhang, Y. Gong, S. Li, Q. Bao and X. Li, Optoelectronic Investigation of Monolayer MoS<sub>2</sub>/WSe<sub>2</sub> Vertical Heterojunction Photoconversion Devices, *Nano Energy*, 2016, **30**, 260–266.

133 L. F. Mattheiss, Band Structures of Transition-Metal-Dichalcogenide Layer Compounds, *Phys. Rev. B: Solid State*, 1973, **8**, 3719–3740.

134 A. D. Yoffe, Layer Compounds, *Annu. Rev. Mater. Sci.*, 1973, **3**, 147–170.

135 Q. H. Wang, K. Kalantar-Zadeh, A. Kis, J. N. Coleman and M. S. Strano, Electronics and Optoelectronics of Two-Dimensional Transition Metal Dichalcogenides, *Nat. Nanotechnol.*, 2012, **7**, 699–712.

136 D. Kufer and G. Konstantatos, Highly Sensitive, Encapsulated MoS<sub>2</sub> Photodetector with Gate Controllable Gain and Speed, *Nano Lett.*, 2015, **15**, 7307–7313.

137 X. Wang, P. Wang, J. Wang, W. Hu, X. Zhou, N. Guo, H. Huang, S. Sun, H. Shen, T. Lin, M. Tang, L. Liao, A. Jiang, J. Sun, X. Meng, X. Chen, W. Lu and J. Chu, Ultrasensitive and Broadband MoS<sub>2</sub> Photodetector Driven by Ferroelectrics, *Adv. Mater.*, 2015, **27**, 6575–6581.

138 Y. Li, J. G. DiStefano, A. A. Murthy, J. D. Cain, E. D. Hanson, Q. Li, F. C. Castro, X. Chen and V. P. Dravid, Superior Plasmonic Photodetectors Based on Au@MoS<sub>2</sub> Core–Shell Heterostructures, *ACS Nano*, 2017, **11**, 10321–10329.

139 Z. P. Ling, R. Yang, J. W. Chai, S. J. Wang, W. S. Leong, Y. Tong, D. Lei, Q. Zhou, X. Gong, D. Z. Chi and K. W. Ang, Large-Scale Two-Dimensional MoS<sub>2</sub> Photodetectors by Magnetron Sputtering, *Opt. Express*, 2015, **23**, 13580–13586.

140 Y. Huang, W. Zheng, Y. Qiu and P. Hu, Effects of Organic Molecules with Different Structures and Absorption Bandwidth on Modulating Photoresponse of MoS<sub>2</sub> Photodetector, *ACS Appl. Mater. Interfaces*, 2016, **8**, 23362–23370.

141 J. Xia, X. Huang, L.-Z. Liu, M. Wang, L. Wang, B. Huang, D.-D. Zhu, J.-J. Li, C.-Z. Gu and X.-M. Meng, CVD Synthesis of Large-Area, Highly Crystalline MoSe<sub>2</sub> Atomic Layers on Diverse Substrates and Application to Photodetectors, *Nanoscale*, 2014, **6**, 8949–8955.

142 Y.-H. Chang, W. Zhang, Y. Zhu, Y. Han, J. Pu, J.-K. Chang, W.-T. Hsu, J.-K. Huang, C.-L. Hsu, M.-H. Chiu, T. Takenobu, H. Li, C.-I. Wu, W.-H. Chang, A. T. S. Wee and L.-J. Li, Monolayer MoSe<sub>2</sub> Grown by Chemical Vapor Deposition for Fast Photodetection, *ACS Nano*, 2014, **8**, 8582–8590.

143 C. Jung, S. M. Kim, H. Moon, G. Han, J. Kwon, Y. K. Hong, I. Omkaram, Y. Yoon, S. Kim and J. Park, Highly Crystalline CVD-Grown Multilayer MoSe<sub>2</sub> Thin Film Transistor for Fast Photodetector, *Sci. Rep.*, 2015, **5**, 15313.

144 P. J. Ko, A. Abderrahmane, N. H. Kim and A. Sandhu, High-Performance Near-Infrared Photodetector Based on Nano-Layered MoSe<sub>2</sub>, *Semicond. Sci. Technol.*, 2017, **32**, 065015.

145 L. Yin, X. Zhan, K. Xu, F. Wang, Z. Wang, Y. Huang, Q. Wang, C. Jiang and J. He, Ultrahigh Sensitive MoTe<sub>2</sub> Phototransistors Driven by Carrier Tunneling, *Appl. Phys. Lett.*, 2016, **108**, 043503.

146 P. Ma, N. Flöry, Y. Salamin, B. Baeuerle, A. Emboras, A. Josten, T. Taniguchi, K. Watanabe, L. Novotny and J. Leuthold, Fast MoTe<sub>2</sub> Waveguide Photodetector with High Sensitivity at Telecommunication Wavelengths, *ACS Photonics*, 2018, **5**, 1846–1852.

147 J. D. Yao, Z. Q. Zheng, J. M. Shao and G. W. Yang, Stable, Highly-Responsive and Broadband Photodetection Based on Large-Area Multilayered WS<sub>2</sub> Films Grown by Pulsed-Laser Deposition, *Nanoscale*, 2015, **7**, 14974–14981.

148 C. Lan, Z. Zhou, Z. Zhou, C. Li, L. Shu, L. Shen, D. Li, R. Dong, S. Yip and J. C. Ho, Wafer-Scale Synthesis of Monolayer WS<sub>2</sub> for High-Performance Flexible Photodetectors by Enhanced Chemical Vapor Deposition, *Nano Res.*, 2018, **11**, 3371–3384.

149 T. H. Tsai, Z. Y. Liang, Y. C. Lin, C. C. Wang, K. I. Lin, K. Suenaga and P. W. Chiu, Photogating WS<sub>2</sub> Photodetectors Using Embedded WSe<sub>2</sub> Charge Puddles, *ACS Nano*, 2020, **14**, 4559–4566.

150 Z. Zheng, T. Zhang, J. Yao, Y. Zhang, J. Xu and G. Yang, Flexible, Transparent and Ultra-Broadband Photodetector Based on Large-Area WSe<sub>2</sub> Film for Wearable Devices, *Nanotechnology*, 2016, **27**, 225501.

151 S.-H. Jo, D.-H. Kang, J. Shim, J. Jeon, M. H. Jeon, G. Yoo, J. Kim, J. Lee, G. Y. Yeom, S. Lee, H.-Y. Yu, C. Choi and J.-H. Park, A High-Performance WSe<sub>2</sub>/h-BN Photodetector Using a Triphenylphosphine (PPh<sub>3</sub>)-Based n-Doping Technique, *Adv. Mater.*, 2016, **28**, 4824–4831.

152 K. Xu, Z. Wang, F. Wang, Y. Huang, F. Wang, L. Yin, C. Jiang and J. He, Ultrasensitive Phototransistors Based on Few-Layered HfS<sub>2</sub>, *Adv. Mater.*, 2015, **27**, 7881–7887.

153 D. Wang, X. Zhang, H. Liu, J. Meng, J. Xia, Z. Yin, Y. Wang, J. You and X.-M. Meng, Epitaxial Growth of HfS<sub>2</sub> on Sapphire by Chemical Vapor Deposition and Application for Photodetectors, *2D Mater.*, 2017, **4**, 031012.

154 E. Zhang, Y. Jin, X. Yuan, W. Wang, C. Zhang, L. Tang, S. Liu, P. Zhou, W. Hu and F. Xiu, ReS<sub>2</sub>-Based Field-Effect Transistors and Photodetectors, *Adv. Funct. Mater.*, 2015, **25**, 4076–4082.



155 J. Shim, A. Oh, D.-H. Kang, S. Oh, S. K. Jang, J. Jeon, M. H. Jeon, M. Kim, C. Choi, J. Lee, S. Lee, G. Y. Yeom, Y. J. Song and J.-H. Park, High-Performance 2D Rhenium Disulfide ( $\text{ReS}_2$ ) Transistors and Photodetectors by Oxygen Plasma Treatment, *Adv. Mater.*, 2016, **28**, 6985–6992.

156 S.-H. Jo, H.-Y. Park, D.-H. Kang, J. Shim, J. Jeon, S. Choi, M. Kim, Y. Park, J. Lee, Y. J. Song, S. Lee and J.-H. Park, Broad Detection Range Rhenium Diselenide Photodetector Enhanced by (3-Aminopropyl) Triethoxysilane and Triphenylphosphine Treatment, *Adv. Mater.*, 2016, **28**, 6711–6718.

157 M. H. Ali, D.-H. Kang and J.-H. Park, Rhenium Diselenide ( $\text{ReSe}_2$ ) Infrared Photodetector Enhanced by (3-Aminopropyl)Trimethoxysilane (APTMS) Treatment, *Org. Electron.*, 2018, **53**, 14–19.

158 G. Su, V. G. Hadjiev, P. E. Loya, J. Zhang, S. Lei, S. Maharjan, P. Dong, P. M. Ajayan, J. Lou and H. Peng, Chemical Vapor Deposition of Thin Crystals of Layered Semiconductor  $\text{SnS}_2$  for Fast Photodetection Application, *Nano Lett.*, 2014, **15**, 506–513.

159 G. Liu, Z. Li, X. Chen, W. Zheng, W. Feng, M. Dai, D. Jia, Y. Zhou and P. Hu, Non-Planar Vertical Photodetectors Based on Free Standing Two-Dimensional  $\text{SnS}_2$  Nanosheets, *Nanoscale*, 2017, **9**, 9167–9174.

160 H. Xue, Y. Dai, W. Kim, Y. Wang, X. Bai, M. Qi, K. Halonen, H. Lipsanen and Z. Sun, High Photoresponsivity and Broadband Photodetection with a Band-Engineered  $\text{WSe}_2/\text{SnSe}_2$  Heterostructure, *Nanoscale*, 2019, **11**, 3240–3247.

161 Y. Kim, H. Bark, B. Kang and C. Lee, Wafer-Scale Substitutional Doping Of Monolayer  $\text{MoS}_2$  Films For High-Performance Optoelectronic Devices, *ACS Appl. Mater. Interfaces*, 2019, **11**, 12613–12621.

162 L. Wang, J. Jie, Z. Shao, Q. Zhang, X. Zhang, Y. Wang, Z. Sun and S.-T. Lee,  $\text{MoS}_2/\text{Si}$  Heterojunction with Vertically Standing Layered Structure for Ultrafast, High-Detectivity, Self-Driven Visible-Near Infrared Photodetectors, *Adv. Funct. Mater.*, 2015, **25**, 2910–2919.

163 Y. Li, J. G. DiStefano, A. A. Murthy, J. D. Cain, E. D. Hanson, Q. Li, F. C. Castro, X. Chen and V. P. Dravid, Superior plasmonic photodetectors based on  $\text{Au}@\text{MoS}_2$  core-shell heterostructures, *ACS Nano*, 2017, **11**, 10321–10329.

164 Y. Xue, Y. Zhang, Y. Liu, H. Liu, J. Song, J. Sophia, J. Liu, Z. Xu, Q. Xu, Z. Wang, J. Zheng, Y. Liu, S. Li and Q. Bao, Scalable Production of a Few-Layer  $\text{MoS}_2/\text{WS}_2$  Vertical Heterojunction Array and Its Application for Photodetectors, *ACS Nano*, 2015, **10**, 573–580.

165 C.-H. Lee, G.-H. Lee, A. M. van der Zande, W. Chen, Y. Li, M. Han, X. Cui, G. Arefe, C. Nuckolls, T. F. Heinz, J. Guo, J. Hone and P. Kim, Atomically Thin p-n Junctions with van der Waals Heterointerfaces, *Nat. Nanotechnol.*, 2014, **9**, 676–681.

166 Y. Ding, N. Zhou, L. Gan, X. Yan, R. Wu, I. H. Abidi, A. Waleed, J. Pan, X. Ou, Q. Zhang, M. Zhuang, P. Wang, X. Pan, Z. Fan, T. Zhai and Z. Luo, Stacking-mode confined growth of 2H- $\text{MoTe}_2/\text{MoS}_2$  bilayer heterostructures for UV-vis-IR photodetectors, *Nano Energy*, 2018, **49**, 200–208.

167 S. Yang, C. Wang, C. Ataca, Y. Li, H. Chen, H. Cai, A. Suslu, J. C. Grossman, C. Jiang, Q. Liu and S. Tongay, Self-Driven Photodetector and Ambipolar Transistor in Atomically Thin  $\text{GaTe}-\text{MoS}_2$  p-n vdW Heterostructure, *ACS Appl. Mater. Interfaces*, 2016, **8**, 2533–2539.

168 M. Long, Y. Wang, P. Wang, X. Zhou, H. Xia, C. Luo, S. Huang, G. Zhang, H. Yan, Z. Fan, X. Wu, X. Chen, W. Lu and W. Hu, Palladium Diselenide Long-Wavelength Infrared Photodetector with High Sensitivity and Stability, *ACS Nano*, 2019, **13**, 2511–2519.

169 (a) Q. Liu, B. Cook, M. Gong, Y. Gong, D. Ewing, M. Casper, A. Stramel and J. Wu, Printable Transfer-Free and Wafer-Size  $\text{MoS}_2$ /Graphene van der Waals Heterostructures for High-Performance Photodetection, *ACS Appl. Mater. Interfaces*, 2017, **9**, 12728–12733; (b) Y. Liu, T. Gong, Y. Zheng, X. Wang, J. Xu, Q. Ai, J. Guo, W. Huang, S. Zhou, Z. Liu and Y. Lin, Ultra-sensitive and plasmon-tunable graphene photodetectors for micro-spectrometry, *Nanoscale*, 2018, **10**, 20013–20019.

170 L. Ye, H. Li, Z. Chen and J. Xu, Near-Infrared Photodetector Based on  $\text{MoS}_2$ /Black Phosphorus Heterojunction, *ACS Photonics*, 2016, **3**, 692–699.

171 O. Lopez-Sanchez, D. Lembke, M. Kayci, A. Radenovic and A. Kis, Ultrasensitive Photodetectors Based on Monolayer  $\text{MoS}_2$ , *Nat. Nanotechnol.*, 2013, **8**, 497–501.

172 W. Zhang, J.-K. Huang, C.-H. Chen, Y.-H. Chang, Y.-J. Cheng and L.-J. Li, High-Gain Phototransistors Based on a CVD  $\text{MoS}_2$  Monolayer, *Adv. Mater.*, 2013, **25**, 3456–3461.

173 Y. Pang, F. Xue, L. Wang, J. Chen, J. Luo, T. Jiang, C. Zhang and Z. L. Wang, Tribotronic Enhanced Photoresponsivity of a  $\text{MoS}_2$  Phototransistor, *Adv. Sci.*, 2016, **3**, 1500419.

174 P. Yang, Z. Zhang, M. Sun, F. Lin, T. Cheng, J. Shi, C. Xie, Y. Shi, S. Jiang, Y. Huan, P. Liu, F. Ding, C. Xiong, D. Xie and Y. Zhang, Thickness Tunable Wedding-Cake-Like  $\text{MoS}_2$  Flakes for High-Performance Optoelectronics, *ACS Nano*, 2019, **26**, 3649–3658.

175 G. H. Shin, J. Park, K. J. Lee, G.-B. Lee, H. B. Jeon, Y.-K. Choi, K. Yu and S.-Y. Choi, Si- $\text{MoS}_2$  Vertical Heterojunction for a Photodetector with High Responsivity and Low Noise Equivalent Power, *ACS Appl. Mater. Interfaces*, 2019, **11**, 7626–7634.

176 H. Yang, A. Giri, S. Moon, S. Shin, J.-M. Myoung and U. Jeong, Highly Scalable Synthesis of  $\text{MoS}_2$  Thin Films with Precise Thickness Control via Polymer-Assisted Deposition, *Chem. Mater.*, 2017, **29**, 5772–5776.

177 M. A. Krainak, X. Sun, G. Yang and W. Lu, Comparison of Linear-Mode Avalanche Photodiode Lidar Receivers for Use at One-Micron Wavelength, in *Proceedings of the SPIE 7681: Advanced Photon Counting Techniques IV*, SPIE, Orlando, FL, 2010, p. 76810Y.

178 P. Xiao, J. Mao, K. Ding, W. Luo, W. Hu, X. Zhang, X. Zhang and J. Jie, Solution-Processed 3D RGO- $\text{MoS}_2$ /Pyramid Si Heterojunction for Ultrahigh Detectivity and Ultra-Broadband Photodetection, *Adv. Mater.*, 2018, **30**, 1801729.



179 Z.-Y. Peng, J.-L. Xu, J.-Y. Zhang, X. Gao and S.-D. Wang, Solution-Processed High-Performance Hybrid Photodetectors Enhanced by Perovskite/MoS<sub>2</sub> Bulk Heterojunction, *Adv. Mater. Interfaces*, 2018, **5**, 1800505.

180 D.-H. Kang, M.-S. Kim, J. Shim, J. Jeon, H.-Y. Park, W.-S. Jung, H.-Y. Yu, C.-H. Pang, S. Lee and J.-H. Park, High-Performance Transition Metal Dichalcogenide Photodetectors Enhanced by Self-Assembled Monolayer Doping, *Adv. Funct. Mater.*, 2015, **25**, 4219–4227.

181 S. H. Yu, Y. Lee, S. K. Jang, J. Kang, J. Jeon, C. Lee, J. Y. Lee, H. Kim, E. Hwang, S. Lee and J. H. Cho, Dye-Sensitized MoS<sub>2</sub> Photodetector with Enhanced Spectral Photoresponse, *ACS Nano*, 2014, **8**, 8285–8291.

182 Y. Huang, F. Zhuge, J. Hou, L. Lv, P. Luo, N. Zhou, L. Gan and T. Zhai, Van der Waals Coupled Organic Molecules with Monolayer MoS<sub>2</sub> for Fast Response Photodetectors with Gate-Tunable Responsivity, *ACS Nano*, 2018, **12**, 4062–4073.

183 G. Wu, X. Wang, Y. Chen, Z. Wang, H. Shen, T. Lin, W. Hu, J. Wang, S. Zhang, X. Meng and J. Chu, Ultrahigh Photoresponsivity MoS<sub>2</sub> Photodetector with Tunable Photocurrent Generation Mechanism, *Nanotechnology*, 2018, **29**, 485204.

184 S. Bang, N. T. Duong, J. Lee, Y. H. Cho, H. M. Oh, H. Kim, S. J. Yun, C. Park, M.-K. Kwon, J.-Y. Kim, J. Kim and M. S. Jeong, Augmented Quantum Yield of a 2D Monolayer Photodetector by Surface Plasmon Coupling, *Nano Lett.*, 2018, **18**, 2316–2323.

185 W. Jing, N. Ding, L. Li, F. Jiang, X. Xiong, N. Liu, T. Zhai and Y. Gao, Ag Nanoparticles Modified Large Area Monolayer MoS<sub>2</sub> Phototransistors with High Responsivity, *Opt. Express*, 2017, **25**, 14565–14574.

186 B. Sun, Z. Wang, Z. Liu, X. Tan, X. Liu, T. Shi, J. Zhou and G. Liao, Tailoring of Silver Nanocubes with Optimized Localized Surface Plasmon in a Gap Mode for a Flexible MoS<sub>2</sub> Photodetector, *Adv. Funct. Mater.*, 2019, 1900541.

187 K. Heo, S.-H. Jo, J. Shim, D.-H. Kang, J.-H. Kim and J.-H. Park, Stable and Reversible Triphenylphosphine-Based n-Type Doping Technique for Molybdenum Disulfide (MoS<sub>2</sub>), *ACS Appl. Mater. Interfaces*, 2018, **10**, 32765–32772.

188 S. Pak, Y. Cho, J. Hong, J. Lee, S. Lee, B. Hou, G.-H. An, Y.-W. Lee, J. E. Jang, H. Im, S. M. Morris, J. I. Sohn, S. Cha and J. M. Kim, Consecutive Junction-Induced Efficient Charge Separation Mechanisms for High-Performance MoS<sub>2</sub>/Quantum Dot Phototransistors, *ACS Appl. Mater. Interfaces*, 2018, **10**, 38264–38271.

189 M. Sun, P. Yang, D. Xie, Y. Sun, J. Xu, T. Ren and Y. Zhang, Self Powered MoS<sub>2</sub>-PDPP3T Heterotransistor Based Broadband Photodetectors, *Adv. Electron. Mater.*, 2018, **5**, 1800580.

190 H. Wu, H. Si, Z. Zhang, Z. Kang, P. Wu, L. Zhou, S. Zhang, Z. Zhang, Q. Liao and Y. Zhang, All-Inorganic Perovskite Quantum Dot-Monolayer MoS<sub>2</sub> Mixed-Dimensional van der Waals Heterostructure for Ultrasensitive Photodetector, *Adv. Sci.*, 2018, **5**, 1801219.

191 (a) X. Song, X. Liu, D. Yu, C. Huo, J. Ji, X. Li, S. Zhang, Y. Zou, G. Zhu, Y. Wang, M. Wu, A. Xie and H. Zeng, Boosting Two-Dimensional MoS<sub>2</sub>/CsPbBr<sub>3</sub> Photodetectors via Enhanced Light Absorbance and Interfacial Carrier Separation, *ACS Appl. Mater. Interfaces*, 2018, **10**, 2801–2809; (b) R. Lin, X. Li, W. Zheng and F. Huang, Balanced Photodetection in Mixed-Dimensional Phototransistors Consisting of CsPbBr<sub>3</sub> Quantum Dots and Few-Layer MoS<sub>2</sub>, *ACS Appl. Nano Mater.*, 2019, **2**, 2599–2605; (c) J. Ghosh, L. P. Mawlong, G. B. Manasa, A. J. Pattison, W. Theis, S. Chakraborty and P. K. Giri, Solid-State Synthesis of Stable and Color Tunable Cesium Lead Halide Perovskite Nanocrystals and Mechanism of High-Performance Photodetection in Monolayer MoS<sub>2</sub>/CsPbBr<sub>3</sub> Vertical Heterojunction, *J. Mater. Chem. C*, 2020, **8**, 8917–8934; (d) L. Zhang, S. Shen, M. Li, L. Li, J. Zhang, L. Fan, F. Cheng, C. Li, M. Zhu, Z. Kang and J. Su, Strategies for Air-Stable and Tunable Monolayer MoS<sub>2</sub>-Based Hybrid Photodetectors with High Performance by Regulating the Fully Inorganic Trihalide Perovskite Nanocrystals, *Adv. Opt. Mater.*, 2019, **7**, 1801744.

192 D.-H. Kang, S. R. Pae, J. Shim, G. Yoo, J. Jeon, J. W. Leem, J. S. Yu, S. Lee, B. Shin and J.-H. Park, An Ultrahigh-Performance Photodetector Based on a Perovskite-Transition-Metal-Dichalcogenide Hybrid Structure, *Adv. Mater.*, 2016, **28**, 7799–7806.

193 N. Huo, S. Gupta and G. Konstantatos, MoS<sub>2</sub>-HgTe Quantum Dot Hybrid Photodetectors Beyond 2 μm, *Adv. Mater.*, 2017, **29**, 1606576.

194 S. Zhang, X. Wang, Y. Chen, G. Wu, Y. Tang, L. Zhu, H. Wang, W. Jiang, L. Sun, T. Lin, H. Shen, W. Hu, J. Ge, J. Wang, X. Meng and J. Chu, Ultrasensitive hybrid MoS<sub>2</sub>-ZnCdSe Quantum Dots Photodetectors with High-Gain, *ACS Appl. Mater. Interfaces*, 2019, **11**, 23667–23672.

195 G. A. Saenz, G. Karapetrov, J. Curtis and A. B. Kaul, Ultra-High Photoresponsivity in Suspended Metal-Semiconductor-Metal Mesoscopic Multilayer MoS<sub>2</sub> Broadband Detector from UV-to-IR with Low Schottky Barrier Contacts, *Sci. Rep.*, 2018, **8**, 1276.

196 Q. A. Vu, J. H. Lee, V. L. Nguyen, Y. S. Shin, S. C. Lim, K. Lee, J. Heo, S. Park, K. Kim, Y. H. Lee and W. J. Yu, Tuning Carrier Tunneling in van der Waals Heterostructures for Ultrahigh Detectivity, *Nano Lett.*, 2016, **17**, 453–459.

197 M. S. Choi, D. Qu, D. Lee, X. Liu, K. Watanabe, T. Taniguchi and W. J. Yoo, Lateral MoS<sub>2</sub> p-n Junction Formed by Chemical Doping for Use in High-Performance Optoelectronics, *ACS Nano*, 2014, **8**, 9332–9340.

198 M. Long, E. Liu, P. Wang, A. Gao, H. Xia, W. Luo, B. Wang, J. Zeng, Y. Fu, K. Xu, W. Zhou, Y. Lv, S. Yao, M. Lu, Y. Chen, Z. Ni, Y. You, X. Zhang, S. Qin, Y. Shi, W. Hu, D. Xing and F. Miao, Broadband Photovoltaic Detectors Based on an Atomically Thin Heterostructure, *Nano Lett.*, 2016, **16**, 2254–2259.

199 Y.-F. Xiong, J.-H. Chen, Y.-Q. Lu and F. Xu, Broadband Optical-Fiber-Compatible Photodetector Based on a Graphene-MoS<sub>2</sub>-WS<sub>2</sub> Heterostructure with a Synergistic



Photogenerating Mechanism, *Adv. Electron. Mater.*, 2018, **5**, 1800562.

200 H. Liu, D. Li, C. Ma, X. Zhang, X. Sun, C. Zhu, B. Zheng, Z. Zou, Z. Luo, X. Zhu, X. Wang and A. Pan, Van der Waals Epitaxial Growth of Vertically Stacked  $\text{Sb}_2\text{Te}_3/\text{MoS}_2$  p-n Heterojunctions for High Performance Optoelectronics, *Nano Energy*, 2019, **59**, 66–74.

201 S. Yang, M. Wu, B. Wang, L.-D. Zhao, L. Huang, C. Jiang and S.-H. Wei, Enhanced Electrical and Optoelectronic Characteristics of Few-Layer Type-II  $\text{SnSe}/\text{MoS}_2$  van der Waals Heterojunctions, *ACS Appl. Mater. Interfaces*, 2017, **9**, 42149–42155.

202 Z. Wang, M. Safdar, M. Mirza, K. Xu, Q. Wang, Y. Huang, F. Wang, X. Zhan and J. He, High-Performance Flexible Photodetectors Based on GaTe Nanosheets, *Nanoscale*, 2015, **7**, 7252–7258.

203 Y. Liu, N. O. Weiss, X. Duan, H.-C. Cheng, Y. Huang and X. Duan, Van der Waals Heterostructures and Devices, *Nat. Rev. Mater.*, 2016, **1**, 16042.

204 B. Li, L. Huang, M. Zhong, Y. Li, Y. Wang, J. Li and Z. Wei, Direct Vapor Phase Growth and Optoelectronic Application of Large Band Offset  $\text{SnS}_2/\text{MoS}_2$  Vertical Bilayer Heterostructures with High Lattice Mismatch, *Adv. Electron. Mater.*, 2016, **2**, 1600298.

205 (a) J. Ahn, J. H. Kang, J. Kyhm, H. T. Choi, M. Kim, D. H. Ahn, D. Y. Kim, I. H. Ahn, J. B. Park, S. Park and Y. Yi, Self-Powered Visible–Invisible Multiband Detection and Imaging Achieved Using High-Performance 2D  $\text{MoTe}_2/\text{MoS}_2$  Semivertical Heterojunction Photodiodes, *ACS Appl. Mater. Interfaces*, 2020, **12**, 10858–10866; (b) B. Wang, S. Yang, C. Wang, M. Wu, L. Huang, Q. Liu and C. Jiang, Enhanced Current Rectification and Self-Powered Photoresponse in Multilayer p- $\text{MoTe}_2$ /n- $\text{MoS}_2$  van der Waals Heterojunctions, *Nanoscale*, 2017, **9**, 10733–10740; (c) Y. Chen, X. Wang, G. Wu, Z. Wang, H. Fang, T. Lin, S. Sun, H. Shen, W. Hu, J. Wang and J. Sun, High-performance photovoltaic detector based on  $\text{MoTe}_2/\text{MoS}_2$  van der Waals heterostructure, *Small*, 2018, **14**, 1703293; (d) F. Wang, L. Yin, Z. X. Wang, K. Xu, F. M. Wang, T. A. Shifa, Y. Huang, C. Jiang and J. He, Configuration-Dependent Electrically Tunable Van der Waals Heterostructures Based on  $\text{MoTe}_2/\text{MoS}_2$ , *Adv. Funct. Mater.*, 2016, **26**, 5499–5506; (e) A. Pezeshki, S. H. H. Shokouh, T. Nazari, K. Oh and S. Im, Electric and photovoltaic behavior of a few-layer  $\alpha$ - $\text{MoTe}_2/\text{MoS}_2$  dichalcogenide heterojunction, *Adv. Mater.*, 2016, **28**, 3216–3222.

206 H. G. Shin, H. S. Yoon, J. S. Kim, M. Kim, J. Y. Lim, S. Yu, J. H. Park, Y. Yi, T. Kim, S. C. Jun and S. Im, Vertical and In-Plane Current Devices Using  $\text{NbS}_2$ /n- $\text{MoS}_2$  van der Waals Schottky Junction and Graphene Contact, *Nano Lett.*, 2018, **18**, 1937–1945.

207 (a) N. Zhou, R. Wang, X. Zhou, H. Song, X. Xiong, Y. Ding, J. Lü, L. Gan and T. Zhai, P-GaSe/N- $\text{MoS}_2$  Vertical Heterostructures Synthesized by van der Waals Epitaxy for Photoresponse Modulation, *Small*, 2018, **14**, 1702731; (b) A. Islam, J. Lee and P. X. L. Feng, Atomic layer GaSe/ $\text{MoS}_2$  van der Waals heterostructure photodiodes with low noise and large dynamic range, *ACS Photonics*, 2018, **5**, 2693–2700.

208 J. Deng, J. Shao, B. Lu, Y. Chen, A. Zaslavsky, S. Cristoloveanu, M. Bawedin and J. Wan, Interface coupled photodetector (ICPD) with high photoresponsivity based on silicon-on-insulator substrate (SOI), *IEEE J. Electron Devices Soc.*, 2018, **6**, 557–564.

209 F. Liao, J. Deng, X. Chen, Y. Wang, X. Zhang, J. Liu, H. Zhu, L. Chen, Q. Sun, W. Hu and J. Wang, A Dual-Gate  $\text{MoS}_2$  Photodetector Based on Interface Coupling Effect, *Small*, 2020, **16**, 1904369.

210 J. Li, Y. Shen, Y. Liu, F. Shi, X. Ren, T. Niu, K. Zhao and S. F. Liu, Stable High-Performance Flexible Photodetector Based on Upconversion Nanoparticles/Perovskite Microarrays Composite, *ACS Appl. Mater. Interfaces*, 2017, **9**, 19176–19183.

211 J. Yao, Z. Zheng and G. Yang, All-layered 2D Optoelectronics: A High-Performance UV-vis-NIR Broadband  $\text{SnSe}$  Photodetector with  $\text{Bi}_2\text{Te}_3$  Topological Insulator Electrodes, *Adv. Funct. Mater.*, 2017, **27**, 1701823.

212 A. S. Aji, P. Solís-Fernández, H. G. Ji, K. Fukuda and H. Ago, High mobility  $\text{WS}_2$  transistors realized by multilayer graphene electrodes and application to high responsivity flexible photodetectors, *Adv. Funct. Mater.*, 2017, **27**, 1703448.

213 W. Yu, S. Li, Y. Zhang, W. Ma, T. Sun, J. Yuan, K. Fu and Q. Bao, Near-Infrared Photodetectors Based on  $\text{MoTe}_2$ /Graphene Heterostructure with High Responsivity and Flexibility, *Small*, 2017, **13**, 1700268.

214 J. Song, J. Yuan, F. Xia, J. Liu, Y. Zhang, Y. L. Zhong, J. Zheng, Y. Liu, S. Li, M. Zhao, Z. Tian, R. A. Caruso, K. P. Loh and Q. Bao, Large-Scale Production of Bismuth Chalcogenide and Graphene Heterostructure and Its Application for Flexible Broadband Photodetector, *Adv. Electron. Mater.*, 2016, **2**, 1600077.

215 C. Xie, C. Mak, X. Tao and F. Yan, Photodetectors Based on Two-Dimensional Layered Materials Beyond Graphene, *Adv. Funct. Mater.*, 2016, **27**, 1603886.

216 *Ferroelectric Polymers: Chemistry, Physics, and Applications*, ed. H. S. Nalwa, CRC Press, Boca Raton, FL, 1995.

217 K. Zhang, M. Peng, A. Yu, Y. Fan, J. Zhai and Z. L. Wang, A substrate-enhanced  $\text{MoS}_2$  photodetector through a dual-photogating effect, *Mater. Horiz.*, 2019, **6**, 826–833.

218 J. Ma, K.-Y. Choi, S. H. Kim, H. Lee and G. Yoo, All Polymer Encapsulated, Highly-Sensitive  $\text{MoS}_2$  Phototransistors on Flexible PAR Substrate, *Appl. Phys. Lett.*, 2018, **113**, 013102.

219 T.-Y. Kim, J. Ha, K. Cho, J. Pak, J. Seo, J. Park, J.-K. Kim, S. Chung, Y. Hong and T. Lee, Transparent Large-Area  $\text{MoS}_2$  Phototransistors with Inkjet-Printed Components on Flexible Platforms, *ACS Nano*, 2017, **11**, 10273–10280.

220 Y. R. Lim, W. Song, J. K. Han, Y. B. Lee, S. J. Kim, S. Myung, S. S. Lee, K.-S. An, C.-J. Choi and J. Lim, Wafer-Scale, Homogeneous  $\text{MoS}_2$  Layers on Plastic Substrates for Flexible Visible-Light Photodetectors, *Adv. Mater.*, 2016, **28**, 5025–5030.



221 K. Zhang, M. Peng, W. Wu, J. Guo, G. Gao, Y. Liu, J. Kou, R. Wen, Y. Lei, A. Yu, Y. Zhang, J. Zhai and Z. L. Wang, A Flexible p-CuO/n-MoS<sub>2</sub> Heterojunction Photodetector with Enhanced Photoresponse by the Piezo-Phototronic Effect, *Mater. Horiz.*, 2017, **4**, 274–280.

222 Q. Zhang, W. Bao, A. Gong, T. Gong, D. Ma, J. Wan, J. Dai, J. N. Munday, J.-H. He, L. Hu and D. Zhang, A Highly Sensitive, Highly Transparent, Gel-Gated MoS<sub>2</sub> Phototransistor on Biodegradable Nanopaper, *Nanoscale*, 2016, **8**, 14237–14242.

223 P. Sahatiya, S. S. Jones and S. Badhulika, Direct, Large Area Growth of Few-Layered MoS<sub>2</sub> Nanostructures on Various Flexible Substrates: Growth Kinetics and Its Effect on Photodetection Studies, *Flexible Printed Electron.*, 2018, **3**, 015002.

224 P. Sahatiya, K. C. S. Reddy and S. Badhulika, Discretely Distributed 1D V<sub>2</sub>O<sub>5</sub> Nanowires Over 2D MoS<sub>2</sub> Nanoflakes for an Enhanced Broadband Flexible Photodetector Covering the Ultraviolet to Near Infrared Region, *J. Mater. Chem. C*, 2017, **5**, 12728–12736.

225 P. Sahatiya, S. S. Jones and S. Badhulika, 2D MoS<sub>2</sub>–Carbon Quantum Dot Hybrid Based Large Area, Flexible UV-vis-NIR Photodetector on Paper Substrate, *Appl. Mater. Today*, 2018, **10**, 106–114.

226 W. Zhang, C.-P. Chuu, J.-K. Huang, C.-H. Chen, M.-L. Tsai, Y.-H. Chang, C.-T. Liang, Y.-Z. Chen, Y.-L. Chueh, J.-H. He, M.-Y. Chou and L.-J. Li, Ultrahigh-Gain Photodetectors Based on Atomically Thin Graphene–MoS<sub>2</sub> Heterostructures, *Sci. Rep.*, 2014, **4**, 3826.

227 M. Z. Iqbal, S. Khan and S. Siddique, Ultraviolet-Light-Driven Photoresponse of Chemical Vapor Deposition Grown Molybdenum Disulfide/Graphene Heterostructured FET, *Appl. Surf. Sci.*, 2018, **459**, 853–859.

228 Y. T. Lee, J.-H. Kang, K. Kwak, J. Ahn, H. T. Choi, B.-K. Ju, S. H. Shokouh, S. Im, M.-C. Park and D. K. Hwang, High-Performance 2D MoS<sub>2</sub> Phototransistor for Photo Logic Gate and Image Sensor, *ACS Photonics*, 2018, **5**, 4745–4750.

229 C. Chen, H. Qiao, S. Lin, C. M. Luk, Y. Liu, Z. Xu, J. Song, Y. Xue, D. Li, J. Yuan, W. Yu, C. Pan, S. P. Lau and Q. Bao, Highly Responsive MoS<sub>2</sub> Photodetectors Enhanced by Graphene Quantum Dots, *Sci. Rep.*, 2015, **5**, 11830.

230 T. Chen, Y. Zhou, Y. Sheng, X. Wang, S. Zhou and J. H. Warner, Hydrogen-Assisted Growth of Large-Area Continuous Films of MoS<sub>2</sub> on Monolayer Graphene, *ACS Appl. Mater. Interfaces*, 2018, **10**, 7304–7314.

231 (a) S. J. Kim, M.-A. Kang, I.-S. Jeon, S. Ji, W. Song, S. Myung, S. S. Lee, J. Lim and K.-S. An, Fabrication of High-Performance Flexible Photodetectors Based on Zn-Doped MoS<sub>2</sub>/Graphene Hybrid Fibers, *J. Mater. Chem. C*, 2017, **5**, 12354–12359; (b) I. S. Jeon, S. J. Kim, W. Song, S. Myung, J. Lim, S. S. Lee, H. K. Jung, J. Hwang and K. S. An, One-step synthesis of Zn-doped MoS<sub>2</sub> nanosheets with tunable doping concentration using dopants-loaded seeding promoters for visible-light flexible photodetectors, *J. Alloys Compd.*, 2020, **835**, 155383.

232 M. Asad, S. Salimian, M. H. Sheikhi and M. Pourfath, Flexible Phototransistors Based on Graphene Nanoribbon Decorated with MoS<sub>2</sub> Nanoparticles, *Sens. Actuators, A*, 2015, **232**, 285–291.

233 D. De Fazio, I. Goykhman, D. Yoon, M. Bruna, A. Eiden, S. Milana, U. Sassi, M. Barbone, D. Dumcenco, K. Marinov, A. Kis and A. C. Ferrari, High Responsivity, Large-Area Graphene/MoS<sub>2</sub> Flexible Photodetectors, *ACS Nano*, 2016, **10**, 8252–8262.

234 M.-A. Kang, S. J. Kim, W. Song, S.-J. Chang, C.-Y. Park, S. Myung, J. Lim, S. S. Lee and K.-S. An, Fabrication of Flexible Optoelectronic Devices Based on MoS<sub>2</sub>/Graphene Hybrid Patterns by a Soft Lithographic Patterning Method, *Carbon*, 2017, **116**, 167–173.

235 B. Sun, T. Shi, Z. Liu, Y. Wu, J. Zhou and G. Liao, Large-Area Flexible Photodetector Based on Atomically Thin MoS<sub>2</sub>/Graphene Film, *Mater. Des.*, 2018, **154**, 1–7.

236 S. Liang, Z. Ma, G. Wu, N. Wei, L. Huang, H. Huang, H. Liu, S. Wang and L.-M. Peng, Microcavity-Integrated Carbon Nanotube Photodetectors, *ACS Nano*, 2016, **10**, 6963–6971.

237 P. Avouris, M. Freitag and V. Perebeinos, Carbon-Nanotube Photonics and Optoelectronics, *Nat. Photonics*, 2008, **2**, 341–350.

238 S. Nanot, A. W. Cummings, C. L. Pint, A. Ikeuchi, T. Akiho, K. Sueoka, R. H. Hauge, F. Léonard and J. Kono, Broadband, Polarization-Sensitive Photodetector Based on Optically-Thick Films of Macroscopically Long, Dense and Aligned Carbon Nanotubes, *Sci. Rep.*, 2013, **3**, 1335.

239 M. Salvato, M. Scagliotti, M. De Crescenzi, M. Crivellari, P. Prospisito, I. Cacciotti and P. Castrucci, Single Walled Carbon Nanotube/Si Heterojunctions for High Responsivity Photodetectors, *Nanotechnology*, 2017, **28**, 435201.

240 A. Behnam, J. Johnson, Y. Choi, L. Noriega, M. G. Ertosun, Z. Wu, A. G. Rinzler, P. Kapur, K. C. Saraswat and A. Ural, Metal-Semiconductor-Metal Photodetectors Based on Single-Walled Carbon Nanotube Film–GaAs Schottky Contacts, *J. Appl. Phys.*, 2008, **103**, 114315.

241 Y. Liu, F. Wang, X. Wang, X. Wang, E. Flahaut, X. Liu, Y. Li, X. Wang, Y. Xu, Y. Shi and R. Zhang, Planar Carbon Nanotube–Graphene Hybrid Films for High-Performance Broadband Photodetectors, *Nat. Commun.*, 2015, **6**, 8589.

242 S. Park, S. J. Kim, J. H. Nam, G. Pitner, T. H. Lee, A. L. Ayzner, H. Wang, S. W. Fong, M. Vosgueritchian, Y. J. Park, M. L. Brongersma and Z. Bao, Significant Enhancement of Infrared Photodetector Sensitivity Using a Semiconducting Single-Walled Carbon Nanotube/C60 Phototransistor, *Adv. Mater.*, 2015, **27**, 759–765.

243 T.-F. Zhang, Z.-P. Li, J.-Z. Wang, W.-Y. Kong, G.-A. Wu, Y.-Z. Zheng, Y.-W. Zhao, E.-X. Yao, N.-X. Zhuang and L.-B. Luo, Broadband Photodetector Based on Carbon Nanotube Thin Film/Single Layer Graphene Schottky Junction, *Sci. Rep.*, 2016, **6**, 38569.

244 Q. Wang, D. Zhang, Y. Wu, T. Li, A. Zhang and M. Miao, Fabrication of Supercapacitors from NiCo<sub>2</sub>O<sub>4</sub> Nanowire/Carbon-Nanotube Yarn for Ultraviolet Photodetectors and Portable Electronics, *Energy Technol.*, 2017, **5**, 1449–1456.



245 J. Cao, Y. Zou, X. Gong, P. Gou, J. Qian, R. Qian and Z. An, Double-Layer Heterostructure of Graphene/Carbon Nanotube Films for Highly Efficient Broadband Photodetector, *Appl. Phys. Lett.*, 2018, **113**, 061112.

246 G. Li, M. Suja, M. Chen, E. Belyarov, R. C. Haddon, J. Liu and M. E. Itkis, Visible-Blind UV Photodetector Based on Single-Walled Carbon Nanotube Thin Film/ZnO Vertical Heterostructures, *ACS Appl. Mater. Interfaces*, 2017, **9**, 37094–37104.

247 Y. Tang, H. Fang, M. Long, G. Chen, Z. Zheng, J. Zhang, W. Zhou, Z. Ning, Z. Zhu, Y. Feng, S. Qin, X. Chen, W. Lu and W. Hu, Significant Enhancement of Single-Walled Carbon Nanotube Based Infrared Photodetector Using PbS Quantum Dots, *IEEE J. Sel. Top. Quantum Electron.*, 2018, **24**, 1–8.

248 I. Ka, L. F. Gerlein, R. Nechache and S. G. Cloutier, High-Performance Nanotube-Enhanced Perovskite Photodetectors, *Sci. Rep.*, 2017, **7**, 45543.

249 W. Xu, Y. Guo, X. Zhang, L. Zheng, T. Zhu, D. Zhao, W. Hu and X. Gong, Room-Temperature-Operated Ultrasensitive Broadband Photodetectors by Perovskite Incorporated with Conjugated Polymer and Single-Wall Carbon Nanotubes, *Adv. Funct. Mater.*, 2017, **28**, 1705541.

250 K. Bergemann and F. Léonard, Room-Temperature Phototransistor with Negative Photoresponsivity of  $108 \text{ A W}^{-1}$  Using Fullerene-Sensitized Aligned Carbon Nanotubes, *Small*, 2018, **14**, 1802806.

251 Z. Zhou, Y. Ding, H. Ma, L. Cao, X. Wang, X. Huang, J. Liu and W. Huang, Bilayer Nanocarbon Heterojunction for Full-Solution Processed Flexible All-Carbon Visible Photodetector, *APL Mater.*, 2019, **7**, 031501.

252 A. Zubair, X. Wang, F. Mirri, D. E. Tsentalovich, N. Fujimura, D. Suzuki, K. P. Soundarapandian, Y. Kawano, M. Pasquali and J. Kono, Carbon Nanotube Woven Textile Photodetector, *Phys. Rev. Mater.*, 2018, **2**, 015201.

253 S. Zhang, L. Cai, T. Wang, J. Miao, N. Sepúlveda and C. Wang, Fully Printed Flexible Carbon Nanotube Photodetectors, *Appl. Phys. Lett.*, 2017, **110**, 123105.

254 S. Pyo, W. Kim, H.-I. Jung, J. Choi and J. Kim, Heterogeneous Integration of Carbon-Nanotube-Graphene for High-Performance, Flexible, and Transparent Photodetectors, *Small*, 2017, **13**, 1700918.

255 V. T. Nguyen, W. Yim, S. J. Park, B. H. Son, Y. C. Kim, T. T. Cao, Y. Sim, Y.-J. Moon, V. C. Nguyen, M.-J. Seong, S.-K. Kim, Y. H. Ahn, S. Lee and J.-Y. Park, Phototransistors with Negative or Ambipolar Photoresponse Based on As-Grown Heterostructures of Single-Walled Carbon Nanotube and MoS<sub>2</sub>, *Adv. Funct. Mater.*, 2018, **28**, 1802572.

256 L. Li, Y. Guo, Y. Sun, L. Yang, L. Qin, S. Guan, J. Wang, X. Qiu, H. Li, Y. Shang and Y. Fang, A General Method for the Chemical Synthesis of Large-Scale, Seamless Transition Metal Dichalcogenide Electronics, *Adv. Mater.*, 2018, **30**, e1706215.

257 N. Huo, J. Kang, Z. Wei, S.-S. Li, J. Li and S.-H. Wei, Novel and Enhanced Optoelectronic Performances of Multilayer MoS<sub>2</sub>-WS<sub>2</sub> Heterostructure Transistors, *Adv. Funct. Mater.*, 2014, **24**, 7025–7031.

258 (a) P. Lin, L. Zhu, D. Li, L. Xu, C. Pan and Z. Wang, Piezo-Phototronic Effect for Enhanced Flexible MoS<sub>2</sub>/WSe<sub>2</sub> van der Waals Photodiodes, *Adv. Funct. Mater.*, 2018, **28**, 1802849; (b) W. Wu, L. Wang, R. Yu, Y. Liu, S. H. Wei, J. Hone and Z. L. Wang, Piezophototronic Effect in Single-Atomic-Layer MoS<sub>2</sub> for Strain-Gated Flexible Optoelectronics, *Adv. Mater.*, 2016, **28**, 8463–8468; (c) X. Liu, X. Yang, G. Gao, Z. Yang, H. Liu, Q. Li, Z. Lou, G. Shen, L. Liao, C. Pan and Z. Lin Wang, Enhancing photoresponsivity of self-aligned MoS<sub>2</sub> field-effect transistors by piezo-phototronic effect from GaN nanowires, *ACS Nano*, 2016, **10**, 7451–7457.

259 Z. Zheng, J. Yao and G. Yang, Centimeter-Scale Deposition of Mo<sub>0.5</sub>W<sub>0.5</sub>Se<sub>2</sub> Alloy Film for High-Performance Photodetectors on Versatile Substrates, *ACS Appl. Mater. Interfaces*, 2017, **9**, 14920–14928.

260 V. Q. Dang, T. Q. Trung, D.-I. Kim, L. T. Duy, B.-U. Hwang, D.-W. Lee, B.-Y. Kim, L. D. Toan and N.-E. Lee, Ultrahigh Responsivity in Graphene-ZnO Nanorod Hybrid UV Photodetector, *Small*, 2015, **11**, 3054–3065.

261 D.-Y. Guo, C.-X. Shan, S.-N. Qu and D.-Z. Shen, Highly Sensitive Ultraviolet Photodetectors Fabricated from ZnO Quantum Dots/Carbon Nanodots Hybrid Films, *Sci. Rep.*, 2014, **4**, 7469.

262 B. D. Boruah and A. Misra, Conjugated Assembly of Colloidal Zinc Oxide Quantum Dots and Multiwalled Carbon Nanotubes for an Excellent Photosensitive Ultraviolet Photodetector, *Nanotechnology*, 2016, **27**, 355204.

263 D. Shao, H. Sun, J. Gao, G. Xin, M. A. Aguilar, T. Yao, N. Koratkar, J. Lian and S. Sawyer, Flexible, Thorn-Like ZnO-Multiwalled Carbon Nanotube Hybrid Paper for Efficient Ultraviolet Sensing and Photocatalyst Applications, *Nanoscale*, 2014, **6**, 13630–13636.

264 W. Wu, L. Wang, R. Yu, Y. Liu, S. H. Wei, J. Hone and Z. L. Wang, Piezophototronic effect in single-atomic-layer MoS<sub>2</sub> for strain-gated flexible optoelectronics, *Adv. Mater.*, 2016, **28**, 8463–8468.

265 N. Nasiri, R. Bo, F. Wang, L. Fu and A. Tricoli, Ultraporous Electron-Depleted ZnO Nanoparticle Networks for Highly Sensitive Portable Visible-Blind UV Photodetectors, *Adv. Mater.*, 2015, **27**, 4336–4343.

266 D.-K. Kwon, S. J. Lee and J.-M. Myoung, High-Performance Flexible ZnO Nanorod UV Photodetectors with a Network-Structured Cu Nanowire Electrode, *Nanoscale*, 2016, **8**, 16677–16683.

267 L. Li, L. Gu, Z. Lou, Z. Fan and G. Shen, ZnO Quantum Dot Decorated Zn<sub>2</sub>SnO<sub>4</sub> Nanowire Heterojunction Photodetectors with Drastic Performance Enhancement and Flexible Ultraviolet Image Sensors, *ACS Nano*, 2017, **11**, 4067–4076.

268 V.-T. Tran, Y. Wei, H. Yang, Z. Zhan and H. Du, All-Inkjet-Printed Flexible ZnO Micro Photodetector for a Wearable UV Monitoring Device, *Nanotechnology*, 2017, **28**, 095204.



269 A. A. Gupta, S. Arunachalam, S. G. Cloutier and R. Izquierdo, Fully Aerosol-Jet Printed, High-Performance Nanoporous ZnO Ultraviolet Photodetectors, *ACS Photonics*, 2018, **5**, 3923–3929.

270 C. G. Núñez, A. Vilouras, W. T. Navaraj, F. Liu and R. Dahiya, ZnO Nanowires-Based Flexible UV Photodetector System for Wearable Dosimetry, *IEEE Sens. J.*, 2018, **18**, 7881–7888.

271 Z. Lou, X. Yang, H. Chen and Z. Liang, Flexible Ultraviolet Photodetectors Based on ZnO–SnO<sub>2</sub> Heterojunction Nanowire Arrays, *J. Semicond.*, 2018, **39**, 024002.

272 D.-H. Kang, S.-T. Hong, A. Oh, S.-H. Kim, H.-Y. Yu and J.-H. Park, Nondegenerate n-Type Doping Phenomenon on Molybdenum Disulfide (MoS<sub>2</sub>) by Zinc Oxide (ZnO), *Mater. Res. Bull.*, 2016, **82**, 26–30.

273 G. Nazir, M. F. Khan, I. Akhtar, K. Akbar, P. Gautam, H. Noh, Y. Seo, S.-H. Chun and J. Eom, Enhanced Photoresponse of ZnO Quantum Dot-Decorated MoS<sub>2</sub> Thin Films, *RSC Adv.*, 2017, **7**, 16890–16900.

274 Y.-J. Hsiao, T.-H. Fang, L.-W. Ji and B.-Y. Yang, Red-Shift Effect and Sensitive Responsivity of MoS<sub>2</sub>/ZnO Flexible Photodetectors, *Nanoscale Res. Lett.*, 2015, **10**, 443.

275 S. W. Pak, D. Chu, D. Y. Song, S. K. Lee and E. K. Kim, Enhancement of Near-Infrared Detectability from InGaZnO Thin Film Transistor with MoS<sub>2</sub> Light Absorbing Layer, *Nanotechnology*, 2017, **28**, 475206.

276 J. Yang, H. Kwak, Y. Lee, Y.-S. Kang, M.-H. Cho, J. H. Cho, Y.-H. Kim, S.-J. Jeong, S. Park, H.-J. Lee and H. Kim, MoS<sub>2</sub>-InGaZnO Heterojunction Phototransistors with Broad Spectral Responsivity, *ACS Appl. Mater. Interfaces*, 2016, **8**, 8576–8582.

277 Y. B. Lee, S. K. Kim, Y. R. Lim, I. S. Jeon, W. Song, S. Myung, S. S. Lee, J. Lim and K.-S. An, Dimensional-Hybrid Structures of 2D Materials with ZnO Nanostructures via pH-Mediated Hydrothermal Growth for Flexible UV Photodetectors, *ACS Appl. Mater. Interfaces*, 2017, **9**, 15031–15037.

278 D. B. Velusamy, M. A. Haque, M. R. Parida, F. Zhang, T. Wu, O. F. Mohammed and H. N. Alshareef, 2D Organic-Inorganic Hybrid Thin Films for Flexible UV-Visible Photodetectors, *Adv. Funct. Mater.*, 2017, **27**, 1605554.

279 F. Yu, M. Hu, F. Kang and R. Lv, Flexible Photodetector Based on Large-Area Few-Layer MoS<sub>2</sub>, *Prog. Nat. Sci.: Mater. Int.*, 2018, **28**, 563–568.

280 J.-W. T. Seo, J. Zhu, V. K. Sangwan, E. B. Secor, S. G. Wallace and M. C. Hersam, Fully Inkjet-Printed, Mechanically Flexible MoS<sub>2</sub> Nanosheet Photodetectors, *ACS Appl. Mater. Interfaces*, 2019, **11**, 5675–5681.

281 E. P. Nguyen, B. J. Carey, J. Z. Ou, J. van Embden, E. D. Gaspera, A. F. Chrimes, M. J. Spencer, S. Zhuiykov, K. Kalantar-zadeh and T. Daeneke, Electronic tuning of 2D MoS<sub>2</sub> through surface functionalization, *Adv. Mater.*, 2015, **27**, 6225–6229.

282 C. Backes, N. C. Berner, X. Chen, P. Lafargue, P. LaPlace, M. Freeley, G. S. Duesberg, J. N. Coleman and A. R. McDonald, Functionalization of liquid-exfoliated two-dimensional 2H-MoS<sub>2</sub>, *Angew. Chem., Int. Ed.*, 2015, **54**, 2638–2642.

283 X. Chen, N. C. Berner, C. Backes, G. S. Duesberg and A. R. McDonald, Functionalization of Two-Dimensional MoS<sub>2</sub>: On the Reaction Between MoS<sub>2</sub> and Organic Thiols, *Angew. Chem., Int. Ed.*, 2016, **55**, 5803–5808.

284 S. Presolski and M. Pumera, Covalent functionalization of MoS<sub>2</sub>, *Mater. Today*, 2016, **19**, 140–145.

285 Q. Tang and D. E. Jiang, Stabilization and band-gap tuning of the 1T-MoS<sub>2</sub> monolayer by covalent functionalization, *Chem. Mater.*, 2015, **27**, 3743–3748.

286 Q. Ding, K. J. Czech, Y. Zhao, J. Zhai, R. J. Hamers, J. C. Wright and S. Jin, Basal-plane ligand functionalization on semiconducting 2H-MoS<sub>2</sub> monolayers, *ACS Appl. Mater. Interfaces*, 2017, **9**, 12734–12742.

287 T. Liu, C. Wang, X. Gu, H. Gong, L. Cheng, X. Shi, L. Feng, B. Sun and Z. Liu, Drug delivery with PEGylated MoS<sub>2</sub> nano-sheets for combined photothermal and chemotherapy of cancer, *Adv. Mater.*, 2014, **26**, 3433–3440.

288 N. F. Chiu and T. L. Lin, Affinity capture surface carboxyl-functionalized MoS<sub>2</sub> sheets to enhance the sensitivity of surface plasmon resonance immunosensors, *Talanta*, 2018, **185**, 174–181.

289 E. E. Benson, H. Zhang, S. A. Schuman, S. U. Nanayakkara, N. D. Bronstein, S. Ferrere, J. L. Blackburn and E. M. Miller, Balancing the hydrogen evolution reaction, surface energetics, and stability of metallic MoS<sub>2</sub> nanosheets via covalent functionalization, *J. Am. Chem. Soc.*, 2017, **140**, 441–450.

290 S. Karunakaran, S. Pandit, B. Basu and M. De, Simultaneous Exfoliation and Functionalization of 2H-MoS<sub>2</sub> by Thiolated Surfactants: Applications in Enhanced Antibacterial Activity, *J. Am. Chem. Soc.*, 2018, **140**, 12634–12644.

291 S. D. Jiang, G. Tang, Z. M. Bai, Y. Y. Wang, Y. Hu and L. Song, Surface functionalization of MoS<sub>2</sub> with POSS for enhancing thermal, flame-retardant and mechanical properties in PVA composites, *RSC Adv.*, 2014, **4**, 3253–3262.

292 L. Zhou, B. He, Y. Yang and Y. He, Facile approach to surface functionalized MoS<sub>2</sub> nanosheets, *RSC Adv.*, 2014, **4**, 32570–32578.

293 S. Pak, A. R. Jang, J. Lee, J. Hong, P. Giraud, S. Lee, Y. Cho, G. H. An, Y. W. Lee, H. S. Shin, S. M. Morris, S. Cha, J. Sohn and J. M. Kim, Surface functionalization-induced photoresponse characteristics of monolayer MoS<sub>2</sub> for fast flexible photodetectors, *Nanoscale*, 2019, **11**, 4726–4734.

294 W. Deng, Y. Chen, C. You, B. Liu, Y. Yang, G. Shen, S. Li, L. Sun, Y. Zhang and H. Yan, High detectivity from a lateral graphene–MoS<sub>2</sub> Schottky photodetector grown by chemical vapor deposition, *Adv. Electron. Mater.*, 2018, **4**, 1800069.

295 J. Ma, K. Y. Choi, S. H. Kim, H. Lee and G. Yoo, All polymer encapsulated, highly-sensitive MoS<sub>2</sub> phototransistors on flexible PAR substrate, *Appl. Phys. Lett.*, 2018, **113**, 013102.



296 M. A. Kang, S. Kim, I. S. Jeon, Y. R. Lim, C. Y. Park, W. Song, S. S. Lee, J. Lim, K. S. An and S. Myung, Highly efficient and flexible photodetector based on MoS<sub>2</sub>-ZnO heterostructures, *RSC Adv.*, 2019, **9**, 19707–19711.

297 S. Mukherjee, S. Jana, T. K. Sinha, S. Das and S. K. Ray, Infrared Tunable, Two Colour-Band Photodetectors on Flexible Platforms using 0D/2D PbS-MoS<sub>2</sub> Hybrids, *Nanoscale Adv.*, 2019, **1**, 3279–3287.

298 R. H. Kim, J. Leem, C. Muratore, S. Nam, R. Rao, A. Jawaid, M. Durstock, M. McConney, L. Drummy, R. Rai and A. Voevodin, Photonic crystallization of two-dimensional MoS<sub>2</sub> for stretchable photodetectors, *Nanoscale*, 2019, **11**, 13260–13268.

299 Y. Wei, V. T. Tran, C. Zhao, H. Liu, J. Kong and H. Du, Robust Photodetectable Paper from Chemically Exfoliated MoS<sub>2</sub>-MoO<sub>3</sub> Multilayers, *ACS Appl. Mater. Interfaces*, 2019, **11**, 21445–21453.

300 P. Han, L. St. Marie, Q. X. Wang, N. Quirk, A. El Fatimy, M. Ishigami and P. Barbara, Highly Sensitive MoS<sub>2</sub> Photodetectors with Graphene Contacts, *Nanotechnology*, 2018, **29**, 20LT01.

301 (a) S. S. Chee, D. Seo, H. Kim, H. Jang, S. Lee, S. P. Moon, K. H. Lee, S. W. Kim, H. Choi and M. H. Ham, Lowering the Schottky Barrier Height by Graphene/Ag Electrodes for High-Mobility MoS<sub>2</sub> Field-Effect Transistors, *Adv. Mater.*, 2019, **31**, 1804422; (b) J. Li, X. Mao, S. Xie, Z. Geng and H. Chen, Bipolar phototransistor in a vertical Au/graphene/MoS<sub>2</sub> van der Waals heterojunction with photocurrent enhancement, *Photonics Res.*, 2020, **8**, 39–45; (c) I. Lee, W. T. Kang, J. E. Kim, Y. R. Kim, U. Y. Won, Y. H. Lee and W. J. Yu, Photoinduced Tuning of Schottky Barrier Height in Graphene/MoS<sub>2</sub> Heterojunction for Ultrahigh Performance Short Channel Phototransistor, *ACS Nano*, 2020, **14**, 7574–7580.

302 S. Kallatt, S. Nair and K. Majumdar, Asymmetrically Encapsulated Vertical ITO/MoS<sub>2</sub>/Cu<sub>2</sub>O Photodetector with Ultrahigh Sensitivity, *Small*, 2017, **14**, 1702066.

303 K. Zhang, M. Peng, A. Yu, Y. Fan, J. Zhai and Z. L. Wang, A Substrate-Enhanced MoS<sub>2</sub> Photodetector Through a Dual-Photogating Effect, *Mater. Horiz.*, 2019, **6**, 826–833.

304 Y. Lee, J. Yang, D. Lee, Y.-H. Kim, J.-H. Park, H. Kim and J. H. Cho, Trap-Induced Photoresponse of Solution-Synthesized MoS<sub>2</sub>, *Nanoscale*, 2016, **8**, 9193–9200.

305 S. Qiao, R. Cong, J. Liu, B. Liang, G. Fu, W. Yu, K. Ren, S. Wang and C. Pan, A Vertically Layered MoS<sub>2</sub>/Si Heterojunction for an Ultrahigh and Ultrafast Photoresponse Photodetector, *J. Mater. Chem. C*, 2018, **6**, 3233–3239.

306 W. Wang, A. Klots, D. Prasai, Y. Yang, K. I. Bolotin and J. Valentine, Hot Electron-Based Near-Infrared Photodetection Using Bilayer MoS<sub>2</sub>, *Nano Lett.*, 2015, **15**, 7440–7444.

307 D.-S. Tsai, K.-K. Liu, D.-H. Lien, M.-L. Tsai, C.-F. Kang, C.-A. Lin, L.-J. Li and J.-H. He, Few-Layer MoS<sub>2</sub> with High Broadband Photogain and Fast Optical Switching for Use in Harsh Environments, *ACS Nano*, 2013, **7**, 3905–3911.

308 W. Choi, M. Y. Cho, A. Konar, J. H. Lee, G.-B. Cha, S. C. Hong, S. Kim, J. Kim, D. Jena, J. Joo and S. Kim, High-Detectivity Multilayer MoS<sub>2</sub> Phototransistors with Spectral Response from Ultraviolet to Infrared, *Adv. Mater.*, 2012, **24**, 5832–5836.

309 H. Xu, J. Wu, Q. Feng, N. Mao, C. Wang and J. Zhang, High Responsivity and Gate Tunable Graphene-MoS<sub>2</sub> Hybrid Phototransistor, *Small*, 2014, **10**, 2300–2306.

310 R. Kumar, N. Goel, R. Raliya, P. Biswas and M. Kumar, High-Performance Photodetector Based on Hybrid of MoS<sub>2</sub> and Reduced Graphene Oxide, *Nanotechnology*, 2018, **29**, 404001.

311 Z. Lou, L. Zeng, Y. Wang, D. Wu, T. Xu, Z. Shi, Y. Tian, X. Li and Y. H. Tsang, High-Performance MoS<sub>2</sub>/Si Heterojunction Broadband Photodetectors from Deep Ultraviolet to Near Infrared, *Opt. Lett.*, 2017, **42**, 3335–3338.

312 (a) V. Dhyani and S. Das, High-Speed Scalable Silicon-MoS<sub>2</sub> P-N Heterojunction Photodetectors, *Sci. Rep.*, 2017, **7**, 44243; (b) V. Dhyani, P. Dwivedi, S. Dhanekar and S. Das, High performance broadband photodetector based on MoS<sub>2</sub>/porous silicon heterojunction, *Appl. Phys. Lett.*, 2017, **111**, 191107.

313 Y. Zhang, Y. Yu, L. Mi, H. Wang, Z. Zhu, Q. Wu, Y. Zhang and Y. Jiang, *In situ* Fabrication of Vertical Multilayered MoS<sub>2</sub>/Si Homotype Heterojunction for High-Speed Visible-Near-Infrared Photodetectors, *Small*, 2016, **12**, 1062–1071.

314 X. Liu, F. Li, M. Xu, T. Shen, Z. Yang, W. Fan and J. Qi, High Response, Self-Powered Photodetector Based on the Monolayer MoS<sub>2</sub>/P-Si Heterojunction with Asymmetric Electrodes, *Langmuir*, 2018, **34**, 14151–14157.

315 J. Deng, Z. Guo, Y. Zhang, X. Cao, S. Zhang, Y. Sheng, H. Xu, W. Bao and J. Wan, MoS<sub>2</sub>/Silicon-on-Insulator Heterojunction Field-Effect-Transistor for High-Performance Photodetection, *IEEE Electron Device Lett.*, 2019, **40**, 423–426.

316 R. Zhuo, Y. Wang, D. Wu, Z. Lou, Z. Shi, T. Xu, J. Xu, Y. Tian and X. Li, High-Performance Self-Powered Deep Ultraviolet Photodetector Based on MoS<sub>2</sub>/GaN p-n Heterojunction, *J. Mater. Chem. C*, 2018, **6**, 299–303.

317 (a) X. Liu, Y. Chen, D. Li, S.-W. Wang, C.-C. Ting, L. Chen, K.-W. Ang, C.-W. Qiu, Y.-L. Chueh, X. Sun and H.-C. Kuo, Nearly Lattice-Matched Molybdenum Disulfide/Gallium Nitride Heterostructure Enabling High-Performance Phototransistors, *Photonics Res.*, 2019, **7**, 311–317; (b) Z. Li, J. Luo, S. Hu, Q. Liu, W. Yu, Y. Lu and X. Liu, Strain enhancement for a MoS<sub>2</sub>-on-GaN photodetector with an Al<sub>2</sub>O<sub>3</sub> stress liner grown by atomic layer deposition, *Photonics Res.*, 2020, **8**, 799–805.

318 Z. Xu, S. Lin, X. Li, S. Zhang, Z. Wu, W. Xu, Y. Lu and S. Xu, Monolayer MoS<sub>2</sub>/GaAs Heterostructure Self-Driven Photodetector with Extremely High Detectivity, *Nano Energy*, 2016, **23**, 89–96.

319 D. Kufer, T. Lasanta, M. Bernechea, F. H. L. Koppens and G. Konstantatos, Interface Engineering in Hybrid Quantum Dot-2D Phototransistors, *ACS Photonics*, 2016, **3**, 1324–1330.



320 K. K. Paul, L. P. L. Mawlong and P. K. Giri, Trion-Inhibited Strong Excitonic Emission and Broadband Giant Photoresponsivity from Chemical Vapor-Deposited Monolayer MoS<sub>2</sub> Grown *in situ* on TiO<sub>2</sub> Nanostructure, *ACS Appl. Mater. Interfaces*, 2018, **10**, 42812–42825.

321 Y. Wen, L. Yin, P. He, Z. Wang, X. Zhang, Q. Wang, T. A. Shifa, K. Xu, F. Wang, X. Zhan, F. Wang, C. Jiang and J. He, Integrated High-Performance Infrared Phototransistor Arrays Composed of Nonlayered PbS-MoS<sub>2</sub> Heterostructures with Edge Contacts, *Nano Lett.*, 2016, **16**, 6437–6444.

322 (a) D. Kufer, I. Nikitskiy, T. Lasanta, G. Navickaite, F. H. L. Koppens and G. Konstantatos, Hybrid 2D-0D MoS<sub>2</sub>-PbS Quantum Dot Photodetectors, *Adv. Mater.*, 2014, **27**, 176–180; (b) Y. Pak, S. Mitra, N. Alaal, B. Xin, S. Lopatin, D. Almalawi, J. W. Min, H. Kim, W. Kim, G. Y. Jung and I. S. Roqan, Dark-current reduction accompanied photocurrent enhancement in p-type MnO quantum-dot decorated n-type 2D-MoS<sub>2</sub>-based photodetector, *Appl. Phys. Lett.*, 2020, **116**, 112102.

323 H.-S. Ra, D.-H. Kwak and J.-S. Lee, A Hybrid MoS<sub>2</sub> Nanosheet–CdSe Nanocrystal Phototransistor with a Fast Photoresponse, *Nanoscale*, 2016, **8**, 17223–17230.

324 Y. Chen, X. Wang, P. Wang, H. Huang, G. Wu, B. Tian, Z. Hong, Y. Wang, S. Sun, H. Shen, J. Wang, W. Hu, J. Sun, X. Meng and J. Chu, Optoelectronic Properties of Few-Layer MoS<sub>2</sub> FET Gated by Ferroelectric Relaxor Polymer, *ACS Appl. Mater. Interfaces*, 2016, **8**, 32083–32088.

325 (a) K. A. N. Duerloo, Y. Li and E. J. Reed, Structural phase transitions in two-dimensional Mo-and W-dichalcogenide monolayers, *Nat. Commun.*, 2014, **5**, 1–9; (b) Y. Guo, D. Sun, B. Ouyang, A. Raja, J. Song, T. F. Heinz and L. E. Brus, Probing the dynamics of the metallic-to-semiconducting structural phase transformation in MoS<sub>2</sub> crystals, *Nano Lett.*, 2015, **15**, 5081–5088; (c) Y. Wang, R. Fullon, M. Acerce, C. E. Petoukhoff, J. Yang, C. Chen, S. Du, S. K. Lai, S. P. Lau, D. Voiry, D. O'Carroll, G. Gupta, A. D. Mohite, S. Zhang, H. Zhou and M. Chhowalla, Solution-Processed MoS<sub>2</sub>/Organolead Trihalide Perovskite Photodetectors, *Adv. Mater.*, 2017, **29**, 1603995; (d) W. Wang, X. Zeng, J. H. Warner, Z. Guo, Y. Hu, Y. Zeng, J. Lu, W. Jin, S. Wang, J. Lu, Y. Zeng and Y. Xiao, Photoresponse-bias Modulation of High-Performance MoS<sub>2</sub> Photodetector with Unique Vertically Stacked 2H-MoS<sub>2</sub>/1T@ 2H-MoS<sub>2</sub> Structure, *ACS Appl. Mater. Interfaces*, 2020, **12**, 33325–33335.

326 J. He, Y. Yang, Y. He, C. Ge, Y. Zhao, L. Gao and J. Tang, Low Noise and Fast Photoresponse of Few-Layered MoS<sub>2</sub> Passivated by MA<sub>3</sub>Bi<sub>2</sub>Br<sub>9</sub>, *ACS Photonics*, 2018, **5**, 1877–1884.

327 F. Bai, J. Qi, F. Li, Y. Fang, W. Han, H. Wu and Y. Zhang, A High-Performance Self-Powered Photodetector Based on Monolayer MoS<sub>2</sub>/Perovskite Heterostructures, *Adv. Mater. Interfaces*, 2018, **5**, 1701275.

328 C. Fang, H. Wang, Z. Shen, H. Shen, S. Wang, J. Ma, J. Wang, H. Luo and D. Li, High-Performance Photodetectors Based on Lead-Free 2D Ruddlesden-Popper Perovskite/MoS<sub>2</sub> Heterostructures, *ACS Appl. Mater. Interfaces*, 2019, **11**, 8419–8427.

329 X. Zhou, N. Zhou, C. Li, H. Song, Q. Zhang, X. Hu, L. Gan, H. Li, J. Lü, J. Luo, J. Xiong and T. Zhai, Vertical Heterostructures Based on SnSe<sub>2</sub>/MoS<sub>2</sub> for High Performance Photodetectors, *2D Mater.*, 2017, **4**, 025048.

330 Y. Peng, R. Ding, Q. Ren, S. Xu, L. Sun, Y. Wang and F. Lu, High Performance Photodiode Based on MoS<sub>2</sub>/Pentacene Heterojunction, *Appl. Surf. Sci.*, 2018, **459**, 179–184.

331 D.-S. Um, Y. Lee, S. Lim, S. Park, H. Lee and H. Ko, High-Performance MoS<sub>2</sub>/CuO Nanosheet-On-One-Dimensional Heterojunction Photodetectors, *ACS Appl. Mater. Interfaces*, 2016, **8**, 33955–33962.

332 J. Jia, S. Jeon, J. Jeon, J. Xu, Y. J. Song, J. H. Cho, B. H. Lee, J. D. Song, H.-J. Kim, E. Hwang and S. Lee, Generalized Scheme for High Performing Photodetectors with a p-Type 2D Channel Layer and n-Type Nanoparticles, *Small*, 2018, **14**, 1703065.

333 H. Li, L. Ye and J. Xu, High-Performance Broadband Floating-Base Bipolar Phototransistor Based on WSe<sub>2</sub>/BP/MoS<sub>2</sub> Heterostructure, *ACS Photonics*, 2017, **4**, 823–829.

334 F. Wang, Z. Wang, K. Xu, F. Wang, Q. Wang, Y. Huang, L. Yin and J. He, Tunable GaTe-MoS<sub>2</sub> van der Waals p–n Junctions with Novel Optoelectronic Performance, *Nano Lett.*, 2015, **15**, 7558–7566.

335 X. Chen, Y. Qiu, H. Yang, G. Liu, W. Zheng, W. Feng, W. Cao, W. Hu and P. Hu, In-Plane Mosaic Potential Growth of Large-Area 2D Layered Semiconductors MoS<sub>2</sub>–MoSe<sub>2</sub> Lateral Heterostructures and Photodetector Application, *ACS Appl. Mater. Interfaces*, 2017, **9**, 1684–1691.

336 R. K. Ulaganathan, K. Yadav, R. Sankar, F. C. Chou and Y.-T. Chen, Hybrid InSe Nanosheets and MoS<sub>2</sub> Quantum Dots for High-Performance Broadband Photodetectors and Photovoltaic Cells, *Adv. Mater. Interfaces*, 2019, **6**, 1801336.

337 S. Li, X. Chen, F. M. Liu, Y. Chen, B. Liu, W. Deng, B. An, F. Chu, G. Zhang, S. Li and X. Li, Enhanced Performance of CVD MoS<sub>2</sub> Photodetector by Chemically *in situ* n-Type Doping, *ACS Appl. Mater. Interfaces*, 2019, **11**, 11636–11644.

338 N. Chaudhary, M. Khanuja and S. S. Islam, Broadband photodetector based on 3D architect of MoS<sub>2</sub>-PANI hybrid structure for high photoresponsive properties, *Polymer*, 2019, **165**, 168–173.

339 H. Im, N. Liu, A. Bala, S. Kim and W. Choi, Large-area MoS<sub>2</sub>-MoO<sub>x</sub> heterojunction thin-film photodetectors with wide spectral range and enhanced photoresponse, *APL Mater.*, 2019, **7**, 061101.

340 X. Wang, H. Shen, Y. Chen, G. Wu, P. Wang, H. Xia, T. Lin, P. Zhou, W. Hu, X. Meng and J. Chu, Multimechanism Synergistic Photodetectors with Ultrabroad Spectrum Response from 375 nm to 10 μm, *Adv. Sci.*, 2019, 1901050.

341 (a) L. Wang, X. Zou, J. Lin, J. Jiang, Y. Liu, X. Liu, X. Zhao, Y. F. Liu, J. C. Ho and L. Liao, Perovskite/Black Phosphorus/MoS<sub>2</sub> Photogate Reversed Photodiodes with Ultrahigh Light On/Off Ratio and Fast Response, *ACS Nano*, 2019, **13**, 4804–4813; (b) M. Long, A. Gao, P. Wang, H. Xia, C. Ott, C. Pan, Y. Fu, E. Liu, X. Chen, W. Lu and



T. Nilges, Room temperature high-detectivity mid-infrared photodetectors based on black arsenic phosphorus, *Sci. Adv.*, 2017, **3**, e1700589.

342 Z.-Q. Wu, J.-L. Yang, N. K. Manjunath, Y.-J. Zhang, S.-R. Feng, Y.-H. Lu, J.-H. Wu, W. W. Zhao, C.-Y. Qiu, J.-F. Li and S.-S. Lin, Gap-Mode Surface-Plasmon-Enhanced Photoluminescence and Photoresponse of MoS<sub>2</sub>, *Adv. Mater.*, 2018, **30**, 1706527.

343 W. Wu, Q. Zhang, X. Zhou, L. Li, J. Su, F. Wang and T. Zhai, Self-powered photovoltaic photodetector established on lateral monolayer MoS<sub>2</sub>-WS<sub>2</sub> heterostructures, *Nano Energy*, 2018, **51**, 45–53.

344 K. Ye, L. Liu, Y. Liu, A. Nie, K. Zhai, J. Xiang, B. Wang, F. Wen, C. Mu, Z. Zhao, Y. Gong, Z. Liu and Y. Tian, Lateral Bilayer MoS<sub>2</sub>-WS<sub>2</sub> Heterostructure Photodetectors with High Responsivity and Detectivity, *Adv. Opt. Mater.*, 2019, 1900815.

345 G. Yoo, S. L. Choi, S. J. Park, K.-T. Lee, S. Lee, M. S. Oh, J. Heo and H. J. Park, Flexible and Wavelength-Selective MoS<sub>2</sub> Phototransistors with Monolithically Integrated Transmission Color Filters, *Sci. Rep.*, 2017, **7**, 40945.

346 (a) N. Huo and G. Konstantatos, Ultrasensitive all-2D MoS<sub>2</sub> phototransistors enabled by an out-of-plane MoS<sub>2</sub> PN homojunction, *Nat. Commun.*, 2017, **8**, 572; (b) S. Liu, C. Nie, D. Zhou, J. Shen and S. Feng, Direct growth of vertical structure MoS<sub>2</sub> nanosheets array film via CVD method for photodetection, *Phys. E*, 2020, **117**, 113592.

347 K. Murali, N. Abraham, S. Das, S. Kallatt and K. Majumdar, Highly Sensitive, Fast Graphene Photodetector with Responsivity  $>10^6$  A W<sup>-1</sup> Using Floating Quantum Well Gate, *ACS Appl. Mater. Interfaces*, 2019, **11**, 30010–30018.

348 K. S. Kim, Y. J. Ji, K. H. Kim, S. Choi, D. H. Kang, K. Heo, S. Cho, S. Yim, S. Lee, J. H. Park and Y. S. Jung, Ultrasensitive MoS<sub>2</sub> photodetector by serial nano-bridge multi-heterojunction, *Nat. Commun.*, 2019, **10**, 1–10.

349 M. M. Furchi, D. K. Polyushkin, A. Pospischil and T. Mueller, Mechanisms of photoconductivity in atomically thin MoS<sub>2</sub>, *Nano Lett.*, 2014, **14**, 6165–6170.

350 M. Sun, D. Xie, Y. Sun, W. Li, C. Teng and J. Xu, Lateral multilayer/monolayer MoS<sub>2</sub> heterojunction for high performance photodetector applications, *Sci. Rep.*, 2017, **7**, 1–7.

351 H. Yan, J. Cheng, K. Zhu, A. Li, T. Peng and Y. Luo, Growth of monolayer and bilayer MoS<sub>2</sub> through the solution precursor for high-performance photodetectors, *Curr. Appl. Phys.*, 2020, **20**, 643–647.

352 (a) S. R. Tamalampudi, Y. Y. Lu, R. Kumar U, R. Sankar, C. D. Liao, K. Moorthy B, C. H. Cheng, F. C. Chou and Y. T. Chen, High performance and bendable few-layered InSe photodetectors with broad spectral response, *Nano Lett.*, 2014, **14**, 2800–2806; (b) S. Lei, F. Wen, L. Ge, S. Najmaei, A. George, Y. Gong, W. Gao, Z. Jin, B. Li, J. Lou and J. Kono, An atomically layered InSe avalanche photodetector, *Nano Lett.*, 2015, **15**, 3048–3055; (c) H. Shang, H. Chen, M. Dai, Y. Hu, F. Gao, H. Yang, B. Xu, S. Zhang, B. Tan, X. Zhang and P. Hu, Mixed-dimensional 1D Se-2D InSe van der Waals heterojunction for high responsivity self-powered photodetectors, *Nanoscale Horiz.*, 2020, **5**, 564–572; (d) Z. Chen, J. Biscaras and A. Shukla, A high performance graphene/few-layer InSe photo-detector, *Nanoscale*, 2015, **7**, 5981–5986.

353 R. K. Ulaganathan, K. Yadav, R. Sankar, F. C. Chou and Y. T. Chen, Hybrid InSe Nanosheets and MoS<sub>2</sub> Quantum Dots for High-Performance Broadband Photodetectors and Photovoltaic Cells, *Adv. Mater. Interfaces*, 2019, **6**, 1801336.

354 P. K. Mohapatra, K. Ranganathan, L. Dezanashvili, L. Houben and A. Ismach, Epitaxial growth of In<sub>2</sub>Se<sub>3</sub> on monolayer transition metal dichalcogenide single crystals for high performance photodetectors, *Appl. Mater. Today*, 2020, **20**, 100734.

355 M. Casalino, G. Coppola, R. M. De La Rue and D. F. Logan, State-of-the-art all-silicon sub-bandgap photodetectors at telecom and datacom wavelengths, *Laser Photonics Rev.*, 2016, **10**, 895–921.

356 J. Guo, S. Li, Y. Ke, Z. Lei, Y. Liu, L. Mao, T. Gong, T. Cheng, W. Huang and X. Zhang, Broadband photodetector based on vertically stage-like MoS<sub>2</sub>/Si heterostructure with ultra-high sensitivity and fast response speed, *Scr. Mater.*, 2020, **176**, 1–6.

357 D. H. Shin, D. H. Jung, Y. Kim, C. Lee, X. L. Wang and S. H. Choi, High-speed heterojunction photodiodes made of single-or multiple-layer MoS<sub>2</sub> directly-grown on Si quantum dots, *J. Alloys Compd.*, 2020, **820**, 153074.

358 C. L. Tan, H. Wei, T. M. K. Thandavam, R. Ramli, M. Park and H. Ahmad, Broadband high responsivity large-area plasmonic-enhanced multilayer MoS<sub>2</sub> on p-type silicon photodetector using Au nanostructures, *Mater. Res. Express*, 2019, **6**, 105090.

359 H. Tan, W. Xu, Y. Sheng, C. S. Lau, Y. Fan, Q. Chen, M. Tweedie, X. Wang, Y. Zhou and J. H. Warner, Lateral graphene-contacted vertically stacked WS<sub>2</sub>/MoS<sub>2</sub> hybrid photodetectors with large gain, *Adv. Mater.*, 2017, **29**, 1702917.

360 J. Zhang, Y. Liu, X. Zhang, Z. Ma, J. Li, C. Zhang, A. Shaikenova, B. Renat and B. Liu, High-Performance Ultraviolet-Visible Light-Sensitive 2D-MoS<sub>2</sub>/1D-ZnO Heterostructure Photodetectors, *ChemistrySelect*, 2020, **5**, 3438–3444.

361 Q. Wang, C. Z. Li, S. Ge, J. G. Li, W. Lu, J. Lai, X. Liu, J. Ma, D. P. Yu, Z. M. Liao and D. Sun, Ultrafast broadband photodetectors based on three-dimensional Dirac semimetal Cd<sub>3</sub>As<sub>2</sub>, *Nano Lett.*, 2017, **17**, 834–841.

362 Z. Huang, Y. Jiang, Q. Han, M. Yang, J. Han, F. Wang, M. Luo, Q. Li, H. Zhu, X. Liu and J. Gou, High responsivity and fast UV-vis-short-wavelength IR photodetector based on Cd<sub>3</sub>As<sub>2</sub>/MoS<sub>2</sub> heterojunction, *Nanotechnology*, 2019, **31**, 064001.

363 Y. Yuan, X. Zhang, H. Liu, T. Yang, W. Zheng, B. Zheng, F. Jiang, L. Li, D. Li, X. Zhu and A. Pan, Growth of CdSe/MoS<sub>2</sub> vertical heterostructures for fast visible-wavelength photodetectors, *J. Alloys Compd.*, 2020, **815**, 152309.

364 S. Ghosh, W. C. Chiang, M. Y. Fakhri, C. T. Wu, R. San Chen and S. Chattopadhyay, Ultrasensitive broadband



photodetector using electrostatically conjugated MoS<sub>2</sub>-upconversion nanoparticle nanocomposite, *Nano Energy*, 2020, **67**, 104258.

365 Y. Xiao, L. Min, X. Liu, W. Liu, U. Younis, T. Peng, X. Kang, X. Wu, S. Ding and D. W. Zhang, Facile integration of MoS<sub>2</sub>/SiC photodetector by direct chemical vapor deposition, *Nanophotonics*, 2020, **9**, 3035–3044.

366 D. Wu, Z. Lou, Y. Wang, Z. Yao, T. Xu, Z. Shi, J. Xu, Y. Tian, X. Li and Y. H. Tsang, Photovoltaic high-performance broadband photodetector based on MoS<sub>2</sub>/Si nanowire array heterojunction, *Sol. Energy Mater. Sol. Cells*, 2018, **182**, 272–280.

367 H. Wang, X. Wang, Y. Chen, S. Zhang, W. Jiang, X. Zhang, J. Qin, J. Wang, X. Li, Y. Pan and F. Liu, Extremely Low Dark Current MoS<sub>2</sub> Photodetector via 2D Halide Perovskite as the Electron Reservoir, *Adv. Opt. Mater.*, 2020, **8**, 1901402.

368 S. W. Shen, D. G. Chen, I. T. Chen, K. H. Chang, C. W. Lee, C. T. Fang, Y. T. Chen, W. T. Chuang, Y. H. Lee, Y. T. Wu and P. T. Chou, Delayed Charge Recombination by Open-Shell Organics: Its Application in Achieving Superb Photodetectors with Broadband (400–1160 nm) Ultrahigh Sensitivity and Stability, *Adv. Opt. Mater.*, 2020, **8**, 1902179.

369 S. Kumar, A. Sharma, Y. T. Ho, A. Pandey, M. Tomar, A. K. Kapoor, E. Y. Chang and V. Gupta, High performance UV photodetector based on MoS<sub>2</sub> layers grown by pulsed laser deposition technique, *J. Alloys Compd.*, 2020, **835**, 155222.

370 D. S. Schneider, A. Grundmann, A. Bablich, V. Passi, S. Kataria, H. Kalisch, M. Heuken, A. Vescan, D. Neumaier and M. C. Lemme, Highly responsive flexible photodetectors based on MOVPE grown uniform few-layer MoS<sub>2</sub>, *ACS Photonics*, 2020, **7**, 1388–1395.

371 R. Singh, A. Srivastava, S. Jit and S. Tripathi, High Responsivity Visible Blind Pd/Al<sub>2</sub>O<sub>3</sub>/MoS<sub>2</sub>/ITO MISIM UV Photodetector, *IEEE Photonics Technol. Lett.*, 2020, **32**, 733–736.

372 K. Ye, L. Liu, J. Huang, A. Nie, K. Zhai, B. Wang, F. Wen, C. Mu, Z. Zhao, Y. Gong and J. Xiang, High-Performance Broadband Photodetectors of Heterogeneous 2D Inorganic Molecular Sb<sub>2</sub>O<sub>3</sub>/Monolayer MoS<sub>2</sub> Crystals Grown via Chemical Vapor Deposition, *Adv. Opt. Mater.*, 2020, 2000168.

373 X. Zhai, X. Xu, J. Peng, F. Jing, Q. Zhang, H. Liu and Z. Hu, Enhanced Optoelectronic Performance from CVD-grown Metal-semiconductor NiTe<sub>2</sub>/MoS<sub>2</sub> Heterostructures, *ACS Appl. Mater. Interfaces*, 2020, **12**, 24093–24101.

374 G. H. Shin, C. Park, K. J. Lee, H. J. Jin and S. Y. Choi, Ultrasensitive Phototransistor Based on WSe<sub>2</sub>–MoS<sub>2</sub> van der Waals Heterojunction, *Nano Lett.*, 2020, DOI: 10.1021/acs.nanolett.0c01460.

375 H. Ying, X. Li, H. Wang, Y. Wang, X. Hu, J. Zhang, X. Zhang, Y. Shi, M. Xu and Q. Zhang, Band Structure Engineering in MoS<sub>2</sub> Based Heterostructures toward High-Performance Phototransistors, *Adv. Opt. Mater.*, 2020, 2000430.

376 J. Meng, G. Wang, X. Li, X. Lu, J. Zhang, H. Yu, W. Chen, L. Du, M. Liao, J. Zhao and P. Chen, Rolling up a monolayer MoS<sub>2</sub> sheet, *Small*, 2016, **12**, 3770–3774.

377 P. Thangasamy and M. Sathish, Rapid, one-pot synthesis of luminescent MoS<sub>2</sub> nanoscrolls using supercritical fluid processing, *J. Mater. Chem. C*, 2016, **4**, 1165–1169.

378 Z. Wang, H. H. Wu, Q. Li, F. Besenbacher, X. C. Zeng and M. Dong, Self-scrolling MoS<sub>2</sub> metallic wires, *Nanoscale*, 2018, **10**, 18178–18185.

379 X. Fang, P. Wei, L. Wang, X. Wang, B. Chen, Q. He, Q. Yue, J. Zhang, W. Zhao, J. Wang and G. Lu, Transforming Monolayer Transition-Metal Dichalcogenide Nanosheets into One-Dimensional Nanoscrolls with High Photosensitivity, *ACS Appl. Mater. Interfaces*, 2018, **10**, 13011–13018.

380 W. Deng, X. Chen, Y. Li, C. You, F. Chu, S. Li, B. An, Y. Ma, L. Liao and Y. Zhang, Strain Effect Enhanced Ultrasensitive MoS<sub>2</sub> Nanoscroll Avalanche Photodetector, *J. Phys. Chem. Lett.*, 2020, **11**, 4490–4497.

381 W. Deng, C. You, X. Chen, Y. Wang, Y. Li, B. Feng, K. Shi, Y. Chen, L. Sun and Y. Zhang, High-Performance Photodiode Based on Atomically Thin WSe<sub>2</sub>/MoS<sub>2</sub> Nanoscroll Integration, *Small*, 2019, **15**, 1901544.

382 L. Wang, Q. Yue, C. Pei, H. Fan, J. Dai, X. Huang, H. Li and W. Huang, Scrolling bilayer WS<sub>2</sub>/MoS<sub>2</sub> heterostructures for high-performance photo-detection, *Nano Res.*, 2020, **13**, 959–966.

383 S. K. Jain, R. R. Kumar, N. Aggarwal, P. Vashishtha, L. Goswami, S. Kuriakose, A. Pandey, M. Bhaskaran, S. Walia and G. Gupta, Current Transport and Band Alignment Study of MoS<sub>2</sub>/GaN and MoS<sub>2</sub>/AlGaN Heterointerfaces for Broadband Photodetection Application, *ACS Appl. Electron. Mater.*, 2020, **2**, 710–718.

384 J. Han, J. Li, W. Liu, H. Li, X. Fan and K. Huang, A novel flexible broadband photodetector based on flower-like MoS<sub>2</sub> microspheres, *Opt. Commun.*, 2020, 125931.

385 K. Hou, Z. Huang, S. Liu, G. Liao, H. Qiao, H. Li and X. Qi, Hydrothermally synthesized MoS<sub>2(1-x)Se<sub>2x</sub></sub> alloy with deep-shallow level conversion for enhanced the performance of photodetector, *Nanoscale Adv.*, 2020, **2**, 2185–2191.

386 Y. R. Lim, J. K. Han, Y. Yoon, J. B. Lee, C. Jeon, M. Choi, H. Chang, N. Park, J. H. Kim, Z. Lee, W. Song, S. Myung, S. K. Lee, K. S. An, J. H. Ahn and J. Lim, Atomic-Level Customization of 4 in. Transition Metal Dichalcogenide Multilayer Alloys for Industrial Applications, *Adv. Mater.*, 2019, **31**, 1901405.

387 J. Jeon, H. Choi, S. Choi, J. H. Park, B. H. Lee, E. Hwang and S. Lee, Transition-Metal-Carbide (Mo<sub>2</sub>C) Multiperiod Gratings for Realization of High-Sensitivity and Broad-Spectrum Photodetection, *Adv. Funct. Mater.*, 2019, **29**, 1905384.

388 T. Ahmed, K. Roy, S. Kakkar, A. Pradhan and A. Ghosh, Interplay of charge transfer and disorder in optoelectronic response in Graphene/hBN/MoS<sub>2</sub> van der Waals heterostructures, *2DMaterials*, 2020, **7**, 025043.

389 N. Abraham and K. Majumdar, *Unified benchmarking and characterization protocol for nanomaterial-based*



heterogeneous photodetector technologies, 2020, arXiv preprint arXiv:2005.04385.

390 (a) G. Konstantatos, I. Howard, A. Fischer, S. Hoogland, J. Clifford, E. Klem, L. Levina and E. H. Sargent, Ultrasensitive solution-cast quantum dot photodetectors, *Nature*, 2006, **442**, 180–183; (b) G. Konstantatos, J. Clifford, L. Levina and E. H. Sargent, Sensitive solution-processed visible-wavelength photodetectors, *Nat. Photonics*, 2007, **1**, 531–534; (c) D. K. Hwang, Y. T. Lee, H. S. Lee, Y. J. Lee, S. H. Shokouh, J. H. Kyhm, J. Lee, H. H. Kim, T. H. Yoo, S. H. Nam and D. I. Son, Ultrasensitive PbS quantum-dot-sensitized InGaZnO hybrid photoconverter for near-infrared detection and imaging with high photogain, *NPG Asia Mater.*, 2016, **8**, e233.

391 B. Jaffe, *Piezoelectric Ceramics*, Elsevier, 2012.

392 *Advanced Piezoelectric Materials: Science and Technology*, ed. K. Uchino, Woodhead Publishing, 2017.

393 *Ferroelectric Polymers: Chemistry, Physics, and Applications*, ed. H. S. Nalwa, CRC Press, Boca Raton, Florida, 1995.

394 H. S. Nalwa, Recent developments in ferroelectric polymers, *Journal of Macromolecular Science, Part C: Polymer Reviews*, 1991, **31**, 341–432.

395 A. Yanaka, W. Sakai, K. Kinashi and N. Tsutsumi, Ferroelectric performance of nylons 6-12, 10-12, 11-12, and 12-12, *RSC Adv.*, 2020, **10**, 15740–15750.

396 E. Fukada, Piezoelectricity of Biopolymers, *Biorheology*, 1995, **32**, 593–609.

397 E. Fukada and Y. Ando, Piezoelectricity in oriented DNA films, *J. Polym. Sci., Part A-2*, 1972, **10**, 565–567.

398 C. Halperin, S. Mutchnik, A. Agronin, M. Molotskii, P. Urenski, M. Salai and G. Rosenman, Piezoelectric effect in human bones studied in nanometer scale, *Nano Lett.*, 2004, **4**, 1253–1256.

399 C. R. Bowen, H. A. Kim, P. M. Weaver and S. Dunn, Piezoelectric and ferroelectric materials and structures for energy harvesting applications, *Energy Environ. Sci.*, 2014, **7**, 25–44.

400 H. Li, C. Tian and Z. D. Deng, Energy harvesting from low frequency applications using piezoelectric materials, *Appl. Phys. Rev.*, 2014, **1**, 041301.

401 H. A. Sodano, D. J. Inman and G. Park, A review of power harvesting from vibration using piezoelectric materials, *Shock and Vibration Digest*, 2004, **36**, 197–206.

402 J. M. Cannata and Q. F. Zhou, Piezoelectric materials for high frequency medical imaging applications: A review, *J. Electroceram.*, 2007, **19**, 141–147.

403 R. Hinchet, U. Khan, C. Falconi and S. W. Kim, Piezoelectric properties in two-dimensional materials: Simulations and experiments, *Mater. Today*, 2018, **21**, 611–630.

404 L. Huang, Y. Li, Z. Wei and J. Li, Strain induced piezoelectric effect in black phosphorus and MoS<sub>2</sub> van der Waals heterostructure, *Sci. Rep.*, 2015, **5**, 1–7.

405 C. Cui, F. Xue, W. J. Hu and L. J. Li, Two-dimensional materials with piezoelectric and ferroelectric functionalities, *npj 2D Mater. Appl.*, 2018, **2**, 1–14.

406 Y. Guo, S. Zhou, Y. Bai and J. Zhao, Enhanced piezoelectric effect in Janus group-III chalcogenide monolayers, *Appl. Phys. Lett.*, 2017, **110**, 163102.

407 X. Zhang, Y. Cui, L. Sun, M. Li, J. Du and Y. Huang, Stabilities, and electronic and piezoelectric properties of two-dimensional tin dichalcogenide derived Janus monolayers, *J. Mater. Chem. C*, 2019, **7**, 13203–13210.

408 J. Zhang, On the piezopotential properties of two-dimensional materials, *Nano Energy*, 2019, **58**, 568–578.

409 V. J. González, A. M. Rodríguez, I. Payo and E. Vázquez, Mechanochemical preparation of piezoelectric nanomaterials: BN, MoS<sub>2</sub> and WS<sub>2</sub> 2D materials and their glycine-cocrystals, *Nanoscale Horiz.*, 2020, **5**, 331–335.

410 A. Rawat, M. K. Mohanta, N. Jena, Dimple, R. Ahammed and A. De Sarkar, Nanoscale interfaces of Janus monolayers of transition metal dichalcogenides for 2D photovoltaic and piezoelectric applications, *J. Phys. Chem. C*, 2020, **124**, 10385–10397.

411 S. K. Kim, R. Bhatia, T. H. Kim, D. Seol, J. H. Kim, H. Kim, W. Seung, Y. Kim, Y. H. Lee and S. W. Kim, Directional dependent piezoelectric effect in CVD grown monolayer MoS<sub>2</sub> for flexible piezoelectric nanogenerators, *Nano Energy*, 2016, **22**, 483–489.

412 M. Y. Tsai, A. Tarasov, Z. R. Hesabi, H. Taghinejad, P. M. Campbell, C. A. Joiner, A. Adibi and E. M. Vogel, Flexible MoS<sub>2</sub> field-effect transistors for gate-tunable piezoresistive strain sensors, *ACS Appl. Mater. Interfaces*, 2015, **7**, 12850–12855.

413 J. Guo, R. Wen, J. Zhai and Z. L. Wang, Enhanced NO<sub>2</sub> gas sensing of a single-layer MoS<sub>2</sub> by photogating and piezo-phototronic effects, *Sci. Bull.*, 2019, **64**, 128–135.

414 K. Zhang, J. Zhai and Z. L. Wang, A monolayer MoS<sub>2</sub> pn homogenous photodiode with enhanced photoresponse by piezo-phototronic effect, *2D Mater.*, 2018, **5**, 035038.

415 L. Tong, X. Duan, L. Song, T. Liu, L. Ye, X. Huang, P. Wang, Y. Sun, X. He, L. Zhang and K. Xu, Artificial control of in-plane anisotropic photoelectricity in monolayer MoS<sub>2</sub>, *Appl. Mater. Today*, 2019, **15**, 203–211.

416 P. Lin, L. Zhu, D. Li, L. Xu, C. Pan and Z. Wang, Piezo-phototronic effect for enhanced flexible MoS<sub>2</sub>/WSe<sub>2</sub> van der Waals photodiodes, *Adv. Funct. Mater.*, 2018, **28**, 1802849.

417 F. Xue, L. Chen, J. Chen, J. Liu, L. Wang, M. Chen, Y. Pang, X. Yang, G. Gao, J. Zhai and Z. L. Wang, p-Type MoS<sub>2</sub> and n-Type ZnO diode and its performance enhancement by the piezophototronic effect, *Adv. Mater.*, 2016, **28**, 3391–3398.

418 F. Xue, L. Yang, M. Chen, J. Chen, X. Yang, L. Wang, L. Chen, C. Pan and Z. L. Wang, Enhanced photoresponsivity of the MoS<sub>2</sub>-GaN heterojunction diode via the piezo-phototronic effect, *NPG Asia Mater.*, 2017, **9**, e418.

419 F. Li, T. Shen, L. Xu, C. Hu and J. Qi, Strain improving the performance of a flexible monolayer MoS<sub>2</sub> photodetector, *Adv. Electron. Mater.*, 2019, **5**, 1900803.



420 P. Gant, P. Huang, D. P. de Lara, D. Guo, R. Frisenda and A. Castellanos-Gomez, A strain tunable single-layer MoS<sub>2</sub> photodetector, *Mater. Today*, 2019, **27**, 8–13.

421 H. Qiao, Z. Huang, X. Ren, S. Liu, Y. Zhang, X. Qi and H. Zhang, Self-powered photodetectors based on 2D materials, *Adv. Opt. Mater.*, 2020, **8**, 1900765.

422 S. Li, Z. He, Y. Ke, J. Guo, T. Cheng, T. Gong, Y. Lin, Z. Liu, W. Huang and X. Zhang, Ultra-sensitive self-powered photodetector based on vertical MoTe<sub>2</sub>/MoS<sub>2</sub> heterostructure, *Appl. Phys. Express*, 2019, **13**, 015007.

423 Z. Yang, B. Jiang, Z. Zhang, Z. Wang, X. He, D. Wan, X. Zou, X. Liu, L. Liao and F. Shan, The photovoltaic and photoconductive photodetector based on GeSe/2D semiconductor van der Waals heterostructure, *Appl. Phys. Lett.*, 2020, **116**, 141101.

424 Y. Xin, X. Wang, Z. Chen, D. Weller, Y. Wang, L. Shi, X. Ma, C. Ding, W. Li, S. Guo and R. Liu, Polarization-Sensitive Self-Powered Type-II GeSe/MoS<sub>2</sub> van der Waals Heterojunction Photodetector, *ACS Appl. Mater. Interfaces*, 2020, **12**, 15406–15413.

425 D. H. Shin, S. H. Shin and S. H. Choi, Self-powered and flexible perovskite photodiode/solar cell bifunctional devices with MoS<sub>2</sub> hole transport layer, *Appl. Surf. Sci.*, 2020, **514**, 145880.

426 D. H. Shin, J. S. Ko, S. K. Kang and S. H. Choi, Enhanced Flexibility and Stability in Perovskite Photodiode–Solar Cell Nanosystem Using MoS<sub>2</sub> Electron-Transport Layer, *ACS Appl. Mater. Interfaces*, 2020, **12**, 4586–4593.

427 Z. He, J. Guo, S. Li, Z. Lei, L. Lin, Y. Ke, W. Jie, T. Gong, Y. Lin, T. Cheng and W. Huang, GaSe/MoS<sub>2</sub> Heterostructure with Ohmic-Contact Electrodes for Fast, Broadband Photoresponse, and Self-Driven Photodetectors, *Adv. Mater. Interfaces*, 2020, **7**, 2070050.

428 A. V. Agrawal, K. Kaur and M. Kumar, Interfacial study of vertically aligned n-type MoS<sub>2</sub> flakes heterojunction with p-type Cu-Zn-Sn-S for self-powered, fast and high performance broadband photodetector, *Appl. Surf. Sci.*, 2020, **514**, 145901.

429 A. V. Agrawal and M. Kumar, Enhance near infrared performance of n-type vertically aligned MoS<sub>2</sub> flakes photodetector with active p-type CZTS electrodes, *Mater. Res. Express*, 2019, **6**, 115011.

430 C. Jia, D. Wu, E. Wu, J. Guo, Z. Zhao, Z. Shi, T. Xu, X. Huang, Y. Tian and X. Li, A self-powered high-performance photodetector based on a MoS<sub>2</sub>/GaAs heterojunction with high polarization sensitivity, *J. Mater. Chem. C*, 2019, **7**, 3817–3821.

431 S. S. Sarkar, S. Mukherjee, R. K. Khatri and S. K. Ray, Solution-processed MoS<sub>2</sub> quantum dot/GaAs vertical heterostructure based self-powered photodetectors with superior detectivity, *Nanotechnology*, 2020, **31**, 135203.

432 K. Shi, J. Li, Y. Xiao, L. Guo, X. Chu, Y. Zhai, B. Zhang, D. Lu and F. Rosei, High-response, ultrafast-speed and self-powered photodetection achieved in InP@ZnS-MoS<sub>2</sub> phototransistors with interdigitated Pt electrodes, *ACS Appl. Mater. Interfaces*, 2020, **12**, 31382–31391.

433 D. K. Singh, R. Pant, A. M. Chowdhury, B. Roul, K. K. Nanda and S. B. Krupanidhi, Defect-Mediated Transport in Self-Powered, Broadband, and Ultrafast Photoresponse of a MoS<sub>2</sub>/AlN/Si-Based Photodetector, *ACS Appl. Electron. Mater.*, 2020, **2**, 944–953.

434 R. Zhang, X. Ma, C. An, D. Zhang, D. Sun, X. Hu and J. Liu, Self-powered photodetector based on vertical MoO<sub>3</sub>/MoS<sub>2</sub> hetero-structure with gate tunable photo-response, *2D Mater.*, 2019, **6**, 035033.

435 H. Xu, J. Zhu, G. Zou, W. Liu, X. Li, C. Li, G. H. Ryu, W. Xu, X. Han, Z. Guo and J. H. Warner, Spatially Bandgap-Graded MoS<sub>2(1-x)Se<sub>2x</sub></sub> Homojunctions for Self-Powered Visible-Near-Infrared Phototransistors, *Nano-Micro Lett.*, 2020, **12**, 26.

436 L. Han, M. Peng, Z. Wen, Y. Liu, Y. Zhang, Q. Zhu, H. Lei, S. Liu, L. Zheng, X. Sun and H. Li, Self-driven photodetection based on impedance matching effect between a triboelectric nanogenerator and a MoS<sub>2</sub> nanosheets photodetector, *Nano Energy*, 2019, **59**, 492–499.

437 L. Zhao, K. Chen, F. Yang, M. Zheng, J. Guo, G. Gu, B. Zhang, H. Qin, G. Cheng and Z. Du, The novel transistor and photodetector of monolayer MoS<sub>2</sub> based on surface-ionic-gate modulation powered by a triboelectric nanogenerator, *Nano Energy*, 2019, **62**, 38–45.

438 Y. Zhang, Y. Yu, X. Wang, G. Tong, L. Mi, Z. Zhu, X. Geng and Y. Jiang, Solution assembly MoS<sub>2</sub> nanopetals/GaAs n-n homotype heterojunction with ultrafast and low noise photoresponse using graphene as carrier collector, *J. Mater. Chem. C*, 2017, **5**, 140–148.

439 R. Zhuo, D. Wu, Y. Wang, E. Wu, C. Jia, Z. Shi, T. Xu, Y. Tian and X. Li, A self-powered solar-blind photodetector based on a MoS<sub>2</sub>/β-Ga<sub>2</sub>O<sub>3</sub> heterojunction, *J. Mater. Chem. C*, 2018, **6**, 10982–10986.

440 L. Z. Hao, W. Gao, Y. J. Liu, Y. M. Liu, Z. D. Han, Q. Z. Xue and J. Zhu, Self-powered broadband, high-detectivity and ultrafast photodetectors based on Pd-MoS<sub>2</sub>/Si heterojunctions, *Phys. Chem. Chem. Phys.*, 2016, **18**, 1131–1139.

441 X. Liu, F. Li and J. Qi, Self-powered, high response and fast response speed metal-insulator-semiconductor structured photodetector based on 2D MoS<sub>2</sub>, *RSC Adv.*, 2018, **8**, 28041.

442 Z. Chen, Z. Zhang, J. Biscaras and A. Shukla, A high performance self-driven photodetector based on a graphene/InSe/MoS<sub>2</sub> vertical heterostructure, *J. Mater. Chem. C*, 2018, **6**, 12407–12412.

443 S. Yang, K. Liu, W. Han, L. Li, F. Wang, X. Zhou, H. Li and T. Zhai, Salt-Assisted Growth of P-type Cu<sub>9</sub>S<sub>5</sub> Nanoflakes for P-N Heterojunction Photodetectors with High Responsivity, *Adv. Funct. Mater.*, 2020, **30**, 1908382.

444 J. F. Gonzalez Marin, D. Unuchek, K. Watanabe, T. Taniguchi and A. Kis, MoS<sub>2</sub> photodetectors integrated with photonic circuits, *npj 2D Mater. Appl.*, 2019, **3**, 14.

445 S. G. Kim, S. H. Kim, J. Park, G. S. Kim, J. H. Park, K. C. Saraswat, J. Kim and H. Y. Yu, Infrared Detectable MoS<sub>2</sub> Phototransistor and Its Application to Artificial Multilevel Optic-Neural Synapse, *ACS Nano*, 2019, **13**, 10294–10300.



446 J. Li, C. Nie, F. Sun, L. Tang, Z. Zhang, J. Zhang, Y. Zhao, J. Shen, S. Feng, H. Shi and X. Wei, Enhancement of the Photoresponse of Monolayer MoS<sub>2</sub> Photodetectors Induced by a Nanoparticle Grating, *ACS Appl. Mater. Interfaces*, 2020, **12**, 8429–8436.

447 N. Mutz, S. Park, T. Schultz, S. Sadofev, S. Dalglish, L. Reissig, N. Koch, E. J. List-Kratochvil and S. Blumstengel, Excited State Charge Transfer Enabling MoS<sub>2</sub>/Phthalocyanine Photodetectors with Extended Spectral Sensitivity, *J. Phys. Chem. C*, 2020, **124**, 2837–2843.

448 H. Y. Jang, J. H. Nam, J. Yoon, Y. Kim, W. Park and B. Cho, One-step H<sub>2</sub>S reactive sputtering for 2D MoS<sub>2</sub>/Si heterojunction photodetector, *Nanotechnology*, 2020, **31**, 225205.

449 S. Pal, S. Mukherjee, M. Nand, H. Srivastava, C. Mukherjee, S. N. Jha and S. K. Ray, Si compatible MoO<sub>3</sub>/MoS<sub>2</sub> core-shell quantum dots for wavelength tunable photodetection in wide visible range, *Appl. Surf. Sci.*, 2020, **502**, 144196.

450 L. Liu, K. Ye, Z. Yu, Z. Jia, J. Xiang, A. Nie, F. Wen, C. Mu, B. Wang, Y. Li and Y. Gong, Photodetection application of one-step synthesized wafer-scale monolayer MoS<sub>2</sub> by chemical vapor deposition, *2D Mater.*, 2020, **7**, 025020.

451 B. P. Majee, Bhawna, A. Singh, R. Prakash and A. K. Mishra, Large Area Vertically Oriented Few-Layer MoS<sub>2</sub> for Efficient Thermal Conduction and Optoelectronic Applications, *J. Phys. Chem. Lett.*, 2020, **11**, 1268–1275.

452 S. Singh and H. S. Nalwa, Nanotechnology and health safety-toxicity and risk assessments of nanostructured materials on human health, *J. Nanosci. Nanotechnol.*, 2007, **7**, 3048–3070.

453 *Nanotoxicology: Interactions of Nanomaterials with Biological Systems*, ed. Y. Zhao and H. S. Nalwa, American Scientific Publishers, Los Angeles, 2007.

454 E. L. K. Chng and M. Pumera, Toxicity of graphene related materials and transition metal dichalcogenides, *RSC Adv.*, 2015, **5**, 3074–3080.

455 W. Z. Teo, E. L. K. Chng, Z. Sofer and M. Pumera, Cytotoxicity of exfoliated transition-metal dichalcogenides (MoS<sub>2</sub>, WS<sub>2</sub>, and WSe<sub>2</sub>) is lower than that of graphene and its analogues, *Chem.-Eur. J.*, 2014, **20**, 9627–9632.

456 E. L. K. Chng, Z. Sofer and M. Pumera, MoS<sub>2</sub> exhibits stronger toxicity with increased exfoliation, *Nanoscale*, 2014, **6**, 14412–14418.

457 E. Tan, B. L. Li, K. Ariga, C. T. Lim, S. Garaj and D. T. Leong, Toxicity of Two-Dimensional Layered Materials and Their Heterostructures, *Bioconjugate Chem.*, 2019, **30**, 2287–2299.

458 P. Yang, S. Ke, L. Tu, Y. Wang, S. Ye, S. Kou and L. Ren, Regulation of Autophagy Orchestrates Pyroptotic Cell Death in Molybdenum Disulfide Quantum Dot-Induced Microglial Toxicity, *ACS Biomater. Sci. Eng.*, 2020, **6**, 1764–1775.

459 C. C. Sheeja, A. Anusri, C. Levna, P. M. Aneesh and D. Lekha, MoS<sub>2</sub> nanoparticles induce behavioral alteration and oxidative stress mediated cellular toxicity in the social insect *Oecophylla smaragdina* (Asian weaver ant), *J. Hazard. Mater.*, 2020, **385**, 121624.

460 X. Zhou, H. Sun and X. Bai, Two-Dimensional Transition Metal Dichalcogenides: Synthesis, Biomedical Applications and Biosafety Evaluation, *Front. Bioeng. Biotechnol.*, 2020, **8**, 236.

